

**Cátia Manuela
Rodrigues Pinho**

**Otimização de Soluções de Fotónica Integrada para
Sistemas Óticos de Nova Geração**

**Optimized Photonic Integrated Solutions for Next
Generation Optical Systems**

Cátia Manuela
Rodrigues Pinho

Otimização de Soluções de Fotónica Integrada para
Sistemas Óticos de Nova Geração

Optimized Photonic Integrated Solutions for Next
Generation Optical Systems

Tese apresentada à Universidade de Aveiro para cumprimento dos requisitos necessários à obtenção do grau de Doutor em Telecomunicações no âmbito do programa doutoral MAP-tele, programa conjunto entre as Universidades de Aveiro, Minho e Porto, realizada sob a orientação científica do Doutor António Luís Jesus Teixeira, Professor Associado com agregação do Departamento de Eletrónica, Telecomunicações e Informática da Universidade de Aveiro, e sob coorientação do Doutor Mário José Neves de Lima, Professor Auxiliar do Departamento de Eletrónica, Telecomunicações e Informática da Universidade de Aveiro.



This work was funded by national funds through FCT - *Fundação para a Ciência e a Tecnologia* under the Ph.D. scholarship PD/BD/105858/2014. Additional financial support was given by FCT/MEC/MCTES and when applicable co-funded by FEDER - PT2020 partnership agreement under the project Compress PTDC/EEITEL/7163/2014; IT (UID/EEA/50008/2019); the CENTRO - PT2020 framework project HeatIT (CENTRO-01-0247-FEDER-017942); the COMPETE - PT2020 framework project Virtual Fiber Box (POCI-01-0247-FEDER-033910); and the COST action CA16220 European Network for High-Performance Integrated Microwave Photonics (EUMWP).

O júri

Presidente

Prof. Doutor Delfim Fernando Marado Torres
Professor Catedrático da Universidade de Aveiro

Prof. Doutora Maria do Carmo Raposo de Medeiros
Professora Associada da Universidade de Coimbra

Prof. Doutor Paulo Vicente da Silva Marques
Professor Associado da Universidade do Porto - Faculdade de Ciências

Prof. Doutor Henrique Manuel de Castro Faria Salgado
Professor Associado da Universidade do Porto

Prof. Doutor Fernando Pedro Pereira Guiomar
Investigador do Instituto de Telecomunicações da Universidade de Aveiro

Prof. Doutor António Luís Jesus Teixeira
Professor Associado c/ Agregação da Universidade de Aveiro

Dedico este trabalho aos meus pais e irmão
por todo o amor e apoio.

Agradecimentos

Sentindo como certo o apoio com que somos brindados nas diferentes etapas da nossa vida, é com grande comoção que agradeço a todos que desde o apoio mais singelo ao mais empenhado contribuíram para a elaboração e conclusão deste trabalho de doutoramento. Começo por distinguir o extraordinário apoio do meu orientador Professor Doutor António Teixeira e coorientador Professor Doutor Mário Lima, pela forma incansável e compreensiva com que me motivaram e guiaram em todo o processo de investigação e produção científica. Os ensinamentos e essencial discussão de ideias, foram fundamentais para a resolução das diferentes questões científicas levantadas. É também com grande reconhecimento que agradeço a impulsão dada no sentido de alargar horizontes para além do confortável da nossa Instituição, promovendo a realização de três missões científicas internacionais. Nomeadamente, na Universidade de Santa Barbara, na qual agradeço a oportunidade de trabalhar em projetos do grupo OCPI, coordenados pelo Professor Doutor D. Blumenthal, salientando a colaboração e amizade de todos os colegas, especialmente o Mestre G. Brodnik e Doutor S. Gundavarapu. Na Universidade de Cambridge, agradeço a oportunidade facultada pelo Professor Doutor T. Wilkinson e a colaboração da equipa do CMMPE, salientando o apoio do Doutor G. Gordon durante a implementação experimental. Na Universidade Politécnica de Valência, agradeço a oportunidade facultada pelo Professor Doutor P. Muñoz e a colaboração da Mestre G. Micó.

Ao Instituto de Telecomunicações e Universidade de Aveiro, agradeço o valioso suporte institucional e logístico, acolhendo-me no desenvolvimento deste doutoramento. Aos colegas investigadores e funcionários do referido centro de investigação, agradeço a ajuda e colaboração na resolução de variadas problemáticas científicas, bem como a simpatia que tornou mais alegre a jornada. Saliento apenas alguns nomes, Doutores B. Neto, A. R. Bastos, D. Dinis, I. Alimi e A. Rocha; Mestres T. Morgado, S. Pandey, V. Duarte, M. Ramos e L. Sousa; Engenheiros J. Prata, P. Gonçalves, N. Silva e Y. Sucá; e o apoio de todo o *staff* administrativo do IT e DETI.

Ao programa doutoral MAP-tele agradeço a oportunidade de realizar este projeto de doutoramento e o suporte financeiro proporcionado pela Fundação para a Ciência e Tecnologia. De salientar ainda, os conhecimentos e promoção da descoberta científica fomentada pelos Professores, bem como o companheirismo e grande apoio de todos os colegas. À empresa PICadvanced agradeço a colaboração e suporte logístico nas diferentes etapas científicas, bem como o apoio de toda a equipa, nomeadamente os Mestres F. Rodrigues, A. Maia, H. Neto, C. Rodrigues e G. Cabral, e Doutor R. Ferreira. Aos colegas do OSA *student chapter* da UA agradeço o voluntarismo e criatividade no desenvolvimento de projetos académicos e em comunidade na área da ótica e fotónica.

Agradeço ainda a todos os meus amigos e família, cujo amor e carinho me acompanha sempre, referindo de forma singela, L. F. Pinho, S. e V. Pinho, Mi E., A. L. Oliveira, E. Vasconcelos, a malta do grupo de Aveiro, os amigos do N.L., e uma amiga muito especial que já não estando entre nós fisicamente é deveras querida, R. Filipe. Por fim, reconhecendo-lhes a grandiosidade em amor e valores, agradeço aos meus pais, cujo apoio incondicional e acreditar inabalável me acompanham desde o primeiro dia de vida.

"We win with people!".

A todos, um enternecido muito obrigada!

Palavras-chave

Circuitos de fotônica integrada (PIC), soluções integralmente óticas, processamento de sinal ótico, interferência multimodal (MMI), otimização de fotônica integrada, modelador ótico espacial (SLM), plataforma flexível de modelação ótica espacial, sistemas óticos de nova geração.

Resumo

Os sistemas óticos de nova geração beneficiam com a otimização de fotônica integrada. Com os circuitos de fotônica integrada (PIC) avançados a surgir como uma tecnologia promissora, dentro da crescente procura por flexibilidade/reconfigurabilidade dos sistemas óticos e redes de telecomunicações. Os sistemas óticos baseados em PIC oferecem soluções eficientes e rentáveis em resposta às necessidades crescentes de transmissão de dados. De modo a contribuir para o desenvolvimento tecnológico associado à fotônica integrada, são investigados no âmbito desta dissertação diferentes soluções otimizadas de PIC, abordando diferentes estágios do seu desenvolvimento, nomeadamente projeto/design, teste e encapsulamento.

Técnicas de compressão de sinais óticos estão a progredir no sentido de apoiar a expansão de velocidade de processamento e quantidade de armazenamento com elevada largura de banda associada. São esperadas vantagens recorrendo a PIC para a implementação de transformadas óticas, e.g., transformada de Haar (HT). Esta necessidade motivou a investigação de soluções de PIC com design otimizado, desenvolvidas em plataforma integrada de nitreto de silício (Si_3N_4). O PIC desenhado é constituído por uma rede 2D a executar a HT para fins de compressão e uma rede de comutação para produzir todas as entradas lógicas esperadas para teste e caracterização. São propostos modelos de design otimizados para a estrutura elementar que compõe o PIC, i.e., componente de interferência multimodal. Adicionalmente, foi realizado o primeiro teste e caracterização experimental de um PIC implementando a HT para fins de compressão, numa plataforma integrada de fosfato de índio (InP) e num material orgânico-inorgânico híbrido.

Tirando partido de um filtro sintonizável para compensação de dispersão, desenvolvido em plataforma integrada de Si_3N_4 , foi demonstrado um link de transmissão alargada (40 km) em modulação PAM-4, com possível aplicação em centros de processamento de dados de interconexão. A necessidade de medições precisas de desempenho para a caracterização efetiva de soluções integradas de ressoadores de elevado fator de qualidade, motivou a implementação de uma técnica de medição eficaz. Esta é baseada num interferómetro de Mach-Zehnder calibrado em rádio frequência e na realização de mediações de ganho de Brillouin por análise Lorentziana de ajuste de curva. Por fim, tendo em conta os rigorosos requisitos técnicos e funcionais associados ao teste/caracterização precisa de PIC e o facto de as atuais soluções serem dispendiosas e pouco flexíveis. Uma prova de conceito de uma nova plataforma flexível de encapsulamento por software é proposta com aplicação em processadores PIC e sistemas com multiplexagem por divisão espacial.

Keywords

Photonic integrated circuits (PIC), all-optical integrated solutions, optical signal processing, multimode interference (MMI), optimized integrated photonics, spatial light modulation (SLM), SLM flexible platform, next generation optical systems.

Abstract

Next generation optical systems can highly benefit from optimized photonic integrated solutions. Photonic integrated circuits (PIC) appear as a promising technology under the current demand for flexibility/reconfigurability in optical systems and telecommunications networks. PIC-based optical systems offer an efficient and cost-effective solution to data transmission increasing claims. In order to contribute to the development of integrated photonic technology, optimized PIC solutions addressing different steps of the PIC development chain, mainly design, testing, and packaging processes, are investigated.

Optical signal data compression techniques are progressing to sustain the fast processing/storing of large amounts of bandwidth demanding data, with the advantage of resorting to photonic integrated solutions for the implementation of optical transforms, e.g., Haar transform (HT). This demand motivated the research of an optimized PIC design solution in silicon nitride (Si_3N_4) based platform comprising a two-level HT network for compression, and a switching network as a framework that supplies all logical inputs of the HT network for testing/characterization purposes. Optimized design models for the multimode interference key building block structure of the PIC design solution, are proposed. Additionally, a first test and characterization of PIC solutions implementing the HT for compression applications in indium phosphide (InP) based platform and in a new organic-inorganic hybrid material were realized. Taking advantage of a tunable lattice filter dispersion compensator in Si_3N_4 -based integrated platform, it was demonstrated a real-time extended reach PAM-4 transmission over 40 km enabled by the photonic integrated dispersion compensator, with application in data center interconnects. Under photonic integrated high-Q resonators need for accurate performance measurement, a technique based on RF calibrated Mach-Zehnder interferometer, and Brillouin gain measurements through Lorentzian fitting analysis were successfully attained.

Finally, as technical and functional requirements of PIC demand a thorough characterization/testing to provide an accurate prediction of its performance, and current testing platforms can be expensive and have low flexibility, a proof of concept of a new soft-packaging flexible platform for photonic integrated processors and spatial division multiplexing systems, based in spatial light modulation operation principle is proposed.

*“Na vida e na ciência que a perseverança
e elevação de propósito sejam uma constante”*

*“In life and in science be perseverance
and higher purpose held constant”*

Cátia Pinho

Contents

List of Figures	v
List of Tables	xiii
Acronyms	xv
Symbols	xxi
1 Introduction	1
1.1 Photonic integrated technology	4
1.2 Research contributions	9
1.2.1 Awards	10
1.2.2 Scientific papers	10
1.2.3 Scientific communications	11
1.2.4 Book chapters	13
1.2.5 Supplementary research/training	14
1.3 Thesis Outline	15
2 Optical integrated approaches for data compression applications	17
2.1 All-optical system architecture for data compression based in HT	20
2.2 Reconfigurable HT PIC design in a Si ₃ N ₄ integrated platform	24
2.2.1 Method	24
2.2.1.1 MMI optical interference principle	25
2.2.1.2 Design rules and procedures methodology	27
2.2.1.3 Design architecture for the integrated Si ₃ N ₄ HT implementation	30
2.2.1.4 BB structure design optimization	34
2.2.1.5 BB design assessment methodology	37
2.2.2 Results and discussion	41
2.2.2.1 Optimized BB design for 2×2 MMI BB structure	41
2.2.2.2 Optimized BB design for 1×2 MMI BB structure	49
2.3 Chapter remarks	55

3	Implementation and testing of integrated HT	57
3.1	HT implementation with AAC in an InP integrated platform	59
3.1.1	InP AAC optical chip – design and characterization	60
3.1.1.1	BPM simulations of theoretical AAC design	62
3.1.1.2	Experimental test and characterization of InP AAC optical chip	64
3.1.1.2.A	Packaging of InP AAC optical chip for testing	65
3.1.1.2.A.1	PCB design and fabrication	65
3.1.1.2.A.2	Management of PIC temperature and laser wavelength stability	67
3.1.1.2.A.3	Fiber coupling for optical measurements	67
3.1.1.2.B	Experimental characterization method	71
3.1.1.2.B.1	Simulation results	73
3.1.1.2.B.2	Experimental results	75
3.1.1.2.B.3	Discussion	76
3.1.2	InP HT optical chip – design and characterization	79
3.1.2.1	Experimental characterization of InP HT optical chip	81
3.1.2.1.A	Electrical measurements from PIN photodiodes	84
3.1.2.1.B	Optical measurements from SSC edge coupling	87
3.2	Integrated HT implementation in a hybrid material platform	90
3.2.1	Design and manufacturing	90
3.2.2	Simulation and experimental results	92
3.3	Chapter remarks	100
4	PIC solutions in an ultra-low loss silicon nitride platform	101
4.1	High-Q resonator measurement technique	103
4.1.1	RF calibrated MZI implementation	103
4.1.2	Setup for resonator characterization measurements	105
4.1.3	Measurement of resonator properties and applied fitting technique	106
4.2	Low-cost interface technology for DCI	109
4.2.1	Dispersion compensation photonic integrated tunable lattice filter	111
4.2.2	Experimental setup	113
4.2.3	Discussion	119
4.3	Chapter remarks	120

5	Spatial light modulator framework	121
5.1	SLM operation principle and applications	122
5.2	SLM framework methodology	126
5.2.1	CGH implemented methods	126
5.2.1.1	Iterative Fourier transform algorithm	127
5.2.1.2	Linear phase mask	128
5.2.1.3	Optimization of the CGH	130
5.2.2	SLM framework setup implementation	132
5.3	Experimental CGH results	136
5.3.1	SLM framework for SDM applications	136
5.3.2	SLM framework for PIC applications	138
5.3.2.1	Results and discussion.....	138
5.4	Chapter remarks.....	145
6	Conclusion and future work	147
	Bibliography	151
	Appendix A	
	BPM simulation results of Si₃N₄ BB designs	167
A.1	BB 2×2 MMI structures.....	168
A.1.1	BB 2×2 MMI – geometry A.....	168
A.1.2	BB 2×2 MMI – geometry B.....	170
A.1.3	BB 2×2 MMI – geometry C.....	172
A.2	BB 1×2 MMI structures.....	174
A.2.1	BB 1×2 MMI – geometry A.....	174
A.2.2	BB 1×2 MMI – geometry B.....	175
A.2.3	BB 1×2 MMI – geometry C.....	176

List of Figures

Figure 1. Recent enabling technologies motivating optical signal processing (OSP) research. Adapted from [21].	3
Figure 2. Global photonic integrated circuits (PIC) market from 2017 to 2023, with an expected compound annual growth rate (CAGR) of approximately 26%. Adapted from [41].	5
Figure 3. Comparison of key features from three of the major photonic integration technology platforms, i.e., InP, Si, and Si ₃ N ₄ . Adapted from [52] [53].	6
Figure 4. Overall functional capabilities and/or limitations associated with the InP, silicon and silicon nitride based integrated platforms. Adapted from [51].	6
Figure 5. Diagram of technology prospects for next generation of PIC, in order to realize future high speed, low cost, power-efficient photonic system-on-chip (SOC). Adapted from [51].	8
Figure 6. Diagram of two-level band decomposition using multi-resolution analysis based on wavelet transform. Low-pass (LP) and high-pass (HP) filters are applied two times to obtain the 1D transform (L and H components) and the 2D transform (LL, LH, HL and HH components). Adapted from [32].	20
Figure 7. All-optical scheme diagram of system BB for Haar wavelet transform processing and compression. 2D transform process schematic describes low-pass (L) and high-pass (H) filtering through sub-band decomposition [32].	21
Figure 8. Diagram of a 3 dB asymmetric optical coupler and scattering matrix given by S.	23
Figure 9. Propagation interference for MMI length $L = p3L_{\pi}$, with $(p = 0, 1, 2, \dots)$. Adapted from [89].	26
Figure 10. MMI symmetric propagation interference for MMI length $L = (p3L_{\pi})/N$, with $(N = 1, 2, 3, \dots)$. Adapted from [89].	26
Figure 11. Block diagram of the rules and procedures implemented for the MMI BB design, based in [89].	28
Figure 12. Schematic diagram of the deep WG structure from silicon nitride CNM design platform. W_{core} and H_{core} denote the WG Si ₃ N ₄ core width and height, respectively. $H_{1\text{clad}}$ and $H_{2\text{clad}}$ refer to the heights of WG SiO ₂ cladding.	29
Figure 13. Effective index of deep WG fundamental mode versus light propagation wavelength, for three different WG core widths (0.8 μm , 1.0 μm , and 1.2 μm). Transverse electric (TE) and transverse magnetic (TM) polarization are presented in continuous and dashed lines, respectively. The black dashed/dotted lines indicate the cutoff index of WG core ($n_{\text{coreSi}_3\text{N}_4}$) and cladding (n_{cladSiO_2}).	29

Figure 14. Diagram of the different designed MMI structures, in rectangular (geometry A) and butterfly (geometry B, C) geometric shapes. [D1]: Set of three MMI geometries of the 2×2 MMI BB tested to implement the two-level HT network and the switching network. [D2]: Set of three MMI geometries of the 1×2 MMI BB tested to implement the switching network. 31

Figure 15. Schematic diagram of the four input two-level HT network main block structure, composed by a cascade of three 2×2 MMI coupler BB, to realize the data compression. The diagram is not in scale. 32

Figure 16. Schematic diagram of the switching network main block structure, composed by a cascade of three 1×2 MMI splitter BB and two 2×2 MMI coupler BB, to address all logical inputs of the HT network. The diagram is not in scale. 33

Figure 17. Design parameters assessed for the optimization of the different MMI geometric structures (i.e., geometry A, B, and C). [D1]: Set of three MMI geometries for the 2×2 MMI BB. [D2]: Set of three MMI geometries for the 1×2 MMI BB..... 35

Figure 18. Diagram of iterations performed in the OptoDesigner scripts to calculate the BPM simulations and determine the optimized design for the 2×2 MMI BB structure..... 36

Figure 19. Diagram of the iterations performed in the OptoDesigner scripts to calculate the BPM simulations and determine the optimized design for the 1×2 MMI BB structure..... 37

Figure 20. Diagram of the general decision-making methodology implemented to quantitatively determine the best BB structure from the different implemented designs. 40

Figure 21. Diagram of the decision-making methodology implemented to quantitatively determine the best design structure for the 2×2 MMI BB..... 42

Figure 22. Model of the BB 2×2 MMI geometry C design corresponding to the best overall performance obtained. The 2nd degree polynomial fit was achieved with a normalized root mean square error (NRMSE) of 2.2%. Constant design parameters (i.e., W_1 , W_2 , L_t , and W_{t_2}) of the BB are provided in the figure top right corner..... 45

Figure 23. Light propagation simulation of the two-level HT main block structure, composed by a cascade of three optimized 2×2 MMI BB structures..... 47

Figure 24. Diagram of the decision-making methodology implemented to quantitatively determine the best design structure for the 1×2 MMI BB..... 49

Figure 25. Model of the BB 1×2 MMI geometry C design corresponding to the best overall performance obtained. The 2nd degree polynomial fit was achieved with a normalized root mean square error (NRMSE) of 1.5%. Constant design parameters (i.e., W_1 , W_2 , L_t , and W_{t_2}) of the BB are provided in the figure top right corner. 52

Figure 26. Light propagation simulation of the switching network main block structure, composed by a cascade of three optimized 1×2 MMI BB and two 2×2 MMI BB. Examples of two sets of logic outputs attained by the switching network block are provided in [A] and [B]. The different sets of logic

outputs is accomplished by changing the phase (ϕ) launched in the input arms of the 2×2 MMI BB, i.e., [A]: $\phi_{\{1,2,3,4\}} = [0, 0, 0, 0]$ resulting in the logic outputs [1 1 1 1]; and [B]: $\phi_{\{1,2,3,4\}} = [\pi/2, 0, 0, \pi/2]$ resulting in the logic outputs [1 0 0 1].....	53
Figure 27. Schematic diagram of the AAC composed of three main elements of different sizes, i.e., straight, taper and bend elements [57]. The diagram is not in scale.	60
Figure 28. Light propagation in the AAC when the input signal is provided in the upper waveguide (WG_2). AAC output power values are presented in percentage.	62
Figure 29. Light propagation in the AAC when the input signal is provided in the lower waveguide (WG_1) of the coupler. AAC output power values are presented in percentage.	63
Figure 30. Light propagation in the AAC when the same input signal is provided in the two input waveguides (WG_1, WG_2) of the coupler. AAC output power values are presented in percentage. ...	63
Figure 31. Microscope image of the chip containing the AAC, input DFB laser sources (L_1 and L_2), phase modulators (PM- L_1 and PM- L_2), multimode interferometers (MMI) splitters 1×2 and spot size converters (SSC $_1$ and SSC $_2$) to collect optical output signal from the AAC. Image obtained with Leica microscope (DM-750M; 1CC50-HD) [110] with a $5 \times$ objective (HI Plan EPI, $5 \times / 0.12$) [57].	64
Figure 32. Schematic diagram of the PCB designed to test the InP AAC optical chip. The diagram is not in scale.....	66
Figure 33. [A]: Diameter profiles for X and Y axis of a ball lens fabricated with $\sim 200 \mu\text{m}$. [B]: Picture of the fabricated ball lens, collected with the Fujikura laser splicing system.	69
Figure 34. Diagram of ball lens endpoint of the coupling fiber for focal lens calculus.	70
Figure 35. Setup for the chip testing illustrating the PCB with the optical chip and the alignment of the SSMF coupling fiber to collect the optical output signal from the SSC. A binocular stereoscope and two 3-axis (X, Y, Z) micro positioners were used for manual adjustment of the fiber coupling... 71	71
Figure 36. Schematic diagram of the AAC characterized. The optical system addressed is composed of one AAC, two DFB lasers, one PM, and two SSC.....	73
Figure 37. Power propagation in the AAC reproducing the experimental conditions for subtraction/addition and splitting coupling behaviors by adding phase to the input 2 of the AAC. [A]: Addition/subtraction behavior coupling ratio of 96:4) with an additional phase of 21° at the input WG_2 . [B]: Splitting behavior (coupling ratio of 50:50) with an additional phase of 113° at the WG_2 . [C]: Subtraction/addition behavior (coupling ratio of 5:95) with an additional phase of 200° at input WG_2	74
Figure 38. Relative power (in percentage) at the two output waveguides of the AAC as a function of phase for the 2D BPM simulation, and experimental optical power measurements (with an experimental standard deviation error $< 4\%$).	76
Figure 39. Phase realized in the AAC input WG_2 as a result of the experimental current applied to PM- L_2	77

Figure 40. Relative power (in percentage) at the two output waveguides of the AAC as a function of the input current applied to the phase modulator PM-L₂. 78

Figure 41. Diagram of the two-level network composed of three InP AAC performing the expected operations of the Haar wavelet transform. 80

Figure 42. Light propagation in the HT two-level network composed of three AAC, when all input WG of the network are powered with signal (1). HT network output power values are given in percentage. 80

Figure 43. [A]: Microscope image of the optical chip (with an objective lens of 5×). [B]: Design architecture of optical chip for data compression based on Haar wavelet transform..... 81

Figure 44. Schematic diagram of the PCB designed to test the InP HT optical chip. The diagram is not in scale..... 82

Figure 45. Photograph from the binocular stereoscope illustrating the edge coupling process with a fiber ball lens being coupled to SSC₁ from the InP HT optical chip..... 83

Figure 46. Circuit diagram of the approach used for electrical power measurements from on-chip PIN photodiodes. The resistor implemented was R = 10 kΩ. 84

Figure 47. Schematic diagram of the optical chip illustrating the network locations of the on-chip photodetectors (PIN-AAC₁, PIN-AAC₂, PIN-AAC₃-M₁, and PIN-AAC₃-M₂) under measurement. 85

Figure 48. Optical power measured from PIN-: AAC₂, AAC₃-M₁, AAC₃-M₂, and AAC₁, when the two-level HT network is powered by the activation of DFB lasers: i) L₁; ii) L₂; iii) L₁ + L₂; iv) L₃; v) L₁ + L₃; vi) L₂ + L₃; and vii) L₁ + L₂ + L₃ [56]..... 86

Figure 49. Optical power measured from SSC₁ and SSC₂, corresponding to AAC₃ output port 1 and port 2, respectively. A relative coupling power between 5 dB and 9 dB was observed at the output of the 2D HT..... 87

Figure 50. Schematic diagram of the MMI magic-T structure design. 91

Figure 51. Schematic diagram of the design of the HT network structure, composed by a two-level network of three 2×2 MMI couplers..... 91

Figure 52. Schematic diagram of the ideal WG structure and WG with a slope deviation. 92

Figure 53. Relative power (%) at the two outputs of the 2×2 MMI structure for a slope deviation range of 15° (i.e., 90° to 75°) for $\Delta n = [2.9, 3.9, 4.9] \times 10^{-3}$, attained with BPM. 93

Figure 54. Relative power (%) at the four outputs of the 2D HT network structure for a slope deviation range of 15° (i.e., 90° to 75°) for $\Delta n = [2.9, 3.9, 4.9] \times 10^{-3}$, attained with BPM..... 93

Figure 55. Design diagram of the manufactured device structures for testing and characterization of HT network operations. [A]: 2×2 MMI structure, with one input and two outputs, through a 1×2 MMI splitter placed before the 2×2 MMI. [B]: 2D HT network structure, with one input and four outputs,

through a 1×4 splitting network (composed by three 1×2 MMI splitters) placed before the 2D HT network.	94
Figure 56. Setup for optical device testing, composed by: infrared (IR) laser ($\lambda = 1555\text{nm}$, $P = 10.5\text{ dBm}$); DUT (e.g., 2×2 MMI and 2D HT network); objective lens (10×); and a charge-coupled device (CCD) image sensor.	95
Figure 57. Experimental results from 2×2 MMI BB. [A]: Intensity profile of CCD image matrix acquired (blue dots) and corresponding Gaussian fit (red line). [B]: Image acquired with the CCD image sensor.	96
Figure 58. Relative power (%) at the two outputs of the 2×2 MMI structure calculated with BPM, and corresponding experimental relative power (%) measured (highlighted in pink).	97
Figure 59. Relative power (%) at the four outputs of the 2D HT network structure calculated with BPM, and corresponding experimental relative power (%) measured (highlighted in pink).....	98
Figure 60. [A]: Diagram of the experimental setup implemented for RF calibrated MZI FSR measurement. [B]: Photograph of built calibrated MZI box (foam peanuts were added to provide stabilization).....	104
Figure 61. [A]: Interferometer optical frequency transfer function (blue line); Frequency sweep ramp at 40 MHz (orange line). [B]: FSR measurement results from calibrated MZI (FSR = $1.070 \pm 0.015\text{ MHz}$).....	105
Figure 62. Calibrated MZI measurement setup. Signal generator with 0-5 V ramp signal to piezo controlled frequency tuning of source laser centered at 1550 nm. DSO traces of frequency standard (yellow line) and DUT resonance (green line) with FWHM are displayed [60].	106
Figure 63. Measurement of resonator properties through Lorentzian fit implementation (with a fit error <3%). Resonator Q spectrum data and Lorentzian fit are presented in blue and red lines, respectively. Calculated properties of the resonator include ring waveguide loss ($\alpha = 0.46\text{ dB/m}$), power coupling coefficient ($k^2 = 0.78\%$), loaded Q ($Q_L = 28.47 \times 10^6$), unloaded Q ($Q_U = 56.82 \times 10^6$), and full width at half maximum (FWHM = 6.77 MHz). The frequency standard of the MZI (with an FSR of 1.07 MHz) is presented in green.....	108
Figure 64. Example of a PAM-4 signal in the time domain.....	109
Figure 65. [A]: Diagram of integrated programmable lattice filter architecture with a delay length of 2 mm for 100 GHz channel spacing. [B]: Photograph of tunable 10-stage dispersion compensating lattice filter, with red light used for coupling alignments [59].	112
Figure 66. Photograph of probe station implementation for the bias settings tuning of the integrated programmable lattice filter.....	113
Figure 67. Experimental setup for the NRZ link implementation for baseline performance testing.	114
Figure 68. Stimulated Brillouin scattering (SBS) suppression measurement for a C-band tunable laser with a booster EDFA and 75 km fiber span.....	115

Figure 69. [A]: Experimental setup for real-time C-band 53.125 Gb/s PAM-4 transmission using 10-stage photonic integrated programmable lattice-filter dispersion compensator. [B]: Photograph of experimental setup implemented. 116

Figure 70. Measured Pre-FEC BER for λ_0 (1560 nm) back-to-back and over 25 km, 35 km, and 40 km of SMF-28 SSMF with the KP4-FEC 2.4×10^{-4} threshold indicated. 117

Figure 71. Measured pre-FEC BER for four 100 GHz spaced channels $\lambda_0 - \lambda_3$ with a received optical power of -7 dBm and performance below KP4-FEC 2.4×10^{-4} threshold (channel λ_3 was not recovered for 40 km due to the total plus residual dispersion exceeding the compensated). 118

Figure 72. Diagram of a Fourier transform through a positive lens. A complex design pattern (diffractive optical element – DOE) is provided to the SLM to generate the expected hologram in the replay field (far-field). 122

Figure 73. LCoS SLM Pluto phase modulator from Holoeye® 2018 Holoeye Photonics AG. 124

Figure 74. Block diagram of the IFTA. The final optimized phase mask to apply to the SLM is given by the phase component of H, i.e., $\angle H$ 127

Figure 75. Diagram in Cartesian coordinate system describing the parameters (x_0, y_0) and (w_x, w_y) used for the estimation of the input beam S_{in} 129

Figure 76. GUI *SLM-mask* developed to generate different phase masks to apply to the SLM [64]. 130

Figure 77. Block diagram of the algorithm applied for the optimization of the CGH [32]. 132

Figure 78. [A]: In-line transmission hologram setup, composed by a red laser ($\lambda = 634$ nm; $P = 10$ mW) and a visible SLM (Holoeye LC2002). [B, C]: Photographs of the setup and generated hologram, respectively. 133

Figure 79. [A]: Diagram of the SLM calibration setup for a linear 2π phase distribution, i.e., generating the phase mask for a 0 to 255 gray level. [B]: Photographs of the setup. 134

Figure 80. Laser beamlets loaded on the LCoS SLM panel. 135

Figure 81. Phase modulation obtained for the linear 2π phase distribution and corresponding lookup table (LUT) values of the gamma curve. 135

Figure 82. [A]: Setup diagram of the SLM platform for MCF applications, with L_{s1} and L_{s2} lens and positioner P_{xy} . [B,C]: photographs of the corresponding setup. 137

Figure 83. [A]: Hologram reconstruction scheme using an infrared (IR) laser of 1550 nm, a polarization controller, lens L_{s1} and L_{s2} , an LCoS-SLM, and an IR camera. [B]: Photography of the implemented setup. 138

Figure 84. [A]: Design architecture of the PIC for data compression based on HT. [B]: Measurements of the distance between the four WG at the end of the two-level HT network of the PIC [32]. 139

Figure 85. Replay field of the hologram acquired by the IR camera for the: [A]: initial hologram; and [B]: optimized hologram.	139
Figure 86. Integrated intensity from the replay field image S_{raw} (red dots), and corresponding smoothing with Savitzky-Golay (SG) filter S_{SG} (blue line). [A]: initial CGH; and [B]: optimized CGH.	140
Figure 87. Gaussian fit (<i>Gauss fit</i> – blue line) of smoothed integrated intensity signal from the replay field image (S_{SG} – red dots) for [A]: initial CGH; and [B]: optimized CGH.	141
Figure 88. Overlap of the Gaussian fit results attained for the initial CGH (I_1) and optimized CGH (I_{opt}), and the expected four WG positions (Pos_{WG}) from HT PIC. The error factor for initial (black) and optimized (blue) CGH implementations associated with the WG_4 position are indicated (δ_{WG_4}) to illustrate the measuring process.	141
Figure A-1. EL metrics of the BB 2×2 MMI geometric shape A for MMI width $W_1 = 8, 9, 10, 11$ and $12 \mu m$, when a range set of values of L and Δd are implemented, and a phase of $\pi/2$ launched in the top input arm of the MMI BB. Best-optimized BB design parameters for the different W_1 widths are provided in the top right of each graph.	168
Figure A-2. EL metrics of the BB 2×2 MMI geometric shape A for MMI width $W_1 = 8, 9, 10, 11$ and $12 \mu m$, when a range set of values of L and Δd are implemented, and a relative phase between the MMI input arms is $\Delta\phi = 0$. Default BB design parameters (matching BB structure in the sum/subtraction operation mode) are provided in the top right of each graph.	169
Figure A-3. EL metrics of the BB 2×2 MMI geometric shape B for MMI width $W_1 = 8, 9, 10, 11$ and $12 \mu m$, when a range set of values of L and Δd are implemented, and a phase of $\pi/2$ launched in the top input arm of the MMI BB. Best-optimized BB design parameters for the different W_1 widths are provided in the top right of each graph.	170
Figure A-4. EL metrics of the BB 2×2 MMI geometric shape B for MMI width $W_1 = 8, 9, 10, 11$ and $12 \mu m$, when a range set of values of L and Δd are implemented, and a relative phase between the MMI input arms is $\Delta\phi = 0$. Default BB design parameters (matching BB structure in the sum/subtraction operation mode) are provided in the top right of each graph.	171
Figure A-5. EL metrics of the BB 2×2 MMI geometric shape C for MMI width $W_1 = 8, 9, 10, 11$ and $12 \mu m$, when a range set of values of L and Δd are implemented, and a phase of $\pi/2$ launched in the top input arm of the MMI BB. Best-optimized BB design parameters for the different W_1 widths are provided in the top right of each graph.	172
Figure A-6. EL metrics of the BB 2×2 MMI geometric shape C for MMI width $W_1 = 8, 9, 10, 11$ and $12 \mu m$, when a range set of values of L and Δd are implemented, and a relative phase between the MMI input arms is $\Delta\phi = 0$. Default BB design parameters (matching BB structure in the sum/subtraction operation mode) are provided in the top right of each graph.	173

Figure A-7. EL metrics of the BB 1×2 MMI geometric shape A for MMI width $W_1 = 8, 9, 10, 11$ and $12 \mu\text{m}$, when a range set of values of L and Δd are implemented. Best-optimized BB design parameters for the different W_1 widths are provided in the top right of each graph..... 174

Figure A-8. EL metrics of the BB 1×2 MMI geometric shape B for MMI width $W_1 = 8, 9, 10, 11$ and $12 \mu\text{m}$, when a range set of values of L and Δd are implemented. Best-optimized BB design parameters for the different W_1 widths are provided in the top right of each graph..... 175

Figure A-9. EL metrics of the BB 1×2 MMI geometric shape C for MMI width $W_1 = 8, 9, 10, 11$ and $12 \mu\text{m}$, when a range set of values of L and Δd are implemented. Best-optimized BB design parameters for the different W_1 widths are provided in the top right of each graph..... 176

List of Tables

Table 1. MMI interference mechanism overview.	27
Table 2. Inputs generated from the switching network block structure framework.....	33
Table 3. Optimized 2×2 MMI BB design dimensions for geometry A, B, and C.....	44
Table 4. Coefficients of 2 nd degree polynomial function model for optimized 2×2 MMI BB structures.	46
Table 5. Optimized 1×2 MMI BB design dimensions for geometry A, B, and C.....	50
Table 6. General dimensions of the AAC.	61
Table 7. AAC experimental optical power measurements.	75
Table 8. AAC experimental relative optical power results for a PM-L ₂ current sweep up to 45 mA and the corresponding phase of AAC input WG ₂	77
Table 9. AAC coupling behavior for $\lambda = [1553 - 1556]$ nm when powering the coupler's top and bottom arms with 1 and 0.1 relative power, respectively.....	88
Table 10. Gaussian fit parameters extracted from DUT output data collected with the CCD.....	97
Table 11. Error Factor (δ_{WG}) values for HT PIC four output WG positions.	143
Table 12. Integration of the intensity profiles for the four beams.	143

Acronyms

1D, 2D	one, two dimension
AAC	adiabatic asymmetric coupler
ADS	advanced design system
APD	avalanche photodiode
ASE	amplified spontaneous emission
ASPIC	application specific photonic integrated circuit
a.u.	arbitrary units
BB	building block
BER	bit-error rate
BFL	back focal length
BG	background
BPM	beam propagation method
CAGR	compound annual growth rate
C-band	infrared (IR) conventional band
CCD	charge-coupled device image sensor
CGH	computer-generated hologram
CITO	research project: image compression using optical transforms (<i>compresssão de imagens usando transformadas óticas</i>)
CMMPE	Centre of Molecular Materials for Photonics and Electronics
CMOS	complementary metal-oxide-semiconductor
CNM	National Center of Microelectronics (<i>Centro Nacional de Microelectronica</i>)
CR	coupling ratio
DBR	distributed Bragg reflector
DC	direct current
DCF	dispersion compensating fiber
DCI	data center interconnects
DCT	discrete cosine transform
DETI	Department of Electronics, Telecommunications and Informatics, University of Aveiro

DFB	distributed feedback
DFT	discrete Fourier transform
DKLA	design kit license agreement
DOE	diffractive optical element
DRC	design rule checking
DSO	digital sampling oscilloscope
DSP	digital signal processing
DUT	device under testing
DWPT	discrete wavelet packet transform
DWT	discrete wavelet transform
EDF	erbium-doped fiber
EDFA	erbium-doped fiber amplifier
EFL	effective focal length
EIC	electronic integrated circuit
EIM	effective index method
EL	excess loss
FBG	fiber Bragg grating
FCT	foundation for science and technology (<i>Fundação para a Ciência e a Tecnologia</i>)
FEC	forward error correction
FFT	fast Fourier transform
FhG-HHI	Fraunhofer Gesellschaft Heinrich Hertz Institute
FSR	free spectral range
FWHM	full width at half maximum
GUI	graphical user interface
HH	high-high (2D high-pass filter)
HP	high-pass (filter)
HT	Haar transform
IBM-CNM	Institute of Microelectronics of Barcelona – CNM
IC	integrated circuit
IDWPT/DWPT	inverse/discrete wavelet packet transform
InP	indium phosphide

InGaAsP	indium gallium arsenide phosphide
IFFT	inverse fast Fourier transform
IFTA	iterative Fourier transform algorithm
IR	infrared
ISO	optical isolator
IT	Institute of Telecommunications (<i>Instituto de Telecomunicações</i>), University of Aveiro
ITU	international telecommunication union
ITU-T	ITU telecommunication standardization sector
JePPIX	joint European platform for indium phosphide based photonic integration of components and circuits
LC	liquid crystal
LCD	liquid crystal display
LCoS	liquid crystal on silicon
LL	low-low (2D low-pass filter)
LP	low-pass (filter)
LUT	lookup table
MCF	multicore fiber
MEMS	micro electro-mechanical system
MMF	multimode fiber
MMI	multimode interference
MPW	multi-project wafer
MZI	Mach-Zehnder interferometer
MZM	Mach-Zehnder modulator
NDA	non-disclosure agreement
NIR	near-infrared
NRMSE	normalized root mean square error
NRZ	non-return-to-zero
OBR	optical backscatter reflectometry
OCPI	Optical Communications and Photonic Integration group
OOK	on-off keying
OPM	optical power meter
OSA	optical spectrum analyzer

OSNR	optical signal-to-noise ratio
OSP	optical signal processing
OTF	optical tunable filter
PAM	pulse-amplitude modulation
PAM-4	pulse-amplitude modulation with four amplitude levels
PARADIGM	photonic advanced research and development for integrated generic manufacturing
PCB	printed circuit board
PD	photodetector
PDK	process design kit
PIC	photonic integrated circuit
PIN	positive-intrinsic-negative photodiode
PLC	planar lightwave circuit
PM	phase modulator
PM-L ₂	phase modulator of laser 2 (L ₂)
PRBS	pseudorandom binary sequence
pre-FEC	pre-forward error correction
PSD	power spectral density
PZT	piezoelectric
Q	quality factor (of the resonator)
RF	radio frequency
RMSE	root mean square error
ROADM	reconfigurable optical add/drop multiplexer
SBS	stimulated Brillouin scattering
SDM	spatial division multiplexing
SFP	small form-factor pluggable
SLM	spatial light modulator
SMA	subminiature version A connector
SMF	single mode fiber
SNR	signal-to-noise ratio
SOC	system-on-chip
SOI	silicon on insulator

SSB	single sideband
SSC	spot size converter
SSMF	standard single mode fiber
TDCM	tunable dispersion compensating module
TE	transverse electric
TEC	thermoelectric cooler controller
TM	transverse magnetic
UCAM	University of Cambridge, United kingdom
UCSB	University of California, Santa Barbara
UPV	Universitat Politècnica de València
UV	ultraviolet
VOA	variable optical attenuator
WDM	wavelength division multiplexing
WG	waveguide
WSS	wavelength selective switch
XT	crosstalk

Symbols

ϕ	phase of BB input WG
$\phi_{\{1, \dots, k\}}$	phase of BB input WG, for k BB input WG
$\Delta\phi$	difference of phase (between BB input arms)
λ	wavelength
$\varphi_\nu(\gamma)$	modal field distribution
β_ν	mode propagation constant
$\angle H$	phase component of H , i.e., phase mask
β_0	fundamental mode propagation
ν_0	frequency carrier of a laser source
β_1	first mode propagation
(c_x, c_y)	horizontal (c_x) and vertical (c_y) frequency delay, for CGH iteration matrix
Δd	distance between MMI access WG (BB design parameter)
(d_1, d_2, d_3)	distance between the four WG outputs of the integrated implementation of the 2D HT network (from InP optical chip)
ν	mode numbers
ν_i	detuning frequency (of the resonator)
θ_{InP}	angle of SSC in the InP PIC
ΔL	unit delay length of dispersion compensation lattice filter
ν_{low}	lower sideband frequency
Δn	refractive index contrast of WG
θ_{SSMF}	angle of SSMF coupled to PIC
(w_x, w_y)	width (w_x) and the height (w_y) of the beam, for CGH iteration matrix
$\Delta\lambda$	wavelength range of tracepoint
$\Psi(0, y)$	electric field distribution of MMI
α	propagation loss of the ring WG
δ	error factor between generated hologram and initial field expected
δ_{WG_k}	error factor for the position of the four beams, i.e., expected output PIC WG ports positions (Pos_{WG_k}) vs. implemented CGH

$A_{access\ WG}$	area of access taper WG of the MMI structure
$A_{geom. A, B, C}$	area of MMI box for structure geometries A, B, and C
a_i	coefficients of HT scattering matrix for a generic 1D input
BFL	back focal lens
b	loss coefficient (of the resonator)
c	speed of light in vacuum
c_{ij}	scaling coefficients (i refers to the transform level and j to the coefficient index obtained from the LP and HP filtering)
c_v	field excitation coefficient
CR_{BB}	coupling ratio of the device under optimal dimensions design
d_{ij}	detail coefficients (i refers to the transform level and j to the coefficient index obtained from the LP and HP filtering)
D_{bl}	diameter of the ball lens
D_{ls}	diameter of the light input source
EFL	effective focal lens
EL_{BB}	excess loss of the device under optimal dimensions design
f	focal length factor (in 4f optical system configuration)
f_{LS}	lens focal length
f_m	microwave frequency
FT_λ	BB design fabrication tolerances for a wavelength range ($\lambda = 1550 \pm 15$ nm)
$FT_{L,\Delta d}$	BB design fabrication tolerances for length range ($\Delta L_{MMI} = 3$ μ m) and Δd range ($\Delta - \Delta d = 0.2$ μ m)
H	Fourier transform of I_i
$H_{4 \times 4}$	HT equation for a 4-pixel image
H_{1clad}	first height section of WG cladding cross-section
H_{2clad}	second height section of WG cladding cross-section
H_{core}	height of WG core cross-section
H_{mask}	mask transfer function (to send to SLM)
I_1	replay field of initial hologram
I_j	image matrix, for j iterations under CGH
I_{opt}	replay field of optimized hologram
I_R	resistor current

I_{SLM}	replay field of the hologram generated by SLM
κ^2	power coupling coefficient
k_{in}, k_{out}	number of input (k_{in}) and output (k_{out}) WG of the MMI BB structures
L	MMI length
L_{π}	MMI beat length
L_R	round-trip length of the resonator
L_t	taper length of the MMI access WG (BB design parameter)
$M(f_x, f_y)$	mask transfer function, for horizontal (f_x) and vertical (f_y) spatial frequencies
m	m^{th} mode of the planar WG
max	maximum element from a subset of values
min	minimum element from a subset of values
$mod2\pi$	modulus after division by 2π
m_{Wlevel}	wavelet levels of a k -pixel transform
$n_{access\ WG}$	number of access WG of the MMI structure
n_{BG}	effective refractive index of background (BG)
n_{clad}	cladding refractive index
n_{core}	core refractive index
n_{eff}	effective refractive index
n_g	group index
n_{InP}	refractive index of InP
n_{SSMF}	refractive index of SSMF
n_{WG}	effective refractive index of WG
N	number of MMI N self-images
NA	lens numerical aperture
n	refractive index
$P(dBm)$	power in dBm
$P_i(mW)$	power in mW, for i tracepoint
P_{in_j}	relative power at the input WG of the BB (j indicates the number of WG inputs)
PIN_R	PIN responsivity
P_{out_j}	relative power at the output WG of the BB (j indicates the number of WG outputs)

Pos_{WG_k}	position of each beam center corresponding to the PIC WG ports
$Pos_{CGH_{WG_k}}$	position of each beam center for the implemented CGH to generate the PIC WG ports
Q	resonator quality factor
Q_L	loaded resonator Q
Q_U	unloaded resonator Q
R	resistor
r	transmission coefficient (of the resonator)
RBW	resolution bandwidth
Si_3N_4	silicon nitride
S_{in}	input signal (for CGH)
SiO_2	silicon oxide or silica
Si	silicon
S_{out}	estimated output signal (for CGH)
S_{raw}	intensity integration of the image matrix (from CGH)
S_{SG}	Savitzky-Golay (SG) filtering on S_{raw}
Std	standard deviation
std_{WG_k}	standard deviation for error factor calculus (δ_{WG_k})
T	transmission (of the resonator)
$T_{4 \times 1}$	transformed coefficients (HT 4-pixel image)
$u_{\{1:6\}}$	coefficients of the 2 nd degree polynomial modeling the BB designed structures
V_R	resistor voltage
W	MMI width
W_1, W_2	widths of MMI (W_1, W_2) under BB design parameters
W_{core}	width of WG core cross-section
W_e	MMI effective width
wf	weighting factor
Wt_1, Wt_2	taper widths of MMI access WG (BB design parameters)
$X_{4 \times 1}$	1D object (4-pixel image)
$XT_{\Delta\phi=\frac{\pi}{2}}$	crosstalk at the MMI output for sum/subtraction mode ($\Delta\phi = \frac{\pi}{2}$)
$XT_{\Delta\phi=0}$	crosstalk at the MMI output for splitter mode ($\Delta\phi = 0$)

Chapter 1

Introduction

Emergent telecommunication systems are facing a significant growth of capacity requirements, which can be attributed to the proliferation of mobile devices, bandwidth-intensive applications, and services [1]–[3]. As a result, a significant increase in the broadband connections as well as the related multimedia traffic on a yearly basis [4]–[6] has been progressing. Traditional electronic transmission systems, based on copper are unable to meet the current system requirements typically in terms of bandwidth and latency [7] [8]. Optical fiber-based transport systems have been widely employed to answer to the reported needs.

Technological breakthroughs in the area of optical communications, such as the development of low loss single mode fiber (SMF), the erbium doped fiber amplifier (EDFA) and more recently high-spectral efficiency coding via digital signal processing (DSP) enabling coherent transmission, provided new tools to cope with the exponential capacity demand in optical networks [9]. Furthermore, the capacity of single-core SMF optical systems has been improved through advanced modulation formats and wavelength division multiplexing (WDM) technologies [10]. Nonetheless, conventional SMF based transport systems have been observed to be approaching Shannon's limit [11] and the achievable

maximum capacity will not be sufficient to support the envisaged massive connection demanded by the next generation networks [12]–[14]. Due to this technology physical limitation, the system capacity is expected to saturate around 100 Tbit/s, and thus conventional SMF schemes with WDM might be unable to meet the power consumption, spatial efficiency, and cost requirements of the emerging communication systems [14] [15]. Therefore, different approaches should be explored to address the demand for higher capacity in optical systems and communications networks, with an eminent milestone expected when optical communications links via SMF reach a physical limitation [16].

From the different physical dimensions available (i.e., time, quadrature, frequency, polarization, and space) the research community has given extra attention to the remaining physical dimension – space [3] [17] [18]. Thus, spatial division multiplexing (SDM) systems potential to substantially increase optical transport capacities, resorting to the use of fibers supporting multiple spatial modes (i.e., multimode fibers – MMF) or fibers containing multiple cores (i.e., multicore fibers – MCF) [9] [19] is a prospective approach to prevent “capacity crunch”. Nevertheless, technological improvements need to be considered to guarantee the efficient use of SDM systems, and several impairments and technological difficulties must be overcome to reduce the energy/cost per bit despite the system capacity increase [20]. For example, MCF system implementation is susceptible to and can be constrained by transmission impairments, such as nonlinearities and inter-core crosstalk (XT) between signals at the neighboring cores, which may be presented via the multiple optical paths, resulting in a system performance decay [14] [15].

Another prominent solution can be given by optical signal processing (OSP), described as a broad knowledge domain that brings together fields of optics and signal processing to achieve high-speed signal processing functions under optical communication systems requirements [21]. Moreover, all-optical signal processing is considered to be a promising approach to overcome the bandwidth and speed limitations imposed by conventional electronic-based systems [22] [23]. Five key enabling technologies associated with recent research in OSP can be highlighted [21]:

- i) photonic integrated circuit (PIC) technologies;
- ii) advances in materials and devices (to achieve more efficient nonlinearities);
- iii) coherent detection for high-speed systems;
- iv) advanced digital signal processing (DSP);

- v) employment of different optical domains (amplitude, phase, polarization, wavelength, and space).

An overall illustration of the OSP key enabling technologies is presented in Figure 1.

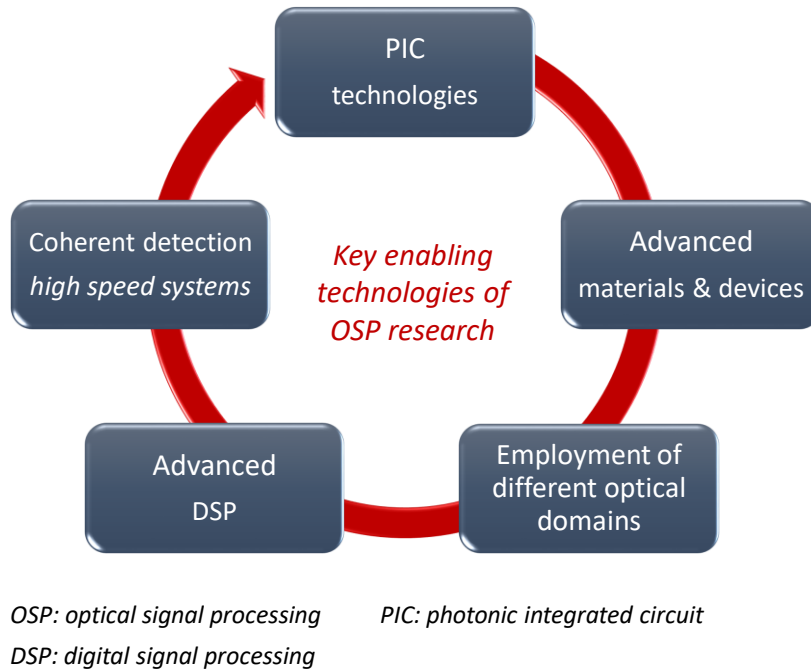


Figure 1. Recent enabling technologies motivating optical signal processing (OSP) research.
Adapted from [21].

In an effort to contribute to the evolution of next generation optical systems, this thesis research work will be mainly focused on optimized photonic integrated solutions.

1.1 Photonic integrated technology

Photonic integrated solutions are a promising technology from the 21st-century optical communication systems, with PIC-based optical communications systems offering an efficient and cost-effective alternative to data transmission [24] [25]. The implementation of integrated photonics can enable power, space, cost savings, and new functionalities, increasing the transmission capacity of the communication systems [26] [27]. Photonic integration appears as a dominant technology in high bandwidth optical communications systems [28], but it also offers increased valuable solutions in several innovative fields, such as bio-photonics [29], sensing [30] and space technology [31]. Nonetheless, PIC technology is still more expensive than standard microelectronics, which can restrict their application to some niche markets [26].

Photonic integrated circuits (PIC) are the equivalent of electronic integrated circuits (EIC) in the optical domain. As an alternative to transistors and other electronic components, PIC contains optical elements, such as modulators, detectors, attenuators, multiplexers, optical amplifiers, and lasers embedded in a single chip using a waveguide (WG) architecture [32]. The photonic integration technology is going through a similar evolution path as microelectronic integration, nevertheless under a time delay of about 20 to 30 years [33].

Historically, the invention of the transistor in 1948 [34] [35] launched microelectronic integration developments, while the invention of the semiconductor laser in 1969 [36] was the breakthrough of photonic integration technology. Transistor and laser technologies were primarily implemented as discrete components. Microelectronics integration technology started with Kilby in 1959 [37] and matured with complementary metal-oxide-semiconductor (CMOS) [38] in the 1970s. A first PIC comprising a laser integrated with a modulator was reported in 1987 [39], marking the start of PIC exponential development, known as Moore's law [33]. Moore's law forecasted a double in the number of components per integrated circuit about every two years, with a new technology generation introduced approximately every three years, and an expected compound annual growth rate (CAGR) under the dozens [40].

Optical communications evolution has brought the advent of improved PIC presenting an economic and sustainable alternative to data transmission [24]. With PIC technology offering compelling performance advances in terms of small weight and volume, low power consumption, high

mechanical and thermal stability, and the ease for assembling a substantial number of complex systems [28].

In summary, PIC-based optical systems offer efficient and cost-effective solutions to data transmission driving to a significant boost in the segment [24], with recent PIC global market projected to expand at CAGR of about 26% during the forecast period of 2017 to 2023 [41], see Figure 2.

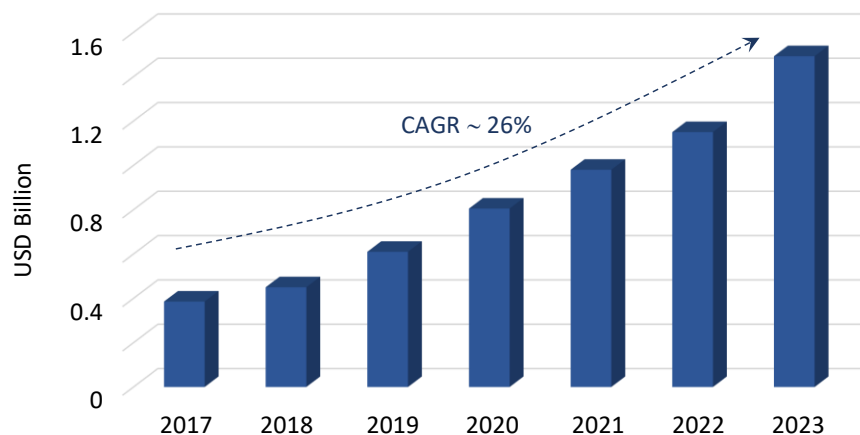


Figure 2. Global photonic integrated circuits (PIC) market from 2017 to 2023, with an expected compound annual growth rate (CAGR) of approximately 26%. Adapted from [41].

Different materials are available to produce PIC, nonetheless only a few have been employed to emulate electronic semiconductor industry and progressed into foundry systems, software suppliers, design houses and fabless companies [42]. Current main photonic integration platform technologies offering access to generic processes and manufacturing through multi-project wafer (MPW) runs are silicon (Si) [43]–[45], indium phosphide (InP) [46]–[48], and silicon nitride (Si_3N_4) [42] [49] [50].

The selection of the integrated photonic platform to realize the PIC is driven by the functional requirements of the device to be developed and the underlying available components (active/passive) of the different platforms [51]. An overview of the key differences between the addressed integrated platform technologies is provided in Figure 3 [52] [53].

Building block	InP	Si	Si ₃ N ₄
Passive components	✓✓	✓✓	✓✓✓
Lasers	✓✓✓	○ H	○ H
Modulators	✓✓✓	✓✓	✓
Switches	✓✓	✓✓	✓
Optical amplifiers	✓✓✓	○ H	○ H
Detectors	✓✓✓	✓✓	○ H
Footprint	✓✓	✓✓✓	✓
Chip cost	✓	✓✓	✓✓
CMOS compatibility	○○	✓✓	✓
Low cost packaging	○	○ ¹ / ✓✓ ²	✓✓

Performance		
✓✓✓	very good	
✓✓	good	○○ medium challenge
✓	modest	○ low challenge

Fabrication technology	
H	Hybrid/Heterogeneous

¹ end-fire coupling (low reflection)
² vertical coupling (medium reflection)

Figure 3. Comparison of key features from three of the major photonic integration technology platforms, i.e., InP, Si, and Si₃N₄. Adapted from [52] [53].

High gain, speed, and low loss are three of the main attributes of optical communication improved performance. A generic response of the platforms to these areas is provided in Figure 4.

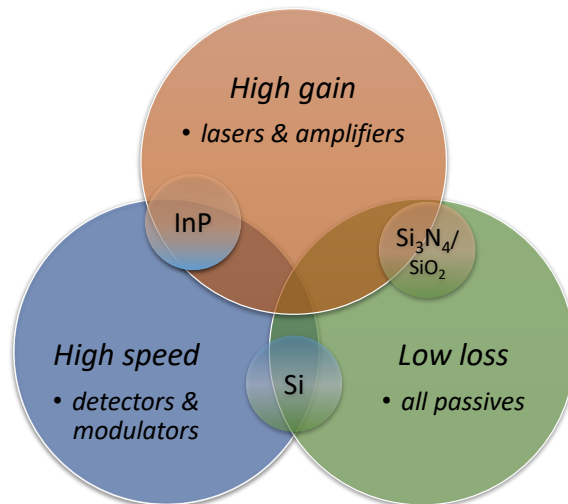


Figure 4. Overall functional capabilities and/or limitations associated with the InP, silicon and silicon nitride based integrated platforms. Adapted from [51].

Several advantages and/or limitations can be highlighted from the referred technologies. As InP is a direct bandgap material, it presents the best available gain performance, but with higher

associated losses due to electrical doping from the current injection, requiring the inclusion of optical amplifiers [51]. Regarding systems-on-chip (SOC) complexity, InP platform has a higher maturity with chips comprising up to hundreds of components. Silicon-based photonic processes are CMOS-compatible allowing its integration to be run in a CMOS foundry, which provides well-controlled and more rapid scalability to fabrication environment [43]. Nevertheless, as silicon substrates size is larger than InP substrates and silicon photonics lacks light sources and amplifiers, InP-based platforms provide a higher potential for volume scaling and integration [33]. Though, the leverage of the higher processing technology maturity of silicon photonics, as an indirect bandgap material, a native gain has been difficult to realize under this platform. The platform features are in between InP and ultra-low loss Si_3N_4 technologies, with some active detection elements but no source solutions, and medial optical losses (amid InP and Si_3N_4) [51]. Regarding wavelength properties, Si/ SiO_2 and InP based platforms are mainly used in near-infrared (NIR), while silicon nitride can operate from visible to NIR [42].

Ultra-low loss Si_3N_4 planar lightwave circuits (PLC) with propagation loss below 0.1 dB/m has been demonstrated by UCSB and LioniX[®] research [54], orders of magnitude lower than other reported platforms. As a result, high-performance passive components are enabled by this platform, though electrical pump for gain is unavailable due to the insulating nature of $\text{Si}_3\text{N}_4/\text{SiO}_2$ glass WG [51]. However, the demonstration of optical gain using erbium-doped WG distributed Bragg reflector (DBR) and distributed feedback (DFB) laser arrays integrated within ultra-low loss Si_3N_4 [55], shows potential for platform's active component integration.

In summa, silicon and silica utilize the most mature materials, leveraging from existing technology like silicon electronics and micro electro-mechanical systems (MEMS) industries, enabling foundry services robustness and products commercialization. InP integrated technology has a maturity in between the two, having several available commercial devices and a promising foundry model. Enhanced architecture choices should combine the advantages of these different integrated photonic technologies, ideally with associated electronics to achieve optimized performance, power, footprint, and cost [51].

Hybrid and monolithic photonic integration are the two leading methods commonly employed to realize integrated photonics. In the hybrid method, the integrated circuit (IC) is a package containing several photonic devices of similar functionality, allowing to combine numerous optic devices of different integrated platforms. While, monolithic photonic integration is based on a single IC containing

different optical devices in the same integrated platform, thus enabling various functionalities on a single chip.

To maximize overall photonic technology advantages, further development should be given to the realization of low cost, foundry compatible, highly functional, SOC solutions, and the relaxation of current power and thermal constraints [51]. Figure 5 illustrates the capabilities that should be attained by PIC technology in order to meet the aforementioned needs.

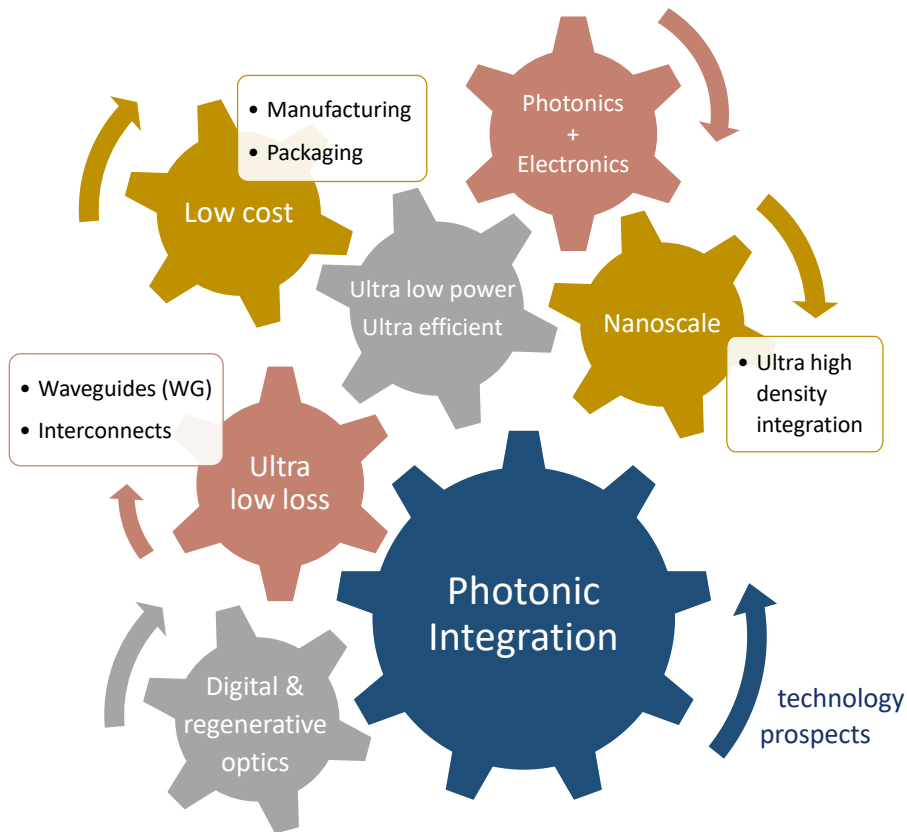


Figure 5. Diagram of technology prospects for next generation of PIC, in order to realize future high speed, low cost, power-efficient photonic system-on-chip (SOC). Adapted from [51].

The presented research work comprehends new photonic integrated solutions (through design, testing, and packaging processes) for data compression applications, under different WG based integrated platforms, i.e., Si_3N_4 , InP and new hybrid material. Furthermore, the development of ultra-low loss Si_3N_4 integrated solutions for lasing and dispersion compensation applications are presented. An overall description of the research contributions attained is provided in section 1.2.

1.2 Research contributions

The development of optimized solutions under the enabling PIC technologies drives the research work under this dissertation, addressing different steps of the PIC development chain, mainly design, testing, and packaging processes.

Driven by the craving for high-speed data transfer and improved efficiency with real-time data availability, optimized integrated photonic solutions for data compression applications are proposed. An optimized design model of multimode interference (MMI) structures in silicon nitride based platform for photonic integrated data compression applications was developed. Different MMI geometries were studied, and discussed the best building block (BB) solution to attain the desired development of an improved reconfigurable all-optical solution for data compression applications based in the photonic integrated implementation of an optical transform, i.e., the Haar transform (HT). Additionally, a first test and characterization of PIC solutions implementing the HT for compression applications in InP based platform [56] [57] and in a new organic-inorganic di-ureasil hybrid material were also realized [58].

Furthermore, under a collaboration with the Optical Communications and Photonic Integration Group (OCPI), from University of California, Santa Barbara (UCSB) was realized the development of an extended reach PAM-4 transmission enabled by a photonic integrated tunable lattice filter dispersion compensator with application as a low-cost interface for data center interconnects (DCI) [59]. Also, a radiofrequency calibrated Mach-Zehnder interferometer (MZI) to measure ultra-narrow linewidth chip-scale Brillouin laser resonator properties was built, and performed the Brillouin gain measurements, through Lorentzian fitting analysis which contributed for [60] [61]. This research was enclosed in the development of a state-of-the-art sub-hertz fundamental linewidth (< 1 Hz) photonic integrated Brillouin laser, narrow enough to move demanding scientific applications to the chip-scale [62], namely photonic micro-chip high-end lasers for spectroscopy, navigation, quantum computation, and optical communications applications.

As technical and functional requirements of the PIC demand a thorough characterization and testing to provide an accurate prediction of the PIC performance, and current testing platforms can be expensive and have a lack of flexibility [46]. A proof of concept of a new soft-packaging flexible platform for photonic integrated processors and SDM systems, based in spatial light modulation operation principle is proposed. The capacity of the spatial light modulator (SLM) to dynamically reconfigure light

is used to feed and/or receive information to the PIC [32] [63] and dynamically optimize the spatial coupling under MCF fiber transmission systems [64].

From the main achievements attained under this research study, the following scientific outputs can be listed.

1.2.1 Awards

Best PhD pitch award – Research Summit 2019

Cátia Pinho, Mário Lima, António Teixeira. “Optimized Photonic Integrated solutions for Next Generation Optical Systems”, at Research Summit 2019, MAP-tele, PDEI, MAP-i session, University of Aveiro, July 3-5, 2019.

Best paper award – AICT 2017

Cátia Pinho, Francisco Rodrigues, Ana Tavares, George S. D. Gordon, Ali Shahpari, Mário Lima, Tim D. Wilkinson, António Teixeira. “Flexible Platform for Feeding Photonic Integrated Processors”. In: 13th Advanced International Conference on Telecommunications (AICT 2017), Venice, Italy, June 25 – 29, 2017.

1.2.2 Scientific papers

- [P1] Cátia Pinho, Berta Neto, Tiago M. Morgado, Hugo Neto, Mário Lima, António Teixeira. “InP AAC for data compression applications”. IET Optoelectronics, Special issue: 2018 European Conference on Integrated Optics (ECIO 2018), vol. 13(2), pp. 67-71, April 2019.
- [P2] Sarat Gundavarapu, Grant M. Brodnik, Matthew Puckett, Taran Huffman, Debapam Bose, Ryan Behunin, Jianfeng Wu, Tiequn Qiu, Cátia Pinho, Nitesh Chauhan, Jim Nohava, Peter T. Rakich, Karl D. Nelson, Mary Salit, Daniel J. Blumenthal, “Sub-hertz fundamental linewidth photonic integrated Brillouin laser”. Nature Photonics, vol. 13(1), pp. 60-67, January 2019.
- [P3] Cátia Pinho, George S. D. Gordon, Berta Neto, Tiago M. Morgado, Francisco Rodrigues, Ana Tavares, Mário Lima, Tim D. Wilkinson, António Teixeira. “Flexible Spatial Light

Modulator Based Coupling Platform for Photonic Integrated Processors”. International Journal on Advances in Telecommunications, vol. 11(1-2), pp. 20-31, 2018.

- [P4] Taran Huffman, Grant M. Brodnik, Cátia Pinho, Sarat Gundavarapu, Douglas Baney, Daniel J. Blumenthal. “Integrated Resonators in an Ultralow Loss Si₃N₄/SiO₂ Platform for Multifunction Applications,” IEEE Journal of Selected Topics in Quantum Electronics, vol. 24(4), pp. 1-9, July 2018.
- [P5] Sarat Gundavarapu, Matthew Puckett, Taran Huffman, Ryan Behunin, Jianfeng Wu, Tiequn Qiu, Grant M. Brodnik, Cátia Pinho, Debapam Bose, Peter T. Rakich, Jim Nohava, Karl D. Nelson, Mary Salit, Daniel J. Blumenthal. “Integrated Waveguide Brillouin Laser”, Physics archive (Physics - arXiv), Cornell University Library, arXiv: 1709.04512, 13 September 2017.

1.2.3 Scientific communications

- [C1] Cátia Pinho, Glória Micó, Mário Lima, Pascual Muñoz, and António Teixeira, “Optimized Design of Si₃N₄ Structures for Photonic Integrated Data Compression Applications”. In: IMOC 2019 - International Microwave and Optoelectronics Conference, pp. 1–3, November 10-14, 2019.
- [C2] Sushma Pandey, Cátia Pinho, Francisco Rodrigues, Hugo Neto, Mário Lima, and António Teixeira, “Laser Thermal Crosstalk Modelling in InP based Photonic Integrated Chips”. In: IMOC 2019 - International Microwave and Optoelectronics Conference, pp. 1–3, November 10-14, 2019.
- [C3] Cátia Pinho, Mário Lima, António Teixeira. “Optimized Photonic Integrated Solutions – via design, packaging, and testing”. In 11th MAP-tele Workshop 2019, FEUP, U. Porto, September 8, 2019. (*abstract*)
- [C4] Cátia Pinho, Berta Neto, Alexander Goltsev, Sandra Vieira, António Teixeira. “Visual Human-Machine Interface Using Compressed Reality”. In: ENBENG 2019 – 6th IEEE Portuguese Meeting on Bioengineering, Lisbon, Portugal, P150, February 22-23, 2019. (*abstract*)
- [C5] Cátia Pinho, Tiago M. Morgado, Berta Neto, Mário Lima, António Teixeira. "Implementation and Optimization of a Cost-Effective 2D Haar Transform Network for Image Compression". In: OSA Frontiers in Optics and Laser Science Conference (FIO+LS 2018), Washington, D.C., United States, JTU3A.88, September 16-20, 2018.

- [C6] Cátia Pinho, Berta Neto, Tiago M. Morgado, Artur Sousa, André Albuquerque, Mário Lima, António Teixeira. "Spatial light modulator based flexible coupling platform for applications in SDM and PIC". In: European Conference on Integrated Optics (ECIO 2018), Valencia, Spain, P16, May 30 – June 1, 2018. (Selected to extend for special issue in the IET Optoelectronics journal)
- [C7] Grant M. Brodnik, Cátia Pinho, Frank Chang, Daniel J. Blumenthal. "Extended Reach 40km Transmission of C-Band Real-Time 53.125 Gbps PAM -4 Enabled with a Photonic Integrated Tunable Lattice Filter Dispersion Compensator". In: OFC 2018 - Optical Fiber Communication Conference, San Diego, California, United States, W2A.30, March 11-15, 2018.
- [C8] Tiago M. Morgado, Cátia Pinho, Berta Neto, Francisco Rodrigues, António Teixeira. "Software Tool to Design MMI Splitters/Couplers for Photonic Integrated Circuits". In: 20th International Conference on Transparent Optical Networks (ICTON 2018), Bucharest, Romania, July 1-5, 2018.
- [C9] Tiago M. Morgado, Berta Neto, Cátia Pinho, Carlos M. Vicente, António Teixeira. "Cost-Effective Magic-T using Organic-Inorganic Hybrid Materials for Image Compression". In: 20th International Conference on Transparent Optical Networks (ICTON 2018), Bucharest, Romania, July 1-5, 2018.
- [C10] Tiago M. Morgado, Berta Neto, Carlos M. Vicente, Cátia Pinho, António Teixeira. "Passive Phase Shifters based in 1x1 MMI for Cost-effective Photonic Integrated Circuits". In: 20th International Conference on Transparent Optical Networks (ICTON 2018), Bucharest, Romania, July 1-5, 2018.
- [C11] Cátia Pinho, Francisco Rodrigues, Ana Tavares, George S. D. Gordon, Ali Shahpari, Mário Lima, Tim D. Wilkinson, António Teixeira. "Flexible Platform for Feeding Photonic Integrated Processors". In: 13th Advanced International Conference on Telecommunications (AICT 2017), Venice, Italy, June 25-29, 2017. (Best paper award, with the invitation to extend to journal)
- [C12] Cátia Pinho, Ana Tavares, Guilherme Cabral, Tiago Morgado, Ali Shahpari, Mário Lima, António Teixeira. "Design and Characterization of an Optical Chip for Data Compression based on Haar Wavelet Transform". In: OFC 2017 - Optical Fiber Communication Conference, Los Angeles, California, United States, Th2A.9, March 19-23, 2017.
- [C13] Tiago Morgado, Francisco Rodrigues, Ali Shahpari, Berta Neto, Cátia Pinho, Mário Lima, António Teixeira. "InP MMI Based Polarization Splitter for Photonic Integrated Circuits". In:

19th International Conference on Transparent Optical Networks (ICTON 2017), Girona, Spain, July 2-6, 2017.

- [C14] Cátia Pinho, Ali Shahpari, Isiaka Alimi, Mário Lima, António Teixeira. “Optical Transforms and CGH for SDM Systems”. In: 18th International Conference on Transparent Optical Networks (ICTON 2016), Trento, Italy, P.31, July 10-14, 2016.
- [C15] Cátia Pinho, Mário Lima, António Teixeira. “Optical compensation approach for SDM systems”. In: XIII Symposium on Enabling Optical Networks and Sensors (SEONs 2016), Covilhã, Portugal, July 8, 2016.
- [C16] Cátia Pinho, Mário Lima, António Teixeira. “Spatial Light Modulation for SDM systems”. In 8th MAP-tele Workshop 2016, FEUP, U. Porto, May 4, 2016. (*abstract*)
- [C17] Cátia Pinho, Mário Lima, António Teixeira. “Spatial Division Multiplexing systems – main perspectives”. In: IONS Valencia 2015, International OSA Network of Students, Valencia, Spain, September 24-26, 2015. (*abstract*)

1.2.4 Book chapters

- [B1] Cátia Pinho, Isiaka A. Alimi, Mário Lima, Paulo Monteiro, António Teixeira. “Spatial Light Modulation as a Flexible Platform for Optical Systems”. Chapter in: Telecommunication Systems, London: IntechOpen, pp. 1-20, September 2019.
<https://www.intechopen.com/online-first/spatial-light-modulation-as-a-flexible-platform-for-optical-systems>
- [B2] Isiaka Alimi, Ana Tavares, Cátia Pinho, Abdelgader M. Abdalla, Paulo Monteiro, António Teixeira. “Enabling optical wired and wireless technologies for 5G and beyond networks”. Chapter in: Telecommunication Systems, London: IntechOpen, pp. 1-31, April 2019.
<https://www.intechopen.com/online-first/enabling-optical-wired-and-wireless-technologies-for-5g-and-beyond-networks>
- [B3] Isiaka Alimi, Nelson Muga, Abdelgader M. Abdalla, Cátia Pinho, Jonathan Rodriguez, Paulo Monteiro, António Teixeira. “Towards a Converged Optical-Wireless Fronthaul/Backhaul Solution for 5G Networks and Beyond”. Chapter in: Optical and Wireless Convergence for 5G Networks, London: Wiley IEEE, pp. 1-30, August 2019.
<https://www.wiley.com/en-pt/Optical+and+Wireless+Convergence+for+5G+Networks-p-9781119491583>

1.2.5 Supplementary research/training

In the scope of the Ph.D. studies, supplementary research/training in the field of optical communications has undertaken at the Optical Communications and Photonic Integration (OCPI) group from the University of California, Santa Barbara (UCSB); the Centre for Advanced Photonics and Electronics (CAPE) - Electrical Engineering Division of the University of Cambridge (UCAM); and the Photonic Research Labs - iTEAM Research Institute from the Universitat Politècnica de València (UPV). A summarized description of each mission is listed below.

- **2018/2019 – total duration: one month**

Short Term Scientific Missions (STSM) under the COST action CA16220 - European Network for High Performance Integrated Microwave Photonics (EUIMWP) at the Photonic Research Labs - iTEAM Research Institute from the Universitat Politècnica de València (UPV).

Main task: Photonic integrated circuit design for silicon nitride technologies under the CNM-VLC design platform.

- **2017 – six months**

Supplementary research/training at the Optical Communications and Photonic Integration (OCPI) group from the University of California, Santa Barbara (UCSB).

Main tasks: Study and characterization of photonic integrated circuits. Optical signal processing and optical system testing.

- **2016 – one month**

Supplementary research/training at the Centre for Advanced Photonics and Electronics (CAPE) - Electrical Engineering Division of the University of Cambridge.

Main tasks: Acquire knowledge and experimental skills in the use of spatial light modulator (SLM) and development/implementation of computer-generated holograms (CGH).

1.3 Thesis Outline

The thesis is organized into four additional chapters. Chapter two presents an optimized reconfigurable PIC design proposal for data compression applications using optimized MMI structures under Si_3N_4 -based integrated WG platform. A full description of the all-optical system architecture for the implementation of the optical transform, i.e., the two-level HT network, is provided. An optimized design model study for 2×2 MMI and 1×2 MMI BB structures is proposed. The extensive optimization design assessment performed, provides an important evaluation of the BB structures performance/behavior to realize the HT compression network.

Chapter three comprises the first experimental characterization of an InP-based platform realizing the HT, with a full characterization of the elementary BB coupler implemented, i.e., the adiabatic asymmetric coupler (AAC), and the 2D HT network. The performed characterization comprises theoretical design simulations and attained experimental results. The methodologies applied for the packaging of the optical chip under testing and fiber coupling are also described. Additionally, taking advantage of low-cost hybrid materials, a potentially cost-effective integrated implementation of a 2D HT under the organic-inorganic di-ureasil hybrid [65] material is also demonstrated.

Chapter four contains the implemented measurement technique for integrated high-Q resonators performance assessment, based in a radiofrequency calibrated MZI. Brillouin gain measurements through Lorentzian fitting analysis, are also described. Furthermore, the first demonstration of an extended reach transmission of C-band PAM-4 enabled with a photonic integrated tunable lattice filter dispersion compensator is attained, with applicability as a low-cost interface for DCI. The scientific research under this chapter proceeds on the collaboration with the OCPI research group from UCSB.

In chapter five is presented a proof of concept of a new soft-packaging flexible platform for photonic integrated processors and SDM systems, based on spatial light modulation operation principle. The development and implementation of an SLM framework as a coupling platform under the capability of the SLM to dynamically reconfigure light with computer-generated holograms (CGH) is explored. SLM operation principle, main challenges, and applications are described. Different methodologies were developed and optimized solutions proposed to implement the CGH, allowing a dynamical improvement of the generated CGH. Experimental results of SLM framework implementation in SDM systems and its potential use for PIC processors are also addressed.

All aforementioned chapters are concluded with a final section summarizing the scientific remarks achieved under the chapter. Lastly, an overall conclusion of the scientific work and contributions attained under this dissertation, with reference to potential future work directions, are outlined in chapter six.

Chapter 2

Optical integrated approaches for data compression applications

The exponential growth of bandwidth demand has drawn significant research efforts into the field of ultra-high capacity optical networks, where optical signal compression plays an important role in fast processing/storing of large amounts of bandwidth demanding data [66]. Data compression emerges as an important field of study with different available techniques to release additional bandwidth.

Specifically, for faster image processing, compression methods are fundamental tools to decrease redundant data. Different compression transformation techniques can be used, with the wavelet-based transforms as the most promising ones due to their simplicity and fast computation capabilities [67]. All-optical network design appears as a prominent solution for the application of such compression methods. Optical transforms can be employed to the compression and decompression processing of data, with higher advantages if implemented in integrated photonics. By applying this architecture into a photonic integrated circuit (PIC), image compression can be attained with potentially lower cost, less power consumption, and high data rate due to an all-optical processing implementation [68]. Among

the wavelet-based methods, Haar transform (HT) offers a promising approach for image processing and pattern recognition due to its simple design, fast computation power, and efficiency, being easily implemented by optical planar interferometry [56] [67] [68].

The use of optical interference components realizing a separate addition and subtraction of incoming inputs signals at its output ports is a key element in the HT implementation. For example, a specific degree of asymmetry applied in 3 dB directional couplers can produce different coupling behaviors [68]–[70], such as magic-T [71]. A magic-T behavior can be attained by structures such as 3 dB asymmetric coupler, where asymmetric waveguides can be used to compensate wavelength dependent coupling ratios [57] [72]. The employment of an adiabatic asymmetric coupler (AAC) to implement the HT network in an indium phosphide (InP) integrated base platform [56] [57] is addressed in chapter 3 – section 3.1.

Furthermore, the magic-T response can also be realized with multimode interference (MMI) coupler devices, where tunable coupling ratio capabilities can be managed by adjusting the phase of the input signals [71] [72]. MMI structure attractive properties can include low inherent losses, large optical bandwidths, low polarization dependence, and relatively simple fabrication [73], against directional coupler dependency on sub-microns gaps between waveguides [73] [74]. Moreover, these structures can also benefit from higher fabrication tolerances on refractive index contrast, wavelength, and waveguide widths [75]. A first numerical proposal of the HT implementation with MMI structures is presented in [76] for an InP based platform, using taper waveguides to comprise phase shifting between the input signals of the MMI coupler. The study [76] reports a simulated design for the 2×2 MMI device with a 260 μm length and a device excess loss of 0.25 dB can be inferred from the linear results presented.

In an effort to improve current existent solutions, it is studied in this chapter a new optimized reconfigurable PIC design proposal for data compression applications using optimized MMI structures. From the available integrated platforms, was selected the silicon nitride (Si_3N_4) due to its reported merits. Silicon nitride on silicon oxide (SiO_2) photonic integration platform presents reduced material losses [44], and a vast set of applications, e.g., optical signal processing, tele/datacom, sensing, and bio-photonics [42]. As design performance predictions toughly match PIC fabrication, reconfigurability can play an important role in order to rectify unwanted drifts in the device functioning and enable additional functionalities in the PIC [77]. Thus, reconfigurability capabilities will be included in the

proposed designed structures through the implementation of thermal tuner components [78] in the input arms of the MMI structures. This procedure allows to change/adjust the relative phase of the input arms of the MMI coupler, and thus the operations performed by the device structure. The HT implementation is realized by a two-level network of three 2×2 MMI coupler building blocks (BB). Furthermore, a switching network to address all logical inputs of the HT network is also designed. The switching network is composed by a cascade of three 1×2 MMI splitter BB and two 2×2 MMI BB. An extensive structure optimization of the network key BB (i.e., the 2×2 MMI and 1×2 MMI) is undertaken in order to minimize: i) device excess loss; ii) MMI coupler/splitter imbalance (associated with the expected BB coupling ratio); and iii) footprint. BB device reconfigurability for different coupling behaviors, and fabrication tolerances under wavelength and design dimensions are also addressed. All BB structure designs were optimized for a wavelength of 1550 nm, moreover structures behavior in wavelength C-band range (1535 nm to 1565 nm) was evaluated as it entails current optical fiber bandwidth with the lowest loss, and thus is commonly used in general optical transmission systems.

The chapter starts with a full description of the all-optical system architecture for the implementation of the HT (section 2.1). In section 2.2 is presented the new reconfigurable PIC design proposal in a Si_3N_4 -based platform for data compress applications using optimized MMI coupler structures. The method implemented for the design architecture and BB optimization is described in subsection 2.2.1. Results and discussion of the optimized BB structure designs developed are addressed in subsection 2.2.2. The chapter is concluded with final remarks presented in section 2.3.

2.1 All-optical system architecture for data compression based in HT

A digital image can be seen as a group of pixels, where neighboring pixels are correlated and usually redundant. Through the decreasing of this redundancy (by compression techniques) the transmission speed and the bandwidth of the system can be optimized. Transforms based on orthogonal functions are the most frequently used in signal compression techniques. The orthogonality is an important property for multi-resolution analysis, where the original signal can be split into low and high-frequency components without duplicating information. These functions only require subtractions and additions for their forward and inverse transforms. Examples of these transforms are the discrete Fourier transform (DFT), the discrete cosine transform (DCT), and the discrete wavelet transforms (DWT) [79]. DWT has the advantage of representing a fundamental tool for local spectral decomposition and nonstationary signal analysis, used in the JPEG2000 standard as wavelet-based compression algorithms [80].

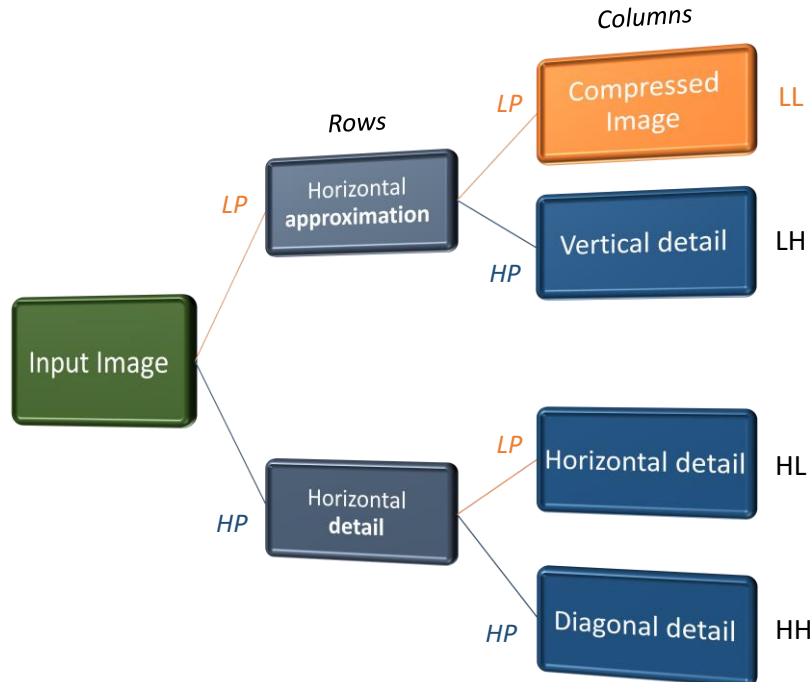


Figure 6. Diagram of two-level band decomposition using multi-resolution analysis based on wavelet transform. Low-pass (LP) and high-pass (HP) filters are applied two times to obtain the 1D transform (L and H components) and the 2D transform (LL, LH, HL and HH components). Adapted from [32].

DWT represent an image as a sum of wavelet functions, with different location and scale [81], i.e., high-pass (detail) and low-pass (approximate) coefficients. Low-pass (LP) and high-pass (HP) filters are applied to the input data with a two-level signal decomposition architecture, as depicted in Figure 6. The Haar wavelet transforms [68] [82] [83] belongs to the family of DWT and thus is based on orthogonal functions. This optical transform was chosen for the proposed all-optical system architecture due to its simplicity and fast computation.

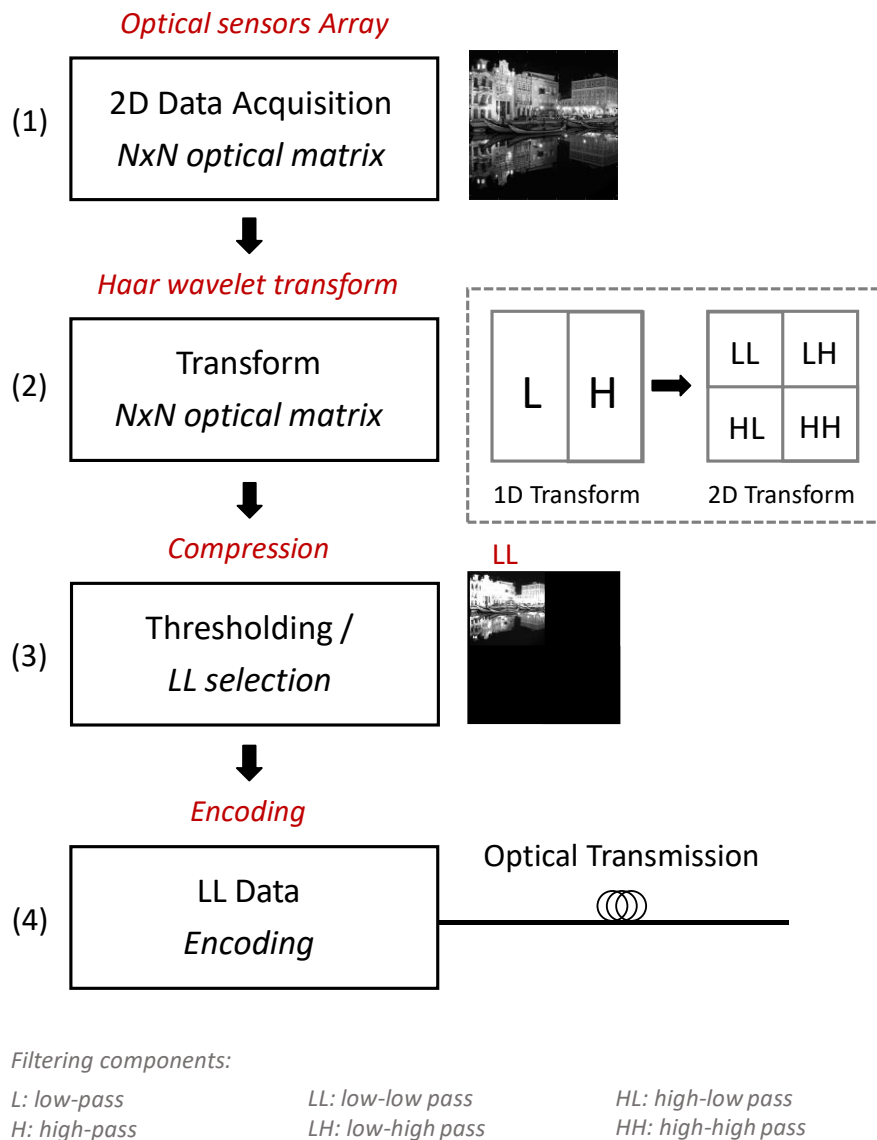


Figure 7. All-optical scheme diagram of system BB for Haar wavelet transform processing and compression. 2D transform process schematic describes low-pass (L) and high-pass (H) filtering through sub-band decomposition [32].

The sub-band decomposition achieved through the wavelet transform enables a direct compression on a specific portion of the spectrum, through spatial frequency characterization. The all-optical system architecture for data compression based on the HT can be divided into four main blocks: i) optical sensors array; ii) Haar wavelet transform; iii) compression; and iv) data encoding section. The scheme for the all-optical image acquisition, processing, and transmission is depicted in Figure 7.

The first block entails the acquisition level with optical sensors for light detection and two dimensional (2D) data sampling. The HT is implemented in the second block, to extract the image properties by exploiting the energy compaction features of the wavelet decomposition.

The HT block (second block) includes low-pass (L) and high-pass (H) filters associated with the Haar wavelet, applied over one dimension (1D) at time. The filtering operation can be simplified as the calculation of the average between two neighbors' pixels values (LP) or the difference between them (HP). Equation (1) presents the HT scattering matrix for a generic 1D input (a_i coefficients), i.e., pixel line or column. LP and HP filters are applied two times to obtain the 1D transform (L and H component) and the 2D transform with the four LL, LH, HL, and HH components, see Figure 6 and Figure 7.

$$\begin{bmatrix} c_{10} \\ d_{10} \\ c_{11} \\ d_{11} \\ c_{12} \\ d_{12} \end{bmatrix} = \frac{1}{\sqrt{2}} \begin{bmatrix} 1 & 1 & 0 & 0 & 0 & 0 \\ 1 & -1 & 0 & 0 & 0 & 0 \\ 0 & 0 & 1 & 1 & 0 & 0 \\ 0 & 0 & 1 & -1 & 0 & 0 \\ 0 & 0 & 0 & 0 & 1 & 1 \\ 0 & 0 & 0 & 0 & 1 & -1 \end{bmatrix} \begin{bmatrix} a_0 \\ a_1 \\ a_2 \\ a_3 \\ a_4 \\ a_5 \end{bmatrix} \quad (1)$$

The coefficients on the left side of equation (1) are the scaling c_{ij} and detail d_{ij} coefficients (where i refers to the transform level and j to the coefficient index) obtained from the LP and HP filtering, respectively, for each pixel pair, which corresponds to the 1D first level of the Haar discrete wavelet transform. In a 2D matrix input ($N \times M$) this operation is performed twice, i.e., horizontally and vertically, for each transformation level, to guarantee that image intensity variations are evaluated along the two dimensions [32].

The same filtering operation is performed in the LL sub-band for the next level of the transform, whereas the other sub-bands (i.e., LH, HL, and HH) can be stored, transmitted or discarded, being the transform coefficients related to higher-frequency components.

The third block carries out the compression and extracts the desirable information from the 2D transform, e.g., LL component. The all-optical system ends with the encoding block where the data stream is delivered through the optical channel [32] [68].

A 3 dB asymmetric coupler (depicted in Figure 8), also known as a magic-T, can be used to implement the HT.

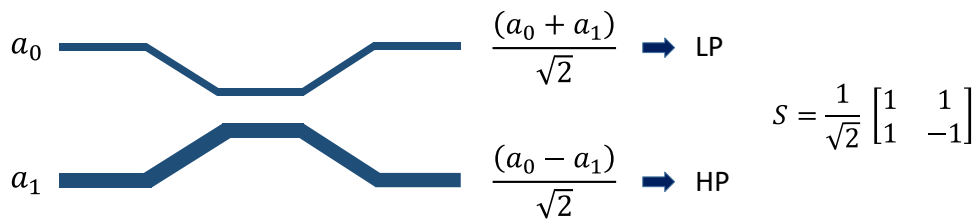


Figure 8. Diagram of a 3 dB asymmetric optical coupler and scattering matrix given by S .

The asymmetric coupler is characterized by having different waveguides widths, which can present a wide range of coupling ratios and an insertion loss up to 0.7 dB, including input and output single mode fiber coupling losses [84]. To perform the HT operations the asymmetric coupler must be designed in order to perform a 50% coupling ratio. A description and testing of an integrated HT implementation using an asymmetric adiabatic coupler are provided in section 3.1.

Likewise, the HT implementation can also be realized by a two-level network of 2×2 MMI coupler devices. In the following section (2.2) is presented a new reconfigurable PIC design proposal in a Si_3N_4 -based platform for data compression applications using optimized MMI coupler structures.

2.2 Reconfigurable HT PIC design in a Si₃N₄ integrated platform

Heterogeneous silicon photonics offers technological breakthroughs with a high expected impact in high-speed communications, future data centers, supercomputers, and sensors [44] [85]. When applying both silicon nitride (Si₃N₄) and silicon waveguide types, e.g., Si₃N₄ on silicon oxide (SiO₂), material losses can be reduced [44]. The broadband nature of Si₃N₄ material, i.e., from visible to mid-infrared wavelengths, makes it feasible for a wide range of applications, namely optical signal processing, tele/datacom, sensing, and bio-photonics [42] [86].

Photonic signal processing, a recognized solution to overcome inherent electronic speed limitations, can highly benefit from fully reconfigurable photonic integrated signal processors [87]. As fabricated PIC hardly matches the design performance expectations due to the high technology sensitivity to fabrication tolerances, PIC reconfigurability can rectify unwanted drifts in the device functioning [77]. Additionally, these reconfiguration capabilities are a promising strategy for the delivering of advanced functionalities on PIC and are becoming progressively advisable in an attempt to reach device demanding new requirements [77] [87].

Taking advantage of the Si₃N₄ based integrated platform and the addition of reconfigurability capabilities to the PIC design, an optimized photonic integrated implementation of the two-level HT network (composed by MMI BB structures) for compression applications is studied.

The method implemented for the proposed PIC design solution is described in section 2.2.1, and in section 2.2.2 are provided the results assessment and discussion of the optimized BB structure designs developed.

2.2.1 Method

The method implemented addresses the MMI interference principle (subsection 2.2.1.1), design rules applied (subsection 2.2.1.2), developed design architecture (subsection 2.2.1.3), BB structure design optimization (subsection 2.2.1.4), and the definition of a decision-making methodology for the assessment of the best-optimized BB design (subsection 2.2.1.5).

2.2.1.1 MMI optical interference principle

The excitation of several modes in a multimode waveguide leads to the formation of replicas (self-images) of the input field at the output plane through the spatial Talbot effect [88]. Depending on the waveguide cross-section, materials and operation wavelength, a given number of modes will be guided, dependent on the propagation constant of each mode (β_ν). The distribution of light injected (at $z = 0$) in an MMI with an electric field distribution $\Psi(0, y)$ is given by equation (2), and after a z distance by equation (3), where c_ν indicate the field excitation coefficients; β_ν the mode propagation constant; $\varphi_\nu(y)$ the modal field distribution; and m is the m^{th} mode of the planar WG. The WG supports m lateral modes with mode numbers $\nu = 0, \dots, (m - 1)$.

$$\Psi(0, y) = \sum_{\nu=0}^{m-1} c_\nu \varphi_\nu(y) \quad (2)$$

$$\Psi(z, y) = \sum_{\nu=0}^{m-1} c_\nu \varphi_\nu(y) \exp(-j\beta_\nu z) \quad (3)$$

The MMI length (also known as the beat length) required for the light to interfere (when the propagation constants β_ν of the first two modes are involved) is presented in equation (4), where n_{eff} represents the effective refractive index (for fundamental n_{eff0} and first n_{eff1} mode), and λ the wavelength of the light.

$$L_\pi = \frac{\pi}{\beta_0 - \beta_1} = \frac{0.5\lambda}{n_{eff0} - n_{eff1}} \quad (4)$$

The difference between the fundamental (β_0) and (β_ν) mode can be given by the approximation provided in equation (5), with the field expansion (at $z = L$) rewritten as presented in equation (6).

$$\beta_0 - \beta_1 = \frac{\nu(\nu + 2)\pi}{3L_\pi} \quad (5)$$

$$\Psi(L, y) = \exp(-j\beta_0 L) \sum_{i=0}^{m-1} c_i \varphi_i(y) \exp\left(\frac{iv(v+2)\pi L}{3L_\pi}\right) \quad (6)$$

The shape of light (at $z = L$) depends on: i) values of c_i (i.e., how light is injected); and ii) the value of L/L_π (i.e., the ratio of L to the beat length). For a particular set of lengths, scaled replicas of the input field pattern appear, known as self-images. The simplest case is described by the MMI length $L = p3L_\pi$, for $p = 0, 1, 2, (\dots)$, as illustrated in Figure 9.

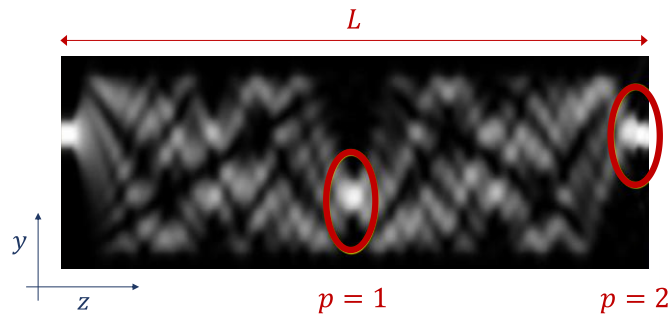


Figure 9. Propagation interference for MMI length $L = p3L_\pi$, with $(p = 0, 1, 2, \dots)$. Adapted from [89].

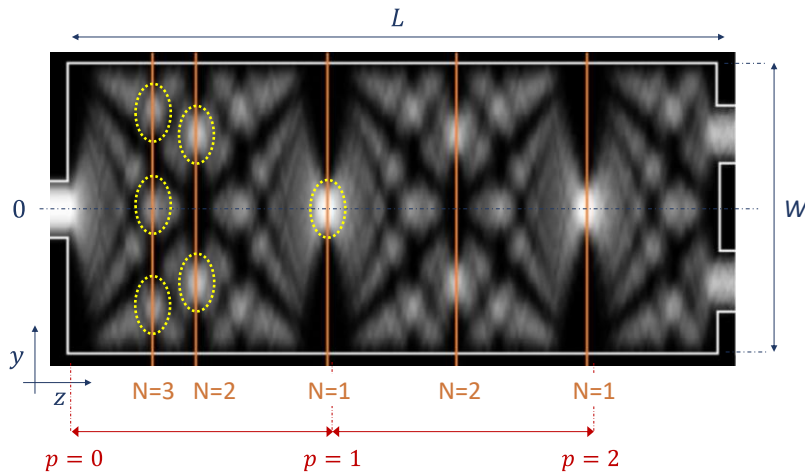


Figure 10. MMI symmetric propagation interference for MMI length $L = (p3L_\pi)/N$, with $(N = 1, 2, 3, \dots)$. Adapted from [89].

The number input WG and its position affect the generated modes. Two interference mechanisms can be highlighted, the symmetric ($y = 0$) and paired ($y = \pm W_e/6$), where W_e is the effective width of

the MMI ($\approx W$ for high contrast platforms). Further details are given in Figure 10, illustrating the symmetric propagation interference mechanism. MMI paired and symmetric interference mechanisms [73] [89] are summarized in Table 1.

Table 1. MMI interference mechanism overview.

Interference mechanism	Paired	Symmetric
Inputs \times Outputs	$2 \times N$	$1 \times N$
First single image distance	L_π	$3L_\pi/4$
First N-fold image distance	L_π/N	$3L_\pi/4N$
Excitation requirements	$c_\nu = 0$ $\nu = 2, 5, 8, (\dots)$	$c_\nu = 0$ $\nu = 1, 3, 5, (\dots)$
Input position	$\pm W_e/6$	0

N : number of self images formed; L_π : beat length; c_ν : field excitation coefficients; ν : mode numbers; W_e : MMI effective width ($\approx W$ for high contrast platforms).

For the proposed PIC design solution, 2×2 MMI couplers and 1×2 MMI splitters were studied and optimized under the Si₃N₄ CNM-VLC[®] Photonics design platform [89] [90]. Design methodology combined theoretical MMI optical interference principle and numerical optimization through beam propagation method.

2.2.1.2 Design rules and procedures methodology

The design and analysis of waveguide (WG) propagation behavior of the newly developed integrated Si₃N₄ structures were addressed numerically, as in general PIC cannot be accurately analyzed by simple analytical solutions, and numerical techniques are the commonly adopted solution to verify new PIC design structures [74]. From the various numerical analysis, beam propagation method (BPM) is generally considered by the scientific community as one of the best approaches for investigating linear and nonlinear lightwave propagation phenomena in axially varying WG such as curvilinear directional couplers and branching, combining and tapered WG [74] [91]. Thus, in the present study, BPM numerical analysis technique was chosen for the design and analysis of the WG propagation behavior/performance of the developed PIC structures.

To test the different designed BB structures a set of design rules and procedures were implemented, as described in the block diagram from Figure 11 [89].

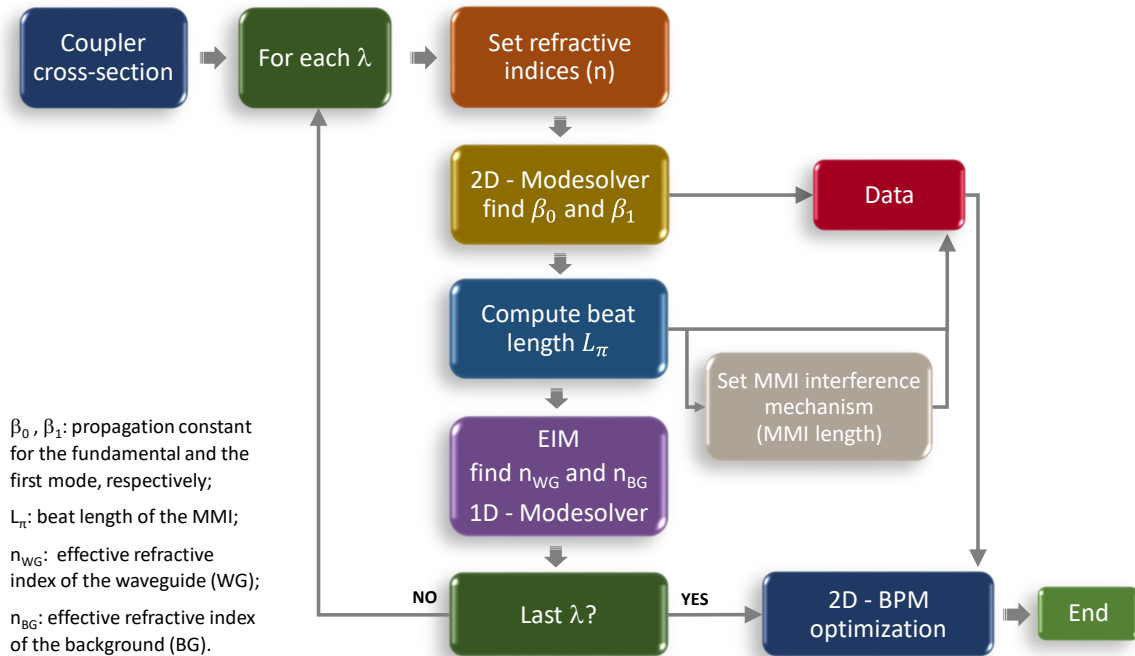


Figure 11. Block diagram of the rules and procedures implemented for the MMI BB design, based in [89].

A 2D mode solver tool was used to compute the effective indices of the MMI cross-section. The effective index method (EIM) [91] was implemented to calculate the effective refractive indices of the WG and background (BG), with the 1D mode solver (reducing the cross-section to one dimension). These values were then applied in the third dimension using the 2D BPM. Optimized EIM and BPM simulations were realized under the transverse electric (TE) mode. All simulations were computed in the OptoDesigner[®] Synopsys software [92].

The developed integrated BB structures were studied and optimized under the silicon nitride technology design platform from Institute of Microelectronics of Barcelona, Centro Nacional de Microelectronica (IBM-CNM) and VLC Photonics[®] [89] [90], through the CNM foundry process design kit (PDK). A deep waveguide was used in the BB structure designs. Owing to the design kit license agreement (DKLA) with CNM foundry limited information about WG structure can be provided. A generic diagram of the passive WG structure implemented is depicted in Figure 12.

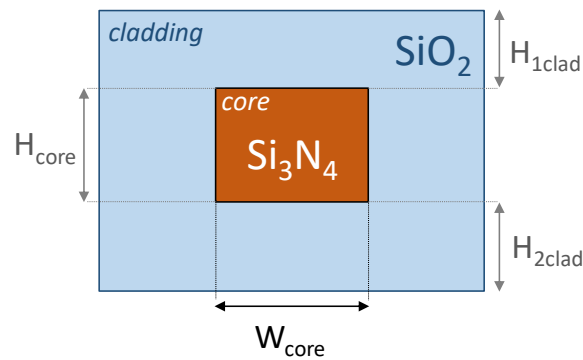


Figure 12. Schematic diagram of the deep WG structure from silicon nitride CNM design platform.

W_{core} and H_{core} denote the WG Si_3N_4 core width and height, respectively.

$H_{1\text{clad}}$ and $H_{2\text{clad}}$ refer to the heights of WG SiO_2 cladding.

Under the CNM-VLC design technology, only the width of WG core (W_{core}) is endorsed to be changed, with a minimum default recommended value of $0.6 \mu\text{m}$.

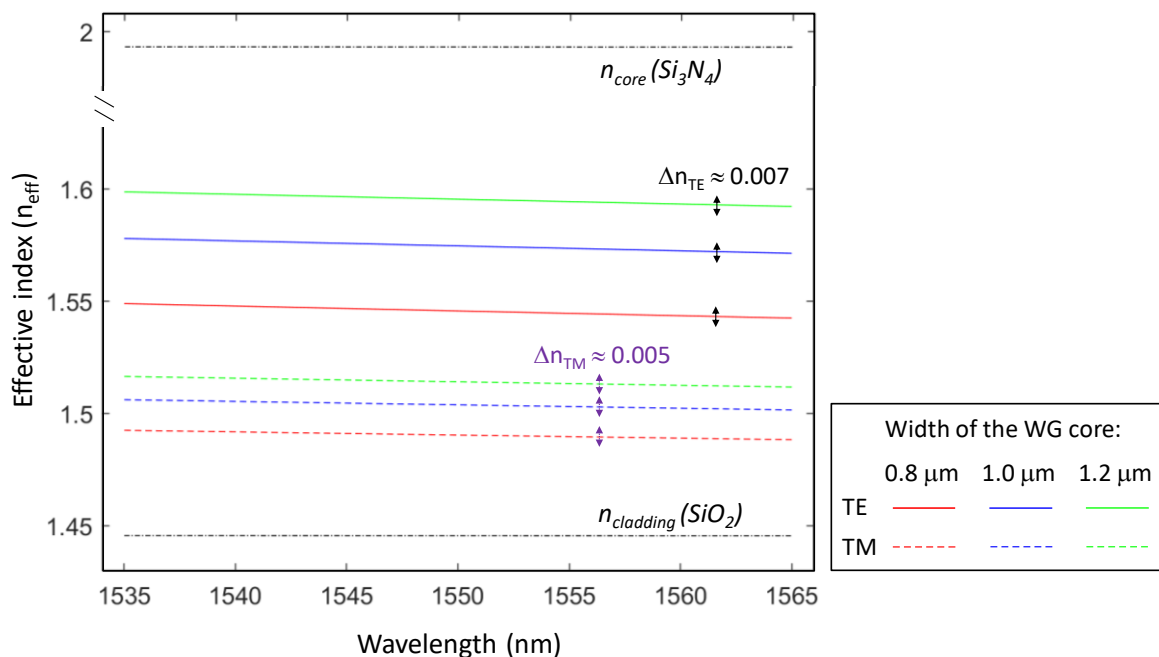


Figure 13. Effective index of deep WG fundamental mode versus light propagation wavelength, for three different WG core widths ($0.8 \mu\text{m}$, $1.0 \mu\text{m}$, and $1.2 \mu\text{m}$). Transverse electric (TE) and transverse magnetic (TM) polarization are presented in continuous and dashed lines, respectively. The black dashed/dotted lines indicate the cutoff index of WG core ($n_{\text{core}}\text{Si}_3\text{N}_4$) and cladding ($n_{\text{clad}}\text{SiO}_2$).

A simulation study of straight deep WG effective index for W_{core} equal to 0.8 μm , 1.0 μm , and 1.2 μm on infrared C-band wavelength range (1535 nm to 1565 nm) under transverse electric (TE) and transverse magnetic (TM) polarization is presented in Figure 13. The WG core width of 1.0 μm was selected for all the structure designs, in a compromise between fabrication recommendations and tolerances, and device footprint. Regarding, the bending radius of deep WG, a default minimum of 50 μm is validated by CNM-VLC silicon nitride technology [89].

2.2.1.3 Design architecture for the integrated Si_3N_4 HT implementation

MMI structures were chosen as the PIC key BB due to their attractive properties (e.g., compact size, and polarization independency for strongly guided structures [75] [93]), and optical interference capabilities (splitting and combination of optical signals). Besides the fundamental canonical MMI [73] (in a rectangular shape), more unconventional geometric designs (such as the butterfly shapes, also labeled widened/narrowed body MMI shapes) were explored to leverage coupling ratio behaviors, BB footprint, and fabrication tolerances (e.g., operational wavelength range). Reported literature on the implementation of similar MMI butterfly geometries in SOI-based platform [94], and InGaAsP/InP-based platform [93] identified benefits, such as small size, polarization insensitivity, and available arbitrary coupling ratio design.

An MMI structure footprint range between $123 \times 10 \mu\text{m}^2$ and $240 \times 10 \mu\text{m}^2$, and an average excess loss of 0.6 dB was reported in [94]. In [93] a MMI structure footprint range between $308 \times 12 \mu\text{m}^2$ and $1224 \times 24 \mu\text{m}^2$ with reported excess losses below 0.7 dB was described. To explore and access these geometries merits under Si_3N_4 -based platform, three MMI geometries were implemented, i.e., the standard MMI rectangular shape [73] (defined as geometry A) and two different butterfly geometric shapes based in [93] [94] (defined as geometry B and C). The geometry shape of the different implemented structure designs is depicted in Figure 14.

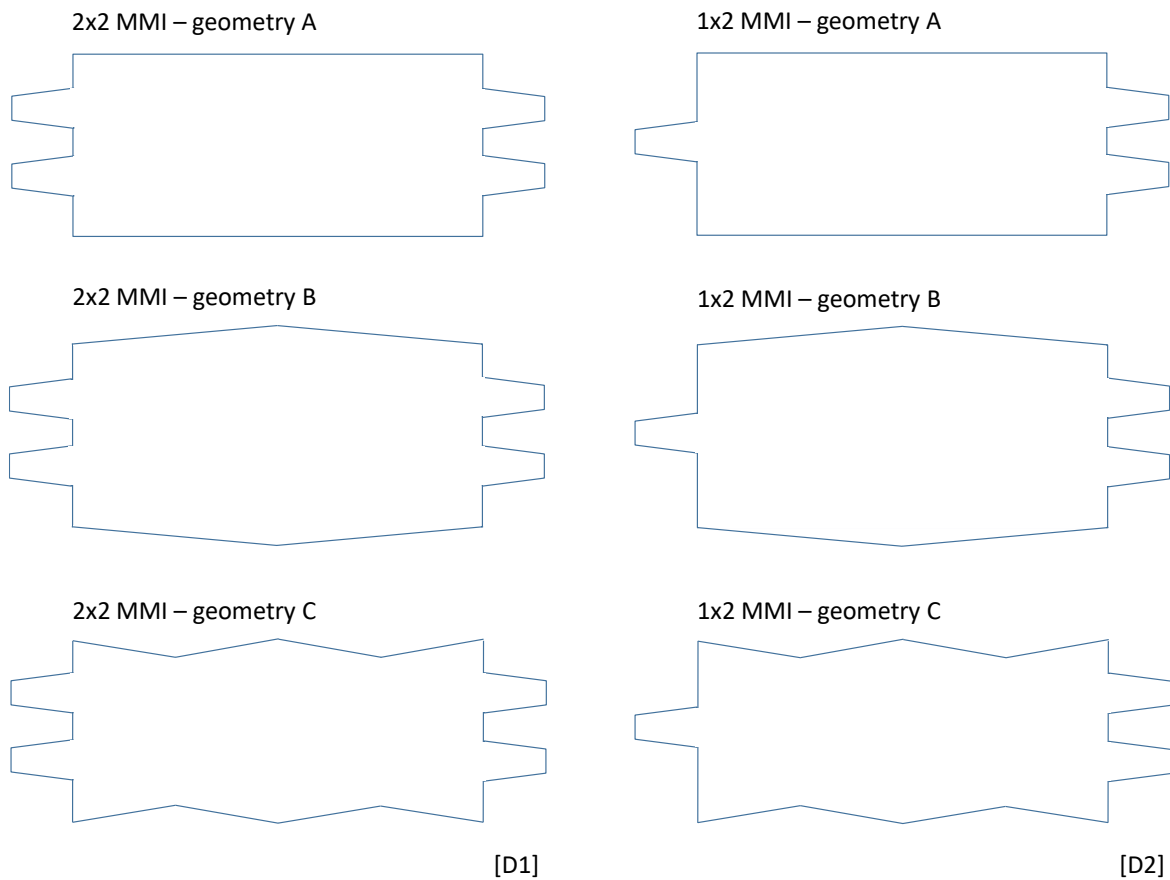


Figure 14. Diagram of the different designed MMI structures, in rectangular (geometry A) and butterfly (geometry B, C) geometric shapes. [D1]: Set of three MMI geometries of the 2×2 MMI BB tested to implement the two-level HT network and the switching network. [D2]: Set of three MMI geometries of the 1×2 MMI BB tested to implement the switching network.

Two main block structures comprise the proposed design of the all-optical photonic integrated approach:

- i) a two-level HT network composed by a cascade of three 2×2 MMI coupler BB, to realize the data compression optical transform (as depicted in Figure 15);
- ii) a switching network to address all logical inputs of the HT network, composed by a cascade of three 1×2 MMI splitter BB and two 2×2 MMI coupler BB (see Figure 16).

The two-level HT network can be composed by a cascaded of three 2×2 MMI, i.e., four inputs and four outputs for a 4-pixel HT, as depicted in Figure 15. A 4-pixel image acquisition process can be mathematically described with the matrix operation presented in equation (7) [95] [96].

$$T_{4 \times 1} = H_{4 \times 4} X_{4 \times 1} \quad (7)$$

Parameters $X_{4 \times 1}$ describes the 1D object, $T_{4 \times 1}$ the transformed coefficients, and $H_{4 \times 4}$ the Haar matrix (equation 1, in section 2.1). A k -pixel transform comprises $m_{Wlevel} = \log_2 k$ wavelet levels. Thus, for a 4-pixel HT, a two-level HT network should be implemented.

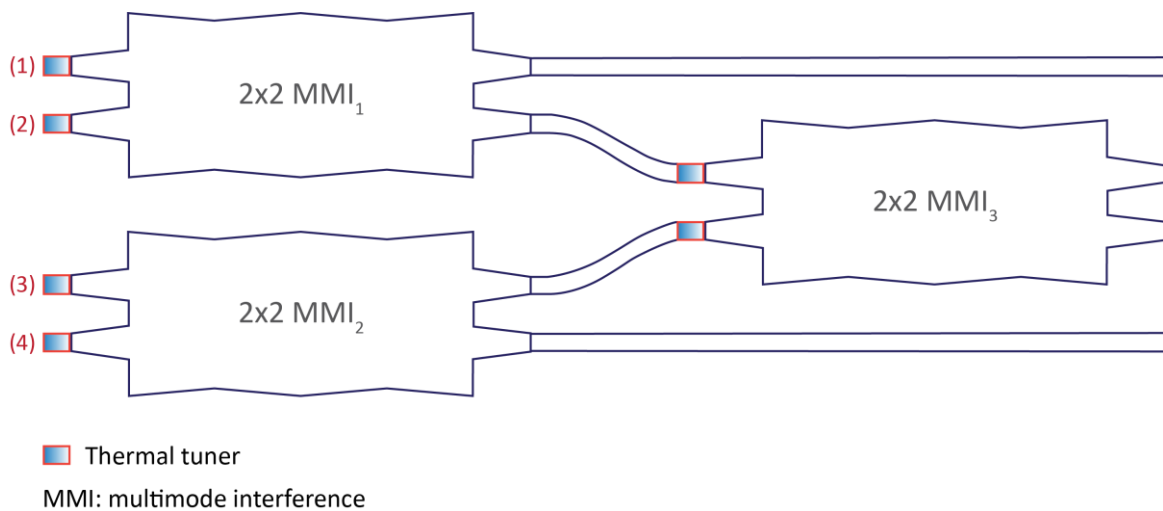


Figure 15. Schematic diagram of the four input two-level HT network main block structure, composed by a cascade of three 2×2 MMI coupler BB, to realize the data compression. The diagram is not in scale.

The switching network main block structure was designed to provide a framework that supplies all logical inputs to the 4-pixel HT network, for study and characterization purposes. The switching network is composed by a cascade of three 1×2 MMI splitter BB and two 2×2 MMI coupler BB as depicted in the schematic diagram of Figure 16.

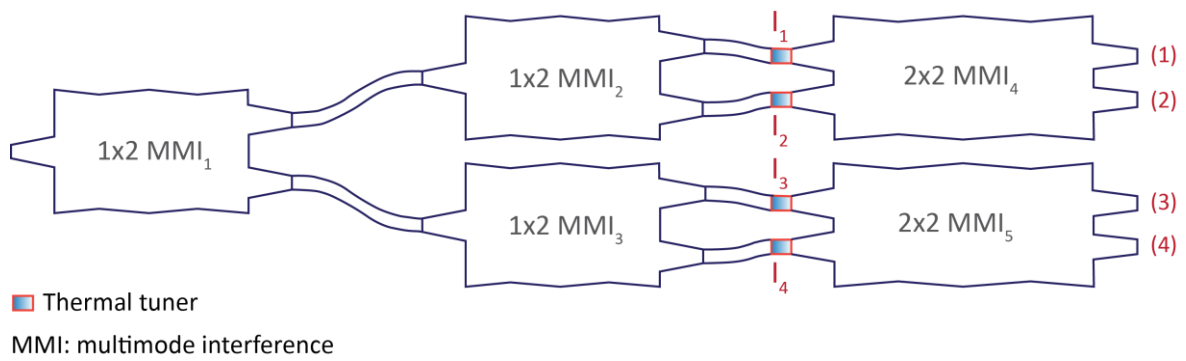


Figure 16. Schematic diagram of the switching network main block structure, composed by a cascade of three 1×2 MMI splitter BB and two 2×2 MMI coupler BB, to address all logical inputs of the HT network. The diagram is not in scale.

From the 4^2 possible logical inputs, due to the unavailability to generate two zero inputs in the 2×2 MMI BB, only nine logical inputs are valid and can be attained with the designed switching network. Relative power for the inputs of the HT network will be considered as 0 versus 1, corresponding to the logical input values under testing.

Table 2. Inputs generated from the switching network block structure framework.

N	Phase of 2×2 MMI ₄ input arms		Phase of 2×2 MMI ₅ input arms		Relative power at the switching network 4 output ports			
	l_1 - top	l_2 - bottom	l_3 - top	l_4 - bottom	(1)	(2)	(3)	(4)
1	0	0	0	0	1	1	1	1
2	$\pi/2$	0	$\pi/2$	0	1	0	1	0
3	0	$\pi/2$	0	$\pi/2$	0	1	0	1
4	$\pi/2$	0	0	$\pi/2$	1	0	0	1
5	0	$\pi/2$	$\pi/2$	0	0	1	1	0
6	$\pi/2$	0	0	0	1	0	0.5	0.5
7	0	$\pi/2$	0	0	0	1	0.5	0.5
8	0	0	$\pi/2$	0	0.5	0.5	1	0
9	0	0	0	$\pi/2$	0.5	0.5	0	1

N : number of the logical output sequence from the switching network framework. Details of the input/output ports and configuration of the switching network block structure are presented in Figure 16.

A description of the nine logic set of combinations and corresponding phase configuration of the input arms of the two 2×2 MMI coupler BB from the switching network is provided in Table 2. The behavior of the integrated optimized 2×2 MMI BB matching the difference of relative power in the logical outputs generated by the switching network framework will be evaluated in the results section (2.2.2), i.e., when half of the relative power is obtained in the output ports of the 2×2 MMI BB, as identified in logical output sequence N = 6, 7, 8, and 9, see Table 2.

Reconfigurability capabilities will be included in the proposed PIC design through the integration of thermal tuner structures [78] in the input arms of the 2×2 MMI coupler BB to realize the different optical interference splitting/coupling ratios functionalities. Design guidelines from Perez et al. [78] will be considered for the thermal tuner implementation (addressing reliability and durability). The separate sum and subtraction of incoming input signals at the output ports of the MMI can be achieved with a $\pi/2$ (or $3/2\pi$) phase change in one of the input WG of the coupler. For design purposes, the device reconfigurability was assessed by changing the phase launched in the input arms of the 2×2 MMI BB. A difference of phase ($\Delta\phi$) between the input arms of the MMI of $\Delta\phi = \pi/2$ results in a sum/subtraction at the output ports (e.g., 100:0 or 0:100 coupling ratio), while $\Delta\phi = 0$ effects in a splitter (50:50) output behavior.

2.2.1.4 BB structure design optimization

MMI structure design optimization was performed for the BB 2×2 MMI coupler and the BB 1×2 MMI splitter. In an effort to achieve the best-optimized BB for the two final block network structure designs (i.e., the 2D HT network and the switching network framework), three different MMI geometric design shapes were designed and evaluated (i.e., rectangular – geometry A, and two different butterfly geometric shapes – geometry B and C).

WG tapers were introduced in the input and output WG of the MMI BB structures to minimize excess loss, reflections, and imbalance in the expected coupling ratios [94] [97]. All BB structures were designed for five different MMI cross-section widths (i.e., 8, 9, 10, 11, and 12 μm), with 8 μm as the minimum width recommended for MMI structures by the Si₃N₄ foundry standards of CNM-VLC Photonics® [89] [90].

To achieve the best optimization of each MMI design structure, script algorithms were developed in OptoDesigner[®]. The MMI structure design parameters assessed in the BPM simulations were:

- i) MMI length (L);
- ii) MMI widths (W_1 and W_2 , for the different MMI geometries designed);
- iii) distance between MMI access WG (Δd);
- iv) taper widths of MMI access WG (W_{t1} and W_{t2} , where $W_{t1} = 1 \mu\text{m}$, the width of the deep WG core selected for the proposed PIC design solution, see section 2.2.1.2);
- v) taper length of the MMI access WG (L_t).

Further details regarding the design parameters evaluated for the different MMI geometries are depicted in Figure 17.

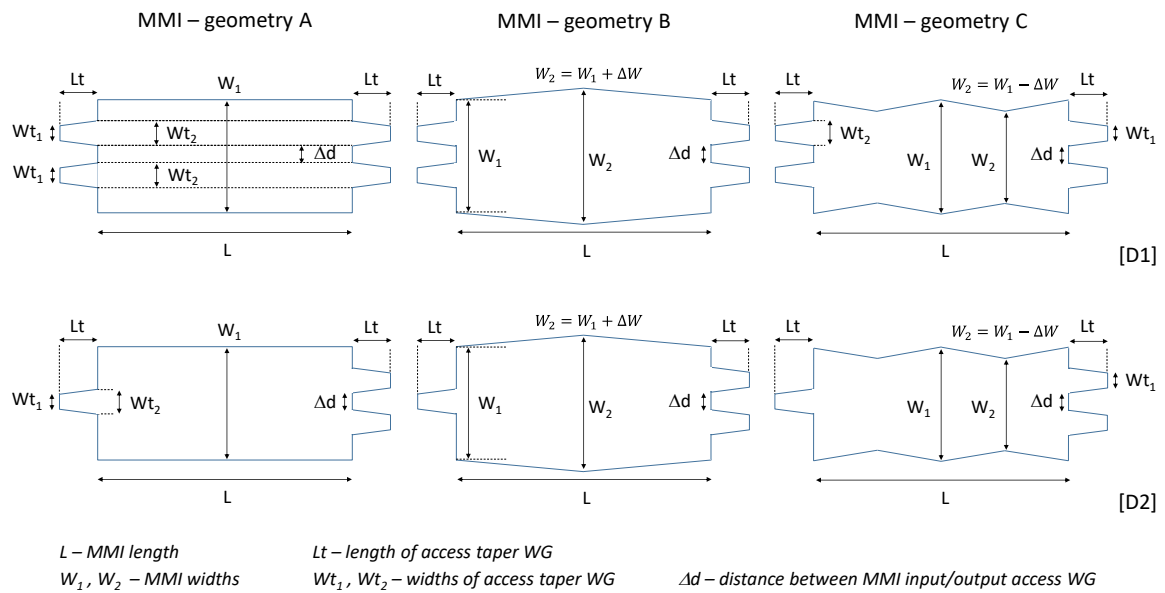


Figure 17. Design parameters assessed for the optimization of the different MMI geometric structures (i.e., geometry A, B, and C). [D1]: Set of three MMI geometries for the 2×2 MMI BB. [D2]: Set of three MMI geometries for the 1×2 MMI BB.

Design optimization steps consisted in a first empirical BPM simulation test to set the best reasonable range of values for the parameters to be assessed. Succeeding, iterative scripts to run the BPM simulations were implemented (with tens of thousands of iterations performed in total). A diagram representing the generic iteration plan performed in the OptoDesigner scripts to calculate the BPM simulations and determine the optimized design for the 2x2 MMI and 1x2 MMI BB structures, are depicted in Figure 18 and Figure 19, respectively.

Boundary design size recommendations from CNM-VLC Si₃N₄ integrated platform technology [89] [90] were assured in all tested design structures, e.g., width of access WG ($\geq 0.6 \mu\text{m}$), width of the MMI structure ($\geq 8 \mu\text{m}$) and distance between MMI access input/output WG ($\geq 1 \mu\text{m}$). Additionally, in all designs, PDK design rule checking (DRC) module was carried out to assure no fundamental errors in the design were held.

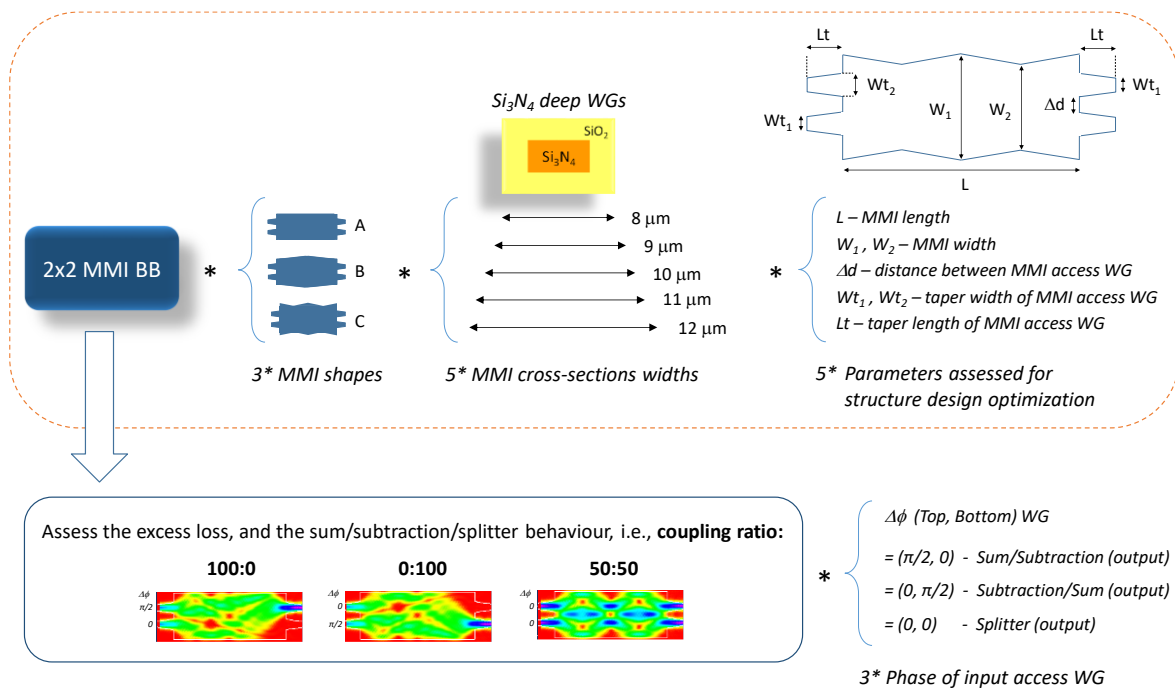


Figure 18. Diagram of iterations performed in the OptoDesigner scripts to calculate the BPM simulations and determine the optimized design for the 2x2 MMI BB structure.

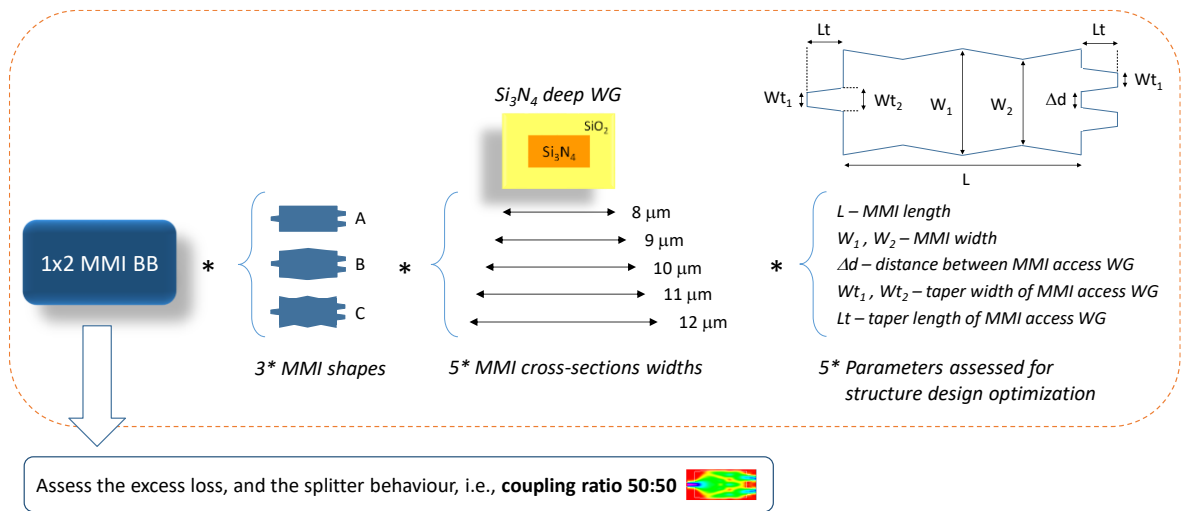


Figure 19. Diagram of the iterations performed in the OptoDesigner scripts to calculate the BPM simulations and determine the optimized design for the 1×2 MMI BB structure.

The first overall set of simulations allowed to identify the MMI length (L) and the distance between the access MMI WG (Δd) as the parameters with higher influence in the overall BB performance. Thus, in the final step of the design optimization methodology was established a constant value for the MMI width W_2 , associated with butterfly geometrical shape, i.e., $W_2 = W_1 + 0.2 \mu\text{m}$ (for geometry B MMI geometry), and $W_2 = W_1 - 0.2 \mu\text{m}$ (for geometry C MMI geometry). Furthermore, MMI access WG taper length (L_t), and access WG taper width (W_{t2}) values with the best-identified performance for each MMI BB structure geometry and W_1 were first empirically established under the design optimization iterative scripts. Then, a range of values was assessed in the design simulations for the length of the MMI BB structure (L) and distance between MMI access WG (Δd).

2.2.1.5 BB design assessment methodology

The metrics used for the assessment of the BB design included device: i) excess loss; ii) coupling ratio; and iii) footprint. BB structures excess loss (EL) and coupling ratio (CR) metrics were calculated from equation (8) and equation (9), respectively. Parameters P_{inj} indicates the linear power at the input WG, and P_{out_j} the linear power at the output WG of the designed MMI BB structures, for k_{in} input WG (i.e., two inputs for the 2×2 MMI and one input for the 1×2 MMI) and k_{out} output WG (i.e., two outputs for both 2×2 MMI and 1×2 MMI).

$$EL = 10 \log_{10} \left(\frac{\sum_{j=1}^{k_{in}} P_{in_j}}{\sum_{j=1}^{k_{out}} P_{out_j}} \right) \quad (8)$$

$$CR = \left(\frac{P_{out_1}}{\sum_{j=1}^2 P_{out_j}} \right) : \left(\frac{P_{out_2}}{\sum_{j=1}^2 P_{out_j}} \right) \quad (9)$$

The BB excess loss and coupling ratio metric under the optimal design dimensions are labeled as EL_{BB} and CR_{BB} , respectively.

The device footprint was calculated from the overall area of the structure, i.e., the area of MMI box plus the area of the MMI access WG. The area of the MMI taper access WG is presented in equation (10), and the area of the MMI structure under the geometries A, B, and C are presented in equations (11), (12), and (13), respectively. The parameter $n_{access\ WG}$ denotes the number of access WG of the structure, i.e., four for the 2×2 MMI and three for the 1×2 MMI structure.

$$A_{access\ WG} = \frac{(Wt_1 + Wt_2)L_t}{2} \quad (10)$$

$$A_{geom.\ A} = LW_1 + n_{access\ WG} A_{access\ WG} \quad (11)$$

$$A_{geom.\ B} = \left(LW_1 + 2 \frac{L|W_1 - W_2|}{2} \right) + n_{access\ WG} A_{access\ WG} \quad (12)$$

$$A_{geom.\ C} = \left(LW_1 - 4 \frac{L|W_1 - W_2|}{2} \right) + n_{access\ WG} A_{access\ WG} \quad (13)$$

All developed MMI BB structures were designed for optimal operation at a wavelength of 1550 nm. Nevertheless, BB structure behavior was also assessed under wavelength C-band range of 1535 nm to 1565 nm, denoted as FT_λ , i.e., a BB design fabrication tolerance for a wavelength range of 1550 ± 15 nm. Furthermore, fabrication tolerances to the BB design dimensions were also evaluated

for an MMI length range of $\Delta L_{\text{MMI}} = 3 \mu\text{m}$, and Δd range of $\Delta - \Delta d = 0.2 \mu\text{m}$, parameter denoted as $FT_{L, \Delta d}$. The aforementioned fabrication tolerances parameters (FT_{λ} , $FT_{L, \Delta d}$) were accessed by the excess loss metric, i.e., the highest EL obtained in response to C-band wavelength bandwidth (FT_{λ} , see formula syntax 14) and the highest EL obtained in response to fabrication tolerances of design parameter L and Δd ($FT_{L, \Delta d}$, see formula syntax 15)

$$FT_{\lambda} \leq \max \{ EL_{\lambda=1535\text{nm}}, EL_{\lambda=1565\text{nm}} \} \quad (14)$$

$$FT_{L, \Delta d} \leq \max \{ EL_{L \pm 1.5 \mu\text{m}}, EL_{\Delta d \pm 0.1 \mu\text{m}} \} \quad (15)$$

A quantitative decision-making method was formulated to determine the best 2×2 and 1×2 MMI design structure by correlating the different metrics used for the assessment of the BB design, i.e., EL_{BB} , CR_{BB} , footprint, FT_{λ} and $FT_{L, \Delta d}$. This method allowed to generate a comprehensive parameter that evaluates the overall performance of the different BB design structures, defined as BB_{eval} . As in all the designs the expected CR was attained (with corresponding crosstalk below 0.2%), this metric was not included in the decision-making formulation. Two main parameter components were established for the BB evaluation, i.e., the excess loss (N_{EL}) and footprint ($N_{\text{footprint}}$). The parameter N_{EL} included EL_{BB} , FT_{λ} and $FT_{L, \Delta d}$, while the footprint was attained by the area of the BB structure.

Weighted arithmetic calculations were carried out to ponder the contribution of the different metrics assessed. Under the excess loss parameter, its linear counterpart ($EL_{\text{linear}} = 10^{EL_{\text{dB}}/10}$) was accounted for the weighted arithmetic calculus. For a rational device structure evaluation, a higher rate was outlined for the EL parameter under the optimal design dimensions (EL_{BB}), with a stipulated weighting factor (wf) of 60%, while for the fabrication tolerances parameters an overall weight of 40% was established, i.e., half for FT_{λ} (wf = 20%) and half for $FT_{L, \Delta d}$ (wf = 20%), see Figure 20.

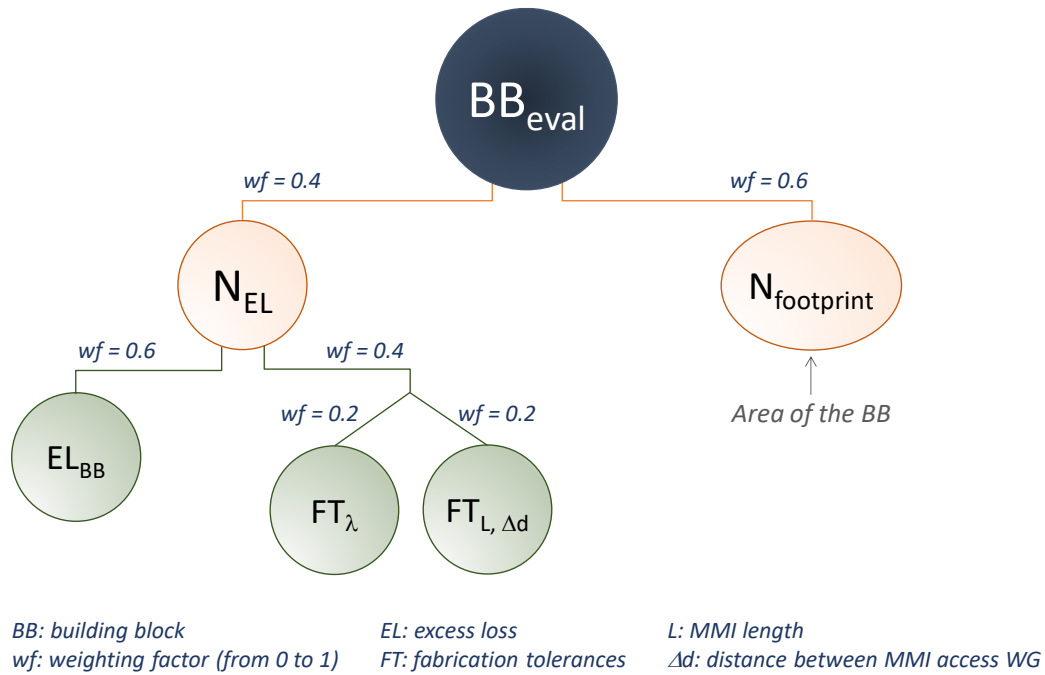


Figure 20. Diagram of the general decision-making methodology implemented to quantitatively determine the best BB structure from the different implemented designs.

To extract the variability of N_{EL} , the offset constant component was removed ($1 - N_{EL}$), and performed the normalization. N_{EL} can be generically defined by equation (16).

$$N_{EL} = 0.6EL_{BB} + 0.2FT_{\lambda} + 0.2FT_{L, \Delta d} \quad (16)$$

The $N_{\text{footprint}}$ parameter was given by the normalization of the BB area obtained for the different designed structures (see equations 11, 12, and 13). The lowest values of N_{EL} and the $N_{\text{footprint}}$ correspond to the best-optimized BB design structures.

The BB_{eval} parameter is then realized by a weighted arithmetic sum between the components N_{EL} and $N_{\text{footprint}}$. Highly optimized excess loss values were obtained under the proposed optimal dimensions designs, i.e., generically with EL_{BB} below 0.02 dB, see results in subsection 2.2.2. Thus, a higher weighting factor was given for the footprint component, i.e., 60% for $N_{\text{footprint}}$ and 40% for N_{EL} . To guarantee that the scale range of values under parameter N_{EL} and $N_{\text{footprint}}$ were comparable, a differential scale factor was considered, given by the division of the amplitude of $N_{\text{footprint}}$ by the

amplitude of N_{EL} , i.e., $S_{factor} = \frac{|\min\{N_{EL}\} - \max\{N_{EL}\}|}{|\min\{N_{footprint}\} - \max\{N_{footprint}\}|}$. The BB_{eval} formulation is presented in equation (17).

$$BB_{eval} = 0.6N_{footprint} + 0.4N_{EL} S_{factor} \quad (17)$$

Under the BB_{eval} formulation, lower values correspond to higher performances of the optimized BB structure designs.

A diagram describing the general decision-making methodology implemented to quantitatively determine the best BB structure from the different implemented designs is depicted in Figure 20. A compromise between the lowest EL, footprint, and response to fabrication tolerances was attained under the calculus of the BB_{eval} parameter for the decision-making of the best-optimized BB structure design. The results of the different optimized BB structure designs implemented are provided in section 2.2.2.

2.2.2 Results and discussion

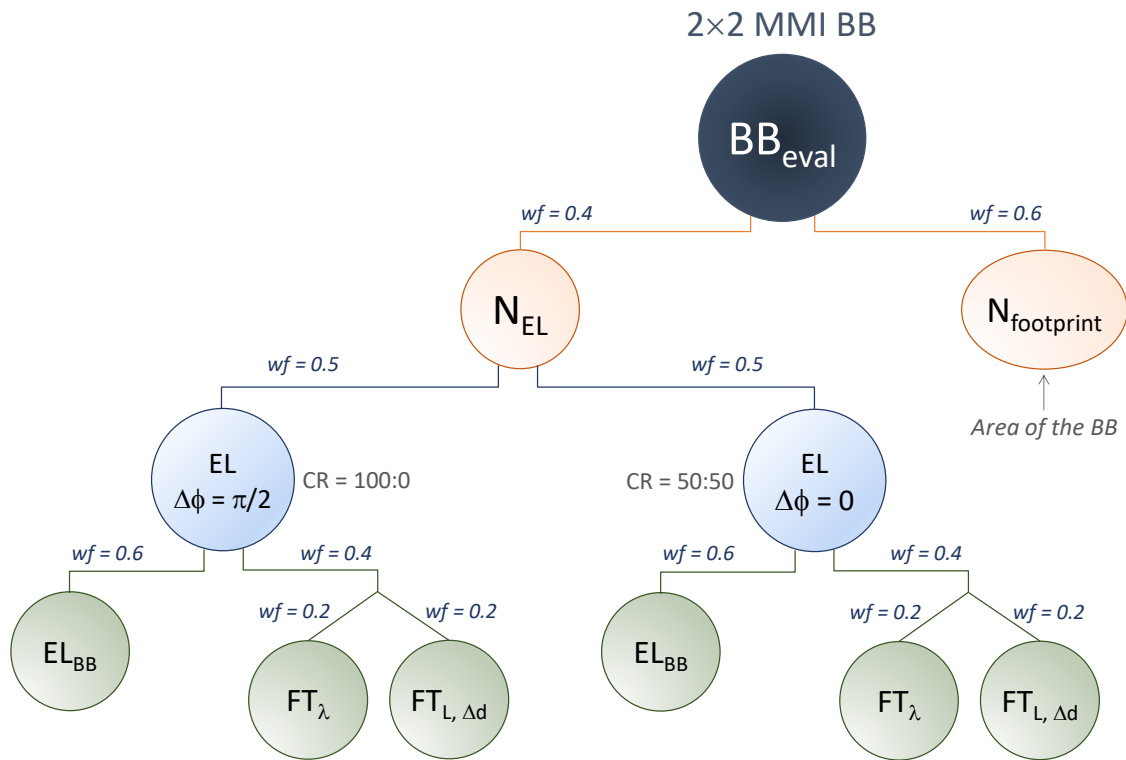
The BB_{eval} decision-making parameter (described in the subsection 2.2.1.5) was used to evaluate BB structure design with the best performance behavior. Results obtained for the design optimization of the BB 2×2 MMI coupler and BB 1×2 MMI splitter are presented in sections 2.2.2.1 and 2.2.2.2, respectively.

2.2.2.1 Optimized BB design for 2×2 MMI BB structure

The 2×2 MMI coupler BB was designed to operate at the following coupling ratios (sum/subtraction: 100:0; subtraction/sum: 0:100; and splitting: 50:50), at the lowest possible excess loss and footprint. As MMI coupler operation mode sum/subtraction (i.e., coupling ratio 100:0) and subtraction/sum (i.e., coupling ratio 0:100) are mirrored equivalent, in the results only sum/subtraction (100:0) operation mode is provided.

The MMI sum/subtraction behavior is achieved when a phase of $\pi/2$ is launched in the top input arm of the MMI (i.e., MMI difference of phase between the input arms of $\Delta\phi = \pi/2$). While the splitting behavior is reached when the difference of phase between the input arms of the MMI is $\Delta\phi = 0$, i.e., no additional phase is launched.

The BB_{eval} formulation (see subsection 2.2.1.5, equation 17) was deployed to evaluate the performance of the different design structures implemented. As for the 2×2 MMI BB structure two operation CR modes (100:0; and 50:50) were required, the BB_{eval} formulation is updated as depicted in Figure 21. The excess loss parameter component (N_{EL}) is attained for N_{EL} under a difference of phase between the MMI input arms of $\Delta\phi = \pi/2$ ($N_{EL, \Delta\phi = \pi/2}$), and $\Delta\phi = 0$ ($N_{EL, \Delta\phi = 0}$), i.e., $N_{EL} = 0.5N_{EL, \Delta\phi = \pi/2} + 0.5N_{EL, \Delta\phi = 0}$, see Figure 21.



BB: building block EL: excess loss L: MMI length
 wf: weighting factor (from 0 to 1) FT: fabrication tolerances Δd : distance between MMI access WG

Figure 21. Diagram of the decision-making methodology implemented to quantitatively determine the best design structure for the 2×2 MMI BB.

The EL metrics for CR = 100:0 ($\Delta\phi = \pi/2$) and CR = 50:50 ($\Delta\phi = 0$) of the optimized 2×2 MMI structure dimensions for each MMI width $W_1 = 8, 9, 10, 11$ and $12 \mu\text{m}$, is provided in Table 3, under the MMI designed geometries A, B, and C.

BB MMI design fabrication tolerances for a wavelength range (FT_λ) of $1550 \pm 15 \text{ nm}$, MMI length range of $\Delta L_{\text{MMI}} = 3 \mu\text{m}$, and Δd range of $\Delta - \Delta d = 0.2 \mu\text{m}$ ($FT_{L, \Delta d}$) are also evaluated. Details regarding the parameters FT_λ and $FT_{L, \Delta d}$ are described in subsection 2.2.1.5, equation (14) and (15), respectively.


BPM simulations results from Table 3 provide a detailed guide of BB design parameters for the selection of the BB design that better matches the functional requirements of the circuit and/or device to be developed. All 2×2 MMI BB structures were designed to realize the expected coupling ratio of 100:0 ($\Delta\phi = \pi/2$), and 50:50 ($\Delta\phi = 0$), and all attained the expected CR with low crosstalk (XT), i.e., $XT < 0.006 \text{ dB}$ (equation 18) for CR = 100:0 mode, and $XT < 0.004 \text{ dB}$ (equation 19) for CR = 50:50 mode. These results corresponded to deviations in the expected CR below 0.2% which validates the expected CR modes. Thus, the results presented in Table 3 are focused on the EL metrics for the optimal BB dimensions (EL_{BB}) and the fabrication tolerance parameters (FT_λ and $FT_{L, \Delta d}$).


$$XT_{\Delta\phi=\pi/2} = 10 \log_{10} \left(\sum_{j=1}^{k_{out}} P_{out_j} / \max \{ P_{out} \} \right) \quad (18)$$


$$XT_{\Delta\phi=0} = 10 \log_{10} \left(\left(\sum_{j=1}^{k_{out}} P_{out_j} / 2 \right) / \min \{ P_{out} \} \right) \quad (19)$$

The BB structure designs with the best-optimized performance (i.e., lowest BB_{eval}) for 2×2 MMI BB geometry A, B, and C are highlighted in bold in Table 3.

Table 3. Optimized 2×2 MMI BB design dimensions for geometry A, B, and C.

2×2 MMI – geometry A 						$\Delta\phi = \pi/2 \rightarrow \text{CR} = 100:0$			$\Delta\phi = 0 \rightarrow \text{CR} = 50:50$			BB _{eval} (a.u.)
BB dimensions (μm)						EL _{BB}	FT _{λ}	FT _{L,Δd}	EL _{BB}	FT _{λ}	FT _{L,Δd}	
L	Δd	W ₁	W ₂	Lt	Wt ₂	EL (dB)	EL \leq (dB)	EL \leq (dB)	EL (dB)	EL \leq (dB)	EL \leq (dB)	
49.0	1.00	8	-	16	1.9	0.00160	0.019	0.21	0.0160	0.017	0.22	0.532
61.0	1.10	9	-	11	2.1	0.00113	0.033	0.15	0.0124	0.044	0.20	0.531
75.5	1.25	10	-	14	2.2	0.00046	0.054	0.13	0.0212	0.014	0.20	0.587
90.0	1.40	11	-	11	2.4	0.00090	0.033	0.11	0.0022	0.062	0.16	0.574
107.0	1.50	12	-	14	2.6	0.00049	0.041	0.09	0.0049	0.056	0.10	0.613

2×2 MMI – geometry B 						$\Delta\phi = \pi/2 \rightarrow \text{CR} = 100:0$			$\Delta\phi = 0 \rightarrow \text{CR} = 50:50$			BB _{eval} (a.u.)
BB dimensions (μm)						EL _{BB}	FT _{λ}	FT _{L,Δd}	EL _{BB}	FT _{λ}	FT _{L,Δd}	
L	Δd	W ₁	W ₂	Lt	Wt ₂	EL (dB)	EL \leq (dB)	EL \leq (dB)	EL (dB)	EL \leq (dB)	EL \leq (dB)	
50.0	1.00	8	8.2	12	1.9	0.00412	0.028	0.21	0.0259	0.024	0.25	0.502
62.0	1.10	9	9.2	10	2.1	0.00033	0.060	0.20	0.0075	0.083	0.28	0.587
76.0	1.20	10	10.2	16	2.2	0.00036	0.080	0.19	0.0201	0.126	0.29	0.737
91.0	1.40	11	11.2	10	2.4	0.00025	0.073	0.15	0.0211	0.110	0.23	0.757
109.0	1.50	12	12.2	14	2.6	0.00174	0.059	0.11	0.0015	0.034	0.08	0.706

2×2 MMI – geometry C 						$\Delta\phi = \pi/2 \rightarrow \text{CR} = 100:0$			$\Delta\phi = 0 \rightarrow \text{CR} = 50:50$			BB _{eval} (a.u.)
BB dimensions (μm)						EL _{BB}	FT _{λ}	FT _{L,Δd}	EL _{BB}	FT _{λ}	FT _{L,Δd}	
L	Δd	W ₁	W ₂	Lt	Wt ₂	EL (dB)	EL \leq (dB)	EL \leq (dB)	EL (dB)	EL \leq (dB)	EL \leq (dB)	
47.5	1.00	8	7.8	7	1.8	0.00474	0.034	0.27	0.0171	0.032	0.33	0.478
59.5	1.35	9	8.8	10	1.8	0.00374	0.054	0.13	0.0131	0.043	0.24	0.458
73.0	1.30	10	9.8	11	2.2	0.00086	0.038	0.14	0.0002	0.026	0.15	0.466
88.0	2.00	11	10.8	10	1.8	0.01938	0.139	0.28	0.0189	0.113	0.26	0.796
104.5	2.10	12	11.8	16	2.0	0.02724	0.135	0.19	0.0404	0.121	0.17	0.887

L: MMI length; W₁, W₂: MMI widths; Lt: length of access taper WG; Wt₁, Wt₂: widths of access taper WG; Δd : distance between MMI input/output access WG; $\Delta\phi$: difference of phase between the input access WG; FT _{λ} : BB fabrication tolerances for $\Delta\lambda = 30 \text{ nm}$ ($\lambda = 1550 \pm 15 \text{ nm}$); FT_{L, Δd} : BB fabrication tolerances for $\Delta L_{\text{MMI}} = 3 \mu\text{m}$, and $\Delta-\Delta d = 0.2 \mu\text{m}$. The 2×2 MMI BB designs with the best performance from geometry A, B, and C are highlighted in bold. In pink is highlighted the overall best-optimized BB structure, corresponding to the lowest value of BB_{eval}.

A compromise between the lowest EL, footprint, and response to fabrication tolerances was accomplished for the selection of the best-optimized BB designs, through the BB_{eval} parameter. From the MMI geometry response assessment can be identified a higher performance behavior under the geometry C for the three lowest footprint designs (i.e., $L \leq 73 \mu\text{m}$), when compared to its counterparts MMI geometry A and B. The 2×2 MMI BB with the best-optimized performance was the one given by the geometry C structure with the dimensions: $L = 59.5 \mu\text{m}$; $\Delta d = 1.35 \mu\text{m}$; $W_1 = 9 \mu\text{m}$; $W_2 = 8.8 \mu\text{m}$; $L_t = 10 \mu\text{m}$; and $W_{t2} = 1.8 \mu\text{m}$, highlighted in pink in Table 3.

The BB performance associated with MMI L and Δd design parameters was used to extrapolate a model based on a second-degree polynomial under the best-optimized 2×2 MMI BB design structure from the MMI geometries studied. In Figure 22 is depicted the extrapolated second-degree polynomial model of the best-optimized 2×2 MMI BB structure from the three implemented geometries, i.e., the 2×2 MMI BB geometry C design with $L = 59.5 \mu\text{m}$.

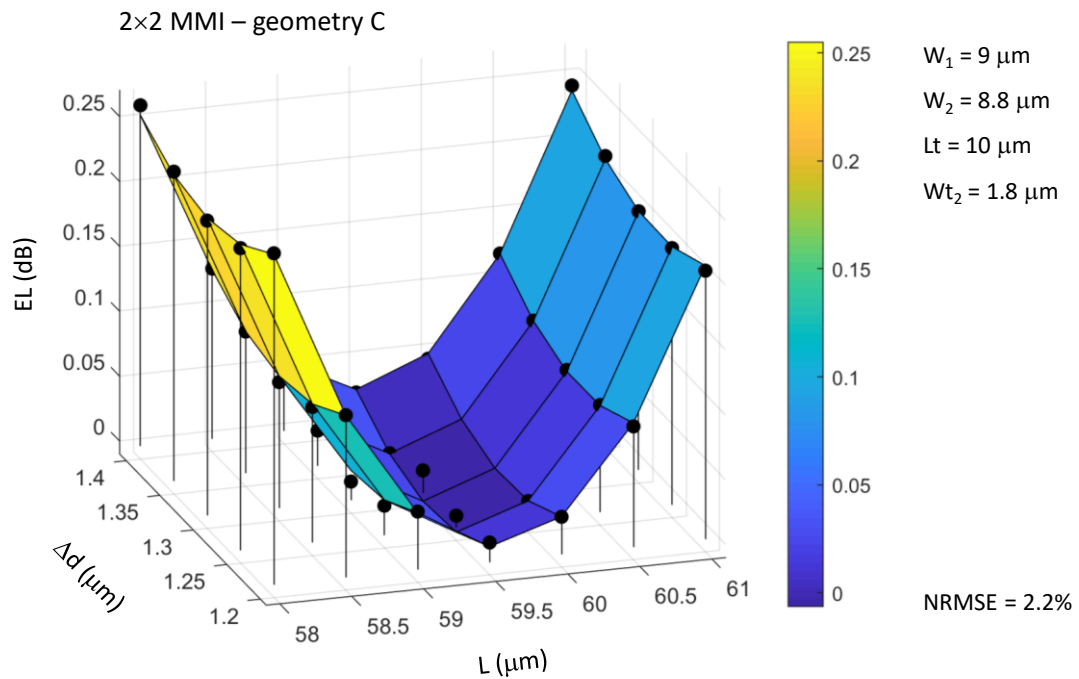


Figure 22. Model of the BB 2×2 MMI geometry C design corresponding to the best overall performance obtained. The 2nd degree polynomial fit was achieved with a normalized root mean square error (NRMSE) of 2.2%. Constant design parameters (i.e., W_1 , W_2 , L_t , and W_{t2}) of the BB are provided in the figure top right corner.

The deduced second-degree polynomial function for the best-optimized 2×2 MMI BB design structure under the three geometry designs (A, B, and C) is described by equation (20). Where EL is the BB design excess loss, L the MMI length, and Δd the distance between the input/output access WG of the 2×2 MMI BB structure. Deduced second-degree polynomial function coefficients are represented by $u_{1:6}$.

$$EL = u_1 L^2 + u_2 L \Delta d + u_3 L + u_4 \Delta d^2 + u_5 \Delta d + u_6 \quad (20)$$




The corresponding equations to estimate L (equation 21) and Δd (equation 22) were derived from equation (20).

$$L = \frac{-(u_3 \pm \sqrt{u_2^2 \Delta d^2 + 2u_2 u_3 \Delta d + u_3^2 - 4(u_1 u_4 \Delta d^2 + u_1 u_5 \Delta d + u_1 u_6 - u_1 EL)} + u_2 \Delta d)}{2u_1} \quad (21)$$

$$\Delta d = \frac{-(u_5 + u_2 L \pm \sqrt{u_2^2 L^2 + 2u_2 u_5 L + u_5^2 - 4(u_1 u_4 L^2 + u_3 u_4 L + u_4 u_6 - u_4 EL)})}{2u_4} \quad (22)$$

The coefficients of the achieved function for the three 2×2 MMI geometries (A, B, and C) are provided in Table 4.

Table 4. Coefficients of 2nd degree polynomial function model for optimized 2×2 MMI BB structures.

MMI geometry	u_1	u_2	u_3	u_4	u_5	u_6
A 	6.00×10^{-2}	-3.42×10^{-2}	-7.28	2.40	-2.88	223.72
B 	7.73×10^{-2}	-1.34×10^{-1}	-7.60	2.78	1.76	188.83
C 	9.82×10^{-2}	4.64×10^{-2}	-11.75	2.55	-9.32	355.89

To realize the HT was implemented the 2×2 MMI BB design with the best overall performance, i.e., the lowest BB_{eval} (0.458), achieved by the BB design geometry C with the MMI length $L = 59.5 \mu\text{m}$ and width $W_1 = 9 \mu\text{m}$ (see Table 3).

The design attained an $EL_{BB} \leq 0.01$ dB for both CR modes, i.e., $EL_{BB} = 0.0037$ dB (and $XT = 0.0047$ dB) for $\Delta\phi = \pi/2$, and $EL_{BB} = 0.013$ dB (and $XT = 0.0039$ dB) for $\Delta\phi = 0$. Furthermore, excess loss $EL \leq 0.05$ dB was attained for wavelength fabrication tolerances (FT_λ), and $EL \leq 0.2$ dB for device dimension fabrication tolerances ($FT_{L, \Delta d}$). As device dimension fabrication tolerances have a higher impact in the EL performance of the BB, greater attention should be given to the fabrication process, in order to guarantee that the BB dimensions are realized as close as possible to the optimal design specifications.

Light propagation simulations of the two-level HT network (see Figure 15, from section 2.2.1.3) composed by a cascade of three optimized 2×2 MMI BB are depicted in Figure 23. The HT operations are carried out as expected, which can be confirmed by the obtained sum power at the output waveguide port (2) of the two-level HT network. The depicted 2D HT network has an overall footprint of $190 \times 21 \mu\text{m}^2$.

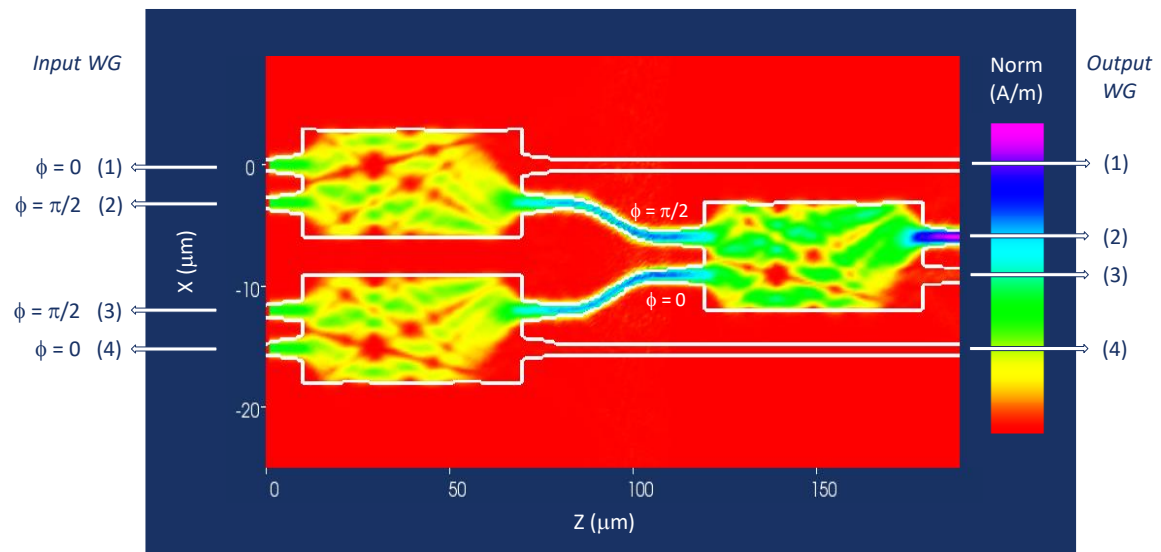


Figure 23. Light propagation simulation of the two-level HT main block structure, composed by a cascade of three optimized 2×2 MMI BB structures.

Furthermore, the same BB design will be implemented in the switching network main block (as depicted in Figure 16, from section 2.2.1.3). To realize the different logic outputs, the 2×2 MMI BB will need to operate as sum/subtraction and splitter mode.

The selected BB with the best-optimized 2×2 MMI design presents an MMI box footprint of $59.5 \mu\text{m} \times 9 \mu\text{m}$ ($536 \mu\text{m}^2$) and an EL of 0.0037 dB, under the optimal design dimensions at the main mode of operation (CR = 100:0).

From the literature can be identified an InP MMI design reporting an MMI box footprint of $260 \times 8 \mu\text{m}^2$ and an EL of 0.25 dB [76], for similar applications. The employment of similar MMI butterfly shapes (as the implemented MMI geometries B and C) are reported in [94] with SOI-based MMI structure footprint designs ranging from $123 \times 10 \mu\text{m}^2$ to $240 \times 10 \mu\text{m}^2$, with an average EL of 0.6 dB; and in [93] with InGaAsP/InP-based MMI structure footprint designs ranging from $308 \times 12 \mu\text{m}^2$ to $1224 \times 24 \mu\text{m}^2$, with an overall EL below 0.7 dB. Furthermore, available Si_3N_4 -based 2×2 MMI structure BB under the CNM PDK with a footprint of $2397 \mu\text{m}^2$ and an expected insertion loss below 1 dB are disclosed [89].

The best-optimized 2×2 MMI design BB proposed in this study shows an overall improved performance when compared to literature, with a reduced footprint, up to 1/4 lower when compared to its implementation for similar applications, such as in [76] and in [89]. Furthermore, the proposed design also entails an EL and XT metrics below 0.005 dB for the sum/subtraction CR mode, and below 0.02 dB for the splitter CR configuration. The use of more unconventional MMI geometries such as the butterfly shape C showed an overall improved performance BB behavior, allowing to attain a device with lower footprint and excess loss, while guarantying the realization of the required CR modes, under wavelength and dimension fabrication tolerances evaluation.

The optimization design study performed provides a relevant evaluation of the BB performance behavior and allowed to select the one that best addresses the HT compression and switching networks purposes. Further simulation graphic results are provided in the Appendix section A.1 and can be used to select a different optimized BB design depending on the functional requirements of the PIC to be developed.

2.2.2.2 Optimized BB design for 1×2 MMI BB structure

The 1×2 MMI BB was designed to provide a splitting behavior with an expected output coupling ratio of 50:50, at the lowest possible excess loss and footprint. The EL metrics for CR = 50:50 of the optimized 1×2 MMI structure dimensions for each MMI width $W_1 = 8, 9, 10, 11$ and $12 \mu\text{m}$, is assessed, see Table 5. The BB_{eval} formulation (see subsection 2.2.1.5, equation 17) was deployed to evaluate the performance of the different design structures implemented.

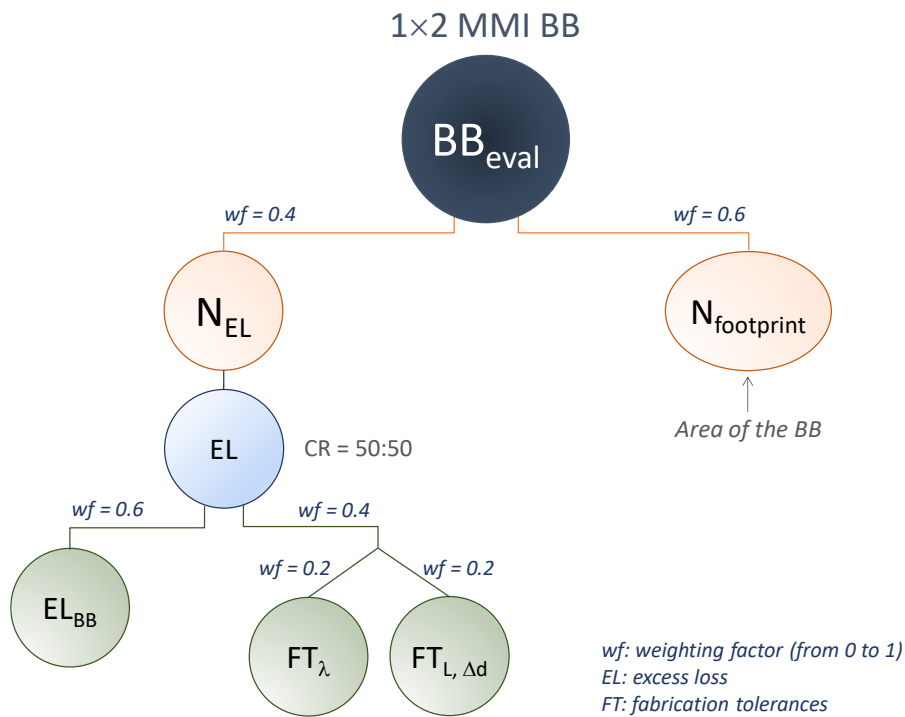





Figure 24. Diagram of the decision-making methodology implemented to quantitatively determine the best design structure for the 1×2 MMI BB.

The BB_{eval} formulation implemented for the decision-making of the best-optimized 1×2 MMI BB structure is depicted in Figure 24. BPM simulations results presented in Table 5 provide a detailed guide of BB design parameters for the selection of the 1×2 MMI BB design that better match the expected functional requirements. Similarly, as for 2×2 MMI BB structure, design fabrication tolerances for a wavelength range (FT_{λ}) of $\lambda = 1550 \pm 15 \text{ nm}$, MMI length range of $\Delta L_{\text{MMI}} = 3 \mu\text{m}$, and Δd range of $\Delta - \Delta d = 0.2 \mu\text{m}$ ($FT_{L, \Delta d}$), are evaluated.

Table 5. Optimized 1×2 MMI BB design dimensions for geometry A, B, and C.

1×2 MMI – geometry A 						$\Delta\phi = 0 \rightarrow \text{CR} = 50:50$			
BB dimensions (μm)						EL _{BB}	FT _{λ}	FT _{L, Δd}	
L	Δd	W ₁	W ₂	Lt	Wt ₂	EL	EL \leq	EL \leq	BB _{eval}
						(dB)	(dB)	(dB)	(a.u)
36.0	2.15	8	-	12	2.0	0.00085	0.033	0.165	0.415
45.0	2.55	9	-	10	2.1	0.00161	0.055	0.151	0.464
55.5	3.10	10	-	13	2.1	0.00031	0.085	0.166	0.575
67.5	3.50	11	-	12	2.1	0.00199	0.031	0.131	0.494
80.0	4.10	12	-	18	2.1	0.00002	0.056	0.148	0.621

1×2 MMI – geometry B 						$\Delta\phi = 0 \rightarrow \text{CR} = 50:50$			
BB dimensions (μm)						EL _{BB}	FT _{λ}	FT _{L, Δd}	
L	Δd	W ₁	W ₂	Lt	Wt ₂	EL	EL \leq	EL \leq	BB _{eval}
						(dB)	(dB)	(dB)	(a.u)
37.0	2.20	8	8.2	12	2.0	0.00020	0.037	0.160	0.412
47.0	2.50	9	9.2	13	2.1	0.00017	0.006	0.156	0.406
57.5	2.95	10	10.2	13	2.2	0.00074	0.023	0.152	0.482
69.0	3.55	11	11.2	12	2.1	0.00011	0.052	0.178	0.620
81.0	4.10	12	12.2	18	2.1	0.00772	0.080	0.168	0.764

1×2 MMI – geometry C 						$\Delta\phi = 0 \rightarrow \text{CR} = 50:50$			
BB dimensions (μm)						EL _{BB}	FT _{λ}	FT _{L, Δd}	
L	Δd	W ₁	W ₂	Lt	Wt ₂	EL	EL \leq	EL \leq	BB _{eval}
						(dB)	(dB)	(dB)	(a.u)
35.5	2.10	8	7.8	7	2.0	0.00055	0.017	0.200	0.411
44.5	2.40	9	8.8	10	2.2	0.00030	0.012	0.174	0.394
54.5	2.85	10	9.8	11	2.2	0.00433	0.022	0.213	0.524
66.0	3.50	11	10.8	11	2.1	0.00337	0.045	0.179	0.545
78.0	4.00	12	11.8	17	2.1	0.00387	0.066	0.179	0.636

L: MMI length; W₁, W₂: MMI widths; Lt: length of access taper WG; Wt₁, Wt₂: widths of access taper WG; Δd : distance between MMI input/output access WG; $\Delta\phi$: difference of phase between the input access WG; FT _{λ} : BB fabrication tolerances for $\Delta\lambda = 30 \text{ nm}$ ($\lambda = 1550 \pm 15 \text{ nm}$); FT_{L, Δd} : BB fabrication tolerances for $\Delta L_{\text{MMI}} = 3 \mu\text{m}$, and $\Delta-\Delta d = 0.2 \mu\text{m}$. The 1×2 MMI BB designs with the best performance from geometry A, B, and C are highlighted in bold. In pink is highlighted the overall best-optimized BB structure, corresponding to the lowest value of BB_{eval}.

A coupling ratio of CR = 50:50 was attained in all the designs with an XT \leq 0.002 dB (equation 19, subsection 2.2.2.1). This XT value corresponds to deviations in the expected CR below 0.05% which strongly validates the expected CR mode. Thus, the results presented in Table 5 are focused on the EL metrics for the optimal BB dimensions (EL_{BB}) and the fabrication tolerance parameters (FT _{λ} and FT_{L, Δ d}). A compromise between the lowest EL, footprint, and response to fabrication tolerances was accomplished for the selection of the best-optimized BB designs, through the BB_{eval} parameter, see Table 5.

The best design performance for the 1 \times 2 MMI BB was attained under geometry C for MMI design dimensions: L = 44.5 μ m; Δ d = 2.4 μ m; W₁ = 9 μ m; W₂ = 8.8 μ m; Lt = 10 μ m; and Wt₂ = 2.2 μ m. The device presents an excess loss of EL_{BB} = 0.0003 dB and XT = 0.0002 dB under the optimal design dimensions, and regarding the assessed fabrication tolerances an EL \leq 0.012 dB for FT _{λ} , and EL \leq 0.17 dB for FT_{L, Δ d}. Likewise to 2 \times 2 MMI BB assessment, fabrication dimension tolerances (FT_{L, Δ d}) has a higher impact in the BB EL performance, thus fabrication should match as possible the optimal design specifications.

Similar design performances (through BB_{eval} assessment) are attained under the three MMI geometries for the lower footprint BB designs, with an L \leq 47 μ m. Thus, good results are predicted with the implementation of any of these designs under the requirements of the integrated approach proposed. Nonetheless, to maximize the PIC performance, the BB with the highest performance was selected.

As well as for the optimized 2 \times 2 MMI BB designs, a BB model based on a second-degree polynomial function under the best-optimized 1 \times 2 MMI BB design structure is realized, see Figure 25. The coefficients of the achieved second-degree polynomial function (from equation 20) are u_{1-6} = [5.36 \times 10⁻², 9.90 \times 10⁻³, -4.77, 1.61, -8.14, 115.23].

The optimized 1 \times 2 MMI BB structure was implemented in the switching network main block composed by a cascade of three 1 \times 2 MMI BB and two 2 \times 2 MMI BB, see Figure 16 from section 2.2.1.3. The switching network allows generating the available nine outputs logic values (see Table 2 from section 2.2.1.3), which will be delivered as the four inputs of the two-level HT network.

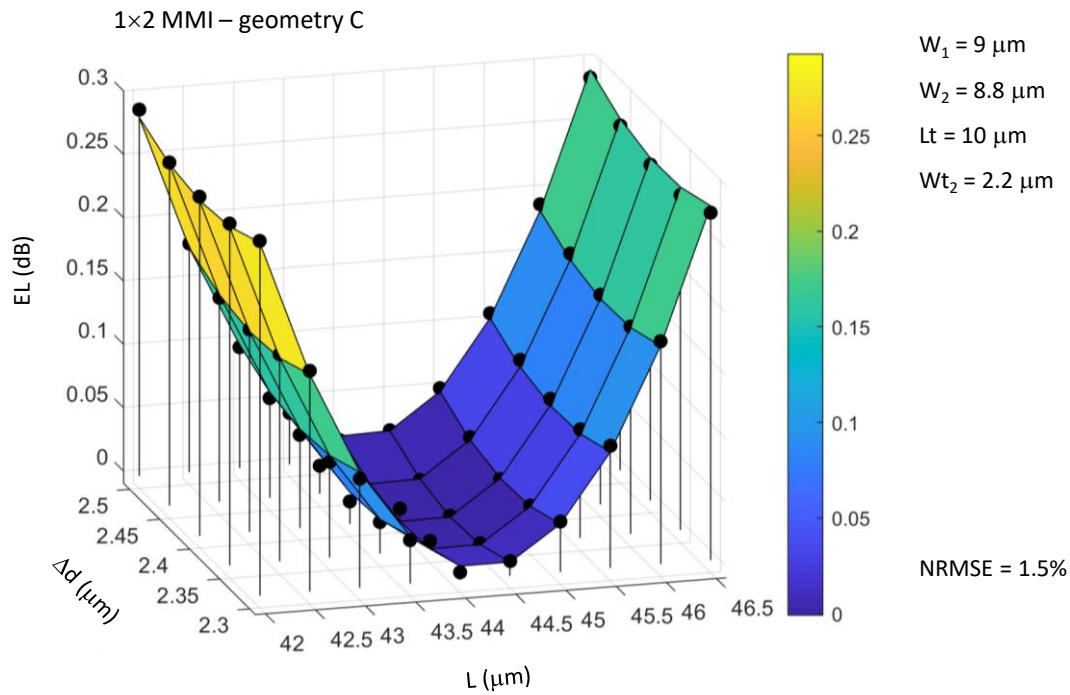


Figure 25. Model of the BB 1×2 MMI geometry C design corresponding to the best overall performance obtained. The 2nd degree polynomial fit was achieved with a normalized root mean square error (NRMSE) of 1.5%. Constant design parameters (i.e., W_1 , W_2 , L_t , and W_{t_2}) of the BB are provided in the figure top right corner.

In Figure 26 are presented two sets of logic outputs attained by the switching network through BPM light propagation simulation. The different sets of logic outputs are realized by changing the phase (ϕ) launched in the input arms of the 2×2 MMI BB.

The complete phase configuration set for the available nine logic outputs of the switching network was previously described in Table 2 from section 2.2.1.3. Switching network operations are carried out as expected, which can be confirmed by the identified network outputs corresponding to a logic output of [1 1 1 1] for a phase input of $\phi_{\{1,2,3,4\}} = [0, 0, 0, 0]$ (see Figure 26-A), and a logic output [1 0 0 1] for a phase input of $\phi_{\{1,2,3,4\}} = [\pi/2, 0, 0, \pi/2]$ (see Figure 26-B). The depicted switching network has an overall footprint of $260 \times 20 \mu\text{m}^2$.

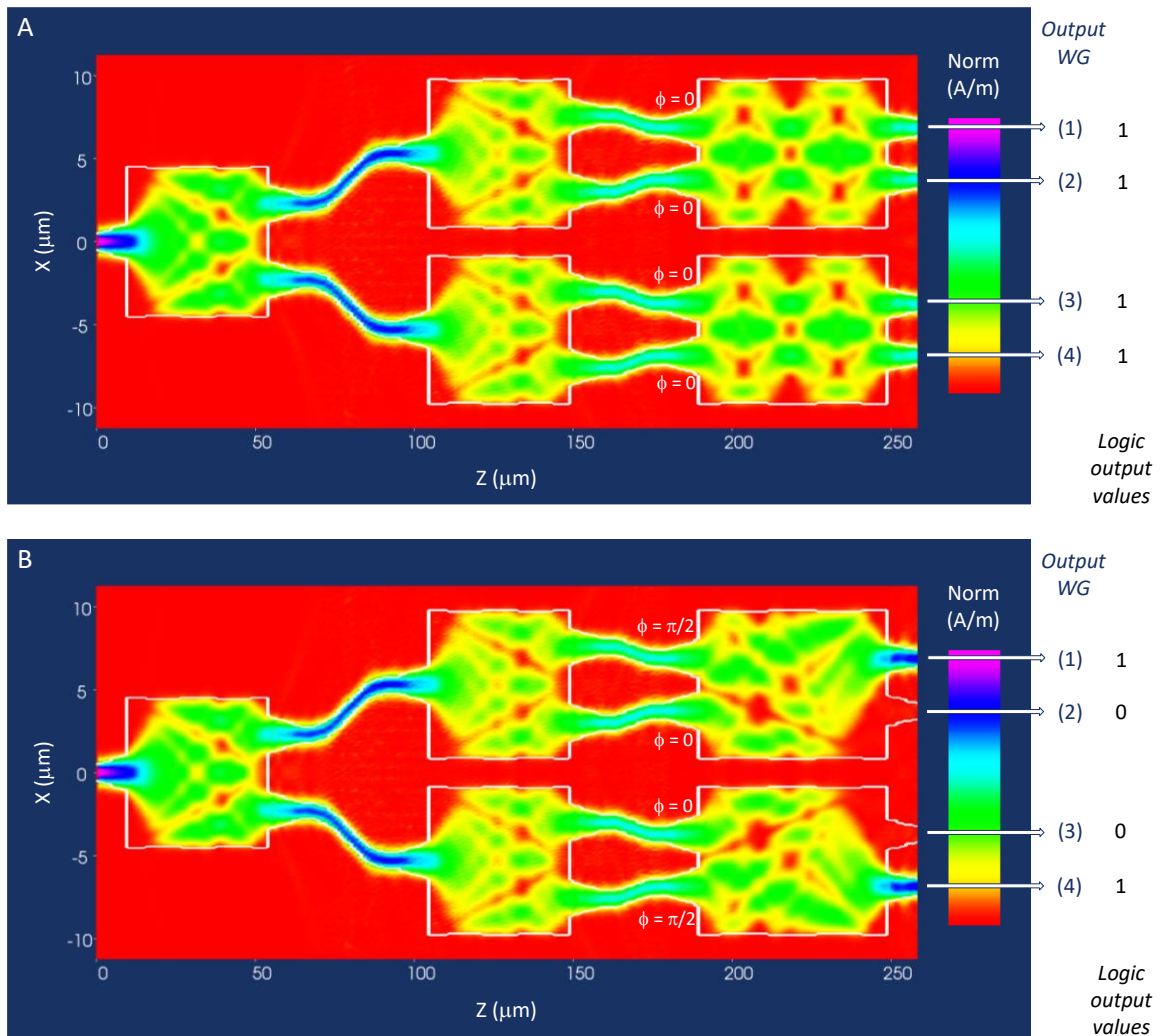


Figure 26. Light propagation simulation of the switching network main block structure, composed by a cascade of three optimized 1x2 MMI BB and two 2x2 MMI BB. Examples of two sets of logic outputs attained by the switching network block are provided in [A] and [B]. The different sets of logic outputs is accomplished by changing the phase (ϕ) launched in the input arms of the 2x2 MMI BB, i.e., [A]: $\phi_{\{1,2,3,4\}} = [0, 0, 0, 0]$ resulting in the logic outputs [1 1 1 1]; and [B]: $\phi_{\{1,2,3,4\}} = [\pi/2, 0, 0, \pi/2]$ resulting in the logic outputs [1 0 0 1].

When half of the relative power is obtained in two of the output ports, as identified in logical output sequence N = 6, 7, 8, and 9 (see Table 2, section 2.2.1.3), the 2x2 MMI BB coupling ratio response suffers a slight performance impairment ($\leq 4\%$, $XT \leq 0.18$ dB), e.g., in a sum/subtraction 2x2 MMI configuration mode, a lower CR performance of 96:4 can be achieved. EL metrics response is the same as characterized in section 2.2.2.1, Table 3.

The selected 1×2 MMI BB with the best-optimized performance presents a footprint of $44.5\ \mu\text{m} \times 9\ \mu\text{m}$ ($401\ \mu\text{m}^2$) and an EL and XT close to 0 dB (i.e., below 0.0003 dB) under the optimal design dimensions. The footprint attained is approximately 1/3 lower than the available Si_3N_4 -based 1×2 MMI BB structure under the CNM PDK, which reports a footprint of $1165\ \mu\text{m}^2$ and an expected insertion loss below 1 dB [89].

Likewise for the best-optimized 2×2 MMI BB, the MMI butterfly geometry C design attained the best performance for the 1×2 MMI BB, nevertheless near performance values were achieved under the remaining studied 1×2 MMI geometries B and A. The optimization design study performed provides a relevant evaluation of the 1×2 MMI BB structure performance behavior under the requirements of the proposed integrated approach for compression applications. Further simulations results are provided in the Appendix section A.2 and can be used to select a different optimized 1×2 MMI BB design depending on the functional requirements of the PIC block structure to be developed.

2.3 Chapter remarks

The use of optical transform architectures in integrated approaches for data compression applications was studied. An optimized PIC design solution in Si₃N₄-based platform was proposed, comprising a two-level HT network for compression, and a switching network as a framework that supplies all logical inputs to the HT network for testing/characterization purposes. The key BB structures designed to realize the main block networks are a 2×2 MMI BB and 1×2 MMI BB. Design methodology combined theoretical MMI optical interference principle and numerical optimization through BPM assessment. Furthermore, in an effort to improve the BB performance behavior under the integrated approach requirements, three different MMI geometries were evaluated, i.e., rectangular shape (geometry A) and two different butterfly shapes (geometry B and C).

An optimized design model study for a 2×2 MMI BB structure is proposed to implement the two-level HT network. The best-optimized 2×2 MMI BB developed presents an EL below 0.004 dB and XT below 0.005 dB for a sum/subtraction MMI operation mode (essential for the 2D HT network implementation) with a device size footprint up to 1/4 lower than reported literature [76] [89]. Additionally, device reconfigurability (with different available MMI coupling ratio behaviors) and wavelength tolerances in the infrared C-band were assured, with an overall EL ≤ 0.05 dB. An optimized design model study for the 1×2 MMI BB structure to realize the switching network is also developed, resulting in an optimized BB, with and EL and XT below 0.0003 dB, wavelength tolerances in the infrared C-band with EL ≤ 0.01 dB, and device size footprint approximately 1/3 lower than reported literature [89]. Both best-optimized BB designs (2×2 MMI and 1×2 MMI) selected, were attained under the MMI butterfly geometry C, which presented the overall best performance.

The comprehensive optimization design study performed provides an important evaluation of the BB structures performance/behavior, to select the ones that best address the HT compression and switching networks. To conclude, the BB structures developed can be implemented in photonic chip design with the possibility to be manufactured under a multi-project wafer (MPW) run.

Chapter 3

Implementation and testing of integrated HT

The use of the Haar wavelet transform as an all-optical encoder/decoder implemented in PIC has been demonstrated, e.g., analytically with a tree of cascaded Mach-Zehnder interferometers (MZI) [98], and for inverse/discrete wavelet packet transform (IDWPT/DWPT) with a PIC-based on silicon on insulator (SOI) platform [99]. Furthermore, the use of planar interferometry in an integrated architecture to implement the HT has been conceptually proposed by Parca et al. [68] with an all-optical scheme composed by optical couplers to realize the image compression process.

Optical couplers are key components with a wide range of applications in integrated photonics. Particularly, when a specific degree of asymmetry is applied on 3 dB directional couplers, different coupling behaviors [68]–[70], such as magic-T [71] can be attained. Its features include the realization of a separate addition and subtraction of incoming input signals at its output ports [68] with available tunable capabilities through phase adjustment of the input signals [71] [72]. The implementation of planar interferometry to realized the HT providing image compression in real-time with an increased power saving due to the all-optical processing is explored. The HT implementation can be realized with a two-level network of adiabatic asymmetric coupler (AAC) devices [32] [56] [57]. Alternatively,

these operations can also be accomplished with the implementation of MMI, as described in chapter 2.

The selection of the photonic integrated platform to fabricate the PIC is driven by the functional requirements of the circuit and/or device to be developed and the underlying components (active/passive) available in the different platforms [51]. Indium phosphide (InP) [47] [48], silicon (Si) [44] [45] and silicon nitride (Si_3N_4) [42] [49] based platforms are among the most commonly used to realize PIC, with recognized different advantages. The silicon nitride platform technology was assessed in a design implementation (addressed in chapter 2). In this chapter will be investigated the implementation of the HT network in an integrated InP-based platform and in a new hybrid material [65].

From InP-based platform merits can be highlighted its excellent electro-optical properties allowing efficient light generation, detection, and guidance [100]. Due to its remarkable advantage of comprising the integration of both passive and active components in a single platform technology, the integrated InP-based platform was chosen for the design and fabrication of an InP optical chip implementing the two-level HT network. In this chapter is presented the first experimental characterization of an InP-based platform realizing the HT (in section 3.1), with a full characterization of the elementary BB coupler implemented, i.e., the AAC (in subsection 3.1.1), and the 2D HT network (in subsection 3.1.2).

Furthermore, taking advantage of new low-cost hybrid materials, such as the organic-inorganic di-ureasil hybrid [65] was explored its employment in planar interferometry to realize the proposed optical HT for compression purposes [58]. Thus, a potential cost-effective 2D HT network (fabricated in this organic-inorganic hybrid material) composed of three 2×2 MMI couplers arranged in a two-level signal decomposition architecture is demonstrated (in section 3.2). Design and manufacturing methodology (in subsection 3.2.1), and simulation/experimental characterization results with discussion (in subsection 3.2.2) are also addressed.

The chapter is concluded with the chapter final remarks summarized in section 3.3.

3.1 HT implementation with AAC in an InP integrated platform

Indium phosphide-based PIC offer promising solutions for high-speed computing and data transmission due to their electro-optical properties [101]–[103]. The merits of this integrated photonic platform include efficient light generation and detection, light guiding, and fast phase modulation, allowing built-in active components, such as lasers and optical amplifiers [48] [100].

Taking advantage of the InP integrated photonic platform, a data compression chip based on Haar wavelet transform was designed in accordance with the rules and using building blocks (BB) available from “Application Specific Photonic Integrated Circuit” (ASPIC) foundries [104], as well as proprietary BB created and simulated by the authors [56]. Furthermore, a chip to test and independently characterize the AAC was designed and fabricated in the same platform conditions. The optical chips were designed under the foundation for science and technology (FCT) research project CITO – *image compression using optical transforms* (PTDC/EEA-TEL/114838/2009), prior to this thesis work plan. The main contribution provided in this study was the first test and characterization (with simulation and experimental results) of the integrated implementation of the optical HT in an InP optical chip [56] [57].

The chips were fabricated through a multi-project wafer (MPW) offered by the consortium “Joint European Platform for Indium Phosphide based Photonic Integration of Components and Circuits” (JePPIX) [105]. This consortium allows the development of low-cost ASPIC using generic foundry model and it supplies design kits for MPW. The fabrication process was achieved under the program “Photonic Advanced Research and Development for Integrated Generic Manufacturing” (PARADIGM) [106], developed to allow access to foundry processes for Universities. This program reduces the costs of the design, development, and manufacture by establishing library-based design combined with technology process flows and design tools [56].

The designed elementary component for the all-optical HT network implementation was the AAC, detailed described and experimentally characterized in section 3.1.1. The full HT testing and characterization are presented in section 3.1.2.

3.1.1 InP AAC optical chip – design and characterization

Optical couplers and splitters are components with a wide range of applications in data communications [72]. Compact tunable power couplers are highly beneficial, providing functionalities as multiplexing/demultiplexing and switching [107]. For example, a specific degree of asymmetry applied to 3 dB directional couplers can produce different coupling behaviors [68]–[70], such as magic-T [71]. A magic-T also known as a 3 dB asymmetric coupler, allows to perform a separate addition and subtraction of incoming input signals at its output ports [68]. Asymmetric waveguides are used to compensate for wavelength-dependent coupling ratios, with tunable capabilities achieved by adjusting the phase of the input signal [71] [72].

An AAC in InP integrated waveguide platform, based on adiabatic coupling arrangement was designed using the medium-index-contrast waveguide E600 structure, available from Fraunhofer Gesellschaft Heinrich Hertz Institute (FhG-HHI) design manual structures [108]. Owing to a non-disclosure agreement (NDA) of Oclaro and HHI generic foundry processes, further details about the waveguide structure (e.g., structure dimensions and refractive indexes) cannot be provided due to propriety rights. The wavelength supported by the developed structure is infrared C-band.

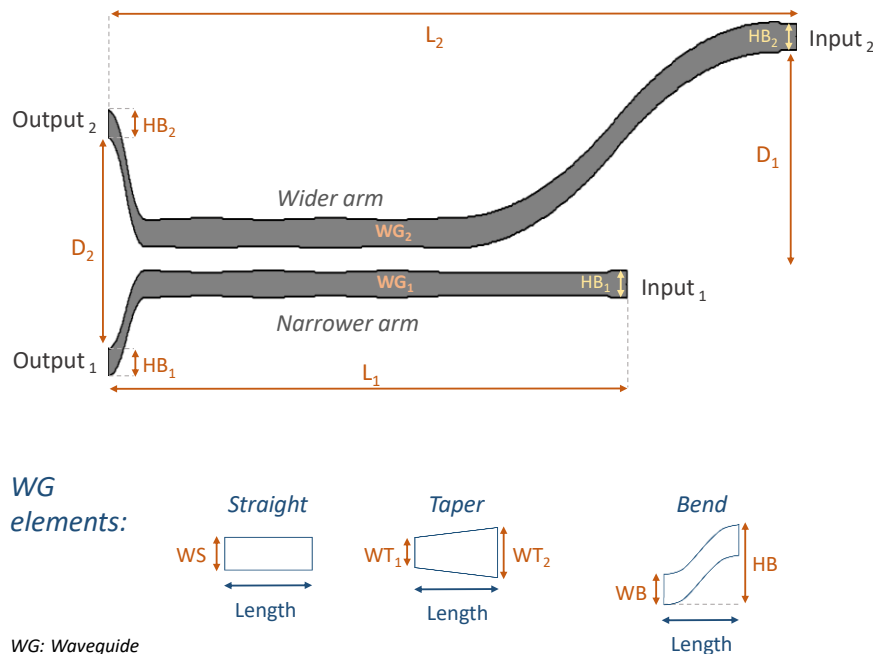


Figure 27. Schematic diagram of the AAC composed of three main elements of different sizes, i.e., straight, taper and bend elements [57]. The diagram is not in scale.

Finding an appropriate design to obtain the specific coupling results, requires several parameters to take into account. Thus, the coupler waveguides were designed with a set of different elements (i.e., straight, taper, and bend elements [109]), to ensure the expected coupler behavior. The design and general dimensions of the developed InP asymmetric coupler are presented in Figure 27 and Table 6. The narrower and wider arms of the AAC are waveguide 1 (WG₁) and waveguide 2 (WG₂) respectively, corresponding to the lowest width of 1 μm for WG₁ and 1.3 μm WG₂.

Table 6. General dimensions of the AAC.

		(μm)
Length of the WG	L ₁	2264
	L ₂	2815
Distance between WG	D ₁	40
	D ₂	70
Width of the <i>straight</i> element	WS	1.15
Width of the <i>taper</i> element for WG ₁	WT ₁	1.00
	WT ₂	1.15
Width of the <i>taper</i> element for WG ₂	WT ₁	1.30
	WT ₂	1.15
Width of the <i>bend</i> element	WB	1.15
Height of the WG ₁ (input/output)	HB ₁	2.00
Height of the WG ₂ (input/output)	HB ₂	2.00
Height of the bend element for WG ₁	HB	3.60
Height of the bend element for WG ₂		5.00

WG: waveguide.

Simulations and fine-tuning of all design parameters were performed to attain the right profiles and output requirements of the AAC. Design and propagation analysis were carried out using the 2D BPM from OptoDesigner[®] Synopsys software [92] [109].

Beam propagation simulations of the theoretical AAC device designed are depicted in section 3.1.1.1. Additionally, in section 3.1.1.2 is provided the experimental testing and characterization of the InP optical chip implementing the AAC.

3.1.1.1 BPM simulations of theoretical AAC design

Light propagation simulations of the designed InP AAC coupler with the input signal in the: i) upper waveguide (WG₂); ii) lower waveguide (WG₁); and iii) same input signal on both WG₁ and WG₂; are presented in Figure 28, Figure 29 and Figure 30, respectively. Propagation analysis was carried out with 2D BPM, transparent to reflections.

An estimation of the AAC coupling ratio (CR) and device excess loss (EL) was derived from the light propagation BPM simulation results as presented in equations (9) and (8), respectively (see subsection 2.2.1.5 from chapter 2). For AAC, P_{in_j} specifies the power at the input arms of the AAC and P_{out_j} indicates the power at the output ports of the AAC, lower (WG₁) and upper (WG₂) WG respectively.

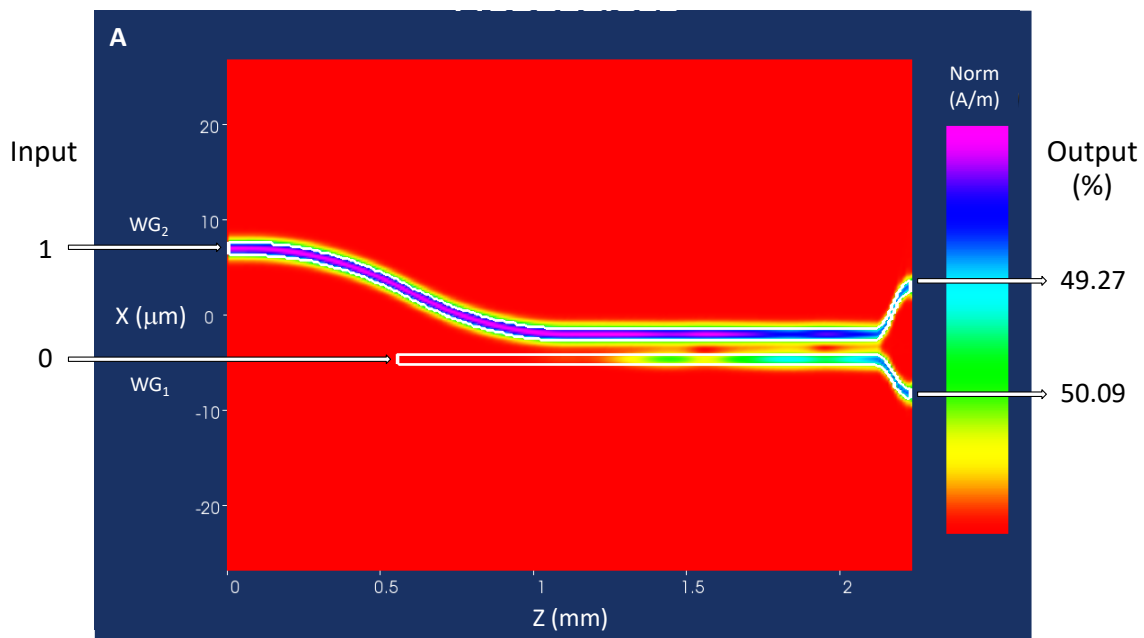


Figure 28. Light propagation in the AAC when the input signal is provided in the upper waveguide (WG₂). AAC output power values are presented in percentage.

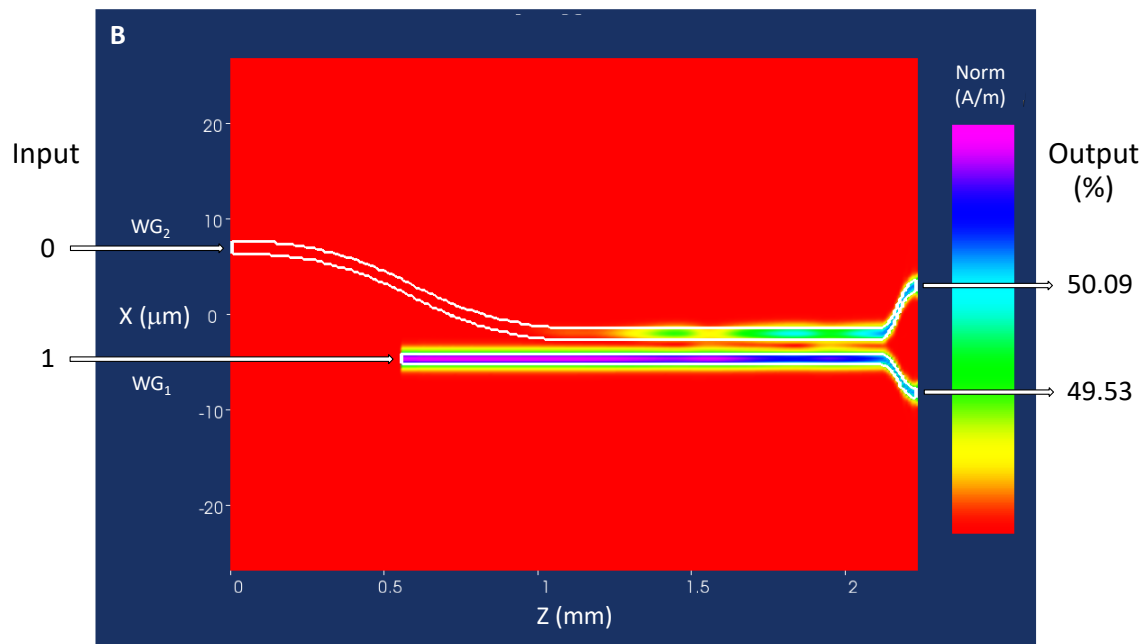


Figure 29. Light propagation in the AAC when the input signal is provided in the lower waveguide (WG_1) of the coupler. AAC output power values are presented in percentage.

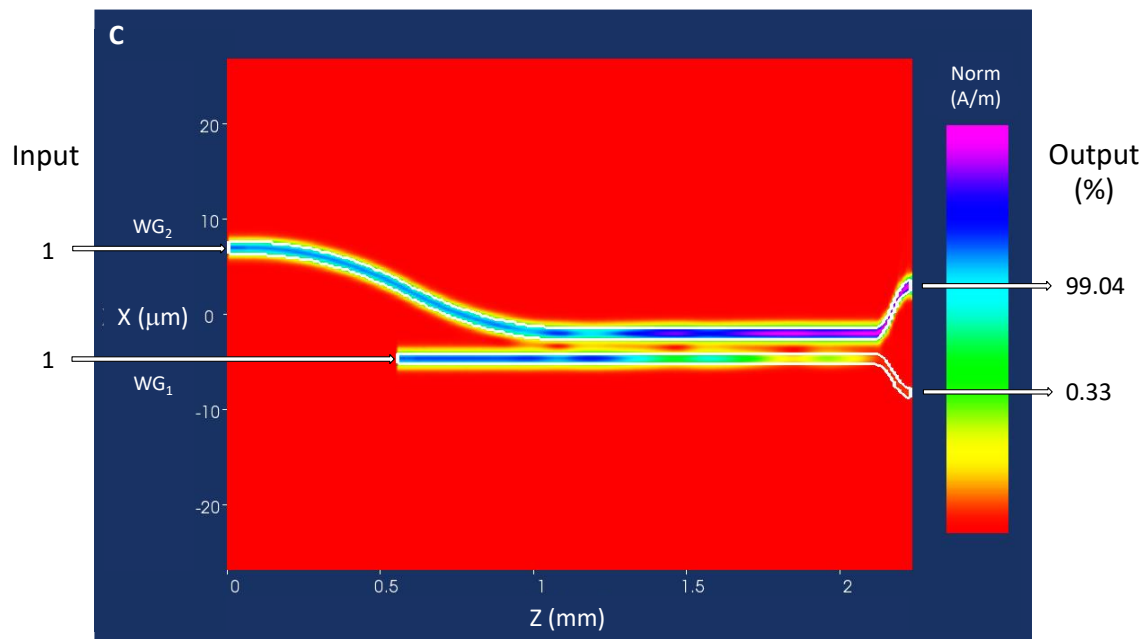


Figure 30. Light propagation in the AAC when the same input signal is provided in the two input waveguides (WG_1 , WG_2) of the coupler. AAC output power values are presented in percentage.

The simulation results demonstrate that the designed coupler is behaving as expected. As depicted in Figure 28 and Figure 29, a 50% (i.e., coupling ratio of 50:50) splitter coupling mode is observed when only one of the input waveguides carries an optical signal.

When both of the input waveguides carry an optical signal, sum and subtraction are achieved at the coupler output waveguides. As can be seen by the duplication of power in the output WG₂ (with 99% of the output signal) and an approximated absence of power in the output WG₁ (0.3%), i.e., an AAC coupling ratio of approximately 99:0, see Figure 30.

Device excess losses lower than 0.03 dB were attained in all BPM simulations.

3.1.1.2 Experimental test and characterization of InP AAC optical chip

The InP chip under testing containing the asymmetric coupler is depicted in Figure 31. The chip is composed of one AAC powered by two distributed feedback (DFB) lasers (L₁ and L₂), four positive-intrinsic-negative (PIN) photodiodes for electrical monitoring, two phase modulators (PM-L₁ and PM-L₂) at coupler's input WG₁ and WG₂ respectively, two multimode interference (MMI) splitters 1×2 and two spot size converters (SSC₁ and SSC₂) at coupler's output port 1 and 2, respectively.

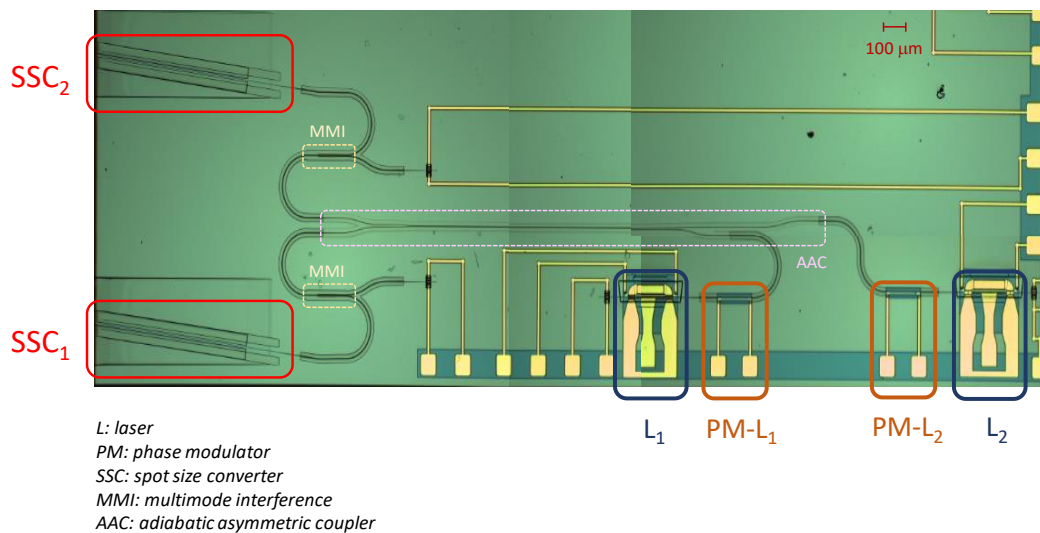


Figure 31. Microscope image of the chip containing the AAC, input DFB laser sources (L₁ and L₂), phase modulators (PM-L₁ and PM-L₂), multimode interferometers (MMI) splitters 1×2 and spot size converters (SSC₁ and SSC₂) to collect optical output signal from the AAC. Image obtained with Leica microscope (DM-750M; 1CC50-HD) [110] with a 5× objective (HI Plan EPI, 5×/0.12) [57].

Implemented DFB lasers, PIN photodiodes, MMI splitters, and SSC are proprietary BB from ASPIC foundries [108]. The DFB laser can be powered by a current up to 100 mA and presents a linear behavior up to a maximum modulation frequency of 10 GHz [108]. The reported optical loss of the SSC, when coupled with a standard single mode fiber (SSMF), is < 2 dB and allows an SSMF alignment tolerance < 2 μm [108]. An electrical power surge during the experiment damage PIN photodetectors and the phase modulator PM-L₁ from the optical chip, inhibiting their use in the experimental characterization. Nonetheless, a full characterization was assured with optical measurements and the second phase modulator in the input WG₂ of the AAC.

This section includes the packaging of the InP AAC optical chip under testing (in subsection 3.1.1.2.A) and the experimental method implemented, with corresponding results and discussion (in subsection 3.1.1.2.B).

3.1.1.2.A Packaging of InP AAC optical chip for testing

In the optical chip packaging is addressed: i) the design and fabrication of the PCB for PIC testing (in subsection 3.1.1.2.A.1); ii) the employed techniques for the management of the PIC temperature and lasers' wavelength stability (in subsection 3.1.1.2.A.2); and iii) the applied fiber coupling approach for optical measurements (in subsection 3.1.1.2.A.3).

3.1.1.2.A.1 PCB design and fabrication

A printed circuit board (PCB) in the RO4000® laminate (material substrate 4360G2, dielectric constant of 6.15 ± 15 , dielectric thickness 0.51 mm, and trace thickness 35 μm) from Rogers corporation [111] was designed and printed to test the InP optical chip. The design and simulation of the PCB were performed with the advanced design system (ADS) [112]. The complete PCB design is presented in Figure 32.

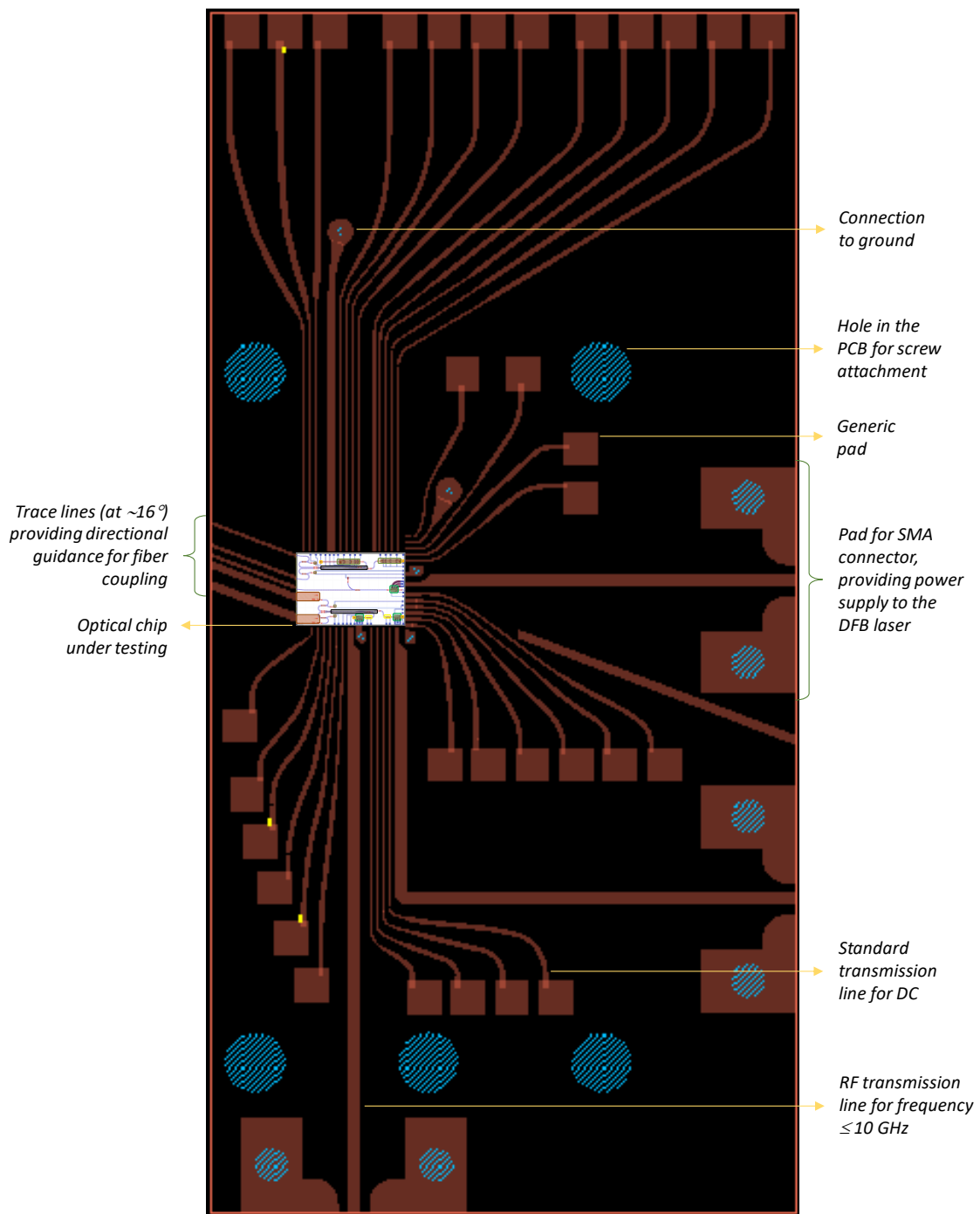


Figure 32. Schematic diagram of the PCB designed to test the InP AAC optical chip. The diagram is not in scale.

The transmission lines designed followed the width and distance between lines recommended for the RO4000® laminate (substrate material 4360G2), i.e., transmission direct current (DC) lines width $\geq 150 \mu\text{m}$ and distance between DC lines $\geq 200 \mu\text{m}$; transmission RF lines width $\geq 724 \mu\text{m}$, and

distance between RF lines $\geq 1448 \mu\text{m}$. Physical parameters of the radio frequency (RF) transmission lines (with an impedance transmission line of 50Ω and frequency up to 10 GHz) were calculated using the *LineCalc* analysis and synthesis program from ADS [112]. Furthermore, RF line/trace corners designs followed the RF/microwave PCB design layout recommendations [113].

Electronic connections between the PIC (square pad with $100 \mu\text{m}$ side length) and the PCB were made with gold (Au) wire-bonding (with $17.5 \mu\text{m}$ of diameter). To reduce induction effects wire-bonds were made as short and straight as possible, maximizing the quality of connections [114] [115].

3.1.1.2.A.2 Management of PIC temperature and laser wavelength stability

Thermal management of the chip was maintained at 25°C , as recommended by the foundry for InP-based PIC [108], with a single-stage thermoelectric cooler (TEC) controller (MD02 series) [116].

For the well-functioning of the AAC, i.e., interference of input signals, is essential to guarantee the same wavelength in the two inputs lasers, but also the same relative phase. Spatial and temporal coherence of both lasers L_1 and L_2 were assumed according to the quality standards of HHI InP PIC with the TEC avoiding thermally induced deviations on the laser output.

The waveguides were also designed to maintain the relative phase between the two lasers so that, the change in the relative phase can only be due to the phase shifter. Furthermore, the wavelength stability was also assessed by measurements using the optical spectrum analyzer (OSA) in which it was verified that the wavelengths of both lasers were not drifting, and the interference pattern guaranteed.

The DFB lasers were powered by current sources through subminiature version A (SMA) connectors (to allow tests up to a maximum of 10 GHz of frequency, maximum validated by the DFB laser BB). The reported wavelength tuning range of the DFB is 4 nm [108].

3.1.1.2.A.3 Fiber coupling for optical measurements

To reduce optical loss in the AAC output coupling was designed in the PIC a waveguide 3D SSC, as they have a reduced loss of approximately 0.5 dB [108]. Additionally, the waveguide SSC was set at a 7° angle (θ_{InP}) to further reduce optical loss, as recommended by InP-based PIC design rules [108]. Taking that into consideration, the fiber coupled to the PIC for optical measurements was placed

at an angle of approximately 16° (see equation 23). The angle (θ_{SSMF}) of the fiber to couple to the PIC is given by the Snell's law as presented in equation (23).

$$\theta_{SSMF} = \text{sen}^{-1} \left(\frac{n_{InP} \text{sen}(\theta_{InP})}{n_{SSMF}} \right) \quad (23)$$

In equation (23) the standard refractive index of the SSMF (n_{SSMF}) was assumed [117] and the InP refractive index (n_{InP}) was calculated with equation (24) [118] [119] where λ is the light wavelength in the waveguide.

$$n_{InP} = \sqrt{6.255 + \frac{2.316 \lambda^2}{\lambda^2 - 0.6263^2} + \frac{2.765 \lambda^2}{\lambda^2 - 32.935^2} + 1} \quad (24)$$

The optical measurements were performed through edge coupling between the PIC output waveguide SSC and an SSMF fiber optic pigtail. Edge-coupling involves the transfer of light between the fiber and tapered waveguides located along the edge of the PIC-die. Polarization-independency and allowing the use of lensed fibers are some of the advantages of this technique, resulting in lower insertion losses (< 1 dB), and a broadband coupling [120] [121].

Grating couplers, although having higher insertion losses when compared to edge coupling, can be employed to simplify the coupling process by relaxing alignment tolerances, with the ability to be placed at any position of the PIC surface (not just on the edge of the chip) [122]. Nonetheless, this approach was not considered in the design of the optical chip under testing, as up to the time of fabrication grating coupler structures were not available under the InP-based platform PDK from HHI [108].

To facilitate and optimize the alignment of the fiber with the SSC of the chip, lensed fibers were fabricated and tested. Lensed fibers are fibers with tips tapered in the form of a microlens. This can be seen as a cost-effective method for aligning the fiber to an integrated optic device [123] [124]. By acting as a lens, the effective numerical aperture of the fiber increases, which can reduce the coupling losses between the fiber and the chip. This behavior provides a more efficient coupling when compared to a non-lensed fiber [125].

Fujikura LAZERMasteR LZM-100P laser splicing system [126] [127] was used to fabricate the lensed fibers. The system comprises a glass processing and splicing technique that uses a carbon dioxide (CO₂) laser heat source and advanced functionalities to provide good performance, reliability for splicing, tapering, ball lensing, and glass-shaping operations on single-mode fibers [115] [128].

Three ball lenses of different diameters (~190, 200 and 210 μm , below the under testing chip thickness of 250 μm) were fabricated and tested. In Figure 33 is presented the diameter profile for X and Y axis of a ball lens fabricated with an approximated diameter of 200 μm (ball lens fabrication settings are: pre-heat time 90 s; absolute power 331 bit; relative power 100 bit; break add power 20 bit; rotator speed 55 deg/s; and feeding speed 0.03 $\mu\text{m}/\text{ms}$).

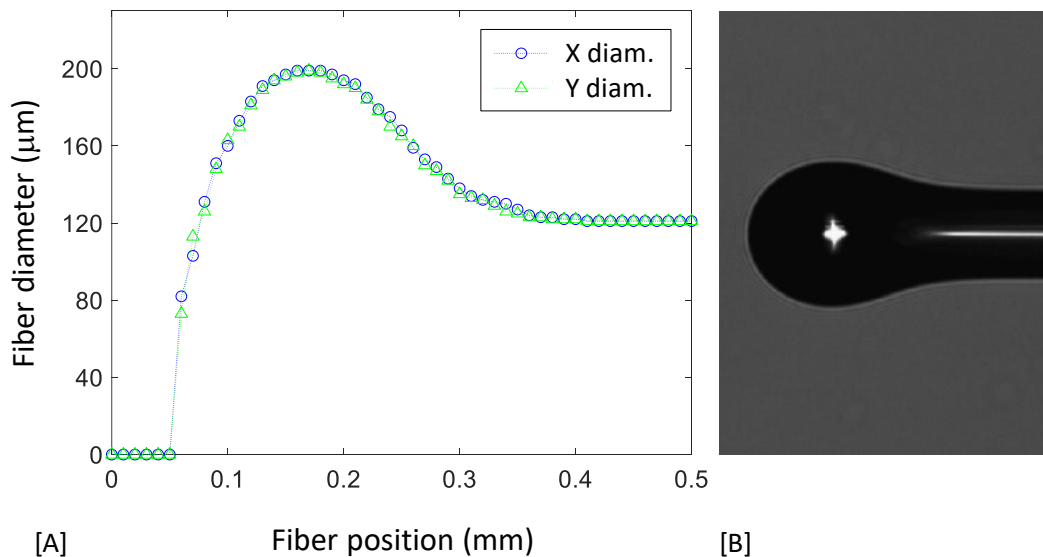
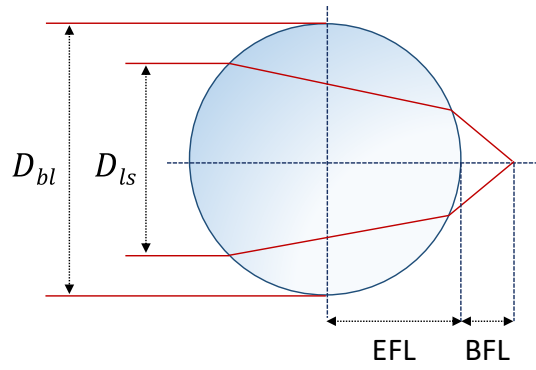


Figure 33. [A]: Diameter profiles for X and Y axis of a ball lens fabricated with ~200 μm . [B]: Picture of the fabricated ball lens, collected with the Fujikura laser splicing system.

A maximized output optical power measurement was obtained for the ball lens diameter of ~200 μm . Under the same conditions, the other ball lens diameters showed lower output powers up to approximately 3 dB of loss, i.e., by experimentally attain the maximization in the measured coupled optical power through a manual mechanically active coupling. Thus, the ball lens with ~200 μm of diameter was the one used for the optical chip characterization.



D_{bl} : diameter of the ball lens
 D_{ls} : diameter of the light input source
 EFL: effective focal lens
 BFL: back focal lens

Figure 34. Diagram of ball lens endpoint of the coupling fiber for focal lens calculus.

The used ball lens (diameter $\sim 200 \mu\text{m}$) for the fiber coupling has a corresponding effective and back focal length of approximately $161 \mu\text{m}$ and $61 \mu\text{m}$, respectively, see Figure 34.

$$EFL = \frac{n_{SSMF} D_{bl}}{4(n_{SSMF} - 1)} \quad (25)$$

$$BFL = EFL - \frac{D_{bl}}{2} \quad (26)$$

$$NA = \frac{2D_{ls}(n_{SSMF} - 1)}{n_{SSMF} D_{bl}} \quad (27)$$

Equations (25) and (26) were used for the calculus of the effective focal length (EFL) and back focal length (BFL) [129]. Where n_{SSMF} represents the refractive index of the coupling fiber (standard refractive index of the SSMF [117] was assumed), and D_{bl} the ball lens diameter. The lens numerical aperture (NA) is given by equation (27), where D_{ls} represents the diameter of the light input source.

3.1.1.2.B Experimental characterization method

The setup implemented for the chip testing consisted in the PCB containing the InP PIC placed over a Peltier device with a thermistor for temperature management (as described in section 3.1.1.2.A.2). The optical chip and coupling fiber (i.e., ball lens with a diameter of $\sim 200\ \mu\text{m}$) were mounted on two separated three-axis micro-positioning adjusting systems to allow a manual adjustment in the X, Y, and Z direction. A binocular stereoscope (Optika SZM-3) with linear zoom magnification (of $0.7\times$ up to $4.5\times$ and eyepieces $10\times$) and a dual fiber output light source (Leica KL200) was used for an efficient system illumination during the alignment process. A general overview of chip testing setup is depicted in Figure 35.

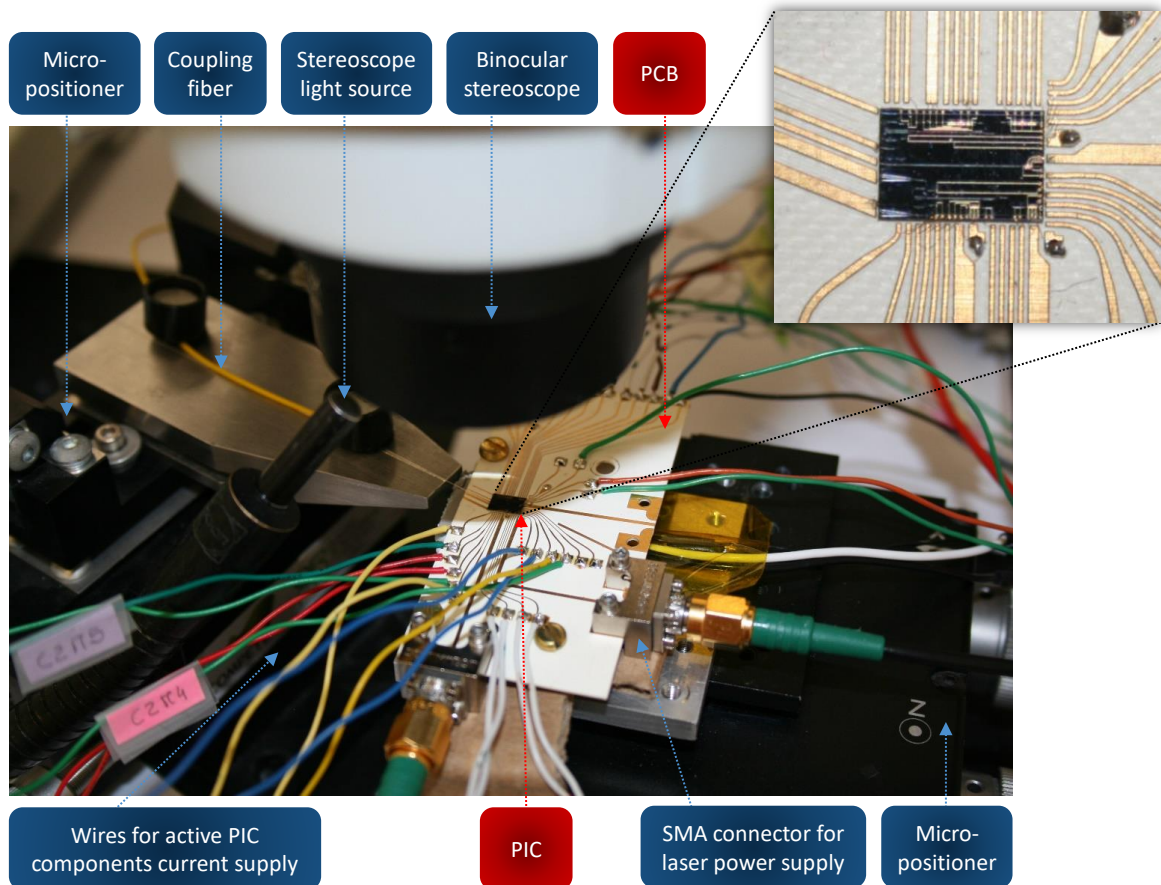


Figure 35. Setup for the chip testing illustrating the PCB with the optical chip and the alignment of the SSMF coupling fiber to collect the optical output signal from the SSC. A binocular stereoscope and two 3-axis (X, Y, Z) micro positioners were used for manual adjustment of the fiber coupling.

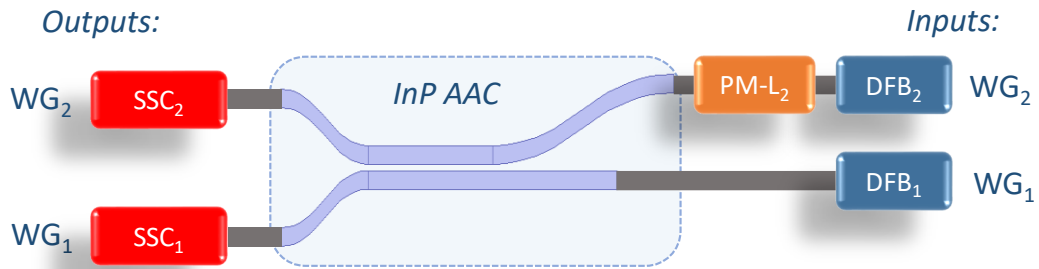
InP optical chip active components (e.g., DFB laser and phase modulators) were powered by current sources. Fiber-to-chip alignment adjustments were performed until a maximized optical power was achieved (when DFB lasers are emitting at a constant input current value), i.e., through active alignment.

The active adjusting techniques use the ability to control the adjustment under real electrical excitation conditions of optical-electronic integrated circuits. This method offers low excess loss, good loss uniformity, and high yield. However, the alignment procedure can be time-consuming and labor-intensive [130], making this method a good approach for research characterization purposes, but not endorsed for low-cost mass-production PIC assessments, where passive adjusting techniques are more appropriate [115] [131].

The fiber-to-chip alignment was based on the maximization of coupled power [130] when a manual mechanically active coupling was performed, by moving either the fiber, the chip or both [132]. Coupling power was measured with a power meter (for first feedback) and an optical spectrum analyzer (OSA) to guarantee wavelength consistency in both DFB lasers. The OSA EXFO, model FTB-500 was used for the optical measurements. Optical power values were calculated from the spectrum provided by OSA measurements. Matlab[®] scripts were implemented to extract the integrated power from the power spectral density ($PSD = P(mW)/RBW$) [133], see equation (28). Where P_i is the power of a single tracepoint, n the number of tracepoints, RBW the resolution bandwidth, and $\Delta\lambda$ the wavelength tracepoint. All optical power values (from OSA measurements) presented in the scope of this thesis reports to these integrated power measurements.

$$Power (dBm) = 10 \log_{10} \left(\sum_{i=1}^n \frac{P_i(mW)}{RBW} \Delta\lambda \right) \quad (28)$$

The optical output of the AAC was measured by collecting the optical power individually in each SSC (firstly on SSC_2 and then on SSC_1), optimized alignment was obtained, guarantying the measurement of the highest optical power in the individual measurements at the SSC_1 and SSC_2 . A schematic diagram of the chip simulated and tested is depicted in Figure 36.



AAC: adiabatic asymmetric coupler
SSC: spot size converter
DFB: distributed feedback laser
PM-L₂: phase modulator of DFB laser 2
WG₁, WG₂: input and output AAC WG arms (1) and (2)

Figure 36. Schematic diagram of the AAC characterized. The optical system addressed is composed of one AAC, two DFB lasers, one PM, and two SSC.

The tunable capabilities of the coupler (i.e., addition, splitter and subtraction behavior of the output port 2 relatively to output port 1) were assessed by scanning a set of phase values generated by the phase modulator PM-L₂ applied to the input 2 of the coupler (input WG₂), see Figure 31 and Figure 36.

For comparison, simulations addressing the experimental conditions (identified in the AAC behavior) were performed using the 2D BPM.

To guarantee wavelength interference (at the AAC experimental operating wavelength of 1555 nm) between the two input DFB lasers, it was necessary to apply different current values in the two lasers, i.e., [78 to 90] mA, which resulted in a 3.7 dB difference of power between the two lasers. This power difference was taken into account in the 2D BPM simulation of the coupler, i.e., an input of $L_1 = 1$ and $L_2 = 0.43$ (normalized values) were simulated for different phase values [0 to 340]° at the input WG₂.

3.1.1.2.B.1 Simulation results

The optical propagation analysis for the AAC BB to access the main coupling behaviors expected, i.e., splitting and addition/subtraction, are depicted in Figure 37.

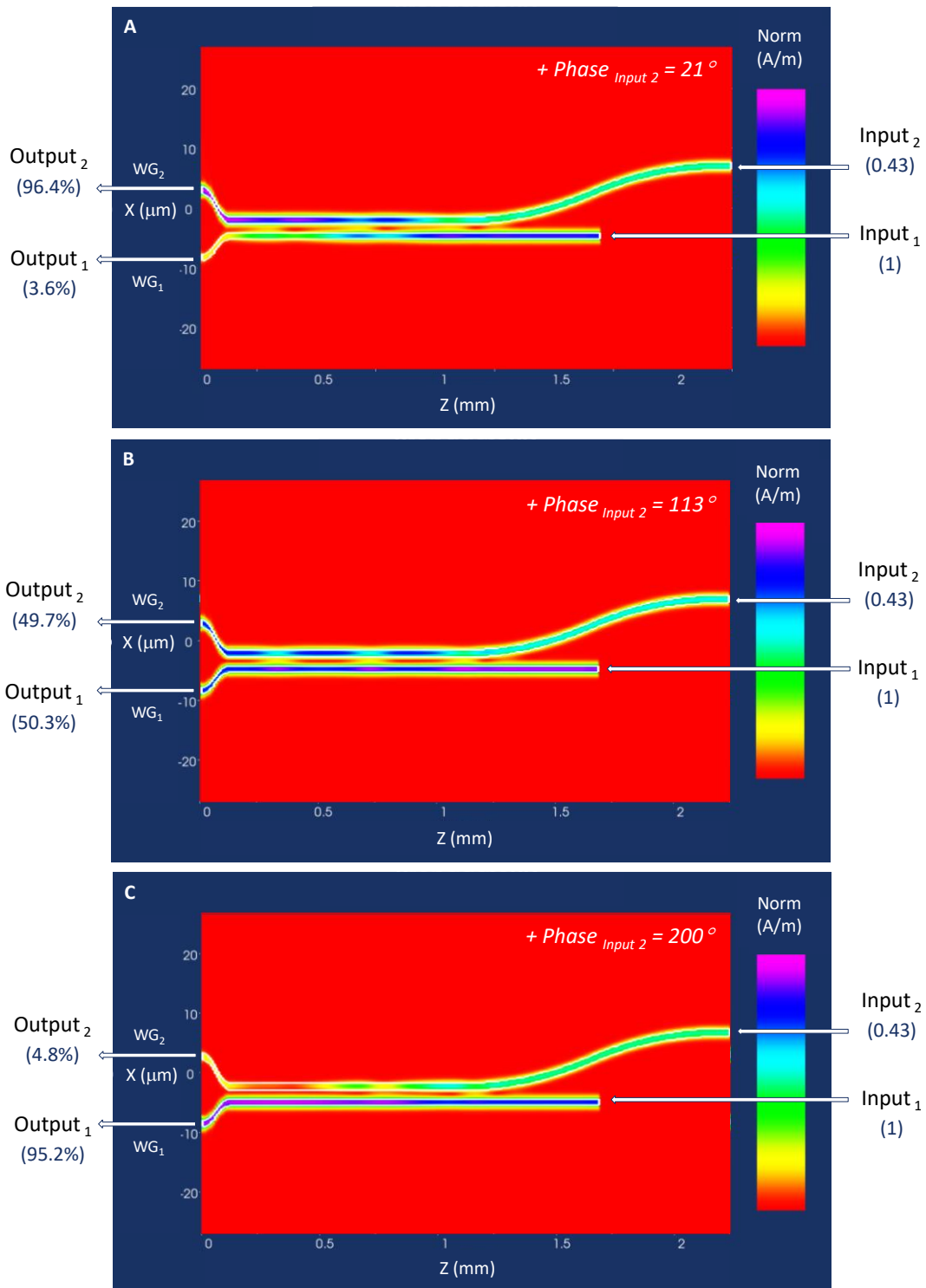


Figure 37. Power propagation in the AAC reproducing the experimental conditions for subtraction/addition and splitting coupling behaviors by adding phase to the input 2 of the AAC. [A]: Addition/subtraction behavior coupling ratio of 96:4 with an additional phase of 21° at the input WG_2 . [B]: Splitting behavior (coupling ratio of 50:50) with an additional phase of 113° at the WG_2 . [C]: Subtraction/addition behavior (coupling ratio of 5:95) with an additional phase of 200° at input WG_2 .

The experimental conditions were taken into account in the 2D BPM simulation, i.e., input normalized values of 1 and 0.43 for the input WG_1 and input WG_2 of the AAC, respectively. Additionally, different values of phase were applied to the input WG_2 of the coupler to model the effect of the phase modulator (PM- L_2) in the InP AAC BB.

The addition and subtraction behavior for both outputs of the AAC was obtained with an additional phase of 21° (coupling ratio of 96:4) and 200° (coupling ratio of 5:95), see Figure 37-A and Figure 37-C, respectively. The splitting behavior (with a coupling ratio of 50:50) was obtained with an additional phase of 113° at the input WG_2 of the AAC, see Figure 37-B. Excess losses lower than 0.03 dB were attained in all simulations.

3.1.1.2.B.2 Experimental results

Experimentally, a phase change in the AAC was realized with a current sweep (from 0 mA to 45 mA) in the phase modulator PM- L_2 to assess the tunable coupling behavior of the coupler. The optical power measurements obtained at the two outputs of the coupler (i.e., measured at SSC_1 and SSC_2) are presented in Table 7.

Table 7. AAC experimental optical power measurements.

Current PM – L_2 (mA)	Optical Power		
	SSC_1 (dBm)	SSC_2 (dBm)	$SSC_1 - SSC_2$ (dB)
0	-19.96	-14.77	-5.19
4.23	-18.23	-14.77	-3.46
13.87	-17.79	-17.44	-0.35
22.75	-13.77	-21.52	7.75
30.99	-14.95	-20.67	5.72
32.89	-17.04	-16.98	-0.06
44.78	-19.57	-15.44	-4.13

SSC_1 , SSC_2 : spot size converters of AAC output WG_1 and output WG_2 , respectively.

PM- L_2 : phase modulator at the input WG_2 of the AAC.

During the PM-L₂ experimental current-scanning, a small wavelength fluctuation of 0.3 nm was detected, i.e., $\lambda = 1555.35 \pm 0.15$ nm, corresponding to a BPM simulated coupling-ratio deviation below 1%.

3.1.1.2.B.3 Discussion

The correspondence of the optical power measurements with the 2D BPM simulations (addressing the experimental conditions, i.e., relative input power between the two input arms of the AAC and propagation wavelength) is depicted in Figure 38.

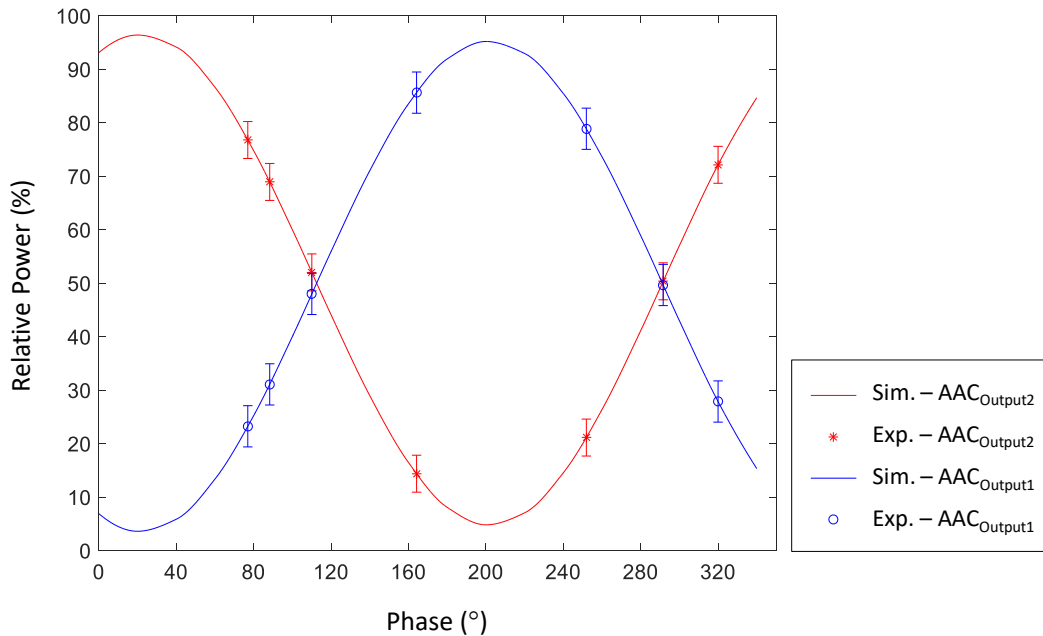


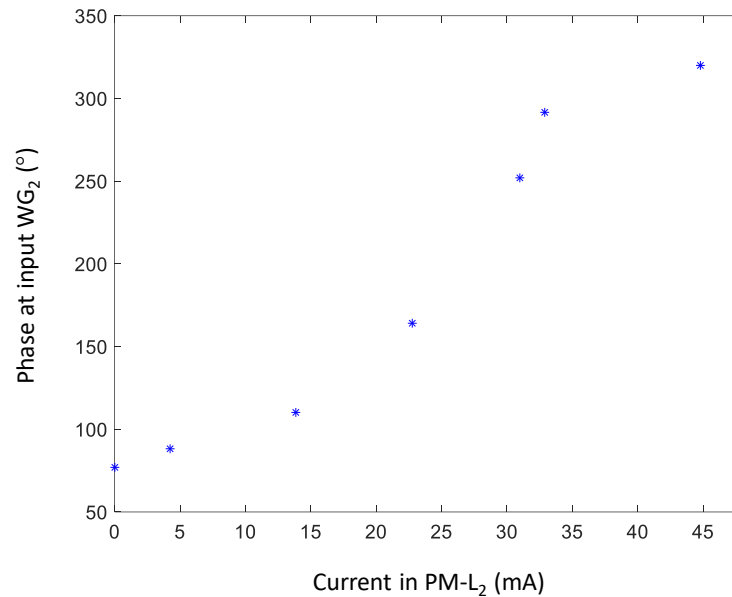
Figure 38. Relative power (in percentage) at the two output waveguides of the AAC as a function of phase for the 2D BPM simulation, and experimental optical power measurements (with an experimental standard deviation error <4%).

The correspondence between the simulation and the experimental results allowed to extrapolate the phase associated with the different current values applied to the PM-L₂ (i.e., phase introduced to the input WG₂ of the AAC), as depicted in Table 8 and Figure 39.

Table 8. AAC experimental relative optical power results for a PM-L₂ current sweep up to 45 mA and the corresponding phase of AAC input WG₂.

Current PM – L ₂ (mA)	Phase AAC input WG ₂ (°)	Relative Optical Power	
		AAC output WG ₁ (%)	AAC output WG ₂ (%)
0	76.98	23.24	76.76
4.23	88.31	31.07	68.93
13.87	110.07	47.99	52.01
22.75	164.20	85.63	14.37
30.99	251.93	78.87	21.13
32.89	291.64	49.65	50.35
44.78	320.00	27.87	72.13

PM-L₂: phase modulator applied in the input WG₂ of the AAC.

**Figure 39.** Phase realized in the AAC input WG₂ as a result of the experimental current applied to PM-L₂.

The coupler was designed in the way that when no additional phase is introduced to any of the AAC input arms (e.g., through current supply to the phase modulators) a separate addition and subtraction of incoming input signals of the coupler are expected at its output ports. Theoretically, for every 90° of phase introduced (to one of the coupler inputs) a switch of the coupling-ratio behavior is predicted. The experimental PM-L₂ current sweeping was performed to provide a current-phase experimental calibration data of at least two maximums for each coupling-ratio behaviors (addition, splitting, subtraction), to prove consistency in the results.

A graph representation of the phase realized into the AAC input WG₂ due to the current applied to the PM-L₂ is presented in Figure 39. The experimental values of the relative power (in percentage) obtained in the two outputs of the AAC as a function of the input current applied to the phase modulator PM-L₂ are depicted in Figure 40.

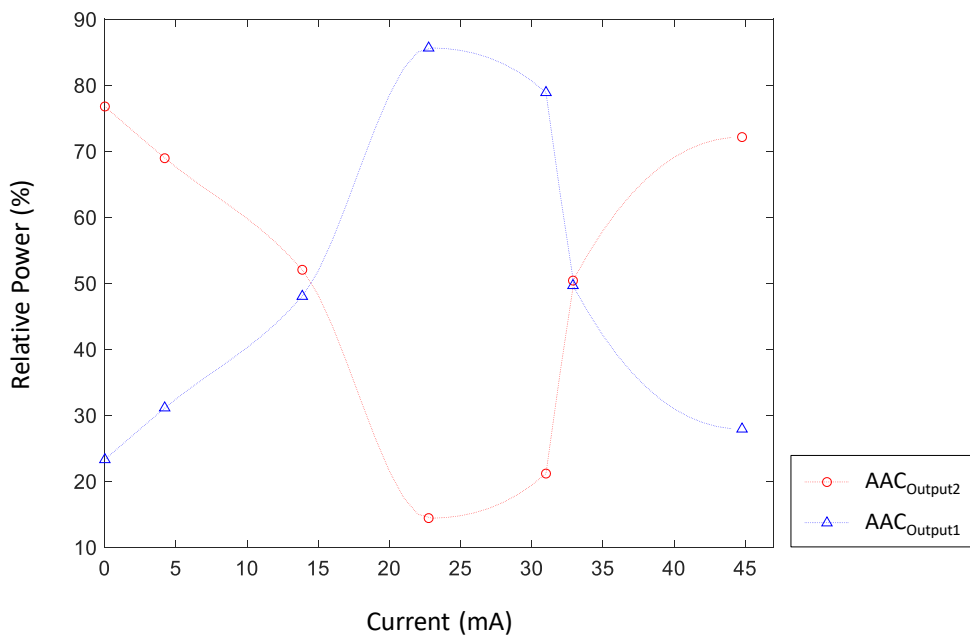


Figure 40. Relative power (in percentage) at the two output waveguides of the AAC as a function of the input current applied to the phase modulator PM-L₂.

The tunable capabilities of the coupler (output port 2 relatively to port 1) are realized for the following values of current applied to the PM-L₂:

- i) < 14 mA (phase of input WG₂ between 0° and 112°) results in an addition behavior;
- ii) ≈ 14 mA (phase of input WG₂ equal to 112°) results in a splitter behavior;
- iii) > 14 mA and < 33 mA (phase of input WG₂ between 112° and 291°) results in a subtraction behavior; and
- iv) ≈ 33 mA (phase of input WG₂ equal to 291°) results in a splitter behavior.

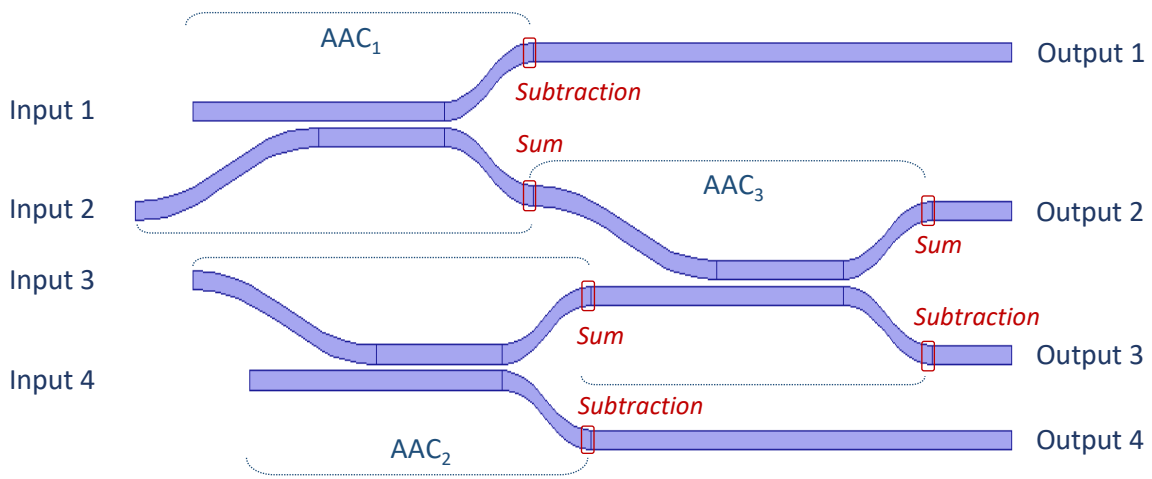
A half-cycle behavior of the coupler (splitter – subtraction/addition – splitter) is obtained with an increment of current in the input WG₂ of 19 mA (i.e., from 14 mA to 33 mA), see Figures 38 – 40, and Table 8.

A full cycle of addition–splitter–subtraction–splitter–addition (between the output port 2 relatively to output port 1 of the AAC) was characterized, allowing to determine the experimental current values of the phase modulator at the input 2 of the coupler to obtain the different coupling behaviors.

A good correspondence between the simulation and experimental results was verified, which validates the tunable capabilities of the asymmetric coupler presented, allowing to determine with acuity the different phases that enable the full cycle of the tuned power. This coupler characterization is fundamental to use its full capabilities in optical processing implementations such as the HT with applications in data compression.

3.1.2 InP HT optical chip – design and characterization

The developed InP AAC structure (presented in section 3.1.1) was used as the elementary key component for the implementation of an integrated approach of the HT for data compression applications (concept detailed in section 2.1). The HT implementation was attained with a two-level network structure, composed of three 2×2 AAC devices, reproducing the required operations, i.e., the average (sum) and the difference (subtraction) between the optical input pairs, as depicted in Figure 41 [32] [56].



AAC: asymmetric adiabatic coupler

Figure 41. Diagram of the two-level network composed of three InP AAC performing the expected operations of the Haar wavelet transform.

Taking into consideration the BPM light propagation simulations for the theoretical designed AAC (see section 3.1.1.1) is presented in Figure 42 the resulting propagation analysis for the two-level HT network composed of three InP AAC. Propagation analysis were carried out with 2D BPM.

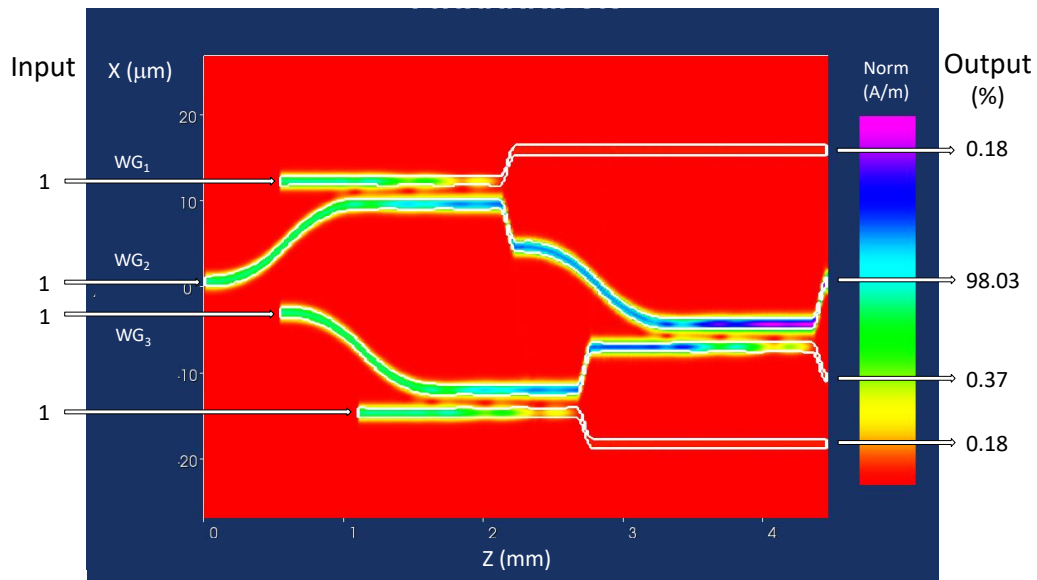


Figure 42. Light propagation in the HT two-level network composed of three AAC, when all input WG of the network are powered with signal (1). HT network output power values are given in percentage.

The HT operations are carried out as expected, which can be confirmed by the power attained at the four output waveguide ports, i.e., the sum at the output WG₂ (98% of the overlap output signal).

3.1.2.1 Experimental characterization of InP HT optical chip

The InP optical chip is composed of four DFB lasers ($L_1 - L_4$), three AAC ($AAC_1 - AAC_3$), six PIN photodiodes for network monitoring, six 1×2 MMI splitters, one 2×2 MMI splitter, and two SSC 3D.

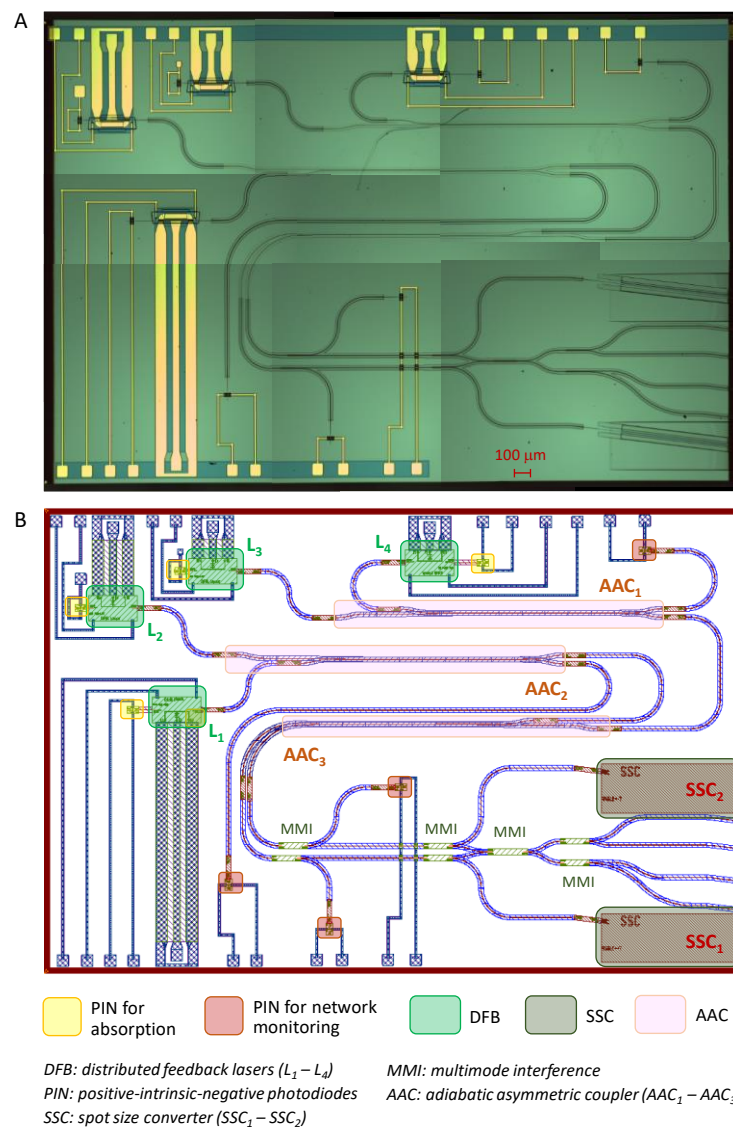


Figure 43. [A]: Microscope image of the optical chip (with an objective lens of $5\times$). [B]: Design architecture of optical chip for data compression based on Haar wavelet transform.

The PIC includes a coupler network for compression and another for decompression. The compression network is composed of the three AAC, arranged in a two-level network, as depicted in Figure 41. The decompression network is composed of four 1×2 MMI and one 2×2 MMI, with four optical WG outputs, as depicted in the bottom right corner of Figure 43-B. The complete circuit architecture is presented in Figure 43. The analysis characterization of the PIC will be focused on the compression coupler network.

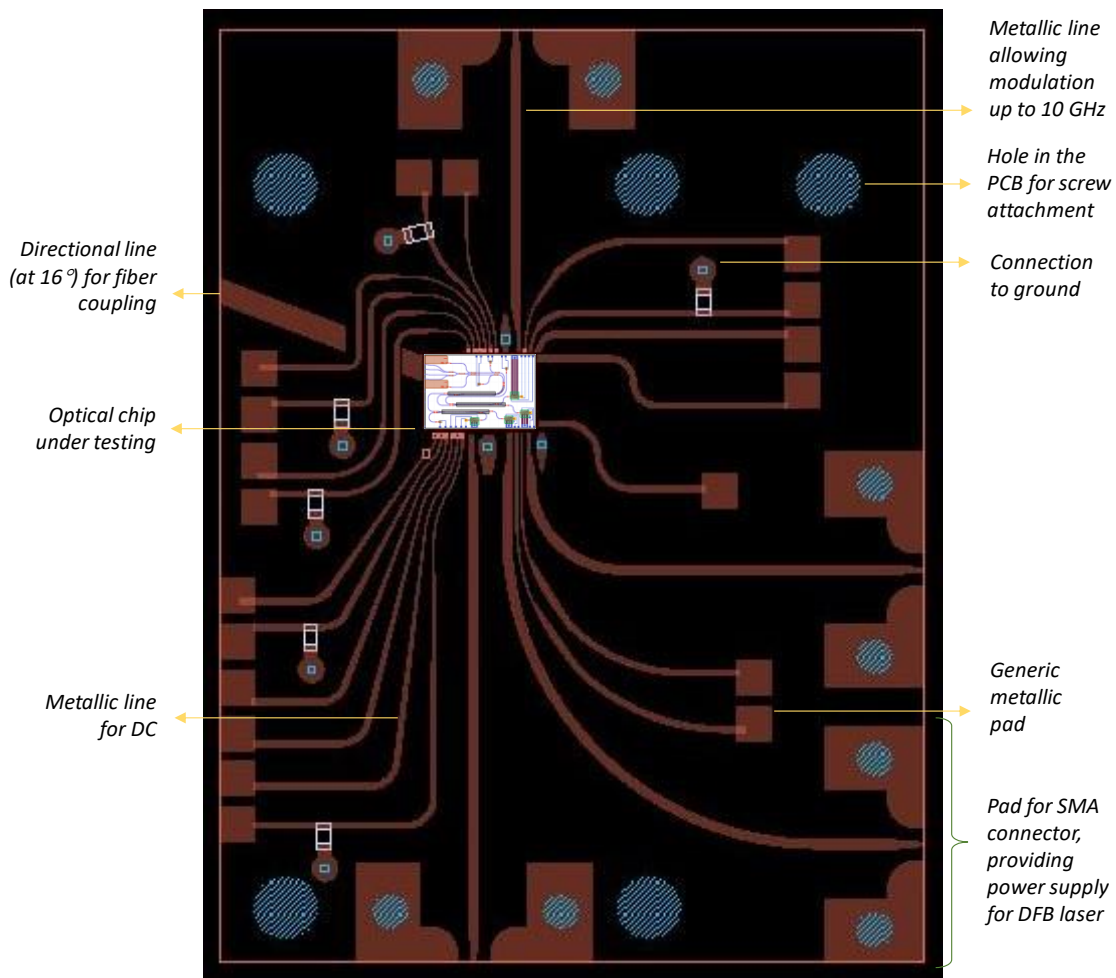


Figure 44. Schematic diagram of the PCB designed to test the InP HT optical chip. The diagram is not in scale.

The inputs of the all-optical HT network are powered by four DFB lasers. The outputs are connected to the two SSC, providing the optical output signal of the HT network corresponding to the LL compression approximation HT component, and the HH detail HT component. PIN photodiodes

providing electrical output signal measurements are also available, as depicted in Figure 43. The complete description of the HT operation principle is detailed in section 2.1. The packaging process of the InP HT optical chip is similar to the one described in subsection 3.1.1.2.A. The PCB design is depicted in Figure 44.

The experimental setup for the InP HT optical chip testing was reproduced as for the InP AAC optical chip (in subsection 3.1.1.2.B), which included the PCB containing the InP PIC placed over a Peltier device with a thermistor for temperature management. The optical chip and coupling fiber (ball lens with a diameter of $\sim 200\ \mu\text{m}$) were mounted on two separated three-axis micro-positioning adjusting systems to allow a manual adjustment in the X, Y, and Z direction. In Figure 45 is illustrated the coupling process with a ball lens in the SSC_1 .

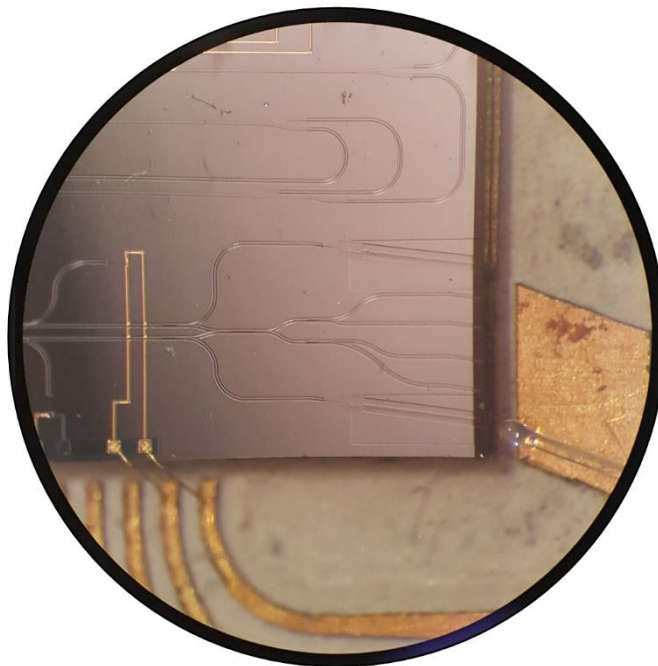


Figure 45. Photograph from the binocular stereoscope illustrating the edge coupling process with a fiber ball lens being coupled to SSC_1 from the InP HT optical chip.

The characterization of the HT optical chip was made in two main steps: i) electrical measurements made with on-chip photodetectors (in subsection 3.1.2.1.A); and ii) optical measurements collected from optical SSC (in subsection 3.1.2.1.B).

3.1.2.1.A Electrical measurements from PIN photodiodes

Electrical measurements were collected from on-chip photodetectors, i.e., PIN photodiodes for network monitoring, see Figure 43-B. The approach implemented for the optical power measurement through the PIN photodiodes, consisted in the placement of a resistor (R) of 10 kΩ in line with each on-chip photodetector using the PCB platform. A voltage of 2V was sourced to the PIN and measured the voltage drop (V_R) at the resistor, as depicted in Figure 46. Voltage measurements were realized with the source meter Keithley 2400-C.

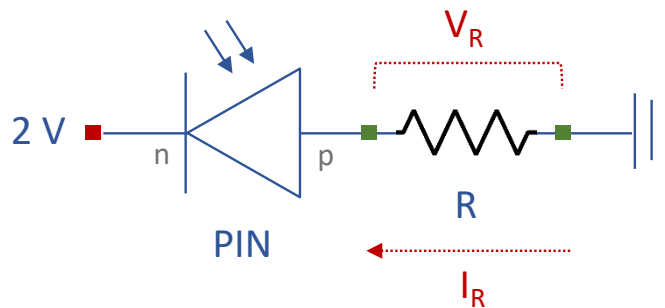


Figure 46. Circuit diagram of the approach used for electrical power measurements from on-chip PIN photodiodes. The resistor implemented was $R = 10 \text{ k}\Omega$.

With the current at the resistor given by ($I_R = V_R/R$), and following InP-based PIC foundry standards [108] for the implemented PIN photodiode, i.e., the responsivity of 0.8 A/W @1550 nm ($PIN_R = I_R/P$), the optical power (P) was calculated as presented in equation (29). Further PIN photodiode optical properties include a linear regime input power below 10 dBm and dark current below 10 nA (@ -2V) [108].

$$P(dBm) = 10 \log_{10} \left(\frac{V_R}{PIN_R R} / 1mW \right) \quad (29)$$

Experimentally was measured the optical power in the PIN photodiodes: PIN-AAC₁, PIN-AAC₂, PIN-AAC₃-M₁, and PIN-AAC₃-M₂, when providing current from 10 to 60 mA into the DFB lasers L₁, L₂, and L₃. The laser L₄ was not activated as it was not emitting power.

A schematic diagram of the optical chip illustrating the location of the photodetectors in the network is presented in Figure 47.

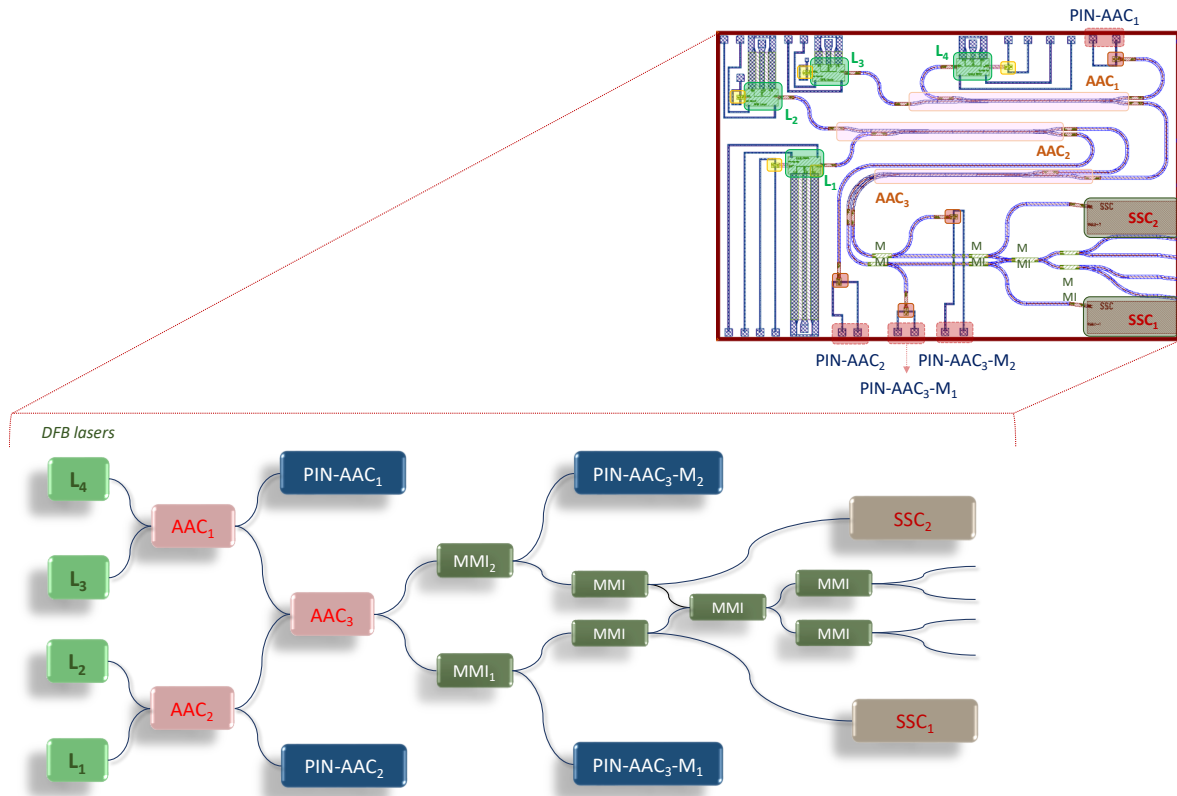


Figure 47. Schematic diagram of the optical chip illustrating the network locations of the on-chip photodetectors (PIN-AAC₁, PIN-AAC₂, PIN-AAC₃-M₁, and PIN-AAC₃-M₂) under measurement.

In Figure 48 is presented a compilation of the optical power measurements when the two-level HT network is powered by seven different laser activation settings: i) L₁; ii) L₂; iii) L₁ + L₂; iv) L₃; v) L₁ + L₃; vi) L₂ + L₃; and vii) L₁ + L₂ + L₃. The power obtained in the PIN-AAC₂ presents similar values when activating the laser L₁ and L₂ independently, i.e., the two lasers have a similar power emission (Figure 48 – A, B). When only laser L₃ was activated, no conclusions were made from coupler AAC₁, as only one of the input arms of the coupler had an available signal.

From the results it is possible to identify a coupling factor of 3 dB in the coupler AAC₂ (PIN-AAC₂), owing to the fact that, when the two lasers (L₁ + L₂) are activated simultaneously an increase of 3 dB

is obtained in comparison with the coupler power output for the activation of only one of the lasers (L_1 or L_2) independently, see Figure 48 – A, B and C.

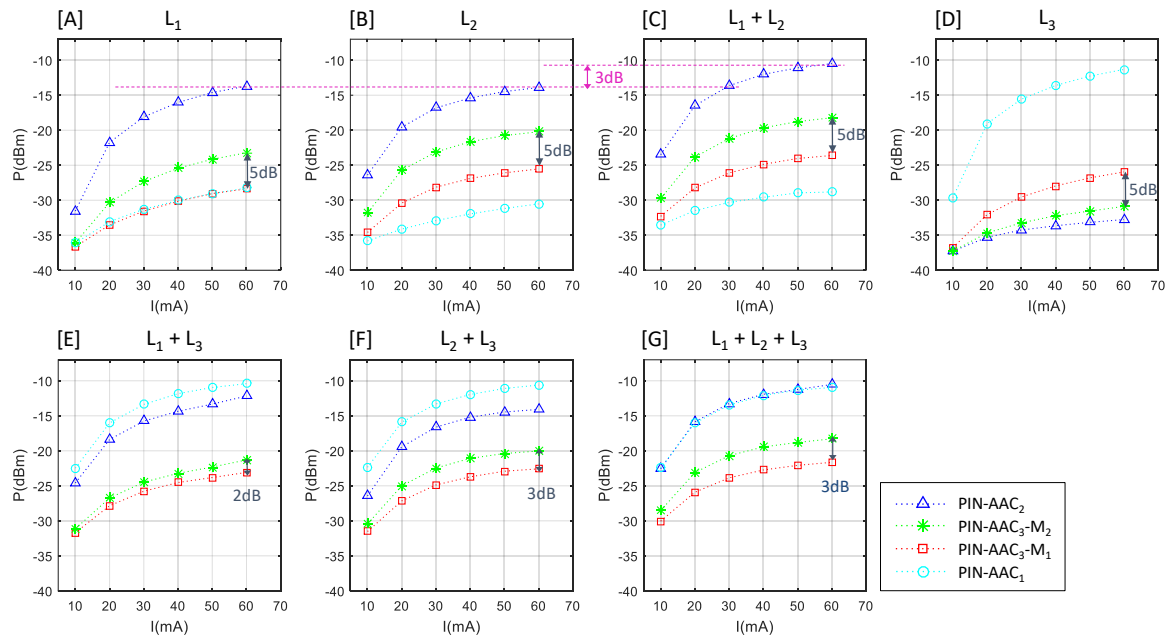


Figure 48. Optical power measured from PIN-: AAC₂, AAC₃-M₁, AAC₃-M₂, and AAC₁, when the two-level HT network is powered by the activation of DFB lasers: i) L_1 ; ii) L_2 ; iii) $L_1 + L_2$; iv) L_3 ; v) $L_1 + L_3$; vi) $L_2 + L_3$; and vii) $L_1 + L_2 + L_3$ [56].

A 5 dB coupling factor between the output ports of the coupler AAC₃ (i.e., PIN-AAC₃-M₁ and PIN-AAC₃-M₂) is identified when in only one input arms is provide signal, i.e., with the activation of: i) L_1 ; ii) L_2 ; and iii) $L_1 + L_3$; and iv) L_3 , see Figure 48 – A, B, C and D. As a result, laser activation scheme (i), (ii) and (iii) bring signal to the upper input arm of the AAC₃; and laser activation scheme (iv) carries signal to the bottom input arm of the same coupler. The AAC was designed to have a splitting behavior (of approximately 50:50 coupling ratio) when only one of the input arms is provided with signal. These findings suggest an atypical behavior of the coupler transfer function for these characteristics. A possible explanation can rely on experimental phase drifting in the input arms of the couplers, which consequently result in a deviation of the coupling behavior of the AAC, as detailed analyzed in the AAC characterization provided in section 3.1.1.2.B.

Nevertheless, when both of the input arms of the coupler AAC₃ are provided with signal a coupler factor of approximately 3 dB is achieved between its output ports, see Figure 48 – E, F and G. The

output ports of the coupler AAC₃ allow to assess the compressed outputs of the two-level HT network, where the higher power is expected to deliver the LL compressed component of the optical transform.

In the obtained results was identified a coupling behavior of approximately 3 dB in the coupler AAC₂ and coupler AAC₃, i.e., a sum is performed in one of the arms and subtraction in the other, as estimated in the chip design. Even though, the complexity of the chip and the difficulty to fully and independently characterize each of its components, this study provides the first demonstration of an integrated all-optical two-level HT operation in an InP platform [56].

3.1.2.1.B Optical measurements from SSC edge coupling

The methodology carried out for the optical measurements was equivalent to the one presented in section 3.1.1.2.B. However, during the experimental assessment procedures an electrical power surge, associated with a mild storm event, damaged the DFB laser L₂ limiting our characterization to only two emitting lasers (i.e., L₁ and L₃). Additionally, in optical experimental measurements, a difference of about 10 dB was identified between the two lasers, further restricting the projected characterization. A small constrained analysis is nonetheless undertaken with the available results.

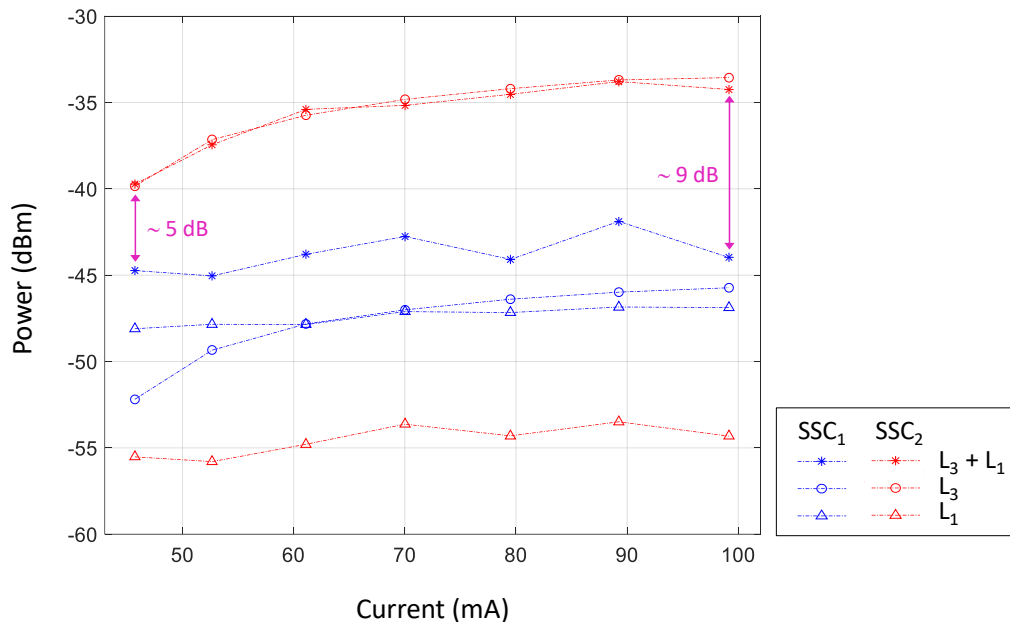


Figure 49. Optical power measured from SSC₁ and SSC₂, corresponding to AAC₃ output port 1 and port 2, respectively. A relative coupling power between 5 dB and 9 dB was observed at the output of the 2D HT.

The wavelength stability between the input lasers was assessed through OSA measurements, in order to ensure wavelength interference in the couplers. For that purpose, small adjustments between the two laser input currents were undertaken (< 10 mA). Optical measurements realized at the output ports of the AAC₃ of the two-level HT network, which correspond to SSC₁ and SSC₂ are presented in Figure 49.

The current sweep of ~ [45 to 100] mA applied to activate the DFB lasers, produced a wavelength linear shift of around 3 nm, i.e., from 1553 nm to 1556 nm. In an effort to better evaluate the experimental data obtained, beam propagation simulation of the AAC for the experimental reported conditions was undertaken. Conditions attained in the AAC coupler simulated included a signal power at the bottom coupler input port with 10 dB less power than its top counterpart, and a laser wavelength operating shift of 3 nm (i.e., at $\lambda = 1553$ nm and $\lambda = 1556$ nm). BPM simulations results of the AAC₃ coupling behavior at the output of the two-level HT network (i.e., SSC₂ and SSC₁) are depicted in Table 9. The device presented an excess loss below 0.03 dB in all the BPM simulations.

Table 9. AAC coupling behavior for $\lambda = [1553 - 1556]$ nm when powering the coupler's top and bottom arms with 1 and 0.1 relative power, respectively.

DFB laser λ (nm)	AAC ₃ coupling	
	Top : Bot (%)	(dB)
1553	77 : 23	5.2
1556	75 : 25	4.8

Top : Bot (%): coupling between the top and bottom output ports of the AAC coupler, correlated with the measurements at the SSC₂ and SSC₁, respectively.

Experimental optical measurements show a coupling range of approximately 5 dB to 9 dB at the output of the two-level HT network (i.e., top and bottom output ports of the AAC₃), with an expected sum at SSC₂ (top output port of the AAC₃) and a subtraction at the SSC₁ (bottom output port of the AAC₃). Simulations of the coupler to address experimental conditions show a coupling ratio of approximately 5 dB, which complies with the experimental coupling values for the DFB lasers activated with ~45 mA input current.

Even though, the complexity of the optical chip under testing and the experimental constrictions limiting the available analysis, an extrapolation of the coupling at the output of the two-level HT network can be inferred with an experimental coupling behavior (sum/subtraction) under the expected theoretical simulated range.

3.2 Integrated HT implementation in a hybrid material platform

The two-level HT network can also be attained using as the elementary BB of the network an MMI device as studied in chapter 2. MMI structure benefits, when compared to directional couplers, may include slower insertion losses, and larger optical bandwidth [75]. Moreover, these structures can also benefit from higher fabrication tolerances on refractive index contrast, wavelength and waveguide widths.

Due to the simplicity and low-cost of the Sol-Gel process, the organic-inorganic di-ureasil hybrid material [65] was chosen for the design and fabrication of the two-level HT network. Di-ureasil is an organic-inorganic hybrid material with acceptable transparency, mechanical flexibility, and thermal stability allowing it to be processed as thin films and tailored monoliths [65] [134]. Its refractive index can be efficiently controlled when combined with metal oxides precursors and the manufacturing of waveguide can be accomplished by single exposure ultraviolet (UV) writing through an amplitude mask, resulting in a cost-effective method [65] [134] [135]. Examples of its application in green integrated photonics include thermal actuated Mach-Zehnder interferometer (MZI) [65], thermo-optic variable wave plate [136], WG high-rejection optical filters [137], coherent receivers for next generation optical access networks [138], and integrated optical MZI for bio-sensing applications [139].

Taking advantage of the MMI magic-T structure design for the HT implementation and the benefits of the organic-inorganic di-ureasil hybrid material [65], a new cost-effective 2D HT network for image compression composed of three 2×2 MMI couplers disposed in a two-level signal decomposition architecture [58] is presented and tested in this section. Device design and manufacturing methodology are addressed in subsection 3.2.1, and in subsection 3.2.2 is presented and discussed the simulation/experimental results.

3.2.1 Design and manufacturing

The 2×2 MMI coupler [140] and the 2D HT network structures were designed and simulated with 3D beam propagation method (BPM) in OptiBPM® for a propagation wavelength of 1555 nm. To implement a subtraction in MMI output 1 (interference of signals in opposition of phase) and a sum in

output 2 (interference of signals in phase), a $\pi/2$ phase shifting with a 1×1 MMI [141] was integrated in the input 1 of the 2×2 MMI structure, as depicted in Figure 50.

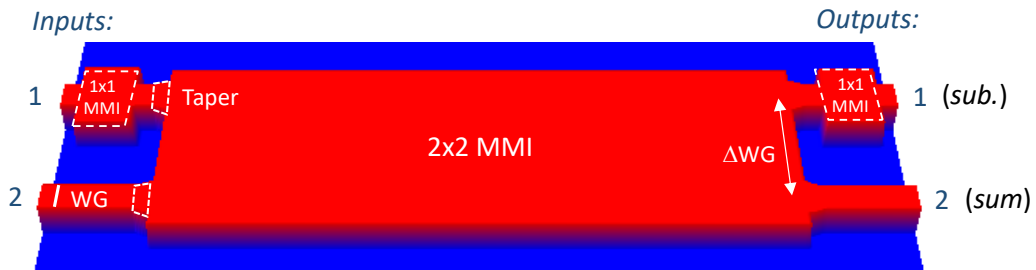


Figure 50. Schematic diagram of the MMI magic-T structure design.

The 2D HT network composed by a two-level network of three 2×2 MMI structures ($\text{MMI}_1 - \text{MMI}_3$) is presented in Figure 51. Design dimensions comprehend a WG width of $6 \mu\text{m}$, a distance between WG (ΔWG) of $125 \mu\text{m}$; a length and width of the 2×2 MMI of $4065 \times 40 \mu\text{m}^2$, length and width of the 1×1 MMI of $382 \times 15 \mu\text{m}^2$, and taper with a length of $100 \mu\text{m}$ and widths of $6 \mu\text{m}$ and $8 \mu\text{m}$.

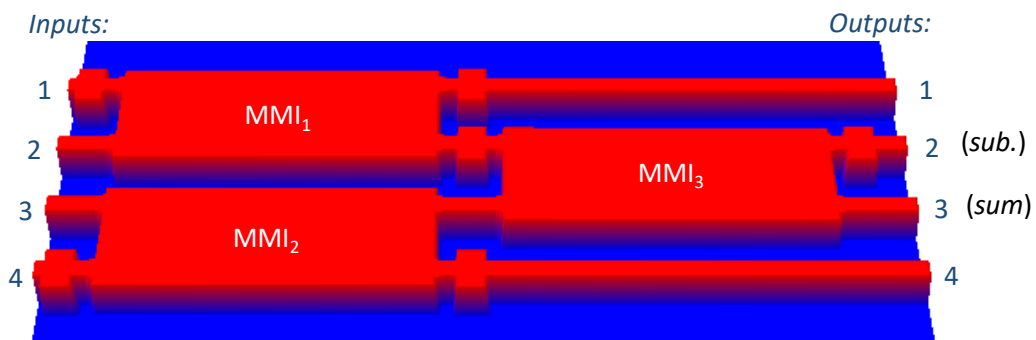


Figure 51. Schematic diagram of the design of the HT network structure, composed by a two-level network of three 2×2 MMI couplers.

The material simulated was the organic-inorganic di-ureasil hybrid, with an expected WG refractive index of 1.4924 (core) and 1.4895 (cladding), i.e., refractive index contrast (Δn) of 2.9×10^{-3} , and a SiO_2 substrate ($n = 1.45$). The structures devices were patterned by UV exposition using a chrome amplitude photomask with a resolution between $0.05 \mu\text{m}$ (500k dpi) and $0.4 \mu\text{m}$

(64k dpi). A UV pulsed laser ($\lambda = 248$ nm, frequency of 500 Hz, 350 μ J per pulse, focused through the objective lens) was used.

The time of exposure of the laser is related to the Δn obtained in the manufactured devices [142]. When compared with the designed structured ($\Delta n \approx 2.9 \times 10^{-3}$), a deviation of 2.0×10^{-3} was identified in the refractive index contrast of the sample manufactured ($\Delta n \approx 4.9 \times 10^{-3}$), measured by spectroscopic ellipsometry [143].

3.2.2 Simulation and experimental results

Simulations with 3D BPM for $\Delta n = [2.9, 3.9, 4.9] \times 10^{-3}$ were performed to assess the behavior of the structure for the designed (2.9×10^{-3}) and experimental (4.9×10^{-3}) Δn obtained. Furthermore, fabrication tolerances were also considered by studying a possible parasite effect, denominated waveguide sloped sidewalls occurrence [144], which can be introduced during the fabrication process, as illustrated in Figure 52.

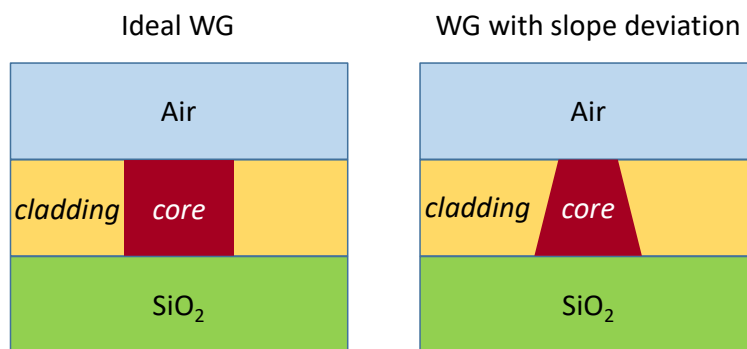


Figure 52. Schematic diagram of the ideal WG structure and WG with a slope deviation.

A slope deviation range, from 0 to 15 degrees, in the vertical sidewalls of the WG core was modeled, see Figure 52. Simulations parameters consisted in the core vertical sidewall with 90° configuration (i.e., with 0° deviation), up to a vertical sidewall configuration of 75° (i.e., with 15° deviation), applied to the 2×2 MMI structure (results presented in Figure 53), and to the 2D HT network structure (results presented in Figure 54).

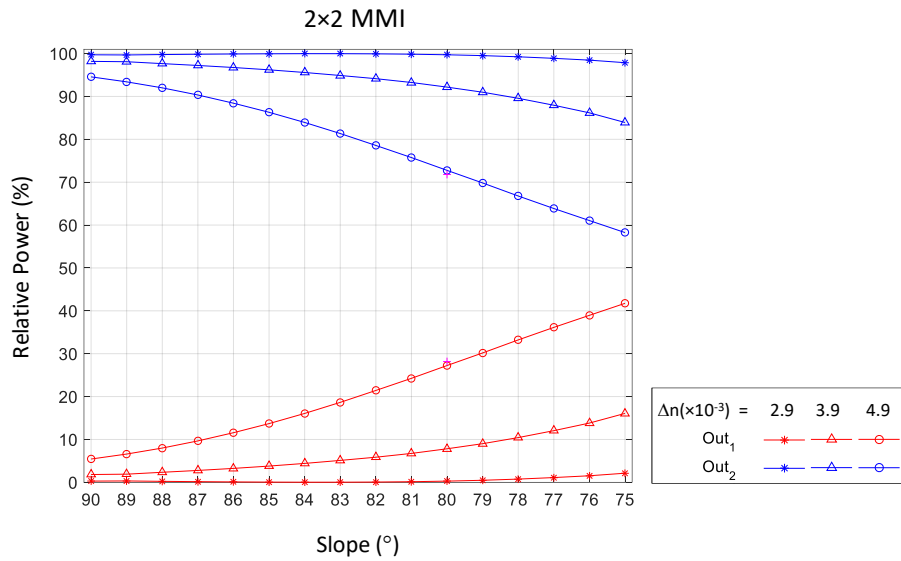


Figure 53. Relative power (%) at the two outputs of the 2x2 MMI structure for a slope deviation range of 15° (i.e., 90° to 75°) for $\Delta n = [2.9, 3.9, 4.9] \times 10^{-3}$, attained with BPM.

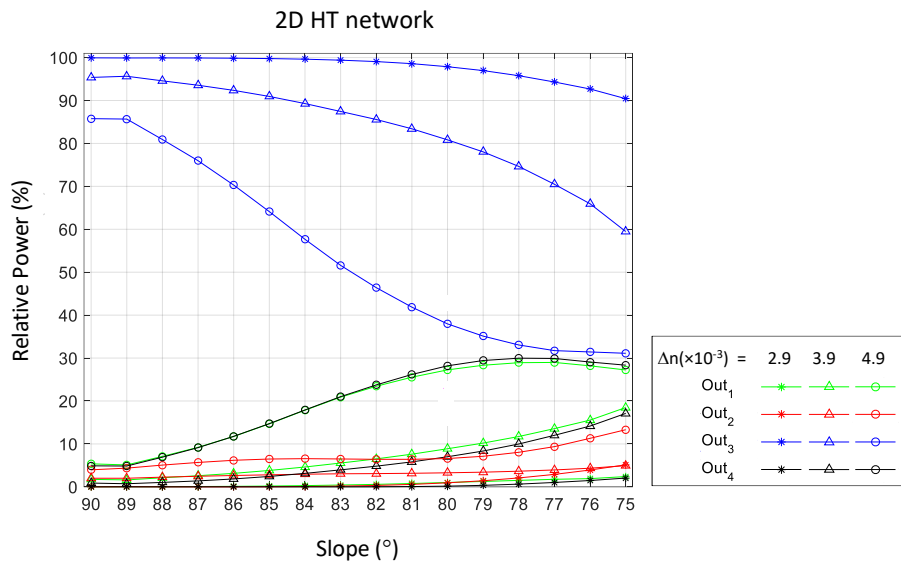


Figure 54. Relative power (%) at the four outputs of the 2D HT network structure for a slope deviation range of 15° (i.e., 90° to 75°) for $\Delta n = [2.9, 3.9, 4.9] \times 10^{-3}$, attained with BPM.

To ensure the same coupling conditions (e.g., phase and wavelength) in the two inputs of the 2x2 MMI structure, a 1x2 splitter was placed before the 2x2 MMI, as depicted in Figure 55-A. The

same approach was applied to the 2D HT network structure, by placing a 1×4 splitting network (of the three 1×2 splitters) before the 2D HT network, as depicted in Figure 55-B.

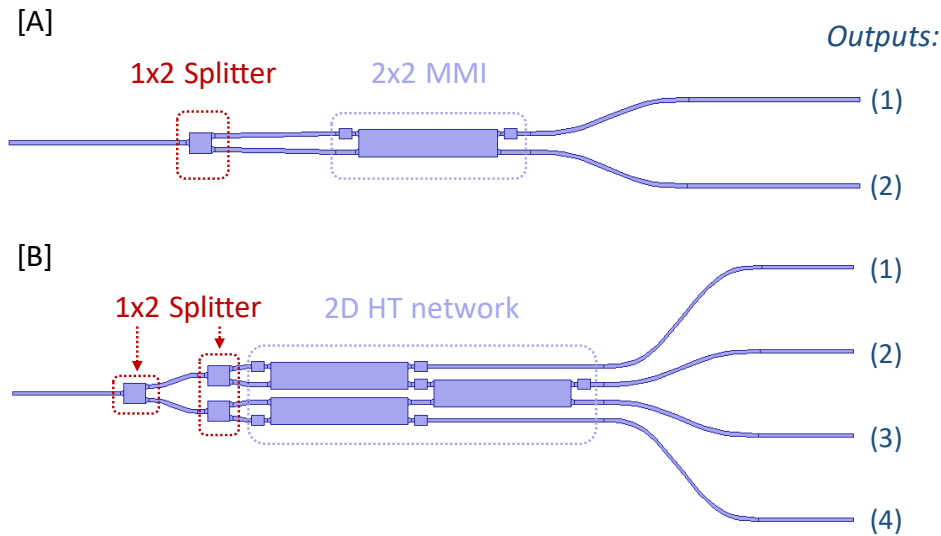


Figure 55. Design diagram of the manufactured device structures for testing and characterization of HT network operations. [A]: 2×2 MMI structure, with one input and two outputs, through a 1×2 MMI splitter placed before the 2×2 MMI. [B]: 2D HT network structure, with one input and four outputs, through a 1×4 splitting network (composed by three 1×2 MMI splitters) placed before the 2D HT network.

A mean normalized power of $50 \pm 1.4\%$ was obtained at the output ports of the 1×2 splitter structure, and $25 \pm 3.8\%$ at the output ports of the 1×4 splitting network. These structures (i.e., 1×2 MMI splitter and 1×4 MMI splitting network) were printed separately in the sample to enable its assessment.

The setup implemented for the optical device testing consisted of three micro-positioning adjusting systems placed inline to provide an efficient alignment, i.e., the:

- i) input optical signal, using an SSMF [117] fiber optic pigtail;
- ii) device under testing (DUT);
- iii) output collecting optical system.

The output collecting optical system was composed by an objective lens (magnification 10×, numerical aperture 0.25, focal length 16.5 mm, model Newport M-10X [145]), and a charge-coupled

device (CCD) image sensor (sensing area: 6.47×4.83 mm, resolution: 752×582 , pixel size: 8.6×8.3 μm), model Duma Optronics Bean on IR1550 [146]. A binocular stereoscope (Optika SZM-3) and a dual fiber output light source (Leica KL200) was used for an efficient system illumination during the alignment process. The input power was given by IR laser source (Phonetics OSICS Model TLS/C) with a wavelength of 1555 nm and 10.5 dBm of power. An overview of the setup implemented is illustrated in Figure 56.

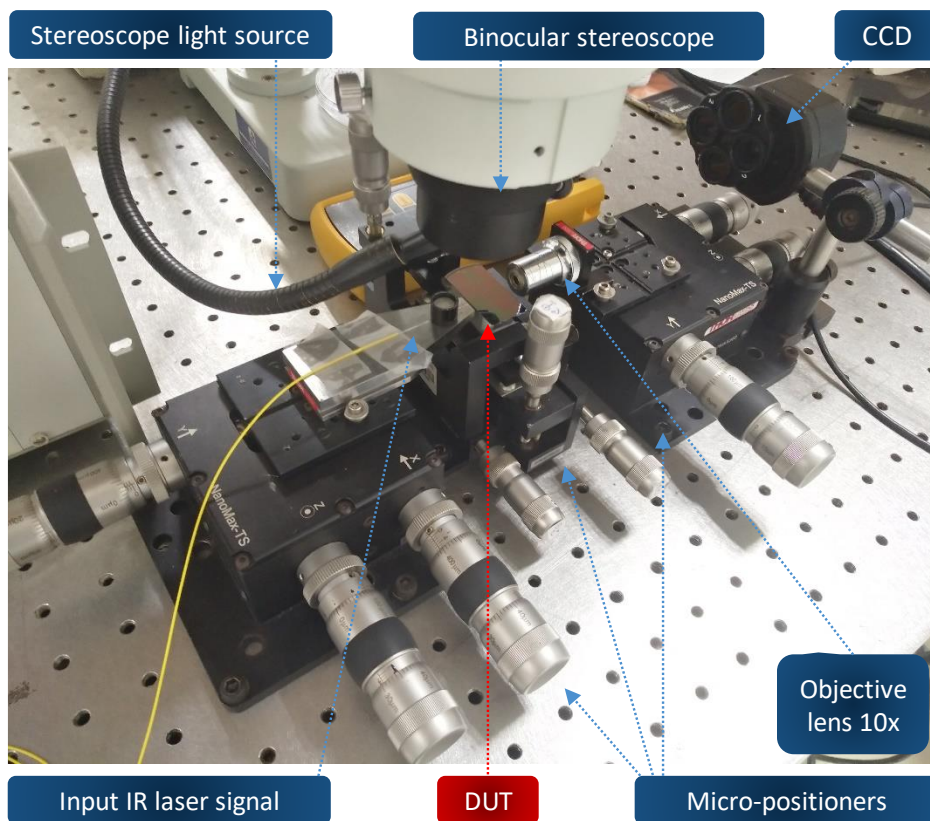


Figure 56. Setup for optical device testing, composed by: infrared (IR) laser ($\lambda = 1555\text{nm}$, $P = 10.5$ dBm); DUT (e.g., 2×2 MMI and 2D HT network); objective lens ($10 \times$); and a charge-coupled device (CCD) image sensor.

The DUT includes several structures, such as the 2D HT network, the 2×2 MMI, the 1×2 splitter, and the 1×4 splitting network. The analysis of the data collected with the CCD image sensor consisted of a first-order Gaussian fit applied to the intensity profile obtained.

To illustrate the data collection/analysis is presented in Figure 57 the experimental results attained for the 2×2 MMI BB. Figure 57-A shows the intensity profile obtained (i.e., the sum of all elements along each line of the image matrix) and the corresponding Gaussian fit, while in Figure 57-B is depicted the image acquired with the CCD image sensor.

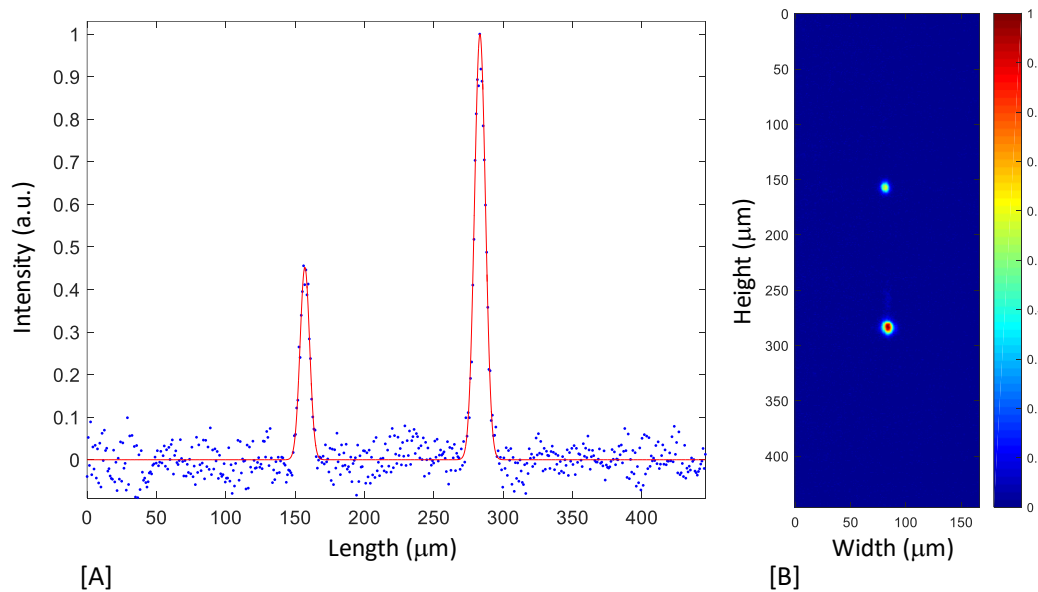


Figure 57. Experimental results from 2×2 MMI BB. [A]: Intensity profile of CCD image matrix acquired (blue dots) and corresponding Gaussian fit (red line). [B]: Image acquired with the CCD image sensor.

Extracted parameters presented in Table 10 include:

- i) full width at half maximum (FWHM);
- ii) peak position;
- iii) normalized relative power calculated from the intensity integral of the Gaussian fit.

Experimental results show an MMI coupling ratio of approximately 4 dB, i.e., a sum/subtraction at the output ports of the 2×2 MMI coupler structure. For the 2D HT network, a coupling ratio of approximately 3.6 dB between the outputs WG_2 and WG_3 was measured. These measurements can be related with the Haar wavelet transform corresponding to the HH detail component (described by the subtraction operation), and the LL approximation component (described by the sum operation).

Table 10. Gaussian fit parameters extracted from DUT output data collected with the CCD.

2×2 MMI				
Output	FWHM (μm)	Peak pos. (μm)	Height (norm.)	Rel. Power (%)
1	8.09	156.97	0.45	28.2
2	9.28	283.22	1.00	71.8
2D HT network				
1	8.11	33.39	0.57	22.9
2	8.39	158.59	0.44	18.5
3	8.61	285.23	1.00	42.8
4	8.72	412.11	0.36	15.8

* FWHM: full width at half maximum;

Peak pos.: peak position in X-axis;

Rel. Power: relative power at the output ports of structures (2×2 MMI and 2D HT network).

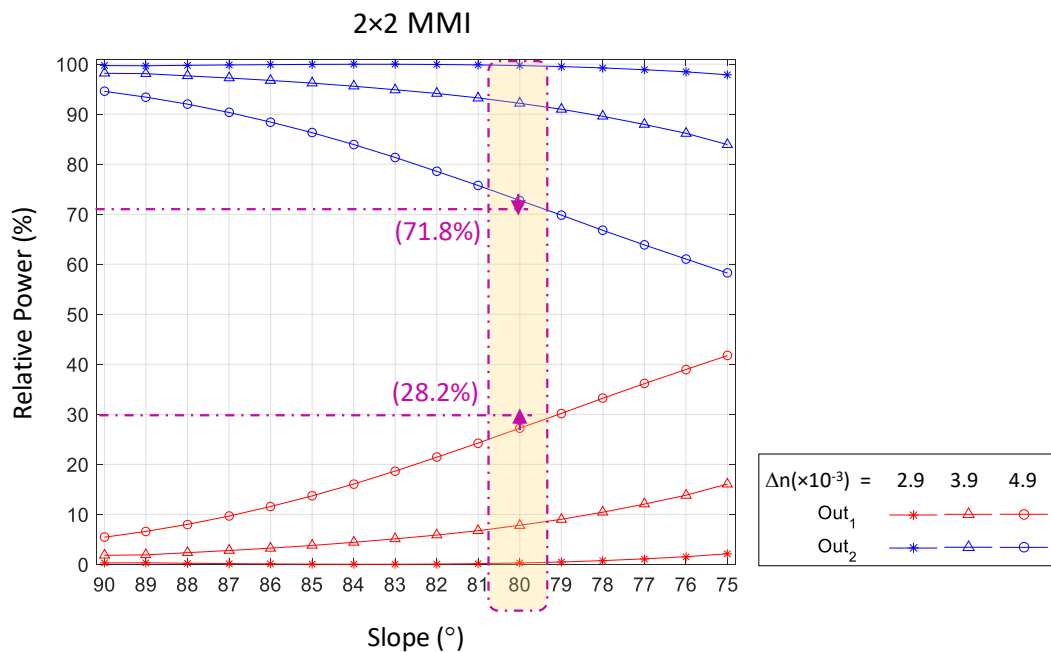


Figure 58. Relative power (%) at the two outputs of the 2×2 MMI structure calculated with BPM, and corresponding experimental relative power (%) measured (highlighted in pink).

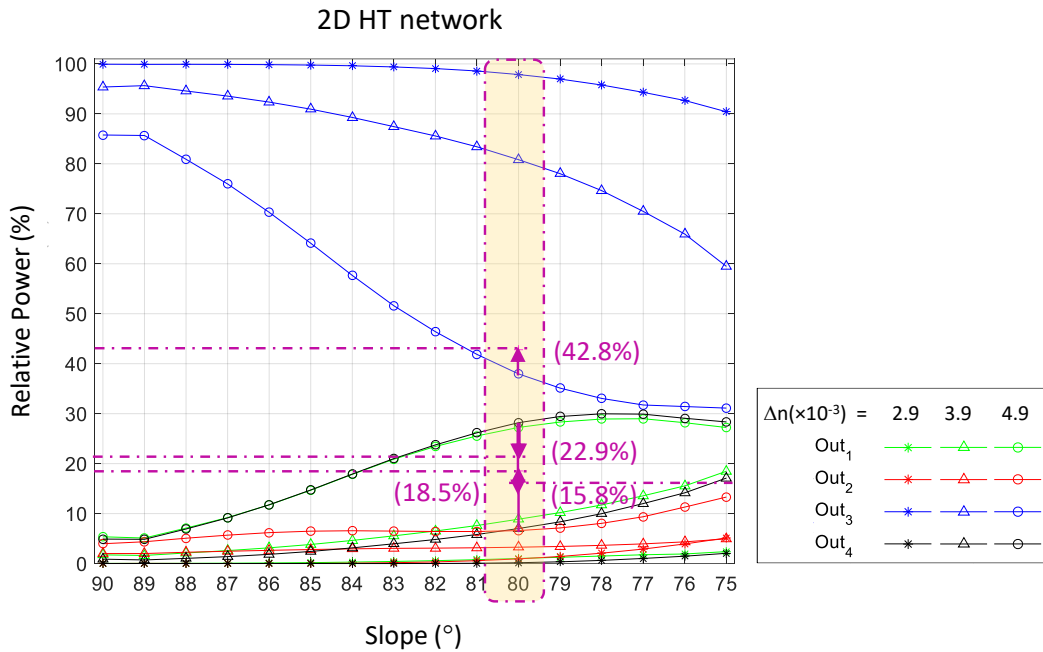


Figure 59. Relative power (%) at the four outputs of the 2D HT network structure calculated with BPM, and corresponding experimental relative power (%) measured (highlighted in pink).

The correlation between simulation (Figure 53 and Figure 54) and experimental (Table 10) results is depicted in Figure 58 and Figure 59 for the 2×2 MMI and 2D HT network structures, respectively.

Taking in consideration the possible slope deviation in the WG side walls and the sample experimental Δn measured (4.9×10^{-3}) can be extrapolated that the device manufactured had a slope of about 80° , as for this value an error $\leq 1\%$ (simulation/experimental) for the 2×2 MMI structure is observed, as depicted in Figure 58. For the same conditions (slope = 80° , $\Delta n = 4.9 \times 10^{-3}$), an error $\leq 12\%$ was identified for the 2D HT network (simulation relative output power of Out₁₋₄ = [27.2, 6.6, 38.0, 28.2]%), see Figure 59 and Table 10.

Thus, by lowering the Δn of the material to 2.9×10^{-3} (the Δn design reference) is expected a behavior very close to the optimal design expectations of the structures. This can be achieved through adjustments in the fabrication process, e.g., by decreasing the exposure time in the UV photolithographic process. Even with an inherent parasite effect such as the modeled slope deviation of 10° in the WG sidewalls, the expected results show a match accuracy of 99%, as presented in

Figure 58 and Figure 59. In these ideal theoretical conditions, a coupling of approximately 20 dB at the output of the third MMI of the 2D HT network can be estimated.

This study provides a first implementation and testing of a potentially cost-effective 2D HT network for image compression. Even considering the difficulty to fully address all the variables associated with the design/fabrication of the structures, a valid demonstration of its functionalities is attained and a design optimization model proposed.

In the scope of this study, acknowledgments are addressed to Professor RAS Ferreira from CICECO – Aveiro Institute of Materials at University of Aveiro (Portugal) for providing the di-ureasil films, within the scope of the CICECO–Aveiro Institute of Materials (FCT UID/CTM/50011/2019), financed by national funds through the FCT/MEC and when appropriate co-financed by FEDER under the PT2020 Partnership agreement, and Instituto de Telecomunicações (UID/EEA/50008/2019). Doctor Ana Rita Bastos and Doctor Carlos Vicente are also acknowledged for their collaboration in the manufacturing of the di-ureasil films, the structures devices patterned process, and spectroscopic ellipsometry measurements.

3.3 Chapter remarks

A first experimental characterization of an InP-based PIC implementing an all-optical AAC network for data compression based on the HT is presented. An extensive characterization of the network elementary BB, i.e., the AAC in an InP-based platform, with the full description of its tunable capabilities, is accomplished. A good correspondence between the simulation and experimental results validates the tunable capabilities of the AAC BB, allowing to determine with acuity the different phases that enable the full cycle of the device's coupling ratios. This coupler characterization provides a fundamental tool for the use of its full coupling capabilities in optical processing implementations such as Haar wavelet transforms with applications in data compression. Additionally, the experimental characterization of a PIC implementing the two-level HT network is also investigated. Even though, the complexity of the optical chip and the difficulty to fully and independently monitor each of its components, the first experimental demonstration of an integrated all-optical two-level HT in an InP-based platform operation is undertaken. Theoretical simulation models mimicking the experimental conditions were realized to better assess experimental results and characterize the PIC under testing. Nevertheless, the experimental characterization limitations due to damaged components, an extrapolation of the two-level HT network output coupling ratio was inferred with an experimental coupling behavior (sum/subtraction) ≥ 3 dB obtained.

Furthermore, taking advantage of low-cost hybrid materials [65], the first implementation and testing of a potentially cost-effective 2D HT network for image compression are realized. Even considering the difficulty to fully address all the variables associated with the design/fabrication of the structures, a valid demonstration of its functionalities is attained and a design optimization model proposed. Experimental characterization results show a coupling ratio behavior of approximately 4 dB for the MMI coupler, and approximately 3.6 dB at the outputs of the third MMI of the 2D HT network. With the implementation of the proposed design optimization model, in ideal theoretical conditions, a coupling ratio of approximately 20 dB is estimated at the output of the third MMI of the 2D HT network.

Chapter 4

PIC solutions in an ultra-low loss silicon nitride platform

Photonic integrated circuits can offer lower-cost smaller footprint solutions with improved performance and stability when compared to bulk and fiber optical systems. A wide range of optical system applications is foreseen, nevertheless with higher standard performance requirements of waveguides with ultra-low propagation loss [147]. Ultra-low propagation losses are essential for different optical system applications, such as high-quality factor (Q) resonators used in photonic rotational velocity sensors [148], optical buffers [149] [150], and narrowband photonic filters [151]. An ultra-low loss Si₃N₄ platform with stated propagation losses below 0.1 dB/m [54] is the based platform implemented in the PIC solutions addressed in this chapter.

For an effective assessment of high-Q resonators properties is essential to accurately evaluate the device performance. Thus, it is addressed in this chapter the implementation of a high-Q measurement technique based in a radio frequency (RF) calibrated Mach-Zehnder interferometer.

This technique was implemented to assess high Q-factor performance and properties of integrated resonators fabricated in ultra-low Si₃N₄ platform as reported in [60]–[62].

Particularly noteworthy the reported sub-hertz fundamental linewidth photonic integrated Brillouin laser [62]. A solution narrow enough (i.e., fundamental linewidth below 1 Hz) to move demanding scientific applications to the chip-scale, e.g., photonic micro-chip high-end lasers for spectroscopy, navigation, quantum computation, and optical communications applications. Photonic integrated sub-hertz linewidth laser can enable commercial applications such as coherent communications [152], next generation data center networks, atomic sensors [153], quantum sensing [154], and atomic clocks [155]. As a result, the implementation of spectrally laser performance to the integrated photonics poses compelling solutions to reduce cost and footprint of applications, such as ultrahigh capacity fiber and data center networks, atomic clocks, and sensing. The single- and multiple-frequency output operation of the sub-hertz fundamental linewidth Brillouin laser provides a versatile low phase-noise solution, highlighted by its demonstration in an optical gyroscope and a low-phase-noise photonic oscillator [62]. The merits of achieving such performance at the chip-scale may also provide a valuable contribution to address the challenge posed by the internet's exploding data-capacity requirements, and the resulting increase in worldwide energy consumption of data centers and fiber optic interconnects.

Furthermore, to address the growing internet traffic demands and the increasing attention given to the necessity of providing low-cost high-capacity data center interconnects (DCI) solutions is studied in this chapter the implementation of a low-cost interface technology for DCI enabled by a dispersion compensating photonic-integrated programmable lattice filter fabricated in a low-loss Si₃N₄ platform [147] [156]. An extended reach C-band transmission of real-time 53.125 Gb/s PAM-4 data over 40 km of standard single mode fiber (SSMF) enabled by photonic integrated dispersion compensation is described, with a transmission of 100 GHz spaced channels error-free below the forward error correction (FEC) threshold [59].

The chapter is organized in two main sections, the first detailing the implemented high-Q resonator measurement technique (section 4.1), and the second presenting the first demonstration of an extended reach transmission of C-band PAM-4 enabled with a photonic integrated tunable lattice filter dispersion compensator (section 4.2). The chapter is concluded with the final remarks addressed in section 4.3.

4.1 High-Q resonator measurement technique

Different high-Q measurement techniques can be explored for the characterization of integrated ring resonators, such as sideband spectroscopy [157], approaches involving RF calibrated swept sources, and photonic cavity ring-down [157] [158]. Based on these approaches is implemented a high-Q resonator measurement technique involving frequency swept laser sources (e.g., piezo tunable laser), which requires an independently calibrated optical frequency standard [159].

The built-in technique mainly comprises an RF calibrated Mach-Zehnder interferometer (MZI) implementation, described in section 4.1.1; the setup implemented for resonator quality factor measurement, presented in section 4.1.2; and the data analysis through Lorentzian fitting employment for the calculus of resonator performance properties, provided in section 4.1.3.

4.1.1 RF calibrated MZI implementation

The optical transmission of an unbalanced MZI was implemented as a suitable frequency standard for the high-Q resonator measurements [60] [160]. The calibrated frequency standard enables direct mapping of the applied piezo voltage signal to the relative optical frequency shift of the probe laser source.

The unbalanced path length of the MZI was chosen such that its free spectral range (FSR) is comparable to the full width at half maximum (FWHM) of the device under test (DUT). Thus, a path length difference of 200 m was employed, in order to produce an FSR of approximately 1 MHz, with enough resolution to efficiently be used as a measurement ruler to characterize the resonator under testing. This FSR can be denominated as calibrated MZI frequency standard.

The FSR independent determination was obtained through the MZI reference calibration process, in which an independent single sideband (SSB) swept-source experiment [160] [161] using a discrete stepped-sweep RF frequency synthesizer was conducted. While the discrete nature of the stepped-sweep limited the resolution of an SSB experiment conducted for high-Q resonator measurements, it was sufficient for accurately determining the MZI FSR [60].

The calibrated MZI frequency reference enabled analog frequency swept resonance width measurements and greater resolution Q measurements. For the SSB calibration of the MZI frequency standard, a laser source with the carrier at ν_0 was externally modulated by an intensity modulator driven by a microwave frequency synthesizer at frequency f_m . Cascaded fiber Bragg grating filters were used to suppress upper sideband and carrier frequencies, resulting in the transmission of only the lower sideband at $\nu_{low} = \nu_0 - f_m$. A linear sweep of the modulation frequency in time generates an RF calibrated optical frequency swept source, $\nu_{low}(t) = \nu_0 - f_m(t)$. Passing the swept source through the unbalanced MZI generates the optical frequency transfer function of the interferometer, with transmitted optical power maxima and minima occurring at integer multiples of the FSR [60].

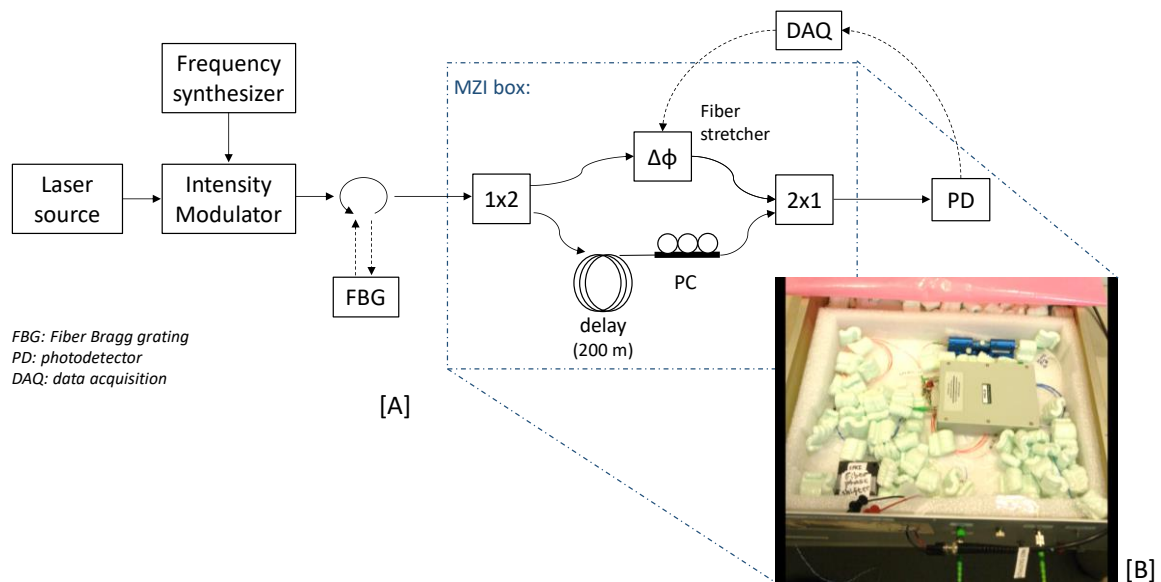


Figure 60. [A]: Diagram of the experimental setup implemented for RF calibrated MZI FSR measurement. [B]: Photograph of built calibrated MZI box (foam peanuts were added to provide stabilization).

A diagram of the built RF calibrated MZI box and implemented experimental setup for FSR calculation is depicted in Figure 60.

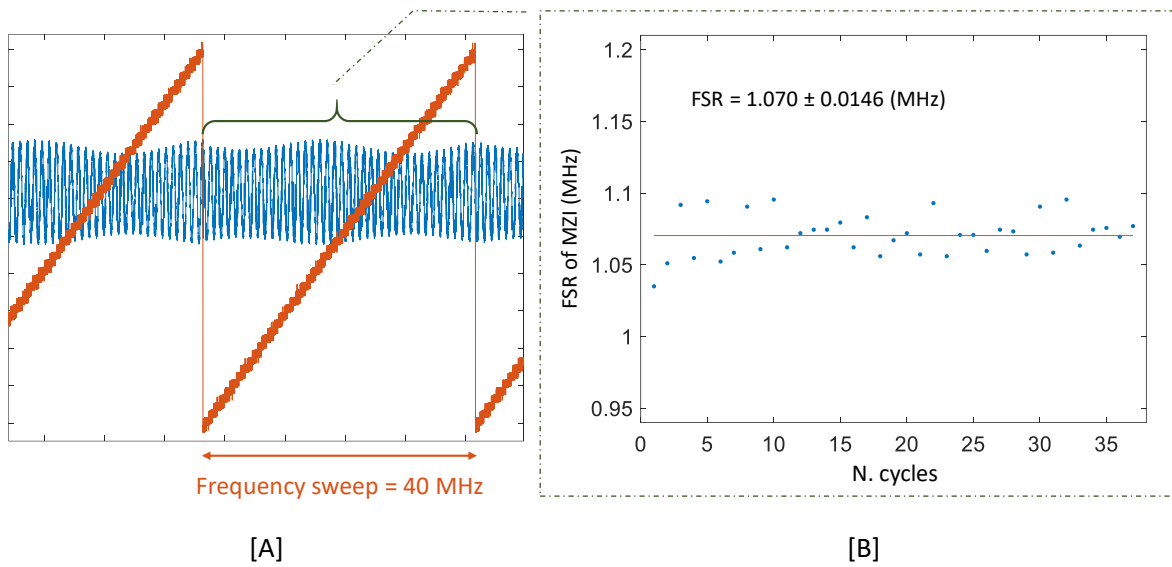


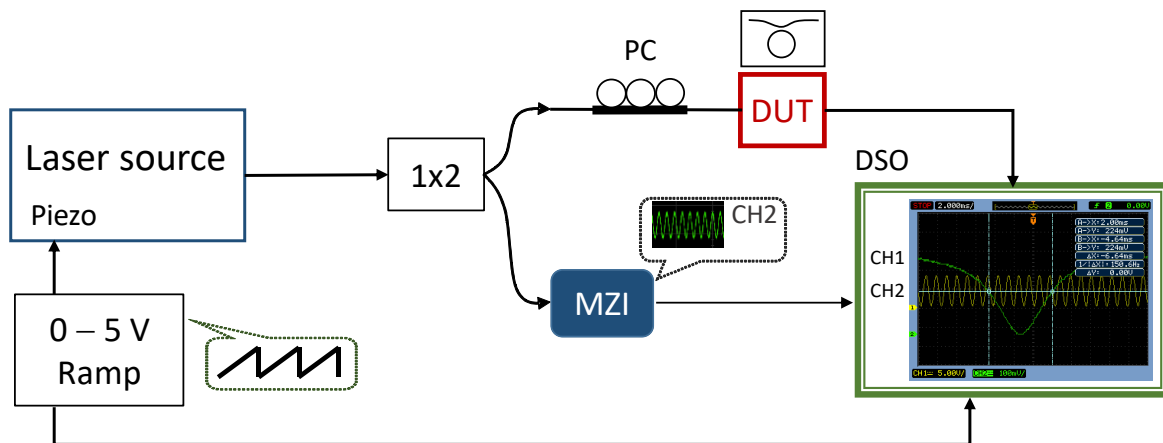
Figure 61. [A]: Interferometer optical frequency transfer function (blue line); Frequency sweep ramp at 40 MHz (orange line). [B]: FSR measurement results from calibrated MZI (FSR = 1.070 ± 0.015 MHz).

The implemented calibration method allowed the mapping of the known RF signal to an optical transfer function resulting in a measured FSR of 1.07 MHz with a standard deviation of 0.0146 MHz, as depicted in Figure 61.

4.1.2 Setup for resonator characterization measurements

The setup implemented for resonator measurements comprises a fiber laser with built-in piezo frequency tuning transmitting simultaneously through both the MZI and the resonator DUT. The MZI fringe spacing (FSR) provides the RF calibrated frequency reference used for the accurate evaluation of resonator Q factors, see Figure 62.

A diagram of the complete MZI based Q measurement setup is presented in Figure 62 [60]. A signal generator with 0-5 V ramp signal to piezo controlled frequency tuning of source laser centered at 1550 nm is applied. Digital sampling oscilloscope (DSO) traces of frequency standard (MZI reference), DUT resonance, and FWHM are also displayed, see Figure 62.



PC: polarization controller *DSO: digital sampling oscilloscope*
DUT: device under testing *MZI: Mach-Zehnder interferometer* *CH: channel*

Figure 62. Calibrated MZI measurement setup. Signal generator with 0-5 V ramp signal to piezo controlled frequency tuning of source laser centered at 1550 nm. DSO traces of frequency standard (yellow line) and DUT resonance (green line) with FWHM are displayed [60].

4.1.3 Measurement of resonator properties and applied fitting technique

Generically, a ring resonator comprises a looped optical waveguide with a coupling mechanism to access the loop. The resonator cavity is in resonance when the waves in the loop build up a round trip of an integer times 2π , i.e., through constructive interference [162].

A key parameter to characterize the performance of the ring resonator is the quality factor. In the frequency domain, it can be featured by the sharpness of the resonance relatively to its central frequency [163]. The Q-factor value depends on two main sources of loss, the loss effects associated with the coupling (power coupling coefficient, κ^2), and with the propagation in the ring (ring waveguide loss, α).

The theoretical loaded Q (Q_L) of a given system can be expressed by equation (30) [60] [164]. Where n_g is the group index, L_R the round-trip length of the resonator, λ the wavelength of light, κ^2 the power coupling coefficient, and α the ring waveguide propagation loss. When the coupling loss is not included, the resonator Q-factor is named intrinsic Q or unloaded Q (Q_U), as expressed in equation (31).

$$Q_L = \frac{2\pi n_g L_R}{\lambda(\kappa^2 + \alpha L_R)} \quad (30)$$

$$Q_U = \frac{2\pi n_g L_R}{\lambda \kappa^2} \quad (31)$$

A Lorentzian fit was applied to the resonator Q spectrum to extract the resonator characteristics (i.e., loaded and unloaded Q, FWHM, power coupling coefficient, and ring waveguide loss). These parameters were calculated from the intensity transmission formulation presented in equation (32) [60] [162].

$$T = \frac{b^2 - 2r \cos \phi + r^2}{1 - 2r \cos \phi + (rb)^2} \quad (32)$$

The variable ϕ is implemented by $2\pi n_g L_R \nu_i / c$, where c is the speed of light in vacuum and ν_i represents the detuning frequency, see Figure 63. It can be described as the single-pass phase shift, given by the multiplication of the round trip length with the propagation constant of the circulating mode [162].

Parameters b (loss coefficient) and r (transmission coefficient) from equation (32) are then used to calculate power coupling coefficient, $\kappa^2 = 1 - r^2$, and ring waveguide loss coefficient, $\alpha = -\log(b^2) L_R^{-1}$.

The Lorentzian fit was implemented using the Matlab function `fit` modeled to fit the measured data into the function provided by the equation (32). The determined fitting curve contains the resonator coefficients (i.e., coupling and waveguide loss) values, enabling the loaded and unloaded Q-factor calculation through equations (30) and (31), respectively. The reliability of the fitting was assessed by the normalized root mean square error (NRMSE) function [165]. An example of a measured resonator DUT through a Lorentzian fit (with an NRMSE of 3%, i.e., fit goodness of 97%) is presented in Figure 63.

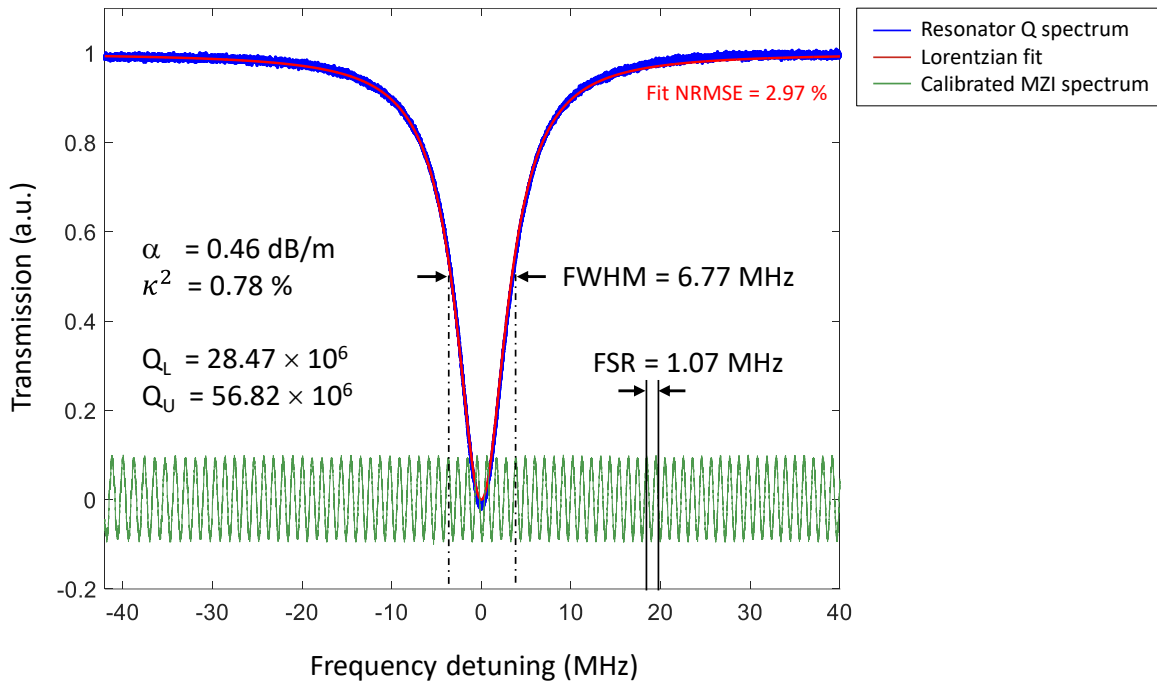


Figure 63. Measurement of resonator properties through Lorentzian fit implementation (with a fit error <3%). Resonator Q spectrum data and Lorentzian fit are presented in blue and red lines, respectively. Calculated properties of the resonator include ring waveguide loss ($\alpha = 0.46 \text{ dB/m}$), power coupling coefficient ($\kappa^2 = 0.78\%$), loaded Q ($Q_L = 28.47 \times 10^6$), unloaded Q ($Q_U = 56.82 \times 10^6$), and full width at half maximum (FWHM = 6.77 MHz). The frequency standard of the MZI (with an FSR of 1.07 MHz) is presented in green.

This measurement technique was successfully applied to the performance assessment of fabricated resonators, as reported in [60]–[62]. These resonators can be successfully used as stimulated Brillouin scattering lasers as detailed in [61]. The first presentation of the design and characterization of a large volume resonators in a unique TE mode with Q_U near 60 million in an ultra-low loss Si_3N_4 platform is detailed in [60]. Furthermore, a state-of-the-art chip-scale Brillouin laser capable of emitting light with a fundamental linewidth of less than 1 Hz is reported in [62].

4.2 Low-cost interface technology for DCI

Increasingly importance as being given to low-cost high-capacity DCI, as a viable solution to connect inter-campus and metro region scales in the 10 - 40 km distance range for certain deployments [59]. Thus, the extension of low-cost interface technologies developed for shorter reaches to this application space is of great interest. Furthermore, to address the growing internet traffic demands higher bandwidth modulation formats are of relevance [166].

A simple “higher-order” modulation scheme based on pulse-amplitude modulation with four amplitude levels (PAM-4) has been proposed for intra- and inter-data center optical links. Four distinct pulse amplitudes are used to convey the information in a PAM-4 modulation technique. Each amplitude level is represented by a symbol, composed of two bits, i.e., 00, 01, 10, 11, as depicted in Figure 64. Since for each amplitude, two bits are transmitted in parallel, PAM-4 modulation is twice as bandwidth-efficient as conventional binary modulation, e.g., non-return-to-zero (NRZ) [167]. Nevertheless, for PAM-4 higher signal-to-noise ratio (SNR) is required, due to the additional voltage levels, which reduce the level spacing by a factor of three, making this modulation scheme more suitable for short-haul optical systems where a higher SNR can be satisfied.

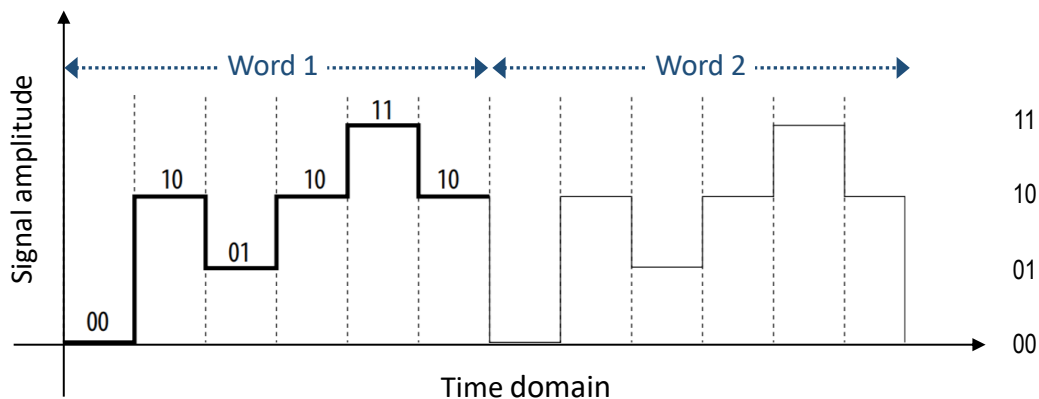


Figure 64. Example of a PAM-4 signal in the time domain.

The commercialization of PAM-4 signaling to replace NRZ has been gaining ground in the last years, with PAM-4 merits for transmission over band-limited channels and the use of lower bandwidth components [168]. As a result, the penetration of PAM-4 as a solution for today’s DCI has been

increasing. Nevertheless, dispersion compensation plays a critical role in optical communication systems as transmission length and bitrate escalates with advanced modulation formats, particularly sensitive to such optical impairments. As PAM-4 modulation tends to limit transmission lengths to approximately 5 km due to dispersion related signal distortion, there is currently a great interest to increase this interface reach via dispersion compensating schemes, which also should be able to accommodate multiple wavelengths [51] [59].

Reach extension beyond the dispersion-limited tolerance of ~5 km SMF 28® for direct detection was focused on using the low dispersion window at 1310 nm [169]–[171]. However, due to fiber scarcity in this application wavelength, there has been increased interest to move PAM-4 to the 1550 nm C-band in order to increase the link capacity [59]. A tradeoff in moving to C-band has been the need for discrete dispersion compensation technologies like dispersion compensating fibers (DCF) or fiber Bragg gratings (FBG). A demonstration of real-time 28 GBd wavelength division multiplexing (WDM) C-band to 80 km and 100 km has been reported [172]–[174], with dispersion compensation attained by the combination of tunable dispersion compensating module (TDCM) and DCF. However, in order to address cost, size, weight, and form factor, compact photonic integrated technologies are critical. These integrated solutions are expected to mitigate PAM-4 dispersion for multiple WDM channels while satisfying the strict optical signal-to-noise ratio (OSNR) requirements.

In this section is reported the first demonstration of C-band transmission of real-time 53.125 Gb/s PAM-4 over 40 km SSMF using a monolithically integrated programmable lattice filter for dispersion compensation [59]. The 10-stage lattice filter [156], capable of tuning ± 500 ps/nm, was fabricated in a low loss silicon nitride platform [147] compensating different channels on a 100 GHz channel spacing. Pre-forward error correction (pre-FEC) bit-error rate (BER) curves demonstrate error-free performance below the FEC threshold for up to four different WDM channels, over fiber lengths of 40 km, 35 km, and 25 km. While the lattice filter used in this study is designed to operate on multiple WDM channels on a 100 GHz grid simultaneously, an upgraded design in this platform to operate on a 50 GHz grid and to lower the overall chip loss to under 4 dB is also feasible [59].

A general overview of the integrated programmable lattice filter and its effective application in the extended PAM-4 link is presented in section 4.2.1. The implemented setup for the extended PAM-4 link testing is provided in section 4.2.2, and the results discussed in section 4.2.3.

4.2.1 Dispersion compensation photonic integrated tunable lattice filter

Chromatic dispersion mitigation in optical fiber transmission results from group delay variations related to wavelength, which can severely degrade the transmitted signal [91] [175]. As a pure single tone is not reachable when a pulse propagates along a fiber, different wavelength components travel at different velocities resulting in a pulse broadening, which limits the data rate and feasible transmission distance. For a fixed modulation format, dispersion tolerance of a transmission system is inversely proportional to the square of bit rate, thus increments in the bit rate highly deteriorate the overall system tolerance, which can pose an important limitation for high-speed communications [156] [176].

The application of integrated optical tunable filters technology can provide a good solution for dispersion compensation, as it can provide a compact approach bit rate independent and capable of compensating phase and amplitude distortions. Design features of such optical filters have a periodic frequency response that allows multiple WDM channels compensation in a single device. Additionally, tunability makes it possible to dynamically compensate residual chromatic dispersion resulting from fluctuations associated with different factors, e.g., temperature variations and path changes in reconfigurable optical networks [156].

The filter used to compensate dispersion in the proposed extended reach PAM-4 link is an integrated programmable lattice filter fabricated in a low-loss silicon nitride platform [54] [147] with heater controlled dispersion tuning [59]. This low-loss platform allows state-of-the-art waveguide losses at a bend radius ten times smaller than in silica platform, making it possible to design/fabricate low footprint lattice filter (even for a large stage number) [156].

A cascade of alternating symmetric and asymmetric MZI compose the filter, as depicted in Figure 65-A. The symmetric MZI acts as a tunable coupler to guide the optical signal path, while asymmetric MZI mostly function as dispersive elements and set the filter order. Delays are obtained through the coupling ratio of couplers with time delays chosen as integer multiples of the unit delay to provide a time domain discrete filter. The filter discreteness in the time domain assures its periodicity in the frequency domain allowing its application in multiple WDM channels. The total dispersion compensation (± 500 ps/nm) comprised by the device is related to the designed unit delay length

($\Delta L = 2$ mm), the FSR (of 100 GHz), and the number of filter stages (10-stage cascaded lattice filter), as reported in [51] [156].

The device has a footprint of 2.2 cm^2 ($22.5 \times 9.89 \text{ mm}^2$) and was designed to operate on simultaneous WDM channels (in a 100 GHz channel spacing grid), with maximum dispersion tuning of $\pm 500 \text{ ps/nm}$ over a 15 GHz bandwidth per channel [156]. The filter and its design architecture are presented in Figure 65.

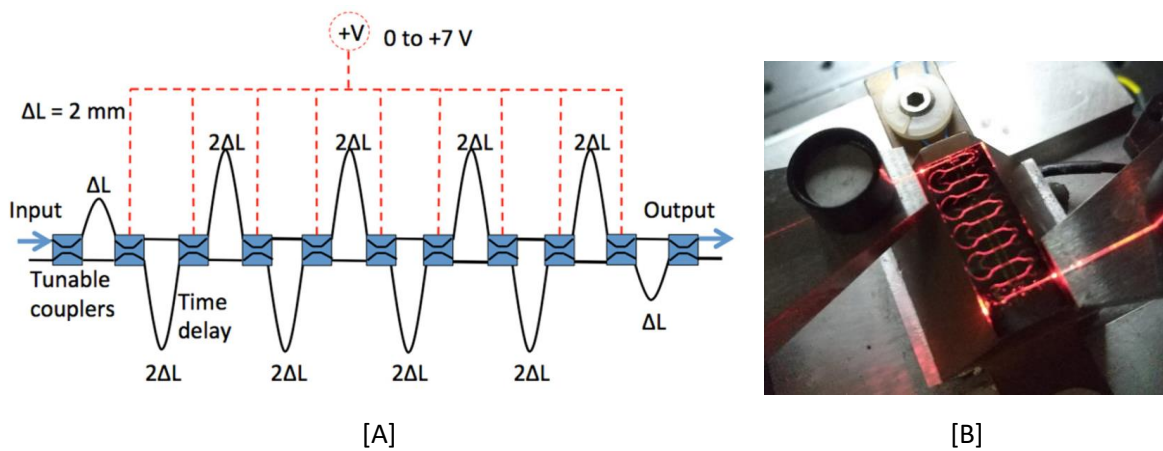


Figure 65. [A]: Diagram of integrated programmable lattice filter architecture with a delay length of 2 mm for 100 GHz channel spacing. [B]: Photograph of tunable 10-stage dispersion compensating lattice filter, with red light used for coupling alignments [59].

For PAM-4 over 40 km in the C-band is expect the required dispersion compensation to be approximately 550 ps/nm assuming the receiver can tolerate 170 ps/nm residual dispersion as reported in [173]. Optical backscatter reflectometry (OBR) measurements of wavelength-dependent group transmission, group delay, and corresponding dispersion are reported in [156].

Dispersion is continuously tuned by adjusting the phase of the couplers, i.e., by applying different voltage bias settings. Changes in the bias settings trigger variations in the couplers coupling ratio, which results in a corresponding change in the filter group delay response. The probe station implemented for bias settings tuning is depicted in Figure 66.

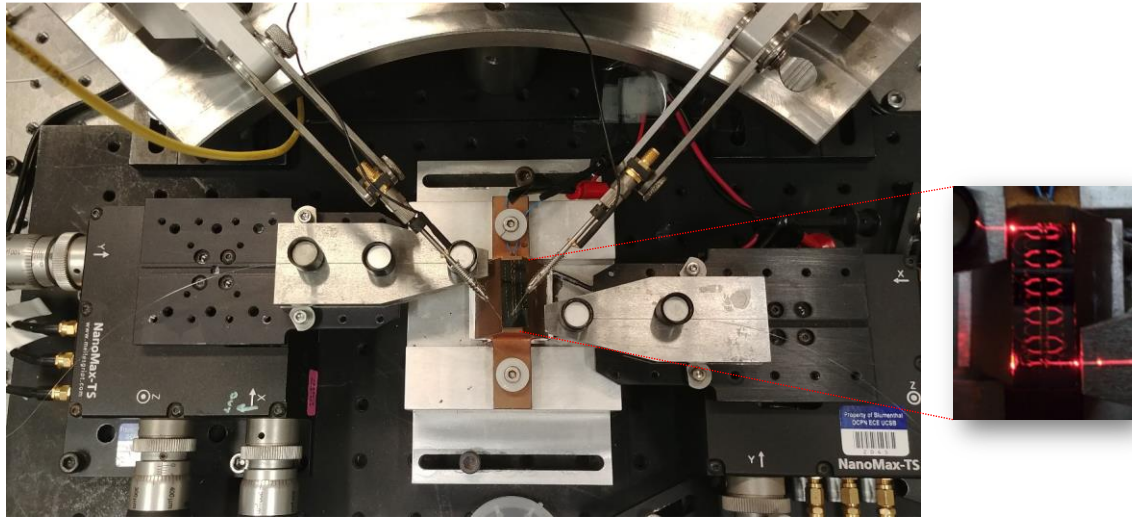


Figure 66. Photograph of probe station implementation for the bias settings tuning of the integrated programmable lattice filter.

The current device has a total through loss of 20 dB due to the absence of fiber coupler tapers and the close proximity of the thermal tuners to the waveguides. Nonetheless, the device loss was not a limiting factor in this demonstration, as the link was dispersion-limited with the OSNR maintained above 40 dB [59].

Nevertheless, key device design features can be readily changed to realize a filter with under 4 dB loss. Critical filter design parameters include the unit optical delay (2 mm for this design) and the number of filter stages, which determine the maximum tunable dispersion, FSR, and bandwidth. To overcome the loss of the current filter, next generation device will incorporate longer unit optical delay length and smaller filter FSR to increase dispersion tuning maximum and enable 50 GHz WDM. Furthermore, the low loss platform (of 0.1 dB/m [54]) potentiates long delays and a large number of stages.

4.2.2 Experimental setup

An optical NRZ on-off keying (OOK) transmission link was initially implemented for baseline performance testing. In Figure 67 is presented the apparatus of the NRZ link. Real-time NRZ signal (amplified bit pattern signal) is interfaced with a C-band Mach-Zehnder modulator (MZM).

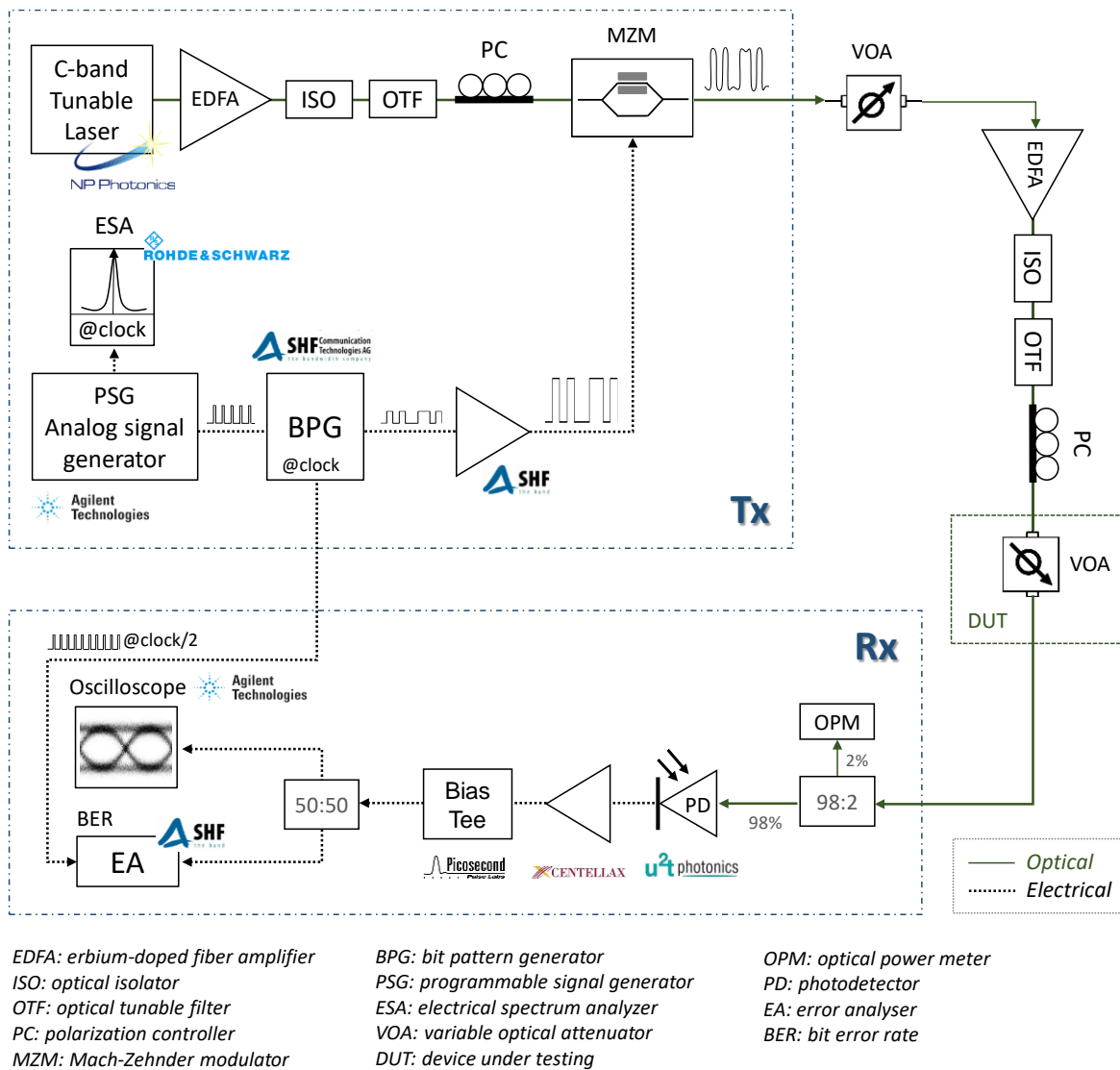


Figure 67. Experimental setup for the NRZ link implementation for baseline performance testing.

The transmitted signal from C-band tunable laser (NP Photonics Rock module laser) and booster erbium-doped fiber amplifier (EDFA) is the input of the MZM. An optical isolator (ISO) is incorporated to block backwardly progressing optical light by reflection, and an optical tunable filter (OTF) to reduce the EDF amplified spontaneous emission (ASE) noise light. After the transmission block, the variable optical attenuator (VOA) is used to control and/or tested the loss associated with a transmission fiber span. The signal is amplified before the DUT to guarantee sufficient power to overcome the device insertion loss, through VOA and/or DUT. At the receiver, the output signal is split in (98:2)%, where 2% of the signal is set for optical monitoring using an optical power meter (OPM). Then, the power

signal (98%) goes to the photodetector (PD) for optical-electrical conversion for BER measurements, as depicted in Figure 67. Optical signal-to-noise ratio (≥ 40 dB) and noise penalties in the link were assessed to guaranty the feasibility of the link and the posterior transition to the PAM-4 modulation scheme.

Stimulated Brillouin scattering (SBS) suppression was evaluated by inserting a circulator before fiber span and measuring reflected power. C-band tunable laser with a booster EDFA and 75 km fiber span showed transmission saturation at inputs above around +7 dBm, see Figure 68.

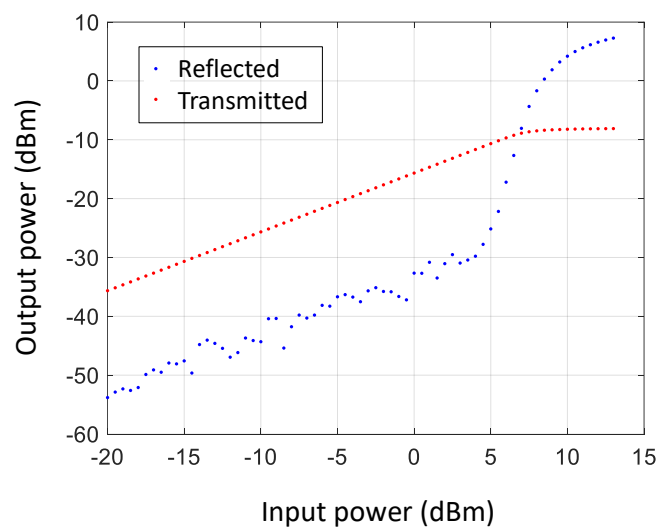
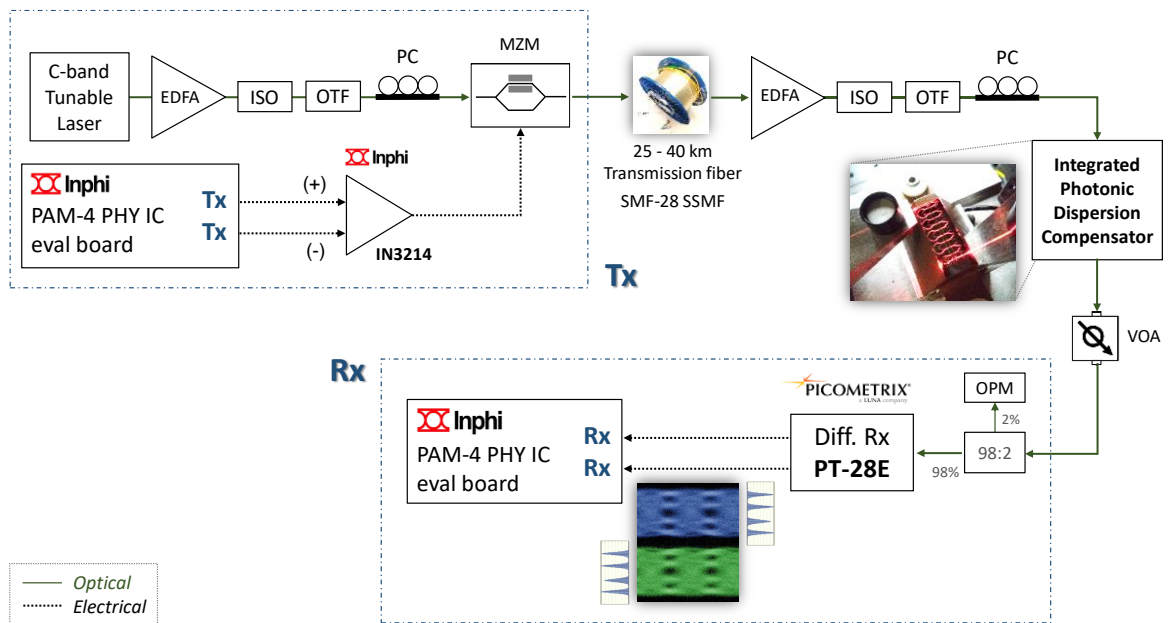
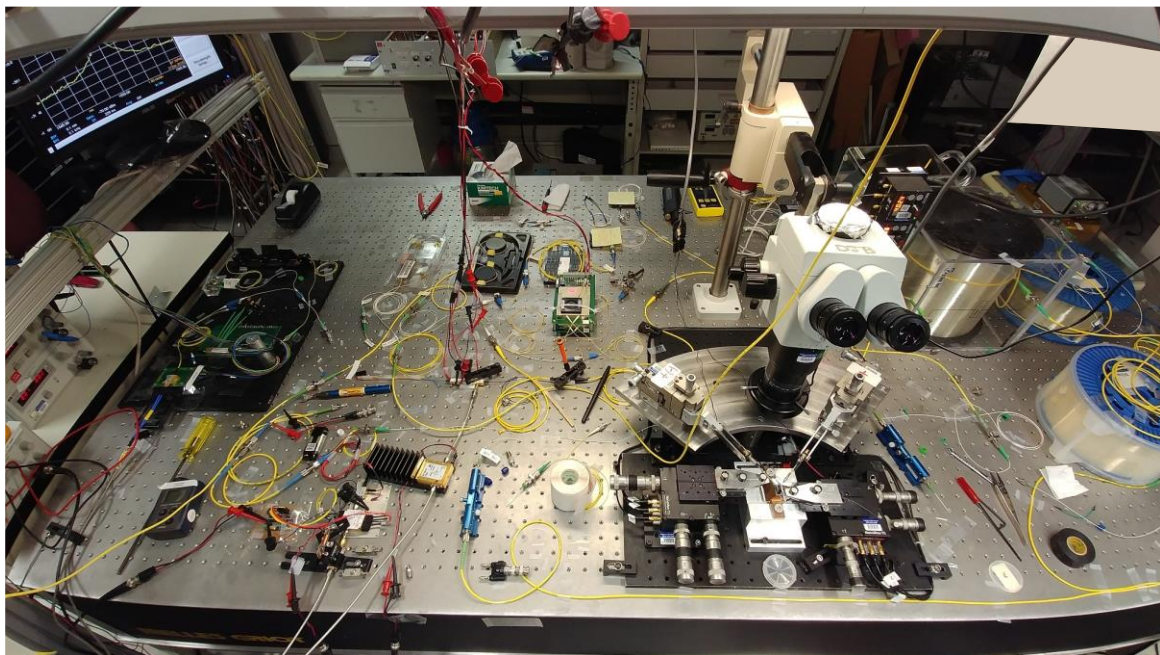


Figure 68. Stimulated Brillouin scattering (SBS) suppression measurement for a C-band tunable laser with a booster EDFA and 75 km fiber span.

The experimental setup implemented for the extended reach PAM-4 link testing is presented in Figure 69. Inphi PAM-4 Phy integrated circuit (IC) [177] transmitter and receiver boards were used to generate and detect real-time PAM-4 pseudorandom binary sequence (PRBS)-31 patterns as well as generate histograms and counting BER. The real-time PAM-4 boards were interfaced with a C-band 40 Gb/s MZM based transmitter and a 32 GHz linear receiver. Transmission booster and receiver optical amplifiers and optical filters were used to set the OSNR with the integrated dispersion compensation chip in place to above 40 dB. The transmitter electrical block consists of an Inphi PAM-4 PHY IC board generating at KR4 (25.78125 GBd) and KP4 (26.56250 GBd) standard IEEE baud rates [170].



[A]



[B]

Figure 69. [A]: Experimental setup for real-time C-band 53.125 Gb/s PAM-4 transmission using 10-stage photonic integrated programmable lattice-filter dispersion compensator. [B]: Photograph of experimental setup implemented.

The PAM-4 integrated circuit board outputs differential signals are drive into a single-ended Sumitomo MZM intensity modulator using a differential to single-ended linear amplifier (IN3214).

The optical signal from a C-band tunable laser and booster EDFA was the input of the modulator at a power level of +7 dBm to transmit 53.125 Gb/s data channels onto a 100 GHz C-band ITU grid. A single-ended optical to differential electrical output linear receiver (Picometrix PT-28E) suitable for 28 GBd direct detection enabled measurements with received power as low as -16 dBm. Receiver side DSP and signal recovery were performed on-board the PHY-IC PAM-4 unit, with built-in pre-FEC BER and SNR analytics. For each real-time pre-FEC BER measurement only the laser frequency and EDFA filter center frequencies were changed, in increments of 100 GHz. For each BER measurement all other transmission components were kept constant, i.e., booster EDFA, MZM, and PAM-4 drive electronics, receiver EDFA, linear receiver gain and bandwidth, and PAM-4 receiver board equalization settings. All BER measurements are pre-FEC and shown relative to the FEC threshold, i.e., KP4-FEC threshold of 2.4×10^{-4} [170].

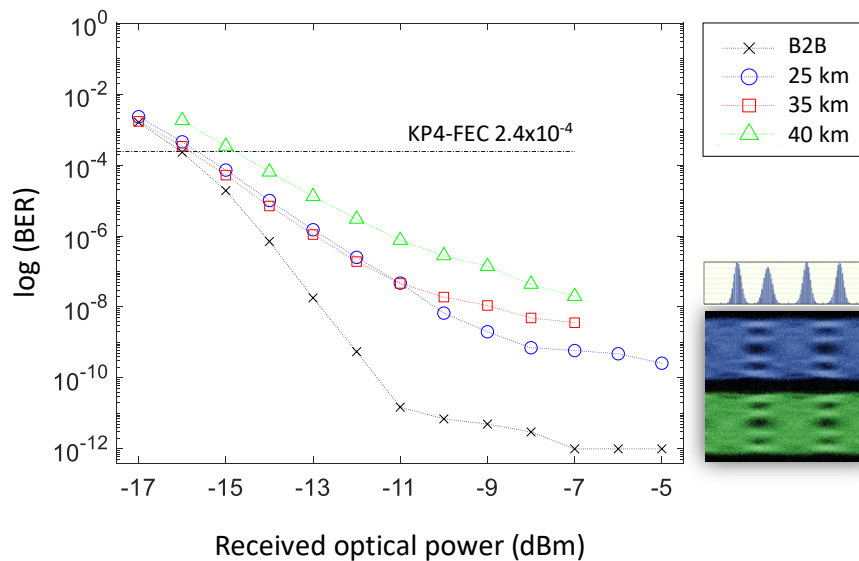


Figure 70. Measured Pre-FEC BER for λ_0 (1560 nm) back-to-back and over 25 km, 35 km, and 40 km of SMF-28 SSMF with the KP4-FEC 2.4×10^{-4} threshold indicated.

Back to back optical pre-FEC BER measurements were made with no transmission fiber in place at a wavelength of 1560 nm (λ_0). A baseline error detection better than the FEC threshold limit was achieved, as depicted in Figure 70. Fiber lengths of 40 km, 35 km, and 25 km were incorporated into

the link for transmission measurements, using an SMF-28[®] SSMF with an dispersion ≤ 18 ps/nm·km (at 1550 nm), and maximum loss of 0.2 dB/km (at 1550-1625 nm range) [117] [178]. Transmission measurements results of pre-FEC BER below the KP4-FEC error threshold (2.4×10^{-4}) for the channel λ_0 (1560 nm) are presented in Figure 70. A sample eye diagram at the receiver differential output and a post-DSP 4-level histogram is also depicted.

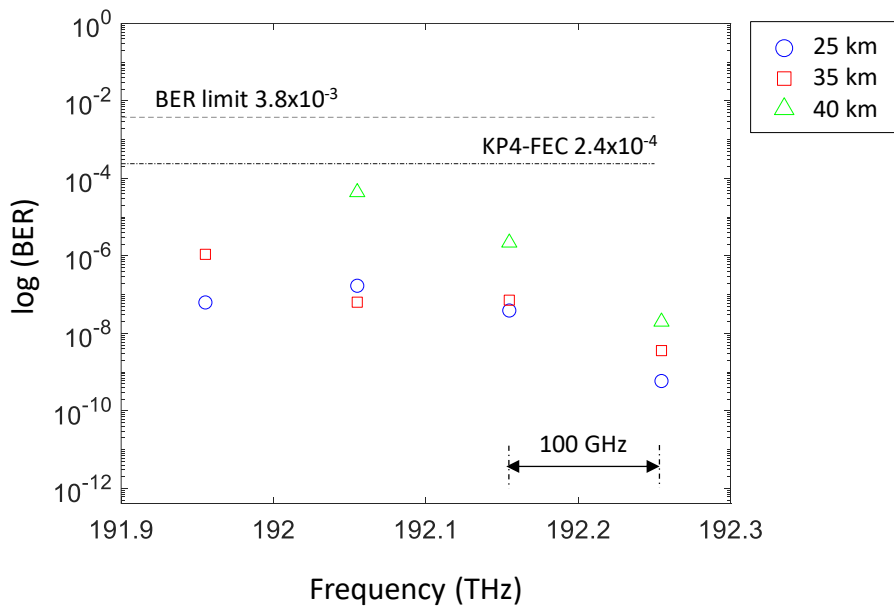


Figure 71. Measured pre-FEC BER for four 100 GHz spaced channels $\lambda_0 - \lambda_3$ with a received optical power of -7 dBm and performance below KP4-FEC 2.4×10^{-4} threshold (channel λ_3 was not recovered for 40 km due to the total plus residual dispersion exceeding the compensated).

A total accumulated dispersion of 720 ps/nm in a transmission length of 40 km, i.e., $40 \text{ km} \times 18 \text{ ps/nm} \cdot \text{km}$, can be estimated. An EDFA was incorporated before the photonic chip to overcome device loss and enable transmission measurements up to -5 dBm received optical power. Optical SNR was maintained above 40 dB for all measurements to ensure the link performance was not limited by the OSNR margin for PAM-4 optical transmission. The measurement of the real-time pre-FEC BER multiple channels at 100 GHz spacing for the three fiber lengths at four wavelengths are presented in Figure 71. Performance is assessed with KP4-FEC error threshold of 2.4×10^{-4} BER [170].

It can be estimated that the link as the ability to compensate for a total accumulated dispersion of approximately 670 ps/nm (i.e., the 500 ps/nm integrated photonic circuit compensation plus the 170 ps/nm residual dispersion tolerance at the PAM-4 receiver board). The system presented good performance for transmission lengths up to 40 km, being just not able to completely recover from the dispersion degradation at 40 km for channel λ_3 (1562.86 nm) as depicted in Figure 71. As a result, the pre-FEC value for channel λ_3 at 40 km was not plotted due to the total accumulated dispersion falling just short of the required compensation at that exact wavelength, see Figure 71. The photonic circuit was operated at 80 mA and 5.9 V, corresponding to 470 mW.

4.2.3 Discussion

The first demonstration of real-time transmission of 53.125 Gb/s PAM-4 over 40 km SSMF using a photonic integrated 10-stage tunable lattice filter for dispersion compensation is presented. Test results show 100 GHz spaced C-band channels to be transmitted error-free below the KP4-FEC 2.4×10^{-4} threshold, and subsequently BER limit threshold 3.8×10^{-3} . The integrated compensator tunable dispersion range of ± 500 ps/nm supported the transmission of three channels over 40 km and four channels over 35 km and 25 km. The dispersion for the fourth channel at 40 km was just under the receiver dispersion tolerance combined with the compensator maximum and therefore was not able to be recovered while keeping all transmission components constant while only the transmission wavelength was changed. It should be noted that this fourth channel was recoverable by slightly adjusting its transmission frequency, however that data point was left out to provide only the exact 100 GHz grid spaced channels.

All measurements were made with dispersion-limited transmission and OSNR above 40 dB. The integrated photonic lattice filter had an insertion loss of 20 dB, which did not limit the link OSNR, but in next generation filters it can be lowered to below 4 dB with design optimization, e.g., using fiber taper couplers on-chip [179] and thickening of upper cladding by moving the thermal tuning metal further away from the optical mode. Tuning using piezoelectric (PZT) is also under investigation to further the loss lowering and decrease the power consumption [59].

4.3 Chapter remarks

PIC solutions with ultra-low loss propagation can pose remarkable merits in a variety of applications, namely integrated high-Q resonators. Nevertheless, accurate performance measurement of the resonators quality factor output should be guaranteed. In this chapter, is reported the implementation of a high-Q resonator measurement technique based on an RF calibrated MZI and data analysis through Lorentzian fit employment. This technique was successfully implemented to evaluate the high Q-factor performance properties of integrated resonators fabricated in ultra-low Si₃N₄ platform as reported in [60]–[62]. Standing out, a state-of-the-art Brillouin laser capable of emitting light with a fundamental linewidth lower than 1 Hz, narrow enough to move demanding scientific applications to the chip-scale [62].

Furthermore, the first demonstration of real-time transmission of 53.125 Gb/s PAM-4 over 40 km SSMF using a photonic integrated 10-stage tunable lattice filter for dispersion compensation was attained. The tunable filter was manufactured under a low-loss Si₃N₄-based integrated WG platform. Additional improvements are expected in the next generation filters by lowering the device insertion loss up to 4 dB and enable a 50 GHz grid WDM, through design optimization. Optimization approaches can include the use of fiber taper couplers on-chip, thickening of upper cladding, design longer unit optical delay lengths and smaller filter FSR, and the investigation of PZT tuning to further decrease loss and power consumption.

Chapter 5

Spatial light modulator framework

Spatial light modulation is a technology with a demonstrated wide range of applications, especially in optical systems. Among the various spatial light modulator (SLM) technologies, e.g., liquid crystal (LC); magneto-optic; deformable mirror; multiple-quantum-well; and acoustic-optic Bragg cells; the ones based on liquid crystal on silicon (LCoS) have been gaining importance and relevance in a plethora of optical contexts, namely in telecom, metrology, optical storage, and microdisplays. Their implementation in optical systems and telecom have enabled the development of high capacity optical components in system functionalities as switching (in reconfigurable optical add/drop multiplexers - ROADM), multiplexing/demultiplexing, and optical signal processing. This technology combines the unique light-modulating properties of LC with the high-performance silicon CMOS properties. Different types of modulation (i.e., phase, amplitude, or combination of the two) can be achieved by combining liquid crystal molecules alignment with the appropriate polarization optics properties of the incident light of the modulator.

The capability of the SLM to dynamically reconfigure light with computer-generated holograms (CGH) is explored in this chapter with the implementation of an optical system SLM framework with

application in SDM systems (e.g., to efficiently excite different cores in MCF) and characterization/test of photonic integrated circuits. In section 5.1 are introduced the basics of SLM operation principle, main challenges, and applications. The implemented SLM framework methodology is discussed in section 5.2. The main experimental results are provided in section 5.3, and the chapter is concluded with the final remarks on section 5.4.

5.1 SLM operation principle and applications

Optical signal processing has been providing relevant solutions to convert data into spatially modulated coherent optical signals with SLM devices, allowing the effective implementation of digital holograms [180]. One of the most useful properties of the hologram is its ability to control the phase and the amplitude of light in the far-field. The Fourier transform describes the relationship between a hologram (near-field) and its corresponding replay field (far-field). The far-field can be formed at the focal point of a positive lens or an infinite distance from the near field plane in free space [180] [181]. An example describing this concept is presented in Figure 72.

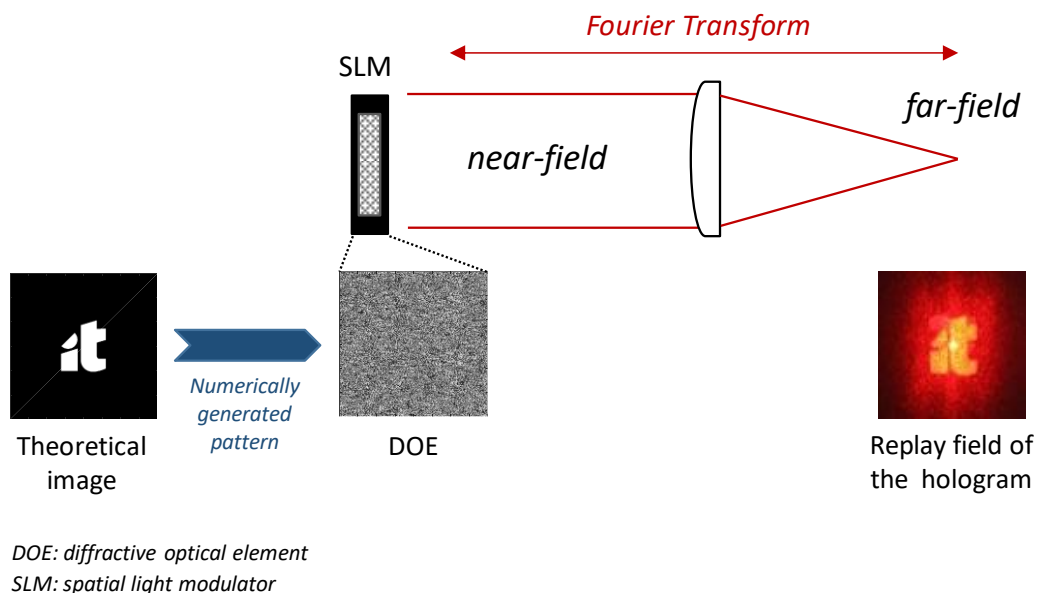


Figure 72. Diagram of a Fourier transform through a positive lens. A complex design pattern (diffractive optical element – DOE) is provided to the SLM to generate the expected hologram in the replay field (far-field).

Holograms can reproduce waveforms from an existing object. With digital advances and optical signal processing is possible to numerically calculate interference patterns to generate completely synthetic wavefronts of arbitrary form. These interference patterns can have different denominations, such as computer-generated holograms (CGH), diffractive optical elements (DOE), phase/amplitude masks, diffractive grating, etc. [181]. All operate in the principle of diffraction, so it is somehow an arbitrary choice of terminology. In the context of this work will be used the CGH, DOE, and phase mask nomenclature to refer to the calculus and generation of numerical interference patterns.

The SLM can be described as an electronically programmable device that modulates light in accordance with a fixed spatial (pixel) pattern. It can be exploited for incident light phase and/or amplitude control. Subsequently, phase-only, amplitude-only, or the combination phase-amplitude can be realized with the SLM. From the different employed modulation mechanisms, the most widely used is the electro-optical SLM, i.e., with the liquid crystal as the modulation material.

A liquid crystal SLM has a microdisplay being employed for the incident light modulation and collection. This can be realized in a transmissive form using a liquid crystal display (LCD) SLM technology or in a reflective form with LCoS SLM technology. From the various SLM technologies, the LCoS will be addressed in more detail in this study due to its relevant applicability in optical systems context. One of the leading features of these modulators is the liquid crystal molecule alignment. Typically, this can be either vertical, parallel, or with twisted formation. Consequently, with suitable polarizing optics is determined which incident light beam properties can be effectively changed, i.e., amplitude, phase, or their combination [32] [63] [182].

Nonetheless, the common hologram generation techniques cannot arbitrarily modulate the beam phase and amplitude simultaneously [181] [182]. It is not then possible to simply address the inverse Fourier transform of the desired pattern into the far-field and replicate the resulting distribution of amplitude and phase directly on the SLM [181]. As a consequence, the employment of optimization algorithms is highly recommended to generate an accurate hologram within the device constraints, e.g., the best pixel distribution in which each pixel will be able to take only one of two states that correspond to a 0 or π phase shift [32] [181].

The device used in the proposed SLM framework is based in the nematic LCoS technology, i.e., a type of SLM with phase-only modulation capability. It belongs to the category of the electrically addressed reflection modulators in which, a direct and accurate voltage controls the liquid crystal, and

modulates the light beam wavefront [183] [184]. An example of an LCoS SLM is illustrated in Figure 73 [32]. The LCoS SLM can be employed as a diffractive device to reconstruct images from computer-generated holography [185], with applications in different communication purposes like in indoor visible light communication systems [186].

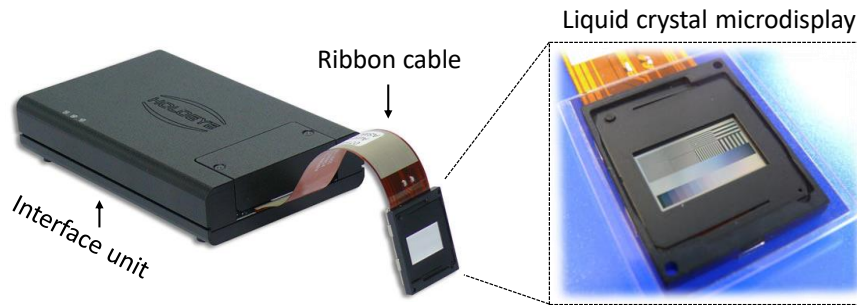


Figure 73. LCoS SLM Pluto phase modulator from Holoeye® 2018 Holoeye Photonics AG.

As aforementioned, LCoS displays have been gaining significant recognition as promising micro-displays for various types of SLM applications. Similarly, they retain attractive and significant features, such as high spatial resolution and light efficiency [187]. Due to this, they have been applicable in a plethora of optical contexts such as communication, reconfigurable interconnects [188], storage [189], diffractive optics [190], metrology [191], and quantum computing [192]. They are also applicable in the waveshaper technology for optical signal processing and monitoring [193]. In addition, LCoS can be seen as a cost-effective solution due to its ability to be flexibly programmed. This helps in supporting a number of additional functions like group delay ripple compensation, wavelength filtering, and chromatic dispersion compensation. Besides, it can aid in ensuring variable attenuation for individual wavelength channels as well as output ports. Consequently, the LCoS device offers a promising solution for the wavelength selective switch (WSS) [189].

The LCoS micro-display SLM has a good implementation background in the WSS systems. Its employment in the WSS system core component can be attributed to a number of advantages such as larger spatial bandwidth, more port availability, enhanced resolution, as well as system miniaturization. The WSS systems have been also exploited in ROADM WDM optical networks. It has been observed that ROADM is one of the promising schemes that can be employed to improve the traffic capacity of the existing and future telecommunication systems [189] [194]. Moreover, in

communication networks, the ease of adding or dropping the wavelength is essential. They can ensure effective information access or re-routing to another appropriate path in the network. It should be noted that WSS is the ROADM sub-system that has been extensively employed in optical switch applications. In addition, micro electro-mechanical systems (MEMS) [195], and WSS based on LCoS [196] have been commercialized for different applications. Also, WSS by means of LCoS operates on the principle of *disperse-and-select*, in which the inward bound WDM channels are dispersed into a distinct wavelength channel, and subsequently relayed by LCoS through programmable grating patterns. This is in an attempt to facilitate an add and drop function. It is envisaged that the next generation ROADM will hold different attractive features such as directionless, colorless, and contentionless in order to improve system performance [189].

LCoS technology can also be employed in flex-grid that has been considered as the major feature for the next generation networks [189] [197]. As the traditional fixed-grid with 50 GHz spacing standardized by the International Telecommunication Union (ITU) Telecommunication Standardization Sector (ITU-T) possesses a number of challenges. The fixed-grid has been observed to bring about the optical spectra being inefficiently used. Besides, it constraints the system transmission capacity considerably. On the other hand, the flex grid implementation enables the use of different modulation formats and their coexistence on a shared infrastructure. They can also be densely and efficiently multiplexed, which aids the optical networks, not only to extend the reach but also the per-channel bit rate. It has also been envisaged that the implementation of WSS and SDM will significantly help further in extending the network reach and capacity [189].

In the present study, SLM LCoS technology will be used as an SLM framework with application in systems with MCF. By allowing to improve alignment and excite different cores of an MCF, this framework can contribute to the impairment mitigation in the system optical path, which can relax the digital signal processing (DSP) equalization requirements of the SDM system [5] [198] [199]. Furthermore, its use as a flexible platform for feeding photonic integrated processors was also explored for the characterization/test of PIC, with results presented for its implementation as a parallel implementation of the Haar transform (HT) image compression algorithm [32] [63] [64].

5.2 SLM framework methodology

The SLM framework methodology can be described by three main blocks: i) the implemented CGH methods to generate the hologram; ii) SLM framework setup implementation; and iii) the experimental results obtained from the CGH.

5.2.1 CGH implemented methods

Different algorithm approaches have been proposed in the literature to overcome the problem of accurately design an interference element to transform a given light distribution into another expected one (the hologram). A variety of techniques such as iterative Fourier transform algorithm (IFTA) [5] [200]–[202]; linear Fourier transform (i.e., linear phase mask) [5] [32] [64] [203]; simulated annealing [204]; and Gerchberg-Saxton algorithm [205] have been explored for the calculus of the numerical interference patterns to generate the holograms (CGH).

Due to the intensive computational requests and high power-loss (up to 9 dB [181]) associated with the implementation of the simulated annealing and Gerchberg-Saxton algorithms, these approaches were not implemented in our framework. To realize and test the proposed SLM framework three main techniques were implemented and tested:

- i) iterative Fourier transform algorithm (IFTA);
- ii) linear phase mask;
- iii) iterative optimization of the CGH.

Complex patterns can be generated with the IFTA based method [200] [201], with additional computational cost (compared to linear phase mask). Linear phase mask can be implemented to generate relatively simple patterns. Further optimization can be achieved with iterative optimization algorithm approaches as presented in [32] [63]. This method delivers a simplified solution based on the implementation of a linear phase mask generation and a new iterative algorithm experimentally driven for CGH effective optimization.

All algorithms were developed and implemented in Matlab[®] [165].

5.2.1.1 Iterative Fourier transform algorithm

The method implemented to generate optimized holograms based in the IFTA technique can be described by the steps listed below:

- i) load the image (i.e., expected hologram to be generated) as the initial field (I_1) to calculate the phase mask;
- ii) calculate the Fourier transform of I_1 , $H = fft(I_1)$;
- iii) calculate the inverse Fourier transform of H , $I_2 = ifft(e^{i\angle H})$,
- iv) iterative verification of constraints in the spectrum domain, i.e., for root mean square error (RMSE) $\leq 10\%$ or until a maximum number of 1000 iterations, repeat steps (ii) and (iii);
- v) the optimized phase mask is given by $\angle H$ (the phase component of H), and the simulated digital hologram by I_j , where j is the total number of iterations to achieve the established constraints.

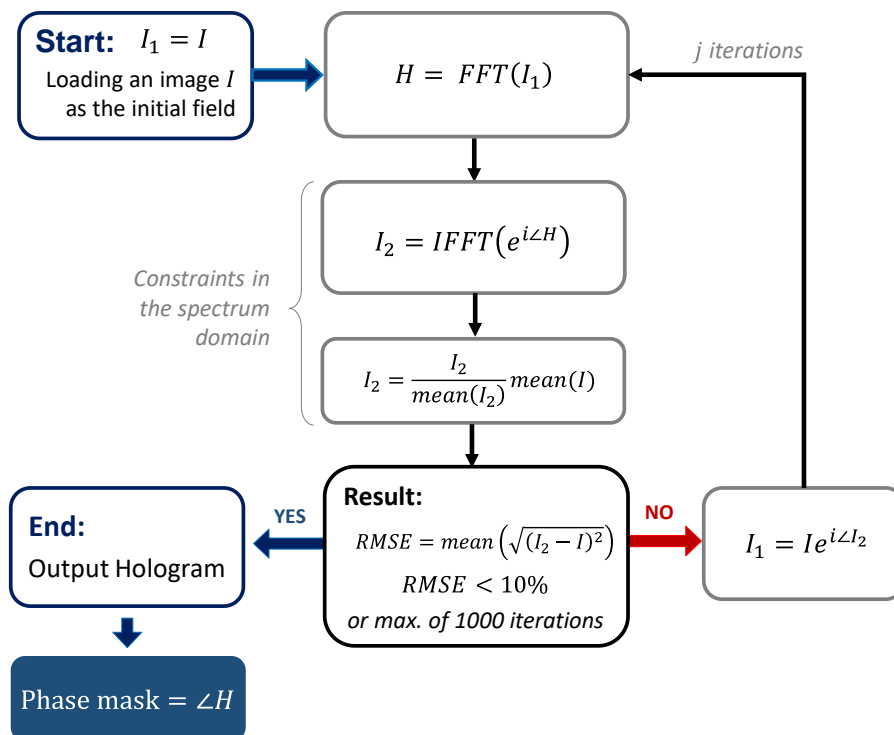


Figure 74. Block diagram of the IFTA. The final optimized phase mask to apply to the SLM is given by the phase component of H , i.e., $\angle H$.

Further details of the implemented algorithm are described in the block diagram presented in Figure 74.

5.2.1.2 Linear phase mask

A linear phase mask can be described as a numerical information transformation (in the Fourier domain) of the input function of interest [180], which allows it to be introduced into the optical system through an SLM. The necessary calculations to achieve the linear phase mask are based on the Fourier optical principles presented in [180]. Thus, CGH is obtained with a linear phase mask calculated in the frequency domain as described in equation (33), where c_x and c_y are the horizontal and vertical tilt parameters, respectively; and f_x and f_y are the components of the spatial frequency vector corresponding to the image to be generated in the horizontal and vertical axis, respectively.

$$M(f_x, f_y) = -2\pi(c_x f_x + c_y f_y) \quad (33)$$

The mask transfer function to be sent to the SLM is given by $H_{mask} = M(f_x, f_y) \bmod 2\pi$, ensuring that the phase values are set in the range of $[-\pi, \pi]$.

A collimated Gaussian beam with a transverse profile S_{in} is imaged into the SLM via a lens. S_{in} describes the signal of the input beam, see equation (34).

$$S_{in} = \exp\left(-\left(2\frac{x-x_0}{w_x \log(\sqrt{2})}\right)^2 - \left(2\frac{y-y_0}{w_y \log(\sqrt{2})}\right)^2\right) \quad (34)$$

Where (x_0, y_0) provides the horizontal and vertical position and (w_x, w_y) the width and the height of the beam, respectively, as depicted in Figure 75.

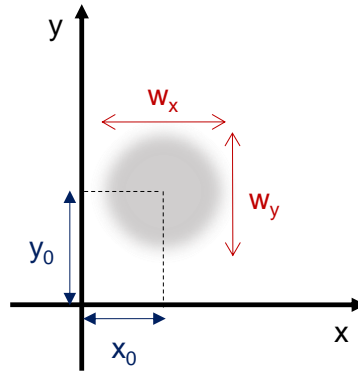


Figure 75. Diagram in Cartesian coordinate system describing the parameters (x_0, y_0) and (w_x, w_y) used for the estimation of the input beam S_{in} .

With the adoption of the Fraunhofer approximation, the Fourier transform is produced at the SLM plane, $fft(S_{in})$. Afterward, the subsequent illumination profile is multiplied with the phase mask, $e^{iH_{mask}}$. The resultant signal is then Fourier transformed via the second lens by means of an inverse Fourier transform to achieve the estimated output signal S_{out} , which can be defined by equation (35).

$$S_{out} = ifft\left(H(fft(S_{in}))\right) \quad (35)$$

A graphical user interface (GUI), named *SLM-Mask*, was also developed to test different masks to be applied to the SLM device [64], see Figure 76. Mathematically, the inherent ability of a converging lens to perform 2D Fourier transforms at its focus was used [180]. The different masks were determined by adjusting different available parameters. For the *Input beam* GUI panel the following input parameters are available: i) horizontal position (x_0); ii) vertical position (y_0); iii) width of the beam (w_x); iv) height of the beam (w_y), see GUI panel *Input Beam* in the Figure 76.

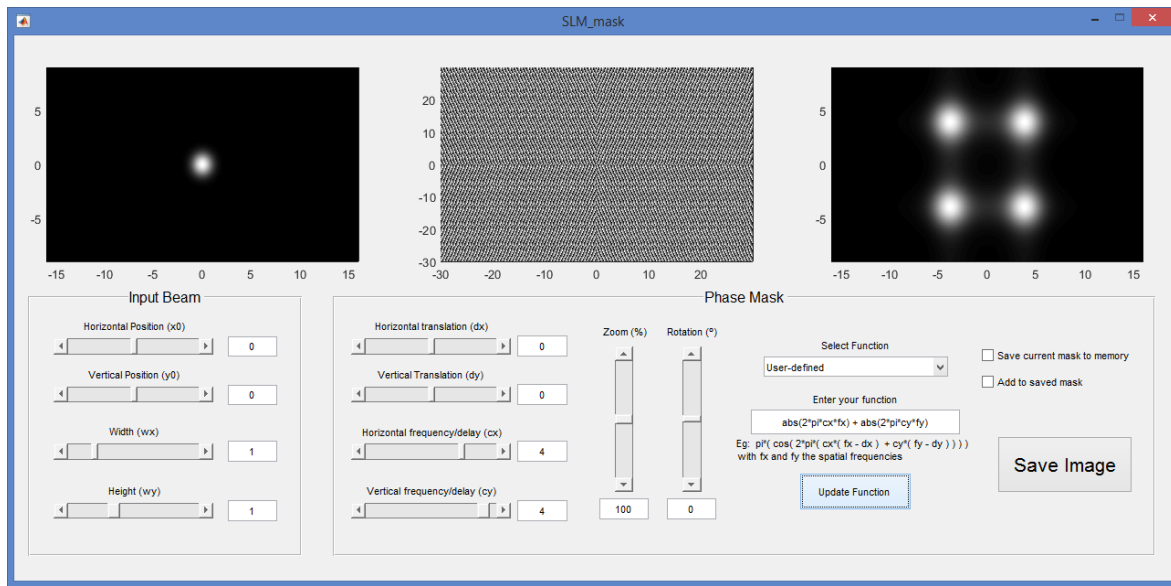


Figure 76. GUI *SLM-mask* developed to generate different phase masks to apply to the SLM [64].

The *Phase Mask* GUI panel retains the corresponding input parameters: i) horizontal translation (d_x); ii) vertical translation (d_y); iii) horizontal frequency delay (c_x); iv) vertical frequency delay (c_y); v) percentage of zoom (%); vi) rotation in degrees ($^\circ$); and vii) selection of three possible input functions, i.e., sinusoidal (36), linear (33), or defined by the user (*user-defined*).

$$M(f_x, f_y) = \pi \sin \left(2\pi (c_x f_x + c_y f_y) \right) \quad (36)$$

The option to save or replace the phase mask file is also made available, see the GUI panel *Phase Mask* in Figure 76.

5.2.1.3 Optimization of the CGH

In an effort to realize the hologram that better replicates the expected signal is estimated the hologram of the beam through the image phase-only information of the generated hologram. For the linear phase CGH method was developed an iterative optimization algorithm feed by experimental data from the generated hologram, collected with an IR camera.

Since a phase-only SLM does not allow the inverse Fourier of the desired pattern to be addressed into the far-field and replicated into the resultant distribution of amplitude and phase on the SLM directly. It is quite demanding to generate a CGH, which guarantees for the light to be spatially modulated with the required accuracy and resolution. To address these challenges and obtain the desired hologram with an error factor $\delta \leq 10\%$, an iterative algorithm to optimize the generation of the linear phase mask was implemented. Also, an error factor threshold was set, so as to prevent an infinite loop in the implemented optimization algorithm, while ensuring that the output result has an accuracy $\geq 90\%$.

The algorithm was implemented to generate a hologram that replicates the output of the four waveguides (WG) of an optical chip for data compression purposes [32] [56] [63]. A hologram of four beams was calculated by a phase-only superimposition of four independent holograms generated by equation (33). Then, the corresponding linear transformations in the Fourier domain provided in equations (37) and (38) were applied [32] [63].

$$H = \angle(e^{iH_1} + e^{iH_2} + e^{iH_3} + e^{iH_4}) \quad (37)$$

$$H_1 = \exp\left(i2\pi(c_{x1}f_x + c_{y1}f_y)\right) \quad (38)$$

The block diagram of the employed algorithm is given in Figure 77, and the major steps of the algorithm are enumerated as follows [32]:

- i) generate a 1st linear phase mask to produce the expected initial field based on equation (37);
- ii) initially set the four coefficients a_{1-4} to 1, from:

$$H = \angle(a_1 e^{iH_1} + a_2 e^{iH_2} + a_3 e^{iH_3} + a_4 e^{iH_4});$$
- iii) acquire the replay field from the hologram generated by SLM (I_{SLM}) with a camera and feed this data to the algorithm;
- iv) calculate the difference between the hologram generated and the initial field expected, defined as error factor: $\delta = |I_{SLM} - I_1| \leq 0.1$;

- v) if the condition $\delta \leq 0.1$ is not satisfied, the steps (ii) to (iv) are repeated by iteratively adjusting the values of a_{1-4} to compensate for the error factor (δ).

The iterative adjustment of a_{1-4} coefficients were based on the mathematical optimization described by the Lagrange multipliers method [206].

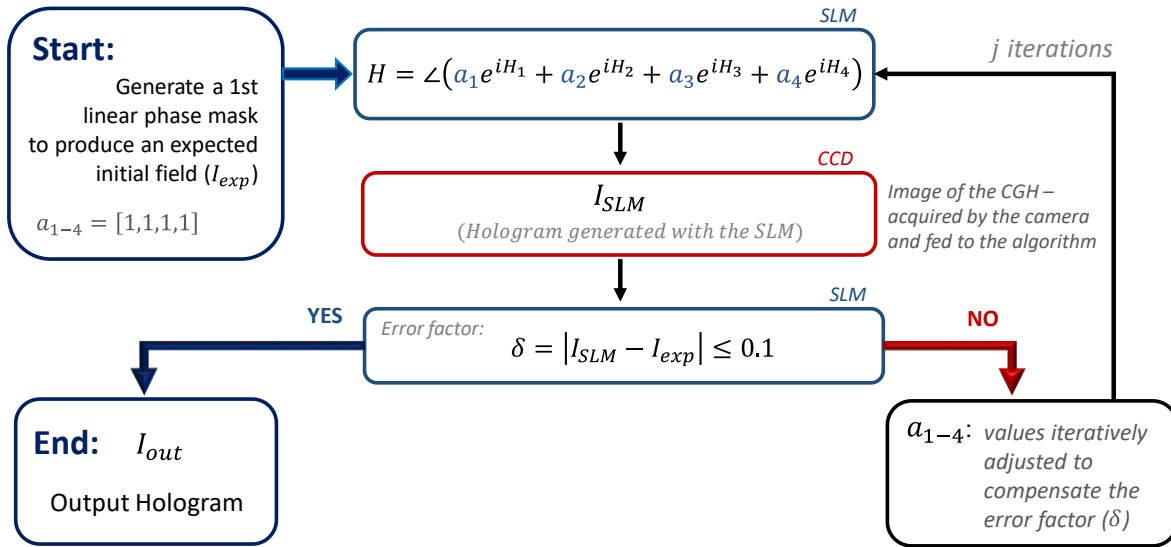


Figure 77. Block diagram of the algorithm applied for the optimization of the CGH [32].

The developed algorithm and scripts were implemented in Matlab[®], and are capable of controlling both SLM, as well as camera hardware. Also, the error factor (δ) is defined to quantify the generated hologram deviation from the optical chip expected output [32] [63].

5.2.2 SLM framework setup implementation

A first testing approach of the SLM framework was performed with a visible SLM, used for testing and generation of images and small videos. The data to be transformed (in the Fourier domain) is introduced into the optical system by the SLM, with an appropriate DOE to generate the expected function of interest. IFTA was the method used to calculate the best interference pattern to produce the hologram (Figure 78-C). The in-line transmission hologram setup consisted of a red laser

($\lambda = 634 \text{ nm}$; $P = 10 \text{ mW}$) and a visible transmissive LC SLM, model Holoeye LC2002 [207], see Figure 78-A,B.

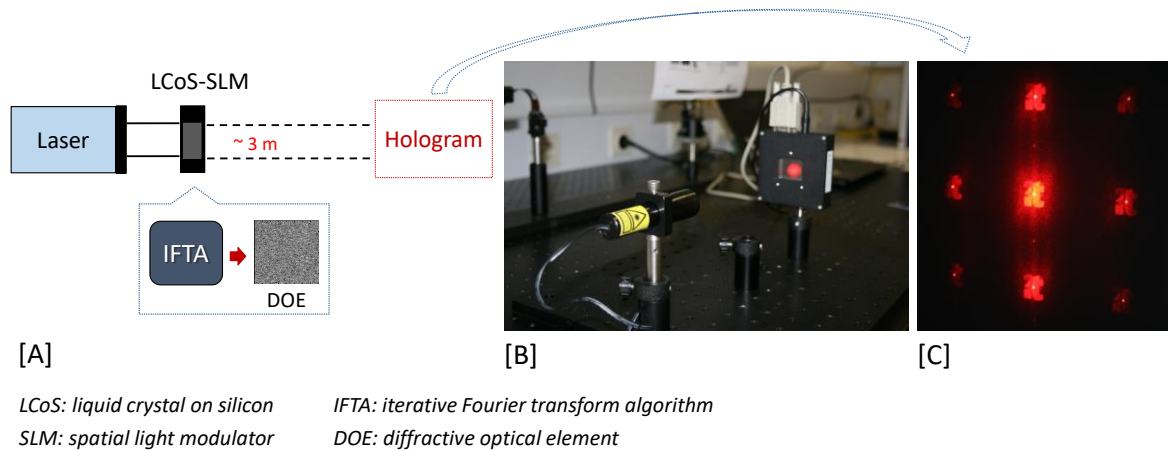


Figure 78. [A]: In-line transmission hologram setup, composed by a red laser ($\lambda = 634 \text{ nm}$; $P = 10 \text{ mW}$) and a visible SLM (Holoeye LC2002). [B, C]: Photographs of the setup and generated hologram, respectively.

This setup allowed a first experimental test of the digital hologram generation and the calculus of the DOE to generate the hologram based on the IFTA method. Matlab[®] scripts were developed to control the SLM and compute the CGH method.

Thereafter, was implemented a reflective LCoS SLM with an operation range in the infrared (IR) typical telecom wavelength range of 1400 – 1700 nm. A calibration process was performed to set the SLM for a linear 2π phase distribution over all 8-bit gray level in order to ensure a stable (as possible) phase response. For that purpose was implemented a path interferometer setup and recorded the intensity distribution of the produced interference pattern with a near-IR camera. The setup was composed by an IR laser ($\lambda = 1550 \text{ nm}$); a polarization controller; two lenses (AC254-050-C-ML, AR coating 1050 - 1620 nm) L_{s1} and L_{s2} with a focal length of 75 mm and 250 mm, respectively; a neutral density filter to avoid saturation in the acquisition (by the camera); and a near-infrared (1460 - 1600 nm) camera (sensing area: $6.4 \times 4.8 \text{ mm}$, resolution: 752×582 , pixel size: $8.6 \times 8.3 \mu\text{m}$) to capture the replay field of the hologram produced. Further details about the setup are depicted in Figure 79.

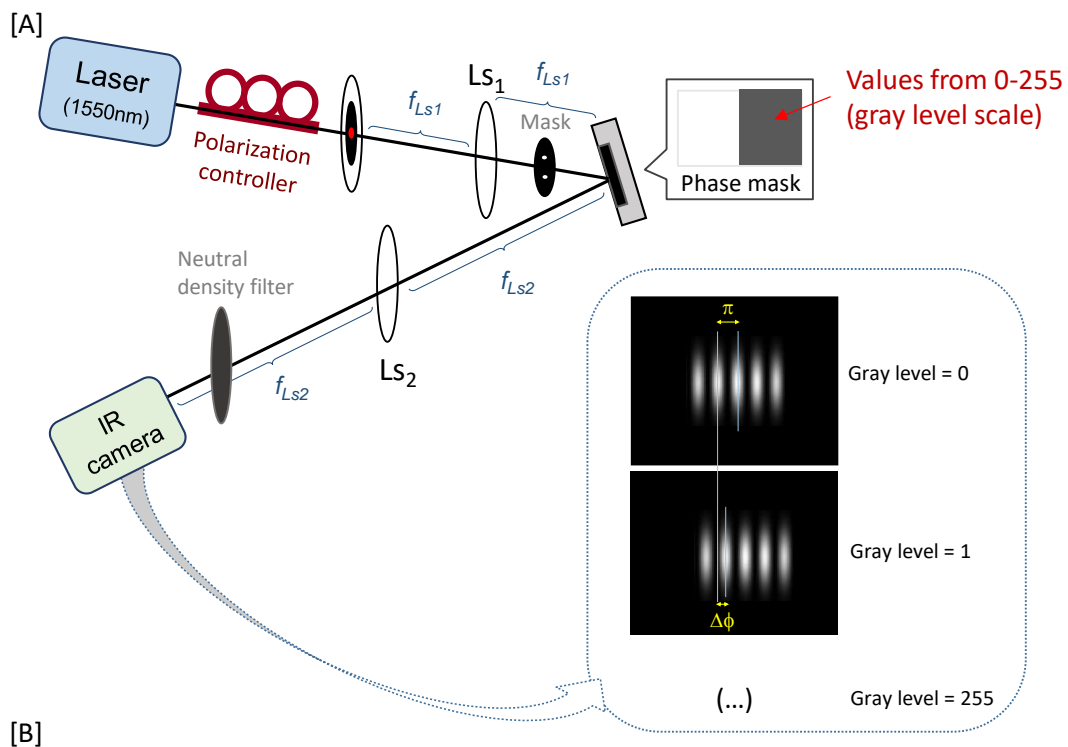


Figure 79. [A]: Diagram of the SLM calibration setup for a linear 2π phase distribution, i.e., generating the phase mask for a 0 to 255 gray level. [B]: Photographs of the setup.

The two holes mask (of diameter 3 mm separated by 7 mm) generates two coherent beamlets, which hit the right and the left part of the vertically divided LCoS panel (centered in the horizontal dimension). A total amount of 256 phase masks were introduced in the SLM, composed by a white and gray face ranging from 0 to 255 gray level, as depicted in Figure 80.

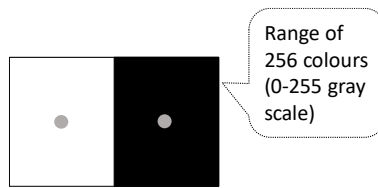


Figure 80. Laser beamlets loaded on the LCoS SLM panel.

The analysis of the results consisted in the sine fit of the interference patterns obtained from each hologram and the calculus of the phase shift from each gray level, i.e., the distance between two fringes maximums corresponded to π , and the deviation from maximums of each hologram generated providing the corresponding phase shift distribution, see Figure 79. The results obtained are presented in Figure 81.

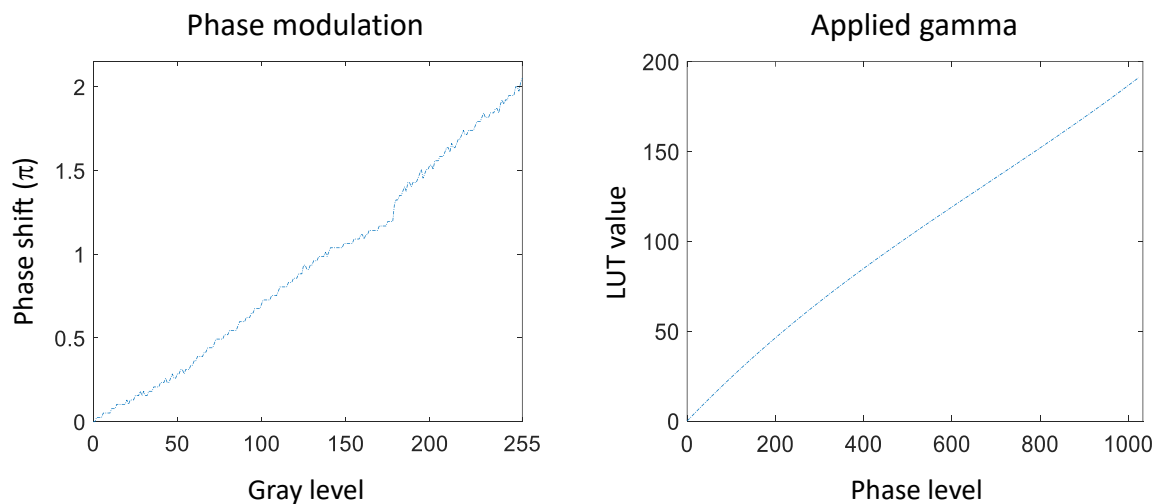


Figure 81. Phase modulation obtained for the linear 2π phase distribution and corresponding lookup table (LUT) values of the gamma curve.

The lookup table (LUT) values obtained from the calibration were provided to the SLM for gamma calibration/correction and white/black balance adjustment.

5.3 Experimental CGH results

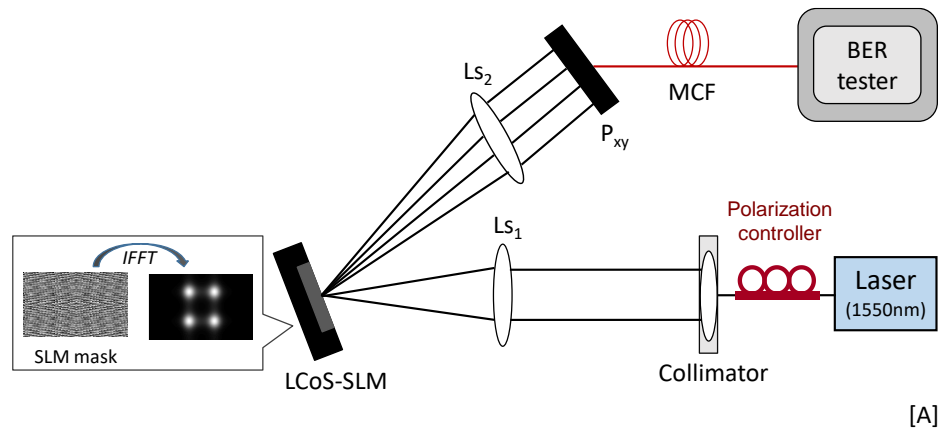
The employed SLM is a reflective LCoS phase-only type, model PLUTO-TELCO-012, operating within the wavelength range of 1400 - 1700 nm. Additional specifications are an active area of $15.36 \times 8.64 \text{ mm}^2$, a pixel pitch of $8.0 \text{ }\mu\text{m}$, a 92% fill factor, and 80% reflectivity [208].

Two different setup arrangements were implemented to create CGH for SDM (e.g., MCF) and PIC applications, presented in sections 5.3.1 and 5.3.2, respectively.

5.3.1 SLM framework for SDM applications

Setup alignments were carried out, using a red laser of 637 nm (power 70 mW, SM Fiber-Pigtailed Laser Diode), a collimator, two lenses (L_{s1} and L_{s2}), a charge-coupled device (CCD) image sensor, and the LCoS-SLM. After the alignments, an MCF of 10 m of length and a bit-error rate (BER) tester was introduced in the setup, as depicted in Figure 82.

The MCF contained four cores arranged in a quadrangular-lattice pattern, with a side length of $36.25 \text{ }\mu\text{m}$ and attenuation @1550 nm of 0.45 dB/km. The non-return-to-zero (NRZ) signal was generated by a pattern generator (Agilent N4901B) using a pseudorandom binary sequence (PRBS) 231-1. The signal was injected into the tunable direct modulator laser to create 10 Gb/s optical signal. After the MCF, the signal was detected by the avalanche photodiode (APD) receiver inside of the small form-factor pluggable (SFP) transceiver. BER measurements were carried out for each core of the MCF, through fan-out single core fibers structures connected to the MCF. A BER of 1.2×10^{-3} comprised the worst measure attained and consequently defined as the system BER performance. The results showed a transmission error-free below the BER limit of 3.8×10^{-3} (7% hard-decision FEC) threshold [209] [210]. Thus, the SLM framework was able to properly function as a spatial coupling interface between the SLM generated pattern and the MCF cores. The platform flexibility allows an easy adjustment of the generated phase mask (CGH), contributing to an effective dynamic optimization of the MCF fiber transmission.



LCoS: liquid crystal on silicon *IFFT: inverse fast Fourier transform*
SLM: spatial light modulator *MCF: multicore fiber*

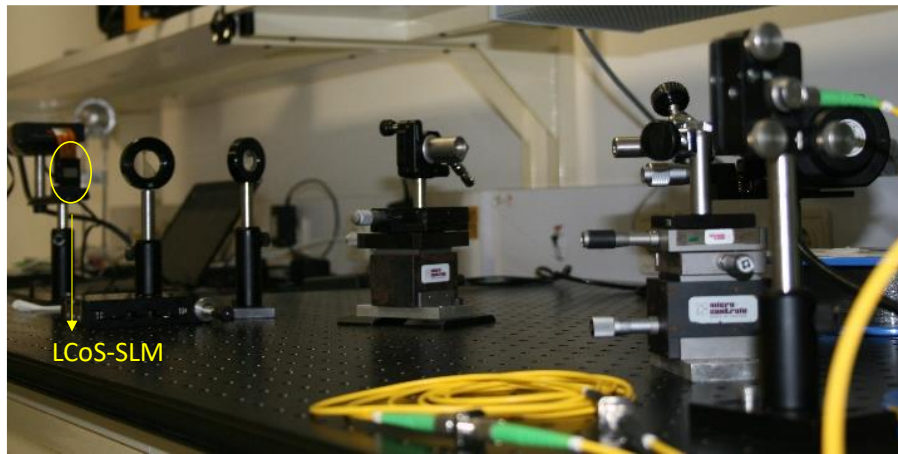
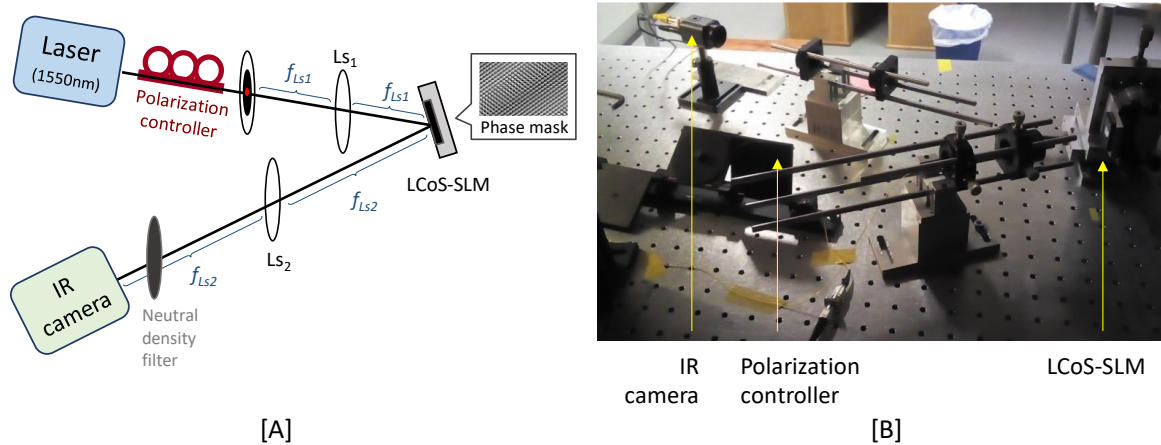


Figure 82. [A]: Setup diagram of the SLM platform for MCF applications, with Ls_1 and Ls_2 lens and positioner P_{xy} . [B,C]: photographs of the corresponding setup.

5.3.2 SLM framework for PIC applications

In an effort to eliminate the phase distortion and enable the full Fourier transform scaled by the focal length (f) factor, the optical system was designed based on the $4f$ system configuration. This forms the basis of a low distortion optical system.



LCoS: liquid crystal on silicon SLM: spatial light modulator IR: infrared

Figure 83. [A]: Hologram reconstruction scheme using an infrared (IR) laser of 1550 nm, a polarization controller, lens Ls_1 and Ls_2 , an LCoS-SLM, and an IR camera. [B]: Photography of the implemented setup.

The setup comprises two lenses (AC254-050-C-ML, AR coating 1050-1620 nm) Ls_1 and Ls_2 with a focal length of 75 mm and 250 mm, respectively; a polarization controller; an IR laser ($\lambda = 1550$ nm); a neutral density filter, to prevent saturation in the camera acquisition; and a Near-Infrared (1460-1600 nm) camera (sensing area: 6.4×4.8 mm, resolution: 752×582 , pixel size: 8.6×8.3 μm) for capturing the generated hologram. Further details about the setup are depicted in Figure 83 [32] [63].

5.3.2.1 Results and discussion

The hologram was generated in an attempt to create the beam profile in the first order of diffraction when being displayed on the SLM. The CGH should reproduce the four WG outputs of the PIC implementing the HT [32] [56], see Figure 84. The measurements of the distance between the four

WG at the end of the two-level HT network are $d_1 = 241.3 \mu\text{m}$; $d_2 = 278.6 \mu\text{m}$; and $d_3 = 248.0 \mu\text{m}$ (using a Leica microscope, DM-750M; 1CC50-HD, and an objective of 20 \times , HI Plan EPI, 20 \times /0.40) [32], see Figure 84. Further details about the InP integrated approach for the realization of the HT can be found in section 3.1.

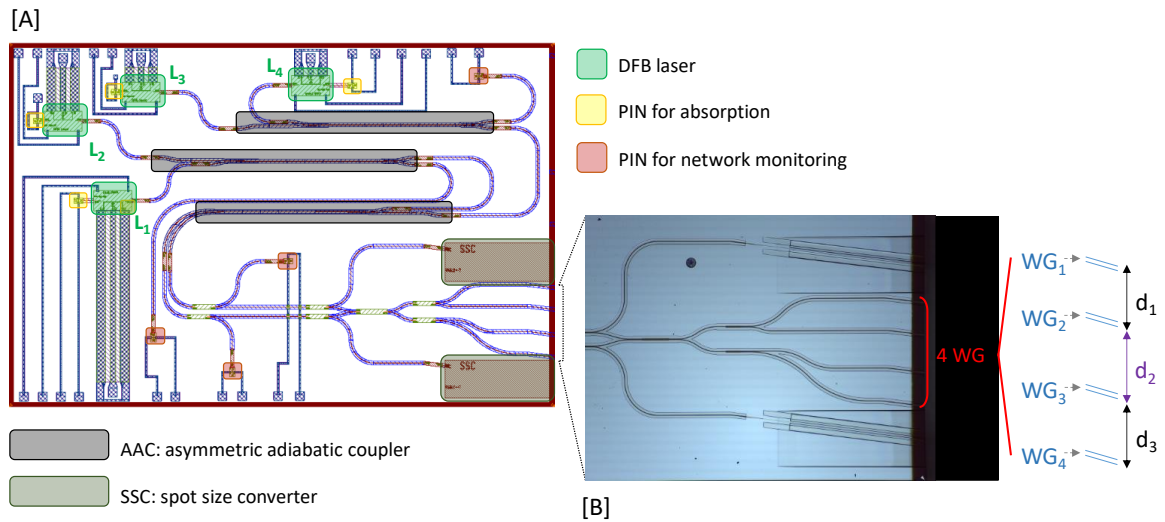


Figure 84. [A]: Design architecture of the PIC for data compression based on HT. [B]: Measurements of the distance between the four WG at the end of the two-level HT network of the PIC [32].

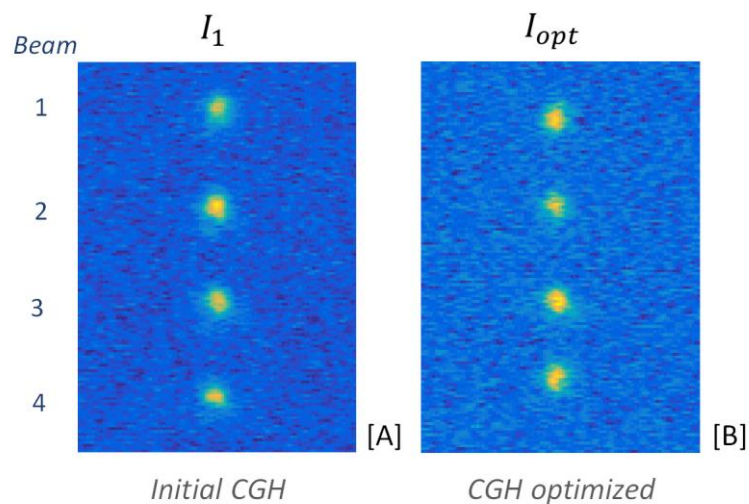


Figure 85. Replay field of the hologram acquired by the IR camera for the: [A]: initial hologram; and [B]: optimized hologram.

The obtained image from the hologram replay field generated with the initial (I_1) and optimized (I_{opt}) CGH are presented in Figure 85 [32] [63]. The analysis of the obtained replay field images are defined by the steps described below:

- i) calculate the intensity integration of the image matrix, i.e., the sum of all elements along each line of the image matrix, depicted as S_{raw} ;
- ii) application of the Savitzky-Golay (SG) filter to smooth the intensity integration signal obtained in step (1), depicted as S_{SG} ;
- iii) implementation of a first-order Gaussian fit curve to the filtered signal depicted as *Gauss fit*;
- iv) extraction of Gaussian parameters to calculate the distances between the four beams (obtained from the CGH) and compare with the expected results (d_1 , d_2 , and d_3 from the optical chip).

The signal smoothing of the intensity integration was obtained with the Savitzky-Golay filter, which can be characterized by a generalized moving average with filter coefficients determined by an unweighted linear least-squares regression and a polynomial model of specified degree [165] [211]. The parameters applied in the filter were a polynomial order 9 and a window length 19.

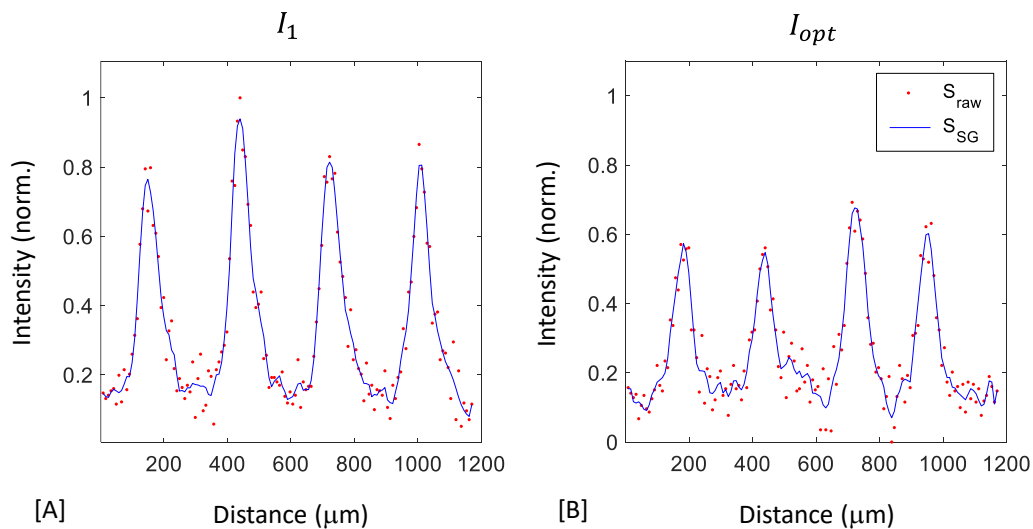


Figure 86. Integrated intensity from the replay field image S_{raw} (red dots), and corresponding smoothing with Savitzky-Golay (SG) filter S_{SG} (blue line). [A]: initial CGH; and [B]: optimized CGH.

Results after steps (1) and (2) are depicted in Figure 86, and after the Gaussian curve fitting application presented in Figure 87.

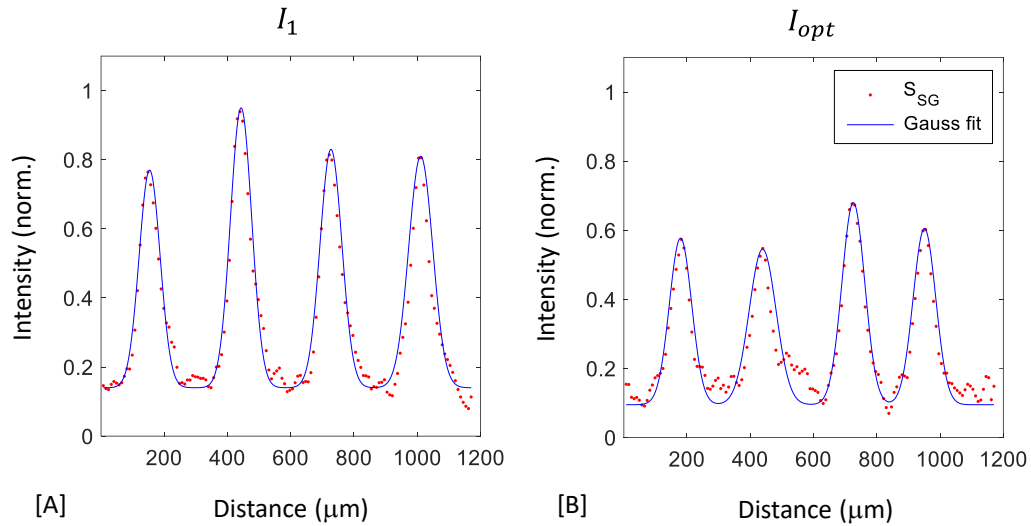


Figure 87. Gaussian fit (*Gauss fit* – blue line) of smoothed integrated intensity signal from the replay field image (S_{SG} – red dots) for [A]: initial CGH; and [B]: optimized CGH.

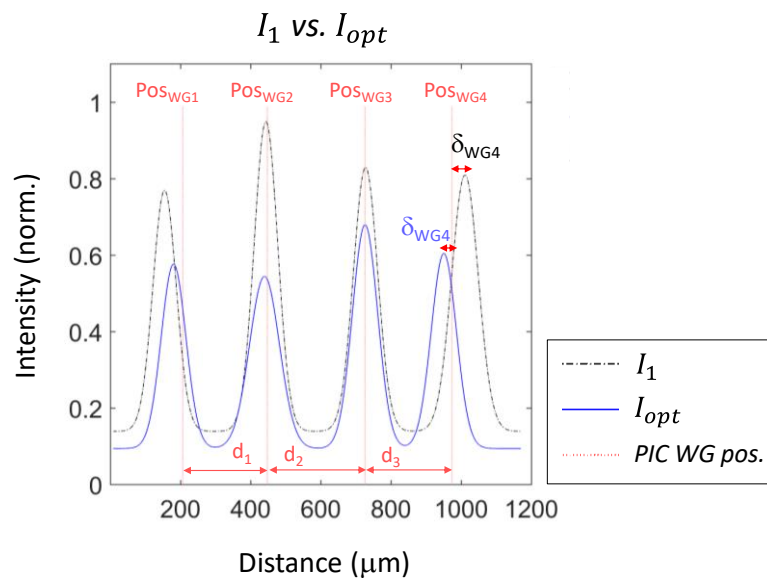


Figure 88. Overlap of the Gaussian fit results attained for the initial CGH (I_1) and optimized CGH (I_{opt}), and the expected four WG positions (POS_{WG}) from HT PIC. The error factor for initial (black) and optimized (blue) CGH implementations associated with the WG_4 position are indicated (δ_{WG4}) to illustrate the measuring process.

In Figure 88 is depicted the overlap of the Gaussian fit results of the integrated intensity signal from the replay field attained for the initial CGH (I_1) and optimized CGH (I_{opt}), and the expected four WG positions of the HT PIC. To illustrate the error factor measuring process, it is indicated δ_{WG_4} for the WG_4 position, under the initial and optimized CGH implementation.

The position of the four beams from the CGH implementation was calculated from the center position of each beam profile, given by the Gaussian fit coefficient, which corresponds to the position of the center of the peak. The coefficients were obtained with 95% confidence bounds.

The deviation values (δ) are calculated by the difference (in percentage) of the distances between the attained position of the center peak and the expected output PIC WG ports positions/distances. The error factor (δ_{WG_k}) formulation syntax is presented in equation 41, by applying the generic standard deviation calculus (std_{WG_k} , see equation 40) in percentage. Where $\overline{Pos_{WG_k}}$ indicates the mean between the expected PIC WG position (Pos_{WG_k}) and the attained beam position from the CGH implemented ($Pos_{CGH_{WG_k}}$), see equation 39; with k as the index corresponding to the four different WG positions (as for the HT PIC).

$$\overline{Pos_{WG_k}} = \frac{Pos_{WG_k} + Pos_{CGH_{WG_k}}}{2}; \quad k = 1, 2, 3, 4. \quad (39)$$

$$std_{WG_k} = \frac{1}{N-1} \sqrt{\sum_{i=1}^N |S_{Pos_i} - \overline{Pos_{WG_k}}|^2}; \quad (40)$$

$$S_{Pos_i} = [Pos_{WG_k}, Pos_{CGH_{WG_k}}]; \quad N = 2.$$

$$\delta_{WG_k}(\%) = \frac{Pos_{WG_k} - std_{WG_k}}{Pos_{WG_k}} 100; \quad k = 1, 2, 3, 4. \quad (41)$$

The deviation values (δ) of the generated hologram (i.e., initial I_1 and optimized I_{opt} holograms), when compared with the expected output of the optical chip (i.e., $Pos_{WG_{1-4}}$, see Figure 84) are presented in Table 11.

Table 11. Error Factor (δ_{WG}) values for HT PIC four output WG positions.

	Initial CGH (%)	Optimized CGH (%)
δ_{WG1}	17.74	8.95
δ_{WG2}	0.64	1.28
δ_{WG3}	0.14	0.00
δ_{WG4}	2.68	1.70

An error factor $\delta \leq 18\%$ was obtained for the initial CGH and $\delta \leq 9\%$ for the final optimized CGH. Though, further optimizations can be attained by lowering the error factor threshold of the CGH optimized algorithm (set for $\delta \leq 10\%$, see section 5.2.1.3).

Power measures of the beams were performed through the integration of intensity profiles, i.e., the integral of the Gaussian fit (see Figure 88). In Table 12 is presented the integration of the intensity profiles for each beam when applying the initial and optimized CGH. Corresponding mean and standard deviation values of the beam profile for both cases are provided.

Table 12. Integration of the intensity profiles for the four beams.

Beam	Initial CGH (a.u.)	Optimized CGH (a.u.)
1	6.30	5.12
2	8.21	5.78
3	7.18	6.37
4	7.69	5.51
Mean	7.35 ± 0.81	5.69 ± 0.52
Std (%)	11.07	9.22

Std: standard deviation. The four beams are numbered from 1 to 4 from top to down, as depicted in Figure 85.

An improved hologram is achieved with the optimization of the linear phase mask CGH, i.e., with a reduction of up to 9% in the error factor (between initial and optimized holograms), see Table 11. Nonetheless, the loss of 1.1 dB identified on the mean beam power for the optimized CGH, an

improved equalization between the beams was observed, with a 2% reduction in the standard deviation, see Table 12.

The phase mask that replicates the expected output of the optical chip can be used to multiplex/demultiplex the obtained result. Furthermore, a phase mask, which addresses the HT operations can also be applied to invert the compression induced by the HT (optically implemented in the chip with the three asymmetric couplers network).

5.4 Chapter remarks

LCoS SLM technology implementation has been gaining importance in different optical systems applications, namely telecom with the development of high capacity optical components in system functionalities as switching, multiplexing and demultiplexing, and optical signal processing. Taking advantage of spatial modulation properties, a proof of concept on the implementation of a new SLM based flexible coupling platform was provided. The implementation of the SLM flexible framework was experimentally demonstrated for SDM systems [5] [64] [202] and PIC characterization/testing [32] [63]. Optimized methodologies to generate the CGH were developed and implemented. Furthermore, an SLM phase mask generator GUI was developed to test different phase masks. Main results include: i) signal recovery for an optical SDM system, i.e., the use of the SLM to efficiently excite the different cores of an MCF [64]; and ii) optimized CGH implementation to feed/receive the output of an optical chip for data compression based on the HT [32] [63].

This SLM flexible framework can positively contribute to the development of multi-dimensional optical communication systems, by providing a versatile optical method to facilitate a dynamic optimization of MCF transmission (e.g., by improving the setup alignment and excitation of different cores in MCF), and to provide a more flexible and robust optical methodology to assess/test PIC (e.g., offering a proof of concept of the PIC HT operation).

Chapter 6

Conclusion and future work

Next generation optical systems requirements can highly benefit from optimized photonic integrated solutions. Integrated photonics appears as a promising solution for the current demand for flexibility and reconfigurability in optical systems and telecommunications networks. PIC-based optical systems can offer an efficient and cost-effective solution to data transmission increasing demands. The work developed in the scope of this thesis addresses relevant components in PIC research, such as design, packaging, and testing.

Optical signal compression plays an important role in the fast processing/storing of large amounts of bandwidth-demanding data, with data compression emerging as a noteworthy technique to release additional bandwidth. The integrated implementation of optical transforms to compress/decompress data processing is advantageous. By applying an optical transform architecture into a PIC, compression can be attained at a lower cost, less power consumption and high data rate due to an all-optical processing implementation. Capitalizing on HT benefits, such as simple design, fast computation power, efficiency, and its straightforward implementation by optical planar interferometry, this optical transform was selected to realize integrated solutions for data compression applications.

A design of optimized structures to implement an all-optical transform architecture for data compression entails the first major contribution reported in the thesis. Taking advantage of silicon nitride integrated platform merits and established foundry PDK [90], an optimized PIC design solution in Si₃N₄ based platform is realized. The design of the developed integrated approach comprises a two-level HT network for compression, and a switching network as a framework that supplies all logical inputs of the HT network for testing/characterization purposes. This study provides optimized design models for the 2×2 MMI BB and the 1×2 MMI BB, to realize the HT proposed PIC approach. The best optimized BB solution proposed, attained an overall excess loss and crosstalk metrics below 0.005 dB (under the required MMI operation mode for the realization of the 2D HT). A device footprint up to 1/4 and 1/3 lower than reported literature was accomplished under the 2×2 MMI BB and 1×2 MMI BB best-optimized design structures, respectively. Additionally, fabrication tolerances of BB operation modes were also guaranteed under the infrared C-band wavelength range, with an overall excess loss ≥ 0.05 dB. The comprehensive optimized design study achieved offers an important evaluation of the BB structures performance/behavior, to select the ones that best address the HT compression and switching networks under the Si₃N₄ integrated approach proposed. The implementation of the optimized BB structures and proposed networks for the HT completion is highly recommended to be manufactured as a future realization.

The second key contribution of this thesis comprises of the first experimental characterization of an InP-based PIC implementing an all-optical AAC network realizing the HT. The InP-based platform was chosen due to its excellent electro-optical properties allowing efficient light generation, detection, and guidance in a monolithic integrated circuit. The tunable operation capabilities of the implemented key BB deploying the HT, i.e., the AAC; were validated through simulation and experimental results. This allowed determining with acuity the different phases that enable the full cycle of the device's expected coupling ratios. The coupler characterization performed, provides a fundamental tool for the use of BB full coupling capabilities in optical processing implementations such as Haar wavelet transforms with applications in data compression. The experimental characterization of the PIC implementing the two-level HT network was also attained. Even though, the complexity of the optical chip and the difficulty to fully and independently monitor each of its components, the first experimental demonstration of an integrated all-optical two-level HT in an InP-based platform was successfully completed.

Furthermore, taking advantage of low-cost hybrid materials [65] with application in integrated photonics, the first implementation and testing of a potentially cost-effective 2D HT network for image compression in an organic-inorganic hybrid material are demonstrated, consisting in the third main contribution under this thesis. To better address the design/fabrication of the integrated structures under the hybrid material, a design optimization model is proposed based on the theoretical simulations and experimental results obtained. Through the implementation of the proposed design optimization model, under ideal theoretical conditions, an HT operation behavior improvement, of about 16 dB, is estimated at the output of the 2D HT network. Nevertheless, under this hybrid material, structure design optimizations should be conducted to decrease the device's footprint, presently up to 300 times higher than the best-optimized design achieved for the 2×2 MMI BB structure in the Si_3N_4 -based platform.

The fourth core contribution addresses Si_3N_4 integrated WG platforms with ultra-low propagation losses, which are essential for different optical system applications, e.g., high-Q resonators and narrowband photonic filters. Namely, integrated high-Q resonators tailor a paradigm shift in a variety of PIC applications, though accurate performance measurement of the resonators quality factor needs to be ensured. Under this requirement, a high-Q resonator measurement technique based on an RF calibrated MZI and Brillouin gain measurements, through Lorentzian fitting analysis was successfully attained. This research was enclosed in the development of a state-of-the-art sub-hertz fundamental linewidth photonic integrated Brillouin laser, capable of emitting light with a fundamental linewidth lower than 1 Hz, narrow enough to move demanding scientific applications to the chip-scale [62]. Future developments through resonator Q design engineering improvements are idealized, paving the way for engineered Brillouin high coherence integrated lasers disruptive applications, namely coherent communications, quantum communication/computing, and positional/navigation sensors.

Furthermore, a fifth major contribution entails the implementation of a low-loss Si_3N_4 -based integrated tunable lattice filter for dispersion compensation enabling the first real-time C-band transmission demonstration of 53.125 Gb/s PAM-4 over 40 km SSMF. The 10-stage lattice filter capable of tuning ± 500 ps/nm allowed to compensate up to three channels on a 100 GHz channel spacing over 40 km. This integrated solution showed to be promising to mitigate PAM-4 dispersion for multiple WDM channels while satisfying the strict OSNR requirements. Additional improvements can be expected in the next generation integrated filters by lowering the device insertion loss up to 4 dB and enable a 50 GHz grid WDM, through engineering design optimization. The foreseen optimization

approaches can include the use of fiber taper couplers on-chip, thickening of upper cladding, design of longer unit optical delay length and smaller filter FSR, and investigation of PZT tuning to further decrease loss and power consumption.

The sixth and final contribution presented under this thesis explored the spatial light modulation principle as a flexible platform with application in photonic integrated processors and spatial division multiplexing systems. SLM technology has been gaining importance in a wide range of optical systems applications, namely telecom with the development of high capacity optical components in system functionalities, multiplexing/demultiplexing, and optical signal processing. As technical and functional requirements of the PIC demand a thorough characterization and testing to provide an accurate prediction of the PIC performance, and current testing platforms can be expensive and have a lack of flexibility. By taking advantage of spatial light modulation operation principle, a proof of concept of a new soft-packaging flexible platform for photonic integrated processors and SDM systems was developed. The capacity of the SLM to dynamically reconfigure light was used to feed and/or receive information to the PIC and dynamically optimize the spatial coupling under MCF transmission systems. Experimental results of the SLM framework implementation in SDM systems and its potential use for PIC processors are demonstrated.

Looking forward, the SLM framework flexibility to dynamically re-generate digital masks, in a feeding loop process, i.e., by collecting the outputs of the PIC and re-adjust the applied digital mask, in order to obtain the optimized output, paves the way for a new product – a soft-packaging for highly complex PIC, named *PICpack*. From the expected framework benefits can be highlighted:

- i) the accurate coupling of light for a vast diversity of PIC systems, available for 2D and 3D packaging configurations;
- ii) the ability to reproduce optical transforms implemented in the PIC under testing;
- iii) the dynamic optimization of SDM optical systems.

Moreover, by allowing to solve 3D coupling light alignments effectively, without resorting to expensive complex optical infrastructures, an overall cost reduction under PIC testing technology/methodology is estimated.

Bibliography

- [1] J. He, R. A. Norwood, M. Brandt-Pearce, I. B. Djordjevic, M. Cvijetic, S. Subramaniam, R. Himmelhuber, C. Reynolds, P. Blanche, B. Lynn, and N. Peyghambarian, "A survey on recent advances in optical communications," *Computers & Electrical Engineering*, vol. 40, no. 1, pp. 216–240, Jan. 2014.
- [2] Ericsson, "Ericsson Mobility Report," 2018, Online: www.ericsson.com/mobility-report.
- [3] P. J. Winzer, "Spatial multiplexing in fiber optics: The 10x scaling of metro/core capacities," *Bell Labs Technical Journal*, vol. 19, pp. 22–30, 2014.
- [4] M. Ayyash, H. Elgala, A. Khreishah, V. Jungnickel, T. Little, S. Shao, M. Rahaim, D. Schulz, J. Hilt, and R. Freund, "Coexistence of WiFi and LiFi toward 5G: concepts, opportunities, and challenges," *IEEE Communications Magazine*, vol. 54, no. 2, pp. 64–71, Feb. 2016.
- [5] C. Pinho, A. Shahpari, I. Alimi, M. Lima, and A. Teixeira, "Optical transforms and CGH for SDM systems," in *18th International Conference on Transparent Optical Networks (ICTON 2016)*, pp. 1–4, 2016.
- [6] I. A. Alimi, P. P. Monteiro, and A. L. Teixeira, "Outage Probability of Multiuser Mixed RF/FSO Relay Schemes for Heterogeneous Cloud Radio Access Networks (H-CRANs)," *Wireless Personal Communications*, vol. 95, no. 1, pp. 27–41, Jul. 2017.
- [7] Grand View Research, "Photonic IC Market Analysis And Segment Forecasts To 2024," 2016.

- [8] Credence Research, "Photonic Integrated Circuits Market," Mar. 2016, Online: <http://www.credenceresearch.com/report/photonic-integrated-circuits-market>.
- [9] D. J. Richardson, J. M. Fini, and L. E. Nelson, "Space-division multiplexing in optical fibres," *Nature Photonics*, vol. 7, no. 5. pp. 354–362, 2013.
- [10] R. M. Ferreira, A. Shahpari, J. D. Reis, and A. L. Teixeira, "Coherent UDWDM-PON With Dual-Polarization Transceivers in Real-Time," *IEEE Photonics Technology Letters*, vol. 29, no. 11, pp. 909–912, Jun. 2017.
- [11] C. E. Shannon, "A mathematical theory of communication," *Bell System Technical Journal, The*, vol. 27, no. 3. pp. 379–423, 1948.
- [12] I. Alimi, A. Shahpari, A. Sousa, R. Ferreira, P. Monteiro, and A. Teixeira, "Challenges and Opportunities of Optical Wireless Communication Technologies," in *Optical Communication Technology*, London: IntechOpen, 2017, pp. 5–43.
- [13] R.-J. Essiambre and R. W. Tkach, "Capacity Trends and Limits of Optical Communication Networks," *Proceedings of the IEEE*, vol. 100, no. 5, pp. 1035–1055, 2012.
- [14] H. Yuan, M. Furdek, A. Muhammad, A. Saljoghei, L. Wosinska, and G. Zervas, "Space-Division Multiplexing in Data Center Networks: On Multi-Core Fiber Solutions and Crosstalk-Suppressed Resource Allocation," *Journal of Optical Communications and Networking*, vol. 10, no. 4, pp. 272–288, Apr. 2018.
- [15] I. Morita, K. Igarashi, and T. Tsuritani, "1 Exabit/s-km transmission with Multi-core Fiber and Spectral Efficient Modulation Format," in *2014 OptoElectronics and Communication Conference and Australian Conference on Optical Fibre Technology*, pp. 316–318, 2014.
- [16] B. Batagelj, V. Janyani, and S. Tomažič, "Research Challenges in Optical Communications Towards 2020 and Beyond," *Informacije MIDE M*, vol. 44, no. 3. pp. 177–184, 01-Jan-2015.
- [17] R. Essiambre and A. Mecozzi, "Capacity limits in single-mode fiber and scaling for spatial multiplexing," *2012 Optical Fiber Communication Conference and Exposition and the National Fiber Optic Engineers Conference (OFC/NFOEC)*. pp. 1–3, 2012.
- [18] P. J. Winzer, "Optical Networking Beyond WDM," *IEEE Photonics Journal*, vol. 4, no. 2. pp. 647–651, 2012.
- [19] R.-J. Essiambre, R. Ryf, N. K. Fontaine, and S. Randel, "Breakthroughs in Photonics 2012: Space-Division Multiplexing in Multimode and Multicore Fibers for High-Capacity Optical Communication," *IEEE Photonics Journal*, vol. 5, no. 2, pp. 0701307–0701307, Apr. 2013.
- [20] P. J. Winzer, "Challenges and evolution of optical transport networks," *ECOC 2010 - European Conference and Exhibition on Optical Communication*. pp. 1–3, 2010.
- [21] A. E. Willner, S. Khaleghi, M. R. Chitgarha, and O. F. Yilmaz, "All-Optical Signal Processing," *Journal of Lightwave Technology*, vol. 32, no. 4, pp. 660–680, Feb. 2014.
- [22] M. Li, Y. Deng, J. Tang, S. Sun, J. Yao, J. Azaña, and N. Zhu, "Reconfigurable Optical Signal Processing Based on a Distributed Feedback Semiconductor Optical Amplifier," *Nature Scientific Reports*, vol. 6, no. 19985, pp. 1–9, Apr. 2016.

-
- [23] J. Capmany and D. Novak, "Microwave photonics combines two worlds," *Nature Photonics*, vol. 1, no. 6, pp. 319–330, Jun. 2007.
- [24] Grand View Research, "Photonic Integrated Circuit (IC) Market Size Report," 2016, Online: <http://www.grandviewresearch.com/industry-analysis/photonic-integrated-circuit-ic-market>.
- [25] E. Desurvire, C. Kazmierski, F. Lelarge, X. Marcadet, A. Scavennec, F. A. Kish, D. F. Welch, *et al.*, "Science and technology challenges in XXIst century optical communications," *Comptes Rendus Physique*, vol. 12, no. 4, pp. 387–416, May 2011.
- [26] J. Chovan and F. Uherek, "Photonic Integrated Circuits for Communication Systems," *Radio Engineering*, vol. 27, no. 2, pp. 357–363, 2018.
- [27] E. Ip and J. M. Kahn, "Increasing optical fiber transmission capacity beyond next-generation systems," *IEEE Lasers and Electro-Optics Society, 2008. LEOS 2008. 21st Annual Meeting of the*, pp. 606–607, 2008.
- [28] M. Smit, K. Williams, and J. van der Tol, "Past, present, and future of InP-based photonic integration," *APL Photonics*, vol. 4, no. 050901, pp. 1–10, May 2019.
- [29] A. B. González and J. Pozo, "The Biophotonics Revolution in Healthcare," *Optik & Photonik*, vol. 12, no. 3, pp. 16–17, Jun. 2017.
- [30] R. Wang, A. Vasiliev, M. Muneeb, A. Malik, S. Sprengel, G. Boehm, M.-C. Amann, *et al.*, "III-V-on-Silicon Photonic Integrated Circuits for Spectroscopic Sensing in the 2–4 μm Wavelength Range," *Sensors*, vol. 17, no. 1778, pp. 1–21, Aug. 2017.
- [31] V. C. Duarte, J. G. Prata, C. F. Ribeiro, R. N. Nogueira, G. Winzer, L. Zimmermann, R. Walker, *et al.*, "Modular coherent photonic-aided payload receiver for communications satellites," *Nature Communications*, vol. 10, no. 1984, pp. 1–9, Dec. 2019.
- [32] C. Pinho, G. S. D. Gordon, B. Neto, T. M. Morgado, F. Rodrigues, A. Tavares, M. Lima, T. D. Wilkinson, and A. Teixeira, "Flexible Spatial Light Modulator Based Coupling Platform for Photonic Integrated Processors," *International Journal on Advances in Telecommunications*, vol. 11, no. 1, pp. 20–31, Jul. 2018.
- [33] M. Smit, J. van der Tol, and M. Hill, "Moore's law in photonics," *Laser & Photonics Reviews*, vol. 6, no. 1, pp. 1–13, Jan. 2012.
- [34] J. Bardeen and W. H. Brattain, "Three-electrode circuit element utilizing semiconductive materials," Patent no. 2524035, United States patent office, Ed., pp. 1–14, Jun. 1948.
- [35] S. William, "Circuit element utilizing semiconductive material," pp. 1–13, Jun. 1948.
- [36] M. K. Alferov, Zh. I., Andreev, V. M., Portnoi, E. L., and Trukan, "AIAs-GaAs Heterojunction injection lasers with a low room-temperature threshold," *Fizika i Tekhnika Poluprovodnikov; Soviet Physics - Semiconductors*, vol. 3, no. 9, pp. 1328–1332; 1107–1110, 1969.
- [37] J. S. Kilby, "Miniaturized electronic circuits," Patent no. 3138743, pp. 1–9, Feb. 1959.
- [38] F. M. Wanlass and C. T. Sah, "Nanowatt logic using field-effect metal-oxide semiconductor triodes," in *IEEE International Solid-State Circuits Conference*, pp. 32–33, vol. VI, 1963.

- [39] M. Suzuki, Y. Noda, H. Tanaka, S. Akiba, Y. Kushiro, and H. Isshiki, "Monolithic integration of InGaAsP/InP distributed feedback laser and electroabsorption modulator by vapor phase epitaxy," *Journal of Lightwave Technology*, vol. 5, no. 9, pp. 1277–1285, 1987.
- [40] G. E. Moore, "Moore's law at 40," in *Understanding Moore's Law: Four Decades of Innovation*, no. Figure 2, D. C. Brock, Ed. Philadelphia, PA, USA: Chemical Heritage Foundation, 2006, pp. 67–84.
- [41] Heraldkeeper via COMTEX, "Photonic Integrated Circuit (PIC) Global Market Report 2019 Industry analysis, size, share, trends, growth, scope, business strategies, future prospects and regional forecast to 2023 - MarketWatch," *Photonic Integrated Circuit Market Synopsis - MarketWatch*, 2019. Online: <https://www.marketwatch.com/press-release/photonic-integrated-circuit-pic-global-market-report-2019-industry-analysis-size-share-trends-growth-scope-business-strategies-future-prospects-and-regional-forecast-to-2023-2019-03-22/print>.
- [42] P. Muñoz, G. Micó, L. A. Bru, D. Pastor, D. Pérez, J. D. Doménech, J. Fernández, R. Baños, B. Gargallo, R. Alemany, A. M. Sánchez, J. M. Cirera, R. Mas, and C. Domínguez, "Silicon nitride photonic integration platforms for visible, near-infrared and mid-infrared applications," *Sensors*, vol. 17, no. 2088, pp. 1–25, 2017.
- [43] A. E.-J. Lim, Junfeng Song, Qing Fang, Chao Li, Xiaoguang Tu, Ning Duan, Kok Kiong Chen, R. P.-C. Tern, and Tsung-Yang Liow, "Review of Silicon Photonics Foundry Efforts," *IEEE Journal of Selected Topics in Quantum Electronics*, vol. 20, no. 4, pp. 405–416, Jul. 2014.
- [44] J. E. Bowers, T. Komljenovic, M. Davenport, J. Hulme, A. Y. Liu, C. T. Santis, A. Spott, S. Srinivasan, E. J. Stanton, and C. Zhang, "Recent advances in silicon photonic integrated circuits," in *Next-Generation Optical Communication: Components, Sub-Systems, and Systems*, pp. 1–18, vol. 977402, Feb. 2016.
- [45] P. Dong, Y.-K. Chen, G.-H. Duan, and D. T. Neilson, "Silicon photonic devices and integrated circuits," *Nanophotonics*, vol. 3, no. 45, pp. 215–228, 2014.
- [46] M. Smit, X. Leijtens, H. Ambrosius, E. Bente, J. Van Der Tol, B. Smalbrugge, T. De Vries, *et al.*, "An introduction to InP-based generic integration technology," *Semiconductor Science and Technology, IOP science*, vol. 29, no. 83001, pp. 1–41, 2014.
- [47] R. Nagarajan, M. Kato, J. Pleumeekers, P. Evans, S. Corzine, S. Hurtt, A. Dentai, *et al.*, "InP Photonic Integrated Circuits," *IEEE Journal of Selected Topics in Quantum Electronics*, vol. 16, no. 5, pp. 1113–1125, Sep. 2010.
- [48] K. Ławniczuk, L. M. Augustin, N. Grote, M. J. Wale, M. K. Smit, and K. A. Williams, "Open access to technology platforms for InP-based photonic integrated circuits," *Advances in Optical Technologies*, vol. 4, no. 2, pp. 157–165, 2015.
- [49] M.-C. Tien, J. F. Bauters, M. J. R. Heck, D. J. Blumenthal, and J. E. Bowers, "Ultra-low loss Si₃N₄ waveguides with low nonlinearity and high power handling capability," *Optics Express*, vol. 18, no. 23, pp. 23562–23568, Nov. 2010.
- [50] A. Leinse, R. G. Heideman, M. Hoekman, F. Schreuder, F. Falke, C. G. H. Roeloffzen, L. Zhuang, M. Burla, D. Marpaung, D. H. Geuzebroek, R. Dekker, E. J. Klein, P. W. L. van Dijk, and R. M. Oldenbeuving, "TriPleX waveguide platform: low-loss technology over a wide wavelength range," in *Proceedings SPIE 8767, Integrated Photonics: Materials, Devices, and Applications II*, pp. 1–13, vol.

87670E, May 2013.

- [51] D. D. John, G. Brodnik, S. Gundavarapu, R. L. Moreira, M. Belt, T. Huffman, and D. J. Blumenthal, "Low-Loss Photonic Integration: Applications in Datacenters," in *Datacenter Connectivity Technologies: Principles and Practice*, F. Chang, Ed. River Publishers Series in Optics and Photonics, 2018, pp. 431–480.
- [52] L. Augustin, M. Smit, N. Grote, M. Wale, and R. Visser, "Standardized process could revolutionize photonic integration," *Euro Photonics*, vol. 18, no. 3, pp. 30–34, 2013.
- [53] JePPIX - Joint European Platform for Photonic Integration of Components and Circuits, "JePPIX Roadmap 2018," May 2018, Online: <http://www.jepix.eu/introduction-to-roadmaps>.
- [54] J. F. Bauters, M. J. R. Heck, D. D. John, J. S. Barton, C. M. Bruinink, A. Leinse, R. G. Heideman, D. J. Blumenthal, and J. E. Bowers, "Planar waveguides with less than 0.1 dB/m propagation loss fabricated with wafer bonding," *Optics Express*, vol. 19, no. 24, pp. 24090–24101, Nov. 2011.
- [55] M. Belt and D. J. Blumenthal, "Erbium-doped waveguide DBR and DFB laser arrays integrated within an ultra-low-loss Si₃N₄ platform," *Optics Express*, vol. 22, no. 9, pp. 10655–10660, May 2014.
- [56] C. Pinho, A. Tavares, G. Cabral, T. Morgado, A. Shahpari, M. Lima, and A. Teixeira, "Design and Characterization of an Optical Chip for Data Compression based on Haar Wavelet Transform," in *OFC 2017 - Optical Fiber Communication Conference*, p. Th2A.9(3), Mar. 2017.
- [57] C. Pinho, B. Neto, T. M. Morgado, H. Neto, M. Lima, and A. Teixeira, "InP AAC for Data Compression Applications," *IET Optoelectronics, Special issue: 2018 European Conference on Integrated Optics (ECIO 2018)*, vol. 13, no. 2, pp. 67–71, Apr. 2019.
- [58] C. Pinho, T. Morgado, B. Neto, M. Lima, and A. Teixeira, "Implementation and Optimization of a Cost-Effective 2D Haar Transform Network for Image Compression," in *FIO+LS 2018 - OSA Frontiers in Optics and Laser Science Conference*, p. JTU3A.88(2), Sep. 2018.
- [59] G. M. Brodnik, C. Pinho, F. Chang, and D. J. Blumenthal, "Extended Reach 40km Transmission of C-Band Real-Time 53.125 Gbps PAM-4 Enabled with a Photonic Integrated Tunable Lattice Filter Dispersion Compensator," in *OFC 2018 - Optical Fiber Communication Conference*, p. W2A.30(3), Mar. 2018.
- [60] T. A. Huffman, G. M. Brodnik, C. Pinho, S. Gundavarapu, D. Baney, and D. J. Blumenthal, "Integrated Resonators in an Ultralow Loss Si₃N₄/SiO₂ Platform for Multifunction Applications," *IEEE Journal of Selected Topics in Quantum Electronics*, vol. 24, no. 4, pp. 1–9, Mar. 2018.
- [61] S. Gundavarapu, M. Puckett, T. Huffman, R. Behunin, J. Wu, T. Qiu, G. M. Brodnik, C. Pinho, D. Bose, P. T. Rakich, J. Nohava, K. D. Nelson, M. Salit, and D. J. Blumenthal, "Integrated Waveguide Brillouin Laser," *Physics archive (Physics - arXiv), Cornell University Library*, pp. 1–15, Sep. 2017.
- [62] S. Gundavarapu, G. M. Brodnik, M. Puckett, T. Huffman, D. Bose, R. Behunin, J. Wu, T. Qiu, C. Pinho, N. Chauhan, J. Nohava, P. T. Rakich, K. D. Nelson, M. Salit, and D. J. Blumenthal, "Sub-hertz fundamental linewidth photonic integrated Brillouin laser," *Nature Photonics*, vol. 13, no. 1, pp. 60–67, Jan. 2019.
- [63] C. Pinho, F. Rodrigues, A. Tavares, G. S. D. Gordon, A. Shahpari, M. M. Lima, T. D. Wilkinson, and A. A. Teixeira, "Flexible Platform for Feeding Photonic Integrated Processors," in *AICT 2017 -*

- Advanced International Conference on Telecommunications*, pp. 1–4, Jun. 2017.
- [64] C. Pinho, B. Neto, T. M. Morgado, A. Sousa, A. Albuquerque, M. Lima, and A. Teixeira, “Spatial light modulator based flexible coupling platform for applications in SDM and PIC,” in *ECIO 2018 - European Conference on Integrated Optics*, pp. 238–240, May 2018.
- [65] R. A. S. Ferreira, C. D. S. Brites, C. M. S. Vicente, P. P. Lima, A. R. N. Bastos, P. G. Marques, M. Hiltunen, L. D. Carlos, and P. S. André, “Photonic-on-a-chip: a thermal actuated Mach-Zehnder interferometer and a molecular thermometer based on a single di-ureasil organic-inorganic hybrid,” *Laser & Photonics Reviews*, vol. 7, no. 6, pp. 1027–1035, Nov. 2013.
- [66] E. Wong, “Next-generation broadband access networks and technologies,” *Journal of Lightwave Technology*, vol. 30, no. 4, pp. 597–608, 2012.
- [67] V. Ashok, T. Balakumaran, C. Gowrishankar, I. L. A. Vennila, and A. N. Kumar, “The Fast Haar Wavelet Transform for Signal & Image Processing,” *International Journal of Computer Science and Information Security (IJCSIS)*, vol. 7, no. 1, pp. 126–130, 2010.
- [68] G. Parca, P. Teixeira, and A. Teixeira, “All-optical image processing and compression based on Haar wavelet transform,” *Applied Optics*, vol. 52, no. 12, pp. 2932–2939, 2013.
- [69] H. Herrmann, K. Schafer, and W. Sohler, “Polarization Independent, Integrated Optical, Acoustically Tunable Wavelength Filters/Switches with Tapered Acoustical Directional Coupler,” *IEEE Photonics Technology Letters*, vol. 6, no. 11, pp. 1335–1337, 1994.
- [70] L. Almeida, N. Kumar, G. Parca, A. Tavares, A. Lopes, and A. Teixeira, “All-Optical image processing based on Integrated Optics,” *ICTON 2014 - International Conference on Transparent Optical Networks*, pp. 1–5, 2014.
- [71] T. Mizumoto and Y. Naito, “Dependence of the Output Phase Difference on the Asymmetry of 3-dB Directional Couplers,” *Journal of Lightwave Technology*, vol. 8, no. 10, pp. 1571–1576, 1990.
- [72] Z. Lu, H. Yun, Y. Wang, Z. Chen, F. Zhang, N. A. F. Jaeger, and L. Chrostowski, “Broadband silicon photonic directional coupler using asymmetric-waveguide based phase control,” *Optics Express*, vol. 23, no. 3, pp. 941–947, 2015.
- [73] L. B. Soldano and E. C. M. Pennings, “Optical Multi-Mode Interference Devices Based on Self-Imaging: Principles and Applications,” *Journal of Lightwave Technology*, vol. 13, no. 4, pp. 615–627, Apr. 1995.
- [74] L. A. Coldren, S. W. Corzine, and M. L. Mašanović, *Diode Lasers and Photonic Integrated Circuits*, 2nd ed. Hoboken, NJ, USA: John Wiley & Sons, Inc., 2012.
- [75] P. A. Besse, M. Bachmann, H. Melchior, L. B. Soldano, and M. K. Smit, “Optical Bandwidth and Fabrication Tolerances of Multimode Interference Couplers,” *Journal of Lightwave Technology*, vol. 12, no. 6, pp. 1004–1009, 1994.
- [76] J. Fernandes, M. Lima, F. Rodrigues, and A. Teixeira, “First approach on the Haar Transform applied with a 2x2 multimode interferometer,” in *AOP 2017 - International Conference on Applications of Optics and Photonics*, pp. 1–7, vol. 10453, Aug. 2017.
- [77] A. Melloni, “Reconfigurable photonic signal processing circuits,” in *OFC 2017 - Optical Fiber*

Communication Conference, p. Tu3F.3(1-3), 2017.

- [78] D. Pérez, J. Fernández, R. Baños, J. D. Doménech, A. M. Sánchez, J. M. Cirera, R. Mas, J. Sánchez, S. Durán, E. Pardo, C. Domínguez, D. Pastor, J. Capmany, and P. Muñoz, "Thermal tuners on a Silicon Nitride platform," *Physics archive (Physics - arXiv)*, Cornell University Library, pp. 1–13, 2016.
- [79] K. Deb, M. S. Al-Seraj, M. M. Hoque, and M. I. H. Sarkar, "Combined DWT-DCT based digital image watermarking technique for copyright protection," in *ICECE 2012 - International Conference on Electrical and Computer Engineering*, pp. 458–461, Dec. 2012.
- [80] C. Christopoulos, A. Skodras, and T. Ebrahimi, "The JPEG2000 still image coding system: an overview," *IEEE Transactions on Consumer Electronics*, vol. 46, no. 4, pp. 1103–1127, 2000.
- [81] K. S. Thyagarajan, *Still Image and Video Compression with MATLAB*. Hoboken, NJ, USA, NJ, USA: John Wiley & Sons, Inc., 2011.
- [82] M. Vetterli, J. Kovačević, and V. K. Goyal, *Foundations of signal processing*. Cambridge University Press, 2014.
- [83] J. Kovacevic, V. K. Goyal, and M. Vetterli, *Fourier and Wavelet Signal Processing*. Cambridge University Press, 2013.
- [84] A. Takagi, K. Jinguji, and M. Kawachi, "Design and fabrication of broad-band silica-based optical waveguide couplers with asymmetric structure," *IEEE Journal of Quantum Electronics*, vol. 28, no. 4, pp. 848–855, Apr. 1992.
- [85] P. Muñoz, J. D. Domenech, C. Dominguez, A. Sanchez, G. Mico, L. A. Bru, D. Perez, and D. Pastor, "State of the art of Silicon Nitride photonics integration platforms," in *ICTON 2017 - International Conference on Transparent Optical Networks*, pp. 1–4, Jul. 2017.
- [86] G. Micó, L. A. Bru, D. Pastor, D. Doménech, J. Fernández, A. Sánchez, J. M. Cirera, C. Domínguez, and P. Muñoz, "Silicon nitride photonics: from visible to mid-infrared wavelengths," in *Silicon Photonics XIII - SPIE OPTO 2018*, pp. 1–9, vol. 10537, no. 105370B, 2018.
- [87] W. Liu, M. Li, R. S. Guzzon, E. J. Norberg, J. S. Parker, M. Lu, L. A. Coldren, and J. Yao, "A fully reconfigurable photonic integrated signal processor," *Nature Photonics*, vol. 10, no. 3, pp. 190–195, 2016.
- [88] H. F. Talbot, "I. Facts relating to optical science. No. III," *Philosophical Magazine Series 3*, vol. 9, no. 56, pp. 401–407, 1836.
- [89] Centro Nacional de Microelectronica (CNM) and VLC Photonics, "CNM-VLC Design Manual v.5.0." pp. 1–38, 2017.
- [90] Institute of Microelectronics of Barcelona IBM-CNM, "Silicon Nitride Technology," 2019. Online: <http://www.imb-cnm.csic.es/index.php/en/clean-room/silicon-nitride-technology>.
- [91] K. Okamoto, *Fundamentals of optical waveguides*, 2nd ed. Academic Press, Elsevier, 2006.
- [92] Synopsys Software, "Synopsys OptoDesigner Tools," 2019. Online: <https://www.synopsys.com/photonic-solutions/pic-design-suite.html?submenu=dfa&subsubmenu=3&prdgprID=3>.

- [93] P. A. Besse, E. Gini, M. Bachmann, and H. Melchior, "New 2×2 and 1×3 multimode interference couplers with free selection of power splitting ratios," *Journal of Lightwave Technology*, vol. 14, no. 10, pp. 2286–2293, 1996.
- [94] J. D. Domenech, J. S. Fandino, B. Gargallo, and P. Munoz, "Arbitrary Coupling Ratio Multimode Interference Couplers in Silicon-on-Insulator," *Journal of Lightwave Technology*, vol. 32, no. 14, pp. 2536–2543, Jul. 2014.
- [95] M. Alemohammad, J. R. Stroud, B. T. Bosworth, and M. A. Foster, "High-speed all-optical Haar wavelet transform for real-time image compression," *Optics Express*, vol. 25, no. 9, pp. 9802–9811, 2017.
- [96] M. Li and J. Yao, "All-Optical Short-Time Fourier Transform Based on a Temporal Pulse-Shaping System Incorporating an Array of Cascaded Linearly Chirped Fiber Bragg Gratings," *IEEE Photonics Technology Letters*, vol. 23, no. 20, pp. 1439–1441, Oct. 2011.
- [97] M. T. Hill, X. J. M. Leijtens, G. D. Khoe, and M. K. Smit, "Optimizing imbalance and loss in 2x2 3dB multimode interference couplers via access waveguide width," *Journal of Lightwave Technology*, vol. 21, no. 10, pp. 2305–2313, Oct. 2003.
- [98] R. Califa, "Post-Fabrication Trimming of Silicon-Photonic Devices using a Photo-Sensitive Upper Cladding," Thesis at Bar-Ilan University, 2015.
- [99] Y. Ben Ezra, D. Munk, A. Zadok, B. I. Lembrikov, and R. Califa, "All-optical wavelet-based orthogonal frequency division multiplexing system based on silicon photonic integrated components," *IET Optoelectronics*, vol. 10, no. 2, pp. 44–50, Apr. 2016.
- [100] R. ; Piramidowicz, S. T. ; Stopinski, K. ; Lawniczuk, K. ; Welikow, P. ; Szczepanski, X. J. M. ; Leijtens, M. K. Smit, *et al.*, "Photonic integrated circuits: a new approach to laser technology," *Bulletin of the Polish Academy of Sciences Technical Sciences*, vol. 60, no. 4, pp. 683–689, 2012.
- [101] D. Verzijl, K. Derojeda, M. Lengton, and A. Koonstra, "InP PICs for data center applications, Report on promising KETs-based product nr. 5," European Union, 2017, Online: https://ec.europa.eu/growth/tools-databases/kets-tools/sites/default/files/documents/analytical_report_nr5_inp_pics_final.pdf.
- [102] G. Gilardi and M. K. Smit, "Generic InP-Based Integration Technology : Present and Prospects," *Progress In Electromagnetics Research*, 2014. Online: <http://www.jpier.org/PIER/pier147/02.14022001.pdf>.
- [103] J. S. Fandiño, P. Muñoz, D. Doménech, and J. Capmany, "A monolithic integrated photonic microwave filter," *Nature Photonics*, vol. 11, no. 2, pp. 124–129, Feb. 2017.
- [104] G. Gilardi and M. K. Smit, "Generic InP-Based Integration Technology : Present and Prospects," *Progress In Electromagnetics Research*. pp. 23–35, 2014.
- [105] JePPIX, "Joint European Platform for InP-based Photonic Integrated Components and Circuits." Online: <http://www.jepix.eu>.
- [106] PARADIGM, "Photonic Advanced Research and Development for Integrated Generic Manufacturing," May 29, 2014, PARADIGM and EuroPIC consortia. Online: <http://www.paradigm.jepix.eu/>.

-
- [107] J. Leuthold and C. H. Joyner, "Multimode Interference Couplers with Tunable Power Splitting Ratios," *Journal of Lightwave Technology*, vol. 19, no. 5, pp. 700–707, 2001.
- [108] JePPIX, "PARADIGM/EuroPIC Design Manual." PARADIGM and EuroPIC consortia, pp. 1–232, 2014.
- [109] PhoeniX Software - Solutions for Micro and Nano Technologies, "PhoeniX Software Manual." PhoeniX Software, pp. 1–1071, 2018.
- [110] Leica Microsystems, "Leica Application Suite," *Leica Microsystems*, 2015. Online: <http://www.leica-microsystems.com/products/microscope-software/life-sciences/las-easy-and-efficient/>.
- [111] Rogers Corporation, "Advanced Connectivity Solutions - RO4000 Laminates," © *Rogers Corporation*, 2018. Online: <https://www.rogerscorp.com/acs/producttypes/9/RO4000-Laminates.aspx>.
- [112] Keysight Technologies, "Advanced Design System (ADS)," © *Keysight Technologies*. Online: <https://www.keysight.com/en/pc-1297113/advanced-design-system-ads?cc=PT&lc=eng>.
- [113] R. Hartley, "RF / Microwave PC Board Design and Layout," *L-3 Avionics Systems*. 2000.
- [114] G. G. Harman, *Wire bonding in microelectronics*, 3rd ed. McGraw-Hill, 2010.
- [115] H. Neto, "Packaging of Photonic Integrated Circuits," Thesis at University of Aveiro, 2017.
- [116] Multicomp, "Thermoelectric Cooling Modules - Peltier Cooler," *Multicomp*, 2013. Online: <http://www.rmtltd.ru/products/temodules/>.
- [117] Corning Product Information, "Corning SMF-28 Ultra Optical Fiber," no. November. Corning Incorporated, pp. 1–2, 2014.
- [118] G. D. Pettit and W. J. Turner, "Refractive Index of InP," *Journal of Applied Physics*, vol. 36, no. 6, pp. 2081–2081, Jun. 1965.
- [119] M. Polyanskiy, "Refractive index database - optical constants of InP," *RefractiveIndex.INFO*. Online: <https://refractiveindex.info/?shelf=main&book=InP&page=Pettit>.
- [120] J. S. Lee, L. Carroll, C. Scarcella, N. Pavarelli, S. Menezo, S. Bernabe, E. Temporiti, and P. O'Brien, "Meeting the Electrical, Optical, and Thermal Design Challenges of Photonic-Packaging," *IEEE Journal of Selected Topics in Quantum Electronics*, vol. 22, no. 6, pp. 409–417, Nov. 2016.
- [121] S. McNab, N. Moll, and Y. Vlasov, "Ultra-low loss photonic integrated circuit with membrane-type photonic crystal waveguides," *Optics Express*, vol. 11, no. 22, pp. 2927–2939, Nov. 2003.
- [122] L. Carroll, J.-S. Lee, C. Scarcella, K. Gradkowski, M. Duperron, H. Lu, Y. Zhao, *et al.*, "Photonic Packaging: Transforming Silicon Photonic Integrated Circuits into Photonic Devices," *Applied Sciences*, vol. 6, no. 426, pp. 1–21, Dec. 2016.
- [123] C. A. Edwards, H. M. Presby, and C. Dragone, "Ideal Microlenses for Laser to Fiber Coupling," *Journal of Lightwave Technology*, vol. 11, no. 2, pp. 252–257, 1993.
- [124] M. Azadeh, *Fiber Optics Engineering*, University. Springer Science+Business Media, LLC, 233 Spring Street, New York, NY 10013, USA, 2009.
- [125] J. H. C. Van Zantvoort, S. G. L. Plukker, E. C. A. Dekkers, G. D. Petkov, G. D. Khoe, A. M. J.

- Koonen, and H. De Waardt, "Lensed fiber-array assembly with individual fiber fine positioning in the submicrometer range," *IEEE Journal on Selected Topics in Quantum Electronics*, vol. 12, no. 5, pp. 931–938, 2006.
- [126] A. Jaffe, "LAZERMaster™ LZM-100 Manual," *Fujikura*, no. June. pp. 1–121, 2014.
- [127] AFL, "LAZERMaster LZM-100 Laser Splicing System," 2019. Online: <https://www.aflglobal.com/Products/Fusion-Splicing/Specialty-Fusion-Splicing-Equipment/Splicers/LAZERMaster-LZM-100-Laser-Splicing-System.aspx>.
- [128] W. Zheng, "Optic Lenses Manufactured on Fiber Ends," in *OGC 2015 - Optoelectronics Global Conference*, pp. 1–7, Aug. 2015.
- [129] Edmund Optics, "Ball Lens Calculator - Edmund Optics," *Edmund Optics Inc.*, 2019. Online: <https://www.edmundoptics.com/resources/tech-tools/ball-lens/>.
- [130] P. Karioja, J. Ollila, V.-P. Putila, K. Keranen, J. Hakkila, and H. Kopola, "Comparison of active and passive fiber alignment techniques for multimode laser pigtailling," in *ECTC 2000 - Electronic Components and Technology Conference*, pp. 244–249, 2000.
- [131] N. Pavarelli, J. S. Lee, and P. A. O'Brien, "Packaging challenges for integrated silicon photonic circuits," in *Silicon Photonics and Photonic Integrated Circuits IV*, pp. 91330F-1–9, vol. 9133, May 2014.
- [132] U. H. P. Fischer, "Opto-Electronic Packaging," in *Optoelectronics - Advanced Materials and Devices*, IntechOpen, 2016, pp. 421–444.
- [133] Agilent Technologies, "Accurate Characterization of Source Spectra Using an Optical Spectrum Analyzer - Application Note 1550-5," 2001.
- [134] C. M. S. Vicente, E. Pecoraro, R. A. S. Ferreira, P. S. André, R. Nogueira, Y. Messaddeq, S. J. L. Ribeiro, and L. D. Carlos, "Waveguides and gratings fabrication in zirconium-based organic/inorganic hybrids," *Journal of Sol-Gel Science and Technology*, vol. 48, no. 1–2, pp. 80–85, Nov. 2008.
- [135] A. R. N. Bastos, "Green photonics: photonic integrated circuits for optical communications and sensing based on organic-inorganic hybrids," Thesis at University of Aveiro, 2018.
- [136] C. M. S. Vicente, P. P. Lima, V. de Z. Bermudez, L. D. Carlos, P. S. André, and R. A. S. Ferreira, "Fabrication of low-cost thermo-optic variable wave plate based on waveguides patterned on di-ureasil hybrids," *Optics Express*, vol. 22, no. 22, pp. 27159–27168, Nov. 2014.
- [137] C. M. S. Vicente, R. Venkatachaam, B. M. Ferreira, P. G. Marques, C. A. F. Marques, E. Pecoraro, L. D. Carlos, P. S. André, and R. A. S. Ferreira, "Thin film optimization design of organic-inorganic hybrids for waveguide high-rejection optical filters," *Physica Status Solidi (RRL) - Rapid Research Letters*, vol. 5, no. 8, pp. 280–282, Aug. 2011.
- [138] A. R. N. Bastos, A. Shahpari, E. Rodríguez-Castellón, M. Lima, P. S. André, and R. A. S. Ferreira, "Green photonics integrated circuit for NGOA coherent receivers," *Optics & Laser Technology*, vol. 115, pp. 222–228, Jul. 2019.
- [139] A. Bastos, C. Vicente, R. Oliveira-Silva, N. Silva, M. Tação, J. Costa, M. Lima, *et al.*, "Integrated Optical Mach-Zehnder Interferometer Based on Organic-Inorganic Hybrids for Photonics-on-a-Chip

- Biosensing Applications,” *Sensors*, vol. 18, no. 840, pp. 1–11, Mar. 2018.
- [140] T. M. Morgado, B. Neto, C. Pinho, C. M. Vicente, and A. Teixeira, “Cost-Effective Magic-T using Organic-Inorganic Hybrid Materials for Image Compression,” in *ICTON 2018 - International Conference on Transparent Optical Networks*, p. Tu.P.6(4), Jul. 2018.
- [141] T. M. Morgado, B. Neto, C. M. S. Vicente, C. Pinho, and A. L. J. Teixeira, “Passive Phase Shifters Based in 1×1 MMI for Cost-Effective Photonic Integrated Circuits,” in *ICTON 2018 - International Conference on Transparent Optical Networks*, p. Tu.P.4(4), Jul. 2018.
- [142] D. C. Oliveira, A. G. Macedo, N. J. O. Silva, C. Molina, R. A. S. Ferreira, P. S. André, K. Dahmouche, V. D. Z. Bermudez, Y. Messaddeq, S. J. L. Ribeiro, and L. D. Carlos, “Photopatternable Di-ureasil–Zirconium Oxocluster Organic–Inorganic Hybrids As Cost Effective Integrated Optical Substrates,” *Chemistry of Materials*, vol. 20, no. 11, pp. 3696–3705, Jun. 2008.
- [143] V. R. Fernandes, C. M. S. Vicente, E. Pecoraro, D. Karpinsky, A. L. Kholkin, N. Wada, P. S. Andre, and R. A. S. Ferreira, “Determination of Refractive Index Contrast and Surface Contraction in Waveguide Channels Using Multiobjective Genetic Algorithm Applied to Spectroscopic Ellipsometry,” *Journal of Lightwave Technology*, vol. 29, no. 19, pp. 2971–2978, Oct. 2011.
- [144] M. U. Khan, J. Justice, J. Petäjä, T. Korhonen, A. Boersma, S. Wiegersma, M. Karppinen, and B. Corbett, “Multi-level single mode 2D polymer waveguide optical interconnects using nano-imprint lithography,” *Optics Express*, vol. 23, no. 11, pp. 14630–14639, Jun. 2015.
- [145] Newport, “Objective lens M-10X,” *Newport Corporation*, 2019. Online: <https://www.newport.com/p/M-10X>.
- [146] Duma Optronics, “Duma Optronics BeamOn IR1550,” *Duma Optronics Ltd*, 2019. Online: <https://www.dumaoptronics.com/beamon>.
- [147] J. F. Bauters, M. J. R. Heck, D. John, D. Dai, M.-C. Tien, J. S. Barton, A. Leinse, R. G. Heideman, D. J. Blumenthal, and J. E. Bowers, “Ultra-low-loss high-aspect-ratio Si₃N₄ waveguides,” *Optics Express*, vol. 19, no. 4, pp. 3163–3174, Feb. 2011.
- [148] C. Ciminelli, F. Dell’Olio, C. E. Campanella, and M. N. Armenise, “Photonic technologies for angular velocity sensing,” *Advances in Optics and Photonics*, vol. 2, no. 3, pp. 370–404, 2010.
- [149] E. F. Burmeister, D. J. Blumenthal, and J. E. Bowers, “A comparison of optical buffering technologies,” *Optical Switching and Networking*, vol. 5, no. 1, pp. 10–18, Mar. 2008.
- [150] E. F. Burmeister, J. P. Mack, H. N. Poulsen, M. L. Mašanovic, B. Stamenic, D. J. Blumenthal, and J. E. Bowers, “Photonic integrated circuit optical buffer for packet-switched networks,” *Optics Express*, vol. 17, no. 8, pp. 6629–6635, Apr. 2009.
- [151] M.-C. Tien, J. F. Bauters, M. J. R. Heck, D. T. Spencer, D. J. Blumenthal, and J. E. Bowers, “Ultra-high quality factor planar Si₃N₄ ring resonators on Si substrates,” *Optics Express*, vol. 19, no. 14, pp. 13551–13556, Jul. 2011.
- [152] K. Kikuchi, “Fundamentals of Coherent Optical Fiber Communications,” *Journal of Lightwave Technology*, vol. 34, no. 1, pp. 157–179, Jan. 2016.
- [153] J. Kitching, S. Knappe, and E. A. Donley, “Atomic Sensors – A Review,” *IEEE Sensors Journal*, vol.

- 11, no. 9, pp. 1749–1758, Sep. 2011.
- [154] C. L. Degen, F. Reinhard, and P. Cappellaro, “Quantum sensing,” *Reviews of Modern Physics*, vol. 89, no. 3–035002, pp. 1–39, Jul. 2017.
- [155] A. D. Ludlow, M. M. Boyd, J. Ye, E. Peik, and P. O. Schmidt, “Optical atomic clocks,” *Reviews of Modern Physics*, vol. 87, no. 2, pp. 637–701, Jun. 2015.
- [156] R. Moreira, S. Gundavarapu, and D. J. Blumenthal, “Programmable eye-opener lattice filter for multi-channel dispersion compensation using an integrated compact low-loss silicon nitride platform,” *Optics Express*, vol. 24, no. 15, pp. 16732–16742, Jul. 2016.
- [157] Y. Xuan, Y. Liu, L. T. Varghese, A. J. Metcalf, X. Xue, P.-H. Wang, K. Han, *et al.*, “High-Q silicon nitride microresonators exhibiting low-power frequency comb initiation,” *Optica*, vol. 3, no. 11, pp. 1171–1180, Nov. 2016.
- [158] D. K. Armani, T. J. Kippenberg, S. M. Spillane, and K. J. Vahala, “Ultra-high-Q toroid microcavity on a chip,” *Nature*, vol. 421, no. 6926, pp. 925–928, Feb. 2003.
- [159] K. Y. Yang, D. Y. Oh, S. H. Lee, Q.-F. Yang, X. Yi, and K. Vahala, “Integrated Ultra-High-Q Optical Resonator,” *arXiv:1702.05076v2 [physics.optics]*, pp. 1–5, 2017.
- [160] J. Li, H. Lee, K. Y. Yang, and K. J. Vahala, “Sideband spectroscopy and dispersion measurement in microcavities,” *Optics Express*, vol. 20, no. 24, pp. 26337–26344, Nov. 2012.
- [161] T. Wei, J. Huang, X. Lan, Q. Han, and H. Xiao, “Optical fiber sensor based on a radio frequency Mach-Zehnder interferometer,” *Optics letters*, vol. 37, no. 4, pp. 647–9, 2012.
- [162] W. Bogaerts, P. de Heyn, T. van Vaerenbergh, K. de Vos, S. Kumar Selvaraja, T. Claes, P. Dumon, P. Bienstman, D. van Thourhout, and R. Baets, “Silicon microring resonators,” *Laser and Photonics Reviews*, vol. 6, no. 1, pp. 47–73, 2012.
- [163] P. Chamorro-Posada, “Q-enhanced racetrack microresonators,” *Physics archive (Physics - arXiv)*, vol. 387, pp. 1–26, Mar. 2016.
- [164] D. T. Spencer, J. F. Bauters, M. J. R. Heck, and J. E. Bowers, “Integrated waveguide coupled Si₃N₄ resonators in the ultrahigh-Q regime,” *Optica*, vol. 1, no. 3, pp. 153–157, Sep. 2014.
- [165] MathWorks, “R2018b - MATLAB and Simulink product families,” *The MathWorks, Inc.* Online: https://www.mathworks.com/products/new_products/latest_features.html.
- [166] M. Chagnon, M. Morsy-Osman, and D. V. Plant, “Multi-Dimensional Formats and Transceiver Architectures for Direct Detection With Analysis on Inter-Polarization Phase Modulation,” *Journal of Lightwave Technology*, vol. 35, no. 4, pp. 885–892, Feb. 2017.
- [167] U. M. Fayyad, G. Piatetsky-Shapiro, and P. Smyth, “From data mining to knowledge discovery: an overview,” *Advances in knowledge discovery and data mining*. American Association for Artificial Intelligence, pp. 1–34, 1996.
- [168] F. Chang and S. Bhoja, “New Paradigm Shift to PAM4 Signalling at 100/400G for Cloud Data Centers: A Performance Review,” in *ECOC 2017 - European Conference on Optical Communication*, pp. 1–3, Sep. 2017.

-
- [169] M. Birk, L. E. Nelson, G. Zhang, C. Cole, C. Yu, M. Akashi, K. Hiramoto, X. Fu, P. Brooks, A. Schubert, T. Baldwin, R. Luking, and G. Pepper, "First 400GBASE-LR8 interoperability using CFP8 modules," in *OFC 2017 - Optical Fiber Communication Conference*, p. Th5B.7(3), 2017.
- [170] F. Chang, S. Bhoja, J. Riani, I. Hosagrahar, J. Wu, S. Herlekar, A. Tiruvur, P. Khandelwal, and K. Gopalakrishnan, "Link Performance Investigation of Industry First 100G PAM4 IC Chipset with Real-time DSP for Data Center Connectivity," in *OFC 2016 - Optical Fiber Communication Conference*, p. Th1G.2(3), 2016.
- [171] T. K. Chan and W. I. Way, "112 Gb/s PAM4 Transmission Over 40km SSMF Using 1.3 μ m Gain-Clamped Semiconductor Optical Amplifier," in *OFC 2015 - Optical Fiber Communication Conference*, p. Th3A.4(3), Mar. 2015.
- [172] M. Filer, S. Searcy, Y. Fu, R. Nagarajan, and S. Tibuleac, "Demonstration and Performance Analysis of 4 Tb / s DWDM Metro-DCI System with 100G PAM4 QSFP28 Modules," in *OFC 2017 - Optical Fiber Communication Conference*, p. W4D.4(3), 2017.
- [173] N. Eiselt, J. Wei, H. Griesser, A. Dochhan, M. Eiselt, J.-P. Elbers, J. J. V. Olmos, and I. T. Monroy, "First Real-Time 400G PAM-4 Demonstration for Inter-Data Center Transmission over 100 km of SSMF at 1550 nm," in *OFC 2016 - Optical Fiber Communication Conference*, p. W1K.5(3), Mar. 2016.
- [174] N. Eiselt, J. Wei, H. Griesser, A. Dochhan, M. H. Eiselt, J.-P. Elbers, J. J. V. Olmos, and I. T. Monroy, "Evaluation of Real-Time 8 \times 56.25 Gb/s (400G) PAM-4 for Inter-Data Center Application Over 80 km of SSMF at 1550 nm," *Journal of Lightwave Technology*, vol. 35, no. 4, pp. 955–962, Feb. 2017.
- [175] G. P. Agrawal, "Fiber-optic communication systems," *Wiley series in microwave and optical engineering*. Wiley-Interscience, New York, pp. xvii, 546 p., 2002.
- [176] P. J. Winzer and R. Essiambre, "Advanced Optical Modulation Formats," *Proceedings of the IEEE*, vol. 94, no. 5. pp. 952–985, 2006.
- [177] Inphi, "Optical PHY - Inphi." Online: <https://www.inphi.com/products/optical-phy/>.
- [178] Corning, "SMF-28® Ultra Optical Fibers," *Corning Incorporated*. Online: <https://www.corning.com/worldwide/en/products/communication-networks/products/fiber/smf-28-ultra.html>.
- [179] T. Zhu, S. Veilleux, J. Bland-Hawthorn, and M. Dagenais, "Ultra-broadband High Coupling Efficiency Using a Si₃N₄/SiO₂ waveguide on silicon," in *SUM 2016 - IEEE Photonics Society Summer Topical Meeting Series*, pp. 92–93, 2016.
- [180] J. W. Goodman, *Introduction to Fourier Optics*, 2nd ed. Stanford: McGraw-Hill Companies, 1996.
- [181] J. Carpenter, "Holographic Mode Division Multiplexing in Optical Fibres," Thesis at University of Cambridge, Cambridge UK, 2012.
- [182] G. Lazarev, A. Hermerschmidt, and S. Kr, "LCOS Spatial Light Modulators: Trends and Applications," in *Optical Imaging and Metrology: Advanced Technologies*, Weinheim: Wiley-VCH, 2012, pp. 1–29.
- [183] Holoeye, "Spatial Light Modulators," *Holoeye Photonics AG*, 2013. Online: <http://holoeye.com/spatial-light-modulators/>.

- [184] Hamamatsu, "Phase spatial light modulator LCOS-SLM," in *Opto-Semiconductor Handbook*, Tokyo: Hamamatsu Photonics, 2012, pp. 1–14.
- [185] M. Kovachev, R. Ilieva, L. Onural, G. B. Esmer, T. Reyhan, P. Benzie, J. Watson, and E. Mitev, "Reconstruction of Computer Generated Holograms by Spatial Light Modulators," *Multimedia Content Representation, Classification and Security*, vol. 4105. Springer Berlin Heidelberg, pp. 706–713, 2006.
- [186] S. H. Younus, A. T. Hussein, M. T. Alresheedi, and J. M. H. Elmirghani, "CGH for Indoor Visible Light Communication System," *IEEE Access*, vol. 5, pp. 24988–25004, 2017.
- [187] N. Collings, T. Davey, J. Christmas, D. Chu, and B. Crossland, "The Applications and Technology of Phase-Only Liquid Crystal on Silicon Devices," *Journal of Display Technology*, vol. 7, no. 3, pp. 112–119, Mar. 2011.
- [188] M. A. F. Roelens, S. Frisken, J. A. Bolger, D. Abakoumov, G. Baxter, S. Poole, and B. J. Eggleton, "Dispersion Trimming in a Reconfigurable Wavelength Selective Switch," *Journal of Lightwave Technology*, vol. 26, no. 1, pp. 73–78, Jan. 2008.
- [189] M. Wang, L. Zong, L. Mao, A. Marquez, Y. Ye, H. Zhao, and F. Vaquero Caballero, "LCoS SLM Study and Its Application in Wavelength Selective Switch," *Photonics*, vol. 4, no. 2, pp. 1–22, 2017.
- [190] J. Turunen and F. Wyrowski, *Diffraction optics for industrial and commercial applications*. Berlin: John Wiley & Sons, 1997.
- [191] W. Osten, C. Kohler, and J. Liesener, "Evaluation and application of spatial light modulators for optical metrology," in *OPTOEL 2005 - Óptica Pura y Aplicada, Reunión Española de Optoelectrónica*, pp. 71–81, 2005.
- [192] J. J. M. Varga, A. M. A. Solís-Prosser, L. Rebón, A. Arias, L. Neves, C. Lemmi, and S. Ledesma, "Preparing arbitrary pure states of spatial qubits with a single phase-only spatial light modulator," *Journal of Physics: Conference Series*, vol. 605, no. 1, pp. 012035–6, Apr. 2015.
- [193] J. Schroder, M. A. F. Roelens, L. B. Du, A. J. Lowery, and B. J. Eggleton, "LCOS based waveshaper technology for optical signal processing and performance monitoring," in *OECC 2012 - Opto-Electronics and Communications Conference*, pp. 859–860, Jul. 2012.
- [194] B. P. Keyworth, "ROADM subsystems and technologies," in *OFC/NFOEC 2005 - Optical Fiber Communication Conference*, p. OWB5(4), 2005.
- [195] S. de Hennin, P. Wall, S. H. Moffat, B. P. Keyworth, and P. D. Colbourne, "Addressing Manufacturability and Reliability of MEMS-based WSS," in *OFC/NFOEC 2007 - Conference on Optical Fiber Communication and the National Fiber Optic Engineers Conference*, pp. OWV1-3, Mar. 2007.
- [196] T. A. Strasser and J. L. Wagener, "Wavelength-Selective Switches for ROADM Applications," *IEEE Journal of Selected Topics in Quantum Electronics*, vol. 16, no. 5, pp. 1150–1157, Sep. 2010.
- [197] M. Shiraiwa, H. Furukawa, T. Miyazawa, Y. Awaji, and N. Wada, "High-Speed Wavelength Resource Reconfiguration System Concurrently Establishing/Removing Multiwavelength Signals," *IEEE Photonics Journal*, vol. 8, no. 2, pp. 1–7, Apr. 2016.

-
- [198] H. J. Lee, H. S. Moon, S.-K. Choi, and H. S. Park, "Multi-core fiber interferometer using spatial light modulators for measurement of the inter-core group index differences," *Optics Express*, vol. 23, no. 10, pp. 12555–12561, May 2015.
- [199] J. Lhermite, E. Suran, V. Kermene, F. Louradour, A. Desfarges-Berthelemot, and A. Barthélémy, "Coherent combining of 49 laser beams from a multiple core optical fiber by a spatial light modulator.," *Optics express*, vol. 18, no. 5, pp. 4783–9, Mar. 2010.
- [200] Y. Torii, L. Balladares-Ocana, and J. Martinez-Castro, "An Iterative Fourier Transform Algorithm for digital hologram generation using phase-only information and its implementation in a fixed-point digital signal processor," *Optik*, vol. 124, no. 22, pp. 5416–5421, 2013.
- [201] O. Ripoll, V. Kettunen, and H. P. Herzig, "Review of iterative Fourier-transform algorithms for beam shaping applications," *Optical Engineering*, vol. 43, no. 11, pp. 2549–2556, 2004.
- [202] C. Pinho, M. Lima, and A. Teixeira, "Optical compensation approach for SDM systems," in *SEONs 2016 - Symposium on Enabling Optical Networks and Sensors*, pp. 1–4, 2016.
- [203] L. B. Lesem, P. M. Hirsch, and J. A. Jordan, "The Kinoform: A New Wavefront Reconstruction Device," *IBM Journal of Research and Development*, vol. 13, no. 2, pp. 150–155, Mar. 1969.
- [204] J. Carpenter and T. D. Wilkinson, "Graphics processing unit-accelerated holography by simulated annealing," *Optical Engineering*, vol. 49, no. 9, pp. 095801–7, 2010.
- [205] R. Gerchberg, W. O. Saxton, B. R. W. Gerchberg, and W. O. Saxton, "A Practical Algorithm for the Determination of Phase from Image and Diffraction Plane Pictures," *Optik*, vol. 35, no. 2, pp. 237–246, 1972.
- [206] D. P. Bertsekas, *Constrained Optimization and Lagrange Multiplier Methods*. Belmonte, MA: Academic Press, Inc., 1996.
- [207] HOLOEYE Photonics AG, "LC 2012 Spatial Light Modulator (transmissive) | HOLOEYE Photonics AG," 2012. Online: <https://holoeye.com/spatial-light-modulators/lc-2012-spatial-light-modulator/>.
- [208] HOLOEYE Photonics AG, "PLUTO-2 Phase Only Spatial Light Modulator (Reflective) | HOLOEYE Photonics AG," 2018. Online: <https://holoeye.com/spatial-light-modulators/slm-pluto-phase-only/>.
- [209] F. Chang, K. Onohara, and T. Mizuochi, "Forward error correction for 100 G transport networks," *IEEE Communications Magazine*, vol. 48, no. 3, pp. S48–S55, Mar. 2010.
- [210] A. Matiss, S. Bottacchi, J. K. Fischer, R. Ludwig, C. C. Leonhardt, C. Schmidt-Langhorst, and C. Schubert, "Performance of an Integrated Coherent Receiver Module for up to 160G DP-QPSK Transmission Systems," *Journal of Lightwave Technology*, vol. 29, no. 7, pp. 1026–1032, Apr. 2011.
- [211] MathWorks, "MATLAB - the language of technical computing - math, graphics, and programming," 2015. Online: <http://www.mathworks.com/products/matlab/>.

Appendix A

BPM simulation results of Si₃N₄ BB designs

Additional BPM optimized simulation results are provided for the 2×2 MMI and 1×2 MMI BB structures designed under: i) three different MMI geometric shapes implemented (i.e., A, B and C); and ii) the MMI widths $W_1 = 8, 9, 10, 11$ and $12 \mu\text{m}$.

EL metrics of the different optimized designs are determined for a range of MMI length (L) values and the distance between MMI input/output access WG (Δd). To access 2×2 MMI BB sum/subtraction coupling ratio behavior a phase of $\pi/2$ is launched in the top input arm of the 2×2 MMI BB structure, i.e., realizing a difference of phase between the MMI input arms of $\Delta\phi = \pi/2$. A coupling ratio of 100:0 is obtained in all 2×2 MMI BB structure designs implemented in the sum/subtraction operation mode. When no additional phase is launched in the 2×2 MMI input arms (i.e., $\Delta\phi = 0$ for the MMI splitting operation mode), a coupling ratio of 50:50 is achieved for all the implemented BB designs. The set of results reached for the 2×2 MMI BB are presented in Appendix section A.1. For the 1×2 MMI splitter BB, a coupling ratio of 50:50 was achieved in all BB structure designs implemented. The corresponding set of results obtained is presented in Appendix section A.2.

A.1 BB 2×2 MMI structures

A.1.1 BB 2×2 MMI – geometry A

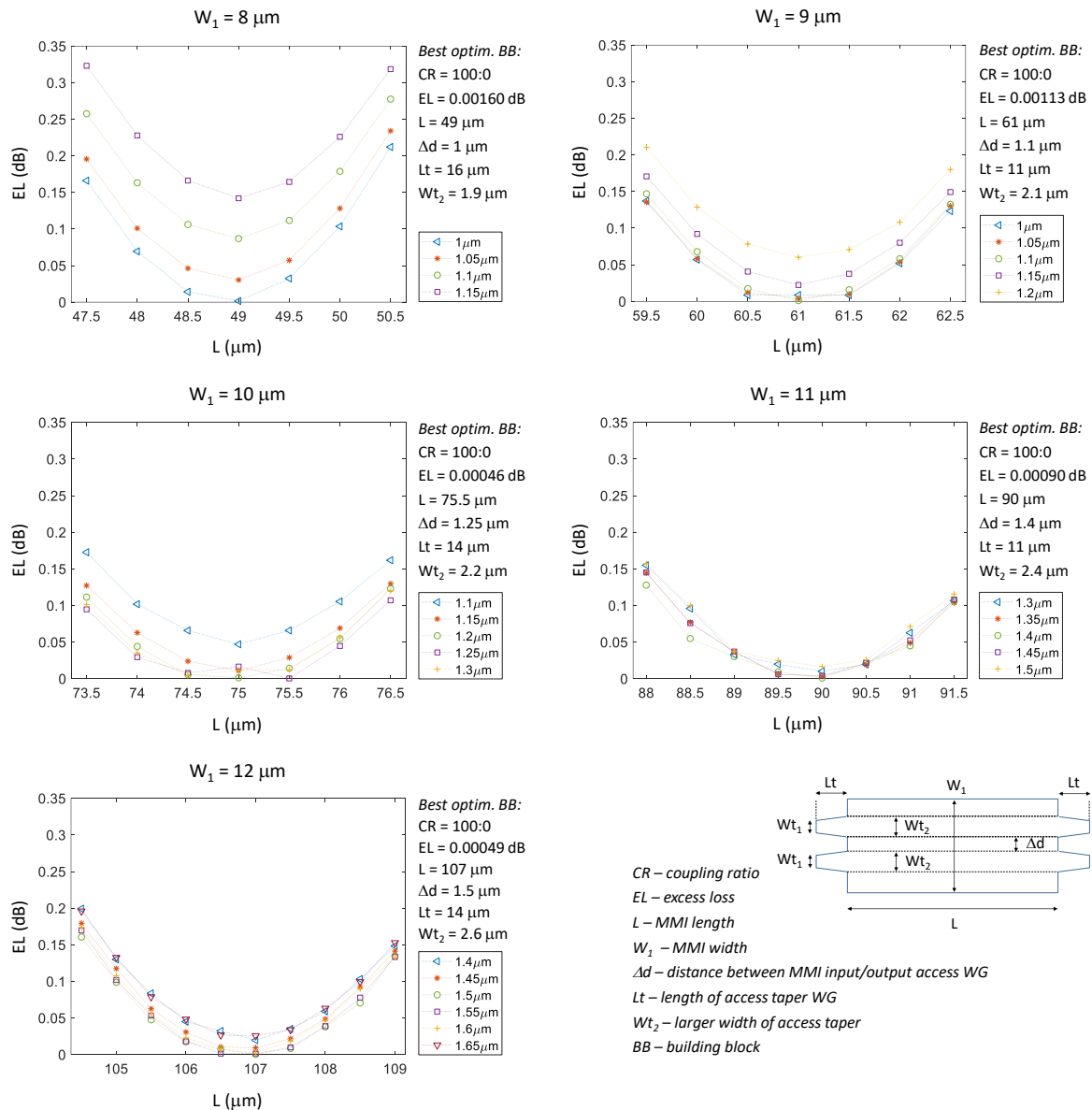


Figure A-1. EL metrics of the BB 2×2 MMI geometric shape A for MMI width $W_1 = 8, 9, 10, 11$ and $12 \mu\text{m}$, when a range set of values of L and Δd are implemented, and a phase of $\pi/2$ launched in the top input arm of the MMI BB. Best-optimized BB design parameters for the different W_1 widths are provided in the top right of each graph.

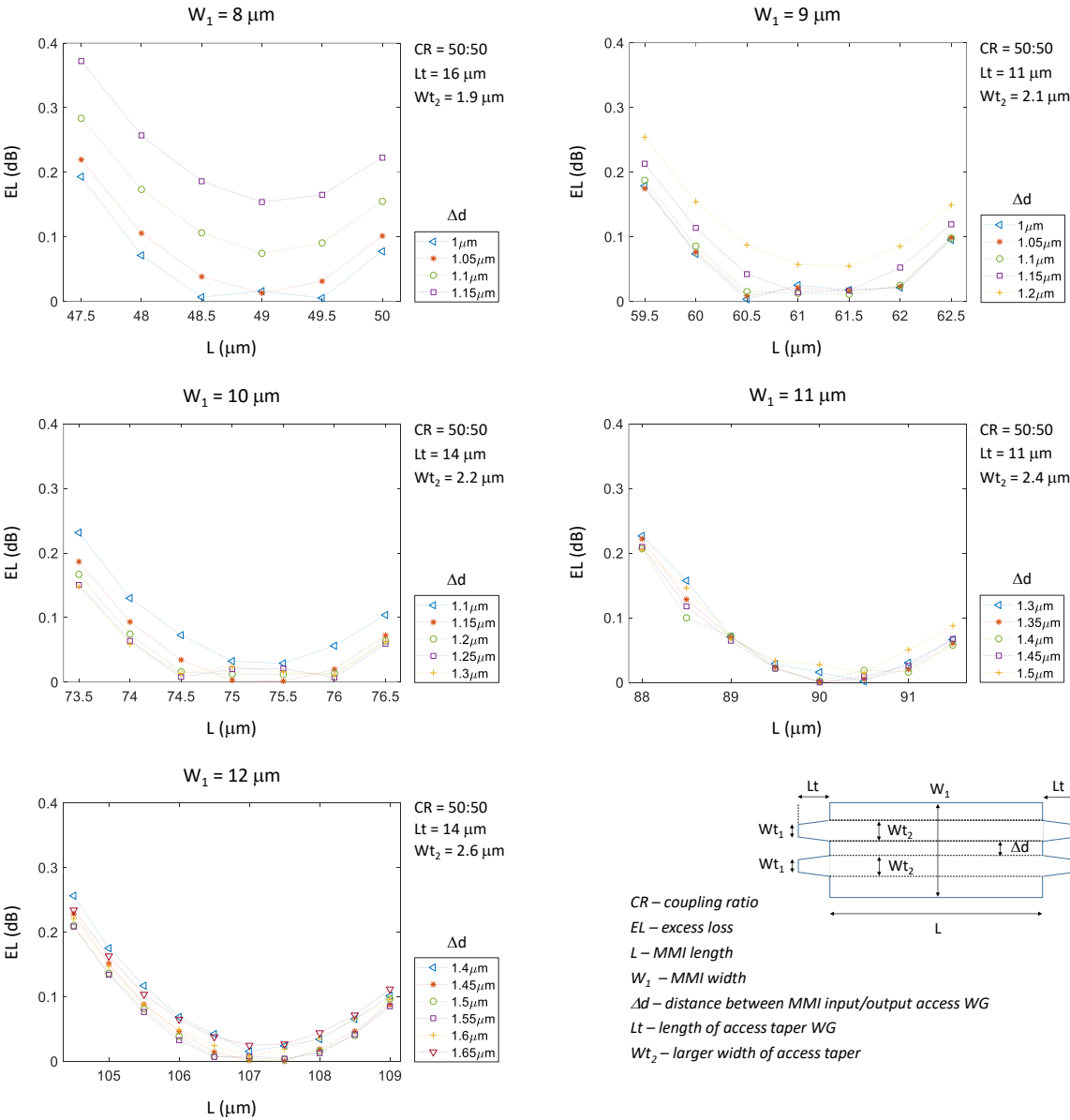


Figure A-2. EL metrics of the BB 2×2 MMI geometric shape A for MMI width $W_1 = 8, 9, 10, 11$ and $12 \mu\text{m}$, when a range set of values of L and Δd are implemented, and a relative phase between the MMI input arms is $\Delta\phi = 0$. Default BB design parameters (matching BB structure in the sum/subtraction operation mode) are provided in the top right of each graph.

A.1.2 BB 2x2 MMI – geometry B

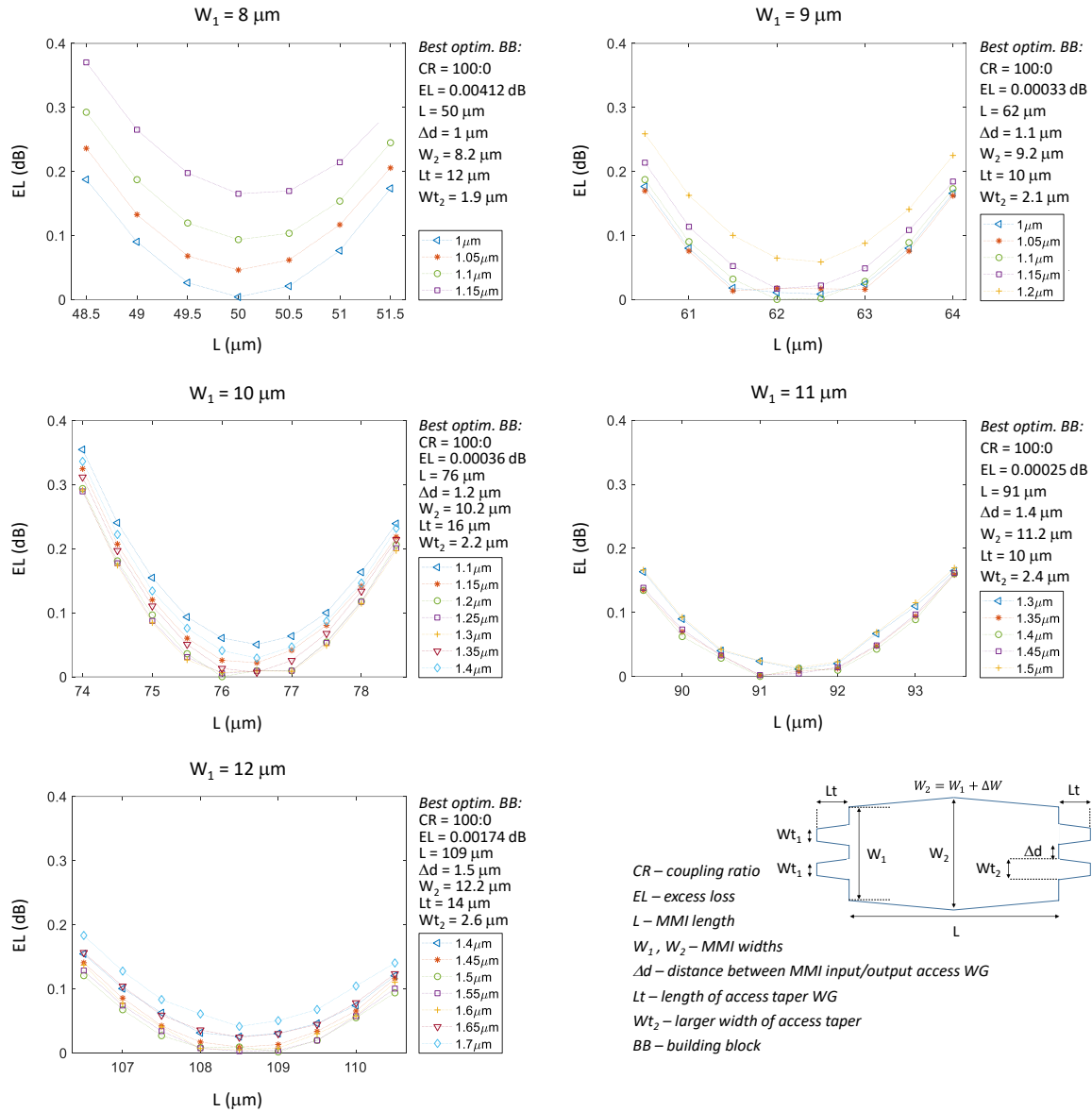


Figure A-3. EL metrics of the BB 2x2 MMI geometric shape B for MMI width W₁ = 8, 9, 10, 11 and 12 μm, when a range set of values of L and Δd are implemented, and a phase of π/2 launched in the top input arm of the MMI BB. Best-optimized BB design parameters for the different W₁ widths are provided in the top right of each graph.

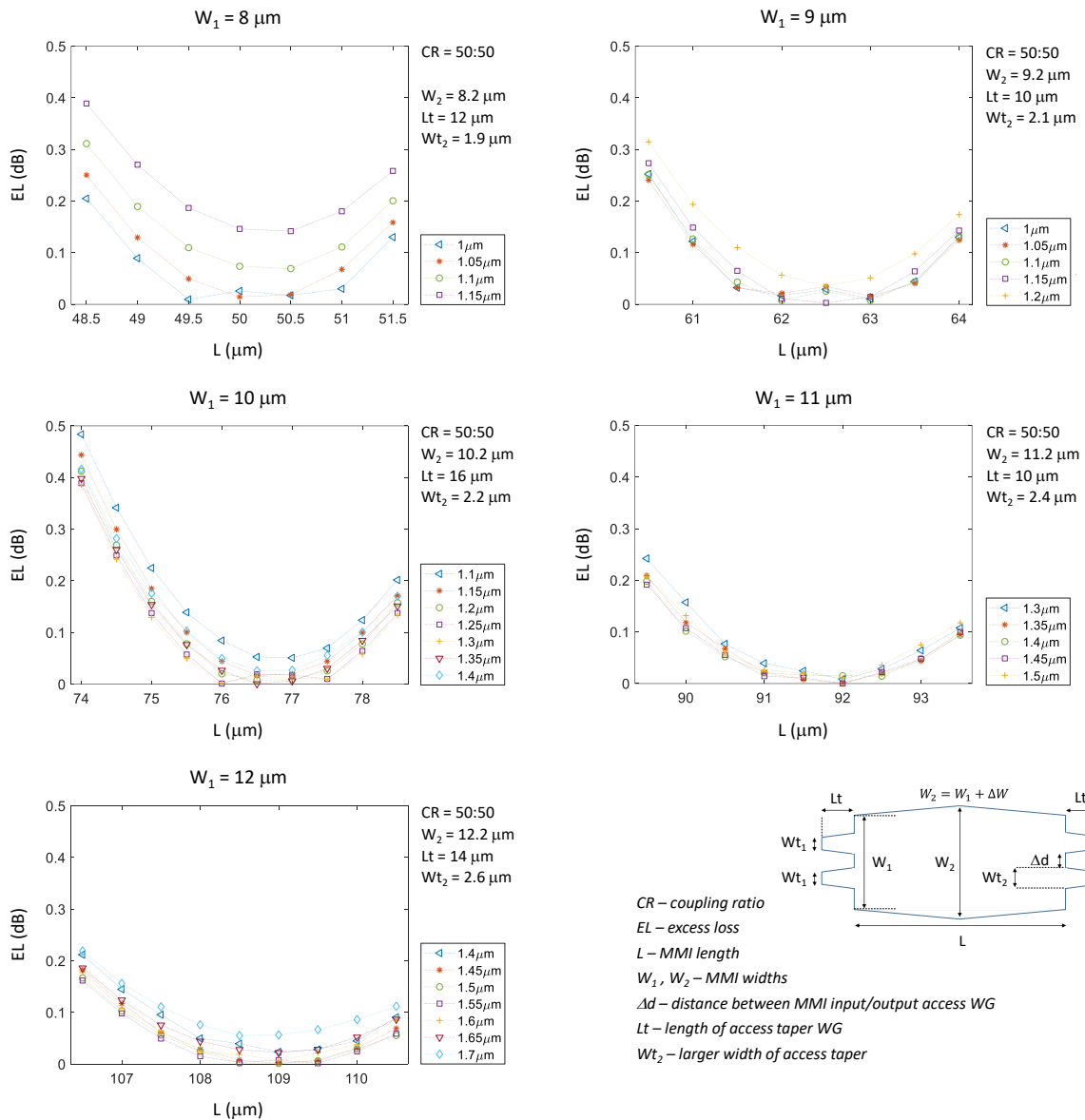


Figure A-4. EL metrics of the BB 2×2 MMI geometric shape B for MMI width $W_1 = 8, 9, 10, 11$ and $12 \mu\text{m}$, when a range set of values of L and Δd are implemented, and a relative phase between the MMI input arms is $\Delta\phi = 0$. Default BB design parameters (matching BB structure in the sum/subtraction operation mode) are provided in the top right of each graph.

A.1.3 BB 2x2 MMI – geometry C

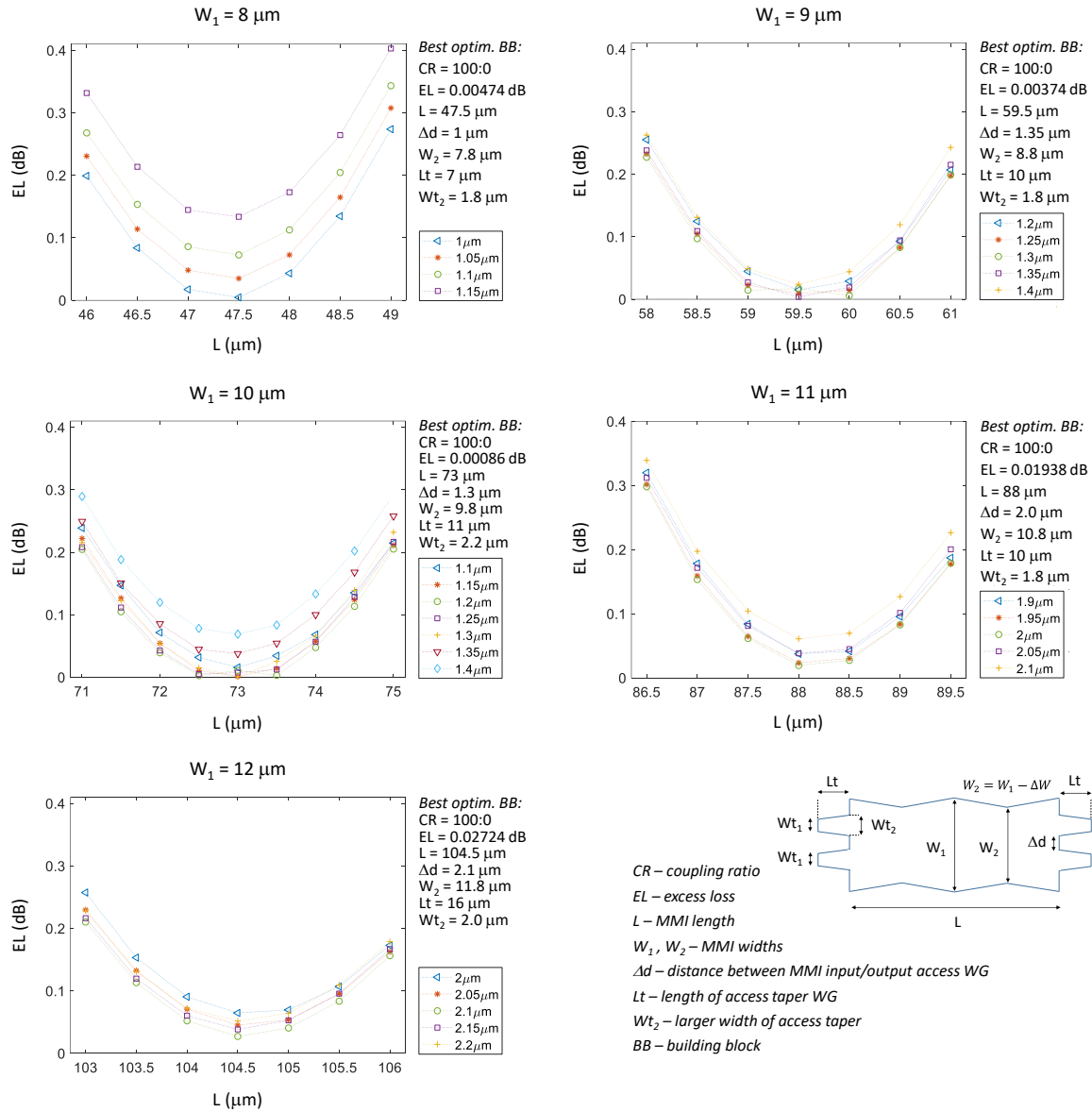


Figure A-5. EL metrics of the BB 2x2 MMI geometric shape C for MMI width W₁ = 8, 9, 10, 11 and 12 μm, when a range set of values of L and Δd are implemented, and a phase of π/2 launched in the top input arm of the MMI BB. Best-optimized BB design parameters for the different W₁ widths are provided in the top right of each graph.

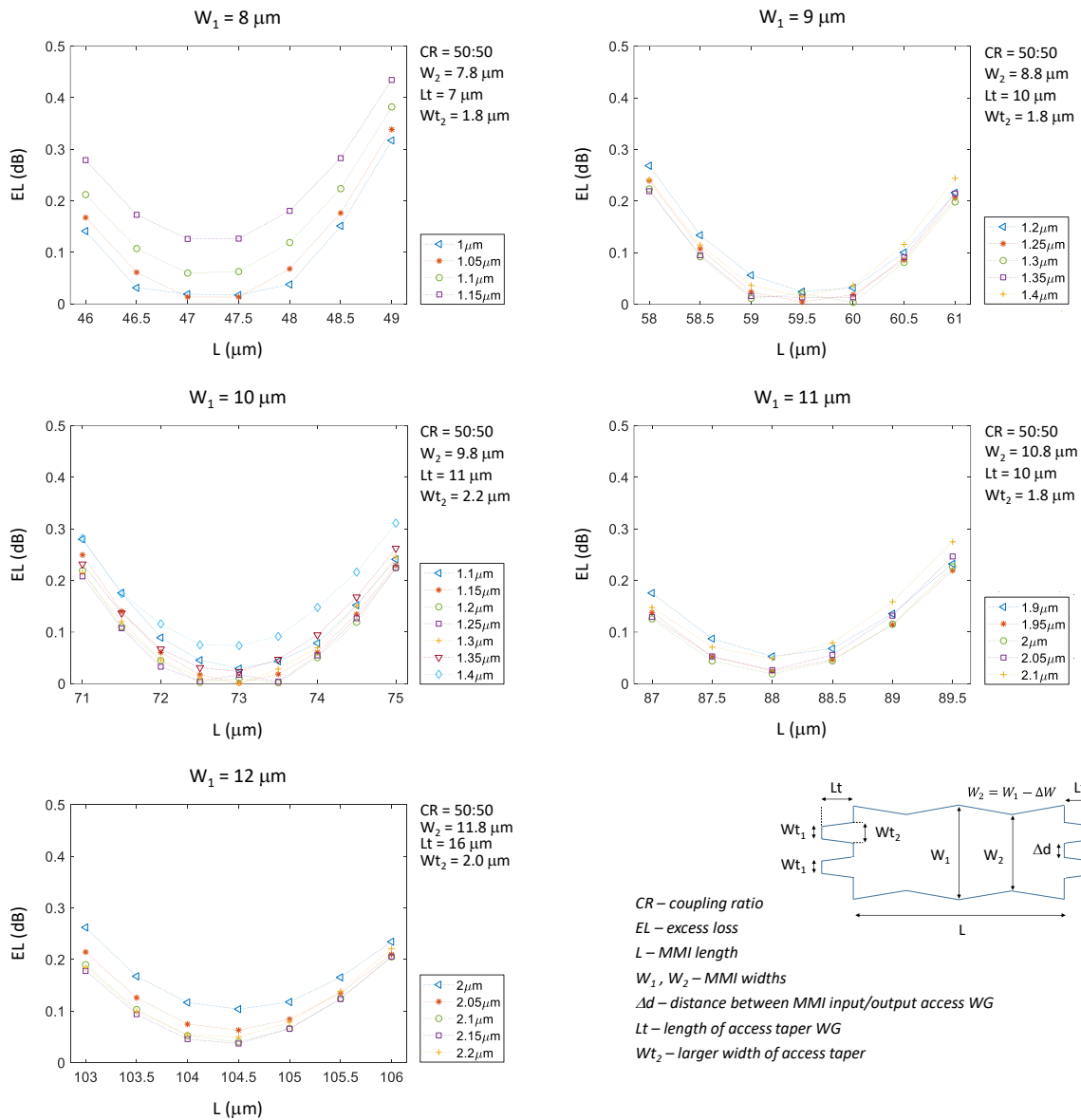


Figure A-6. EL metrics of the BB 2×2 MMI geometric shape C for MMI width $W_1 = 8, 9, 10, 11$ and $12 \mu\text{m}$, when a range set of values of L and Δd are implemented, and a relative phase between the MMI input arms is $\Delta\phi = 0$. Default BB design parameters (matching BB structure in the sum/subtraction operation mode) are provided in the top right of each graph.

A.2 BB 1×2 MMI structures

A.2.1 BB 1×2 MMI – geometry A

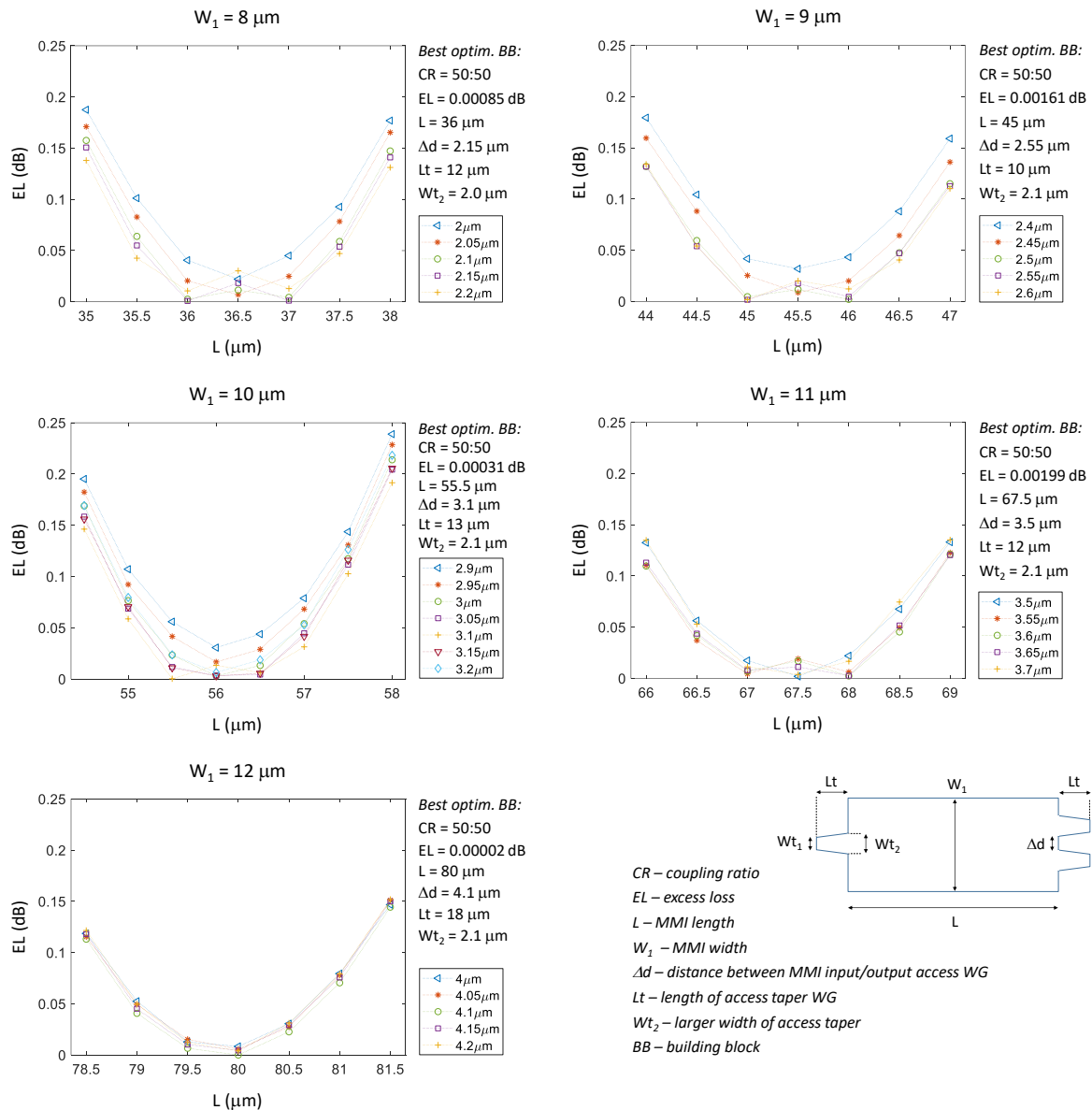


Figure A-7. EL metrics of the BB 1×2 MMI geometric shape A for MMI width $W_1 = 8, 9, 10, 11$ and $12 \mu\text{m}$, when a range set of values of L and Δd are implemented. Best-optimized BB design parameters for the different W_1 widths are provided in the top right of each graph.

A.2.2 BB 1×2 MMI – geometry B

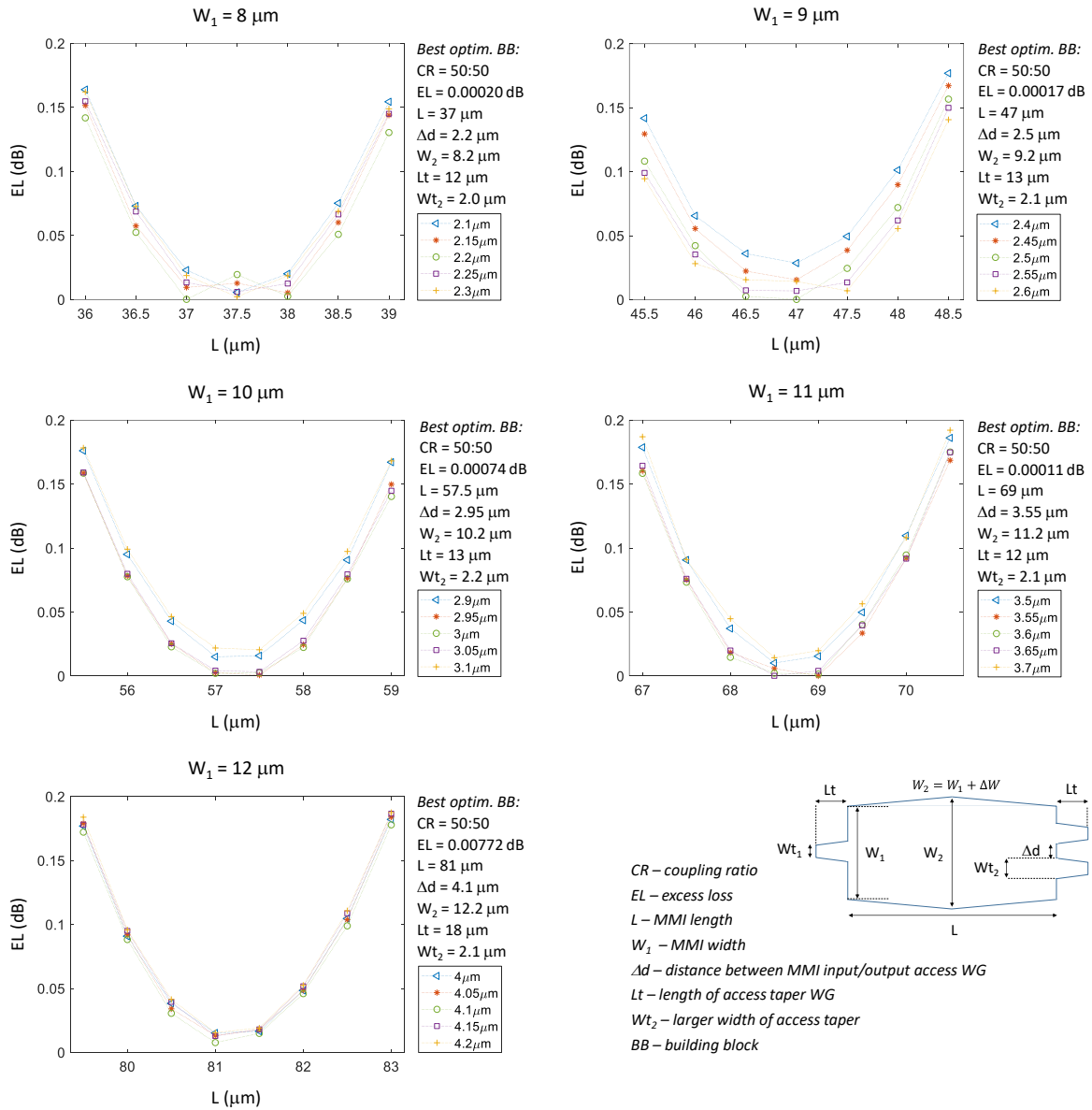


Figure A-8. EL metrics of the BB 1×2 MMI geometric shape B for MMI width $W_1 = 8, 9, 10, 11$ and $12 \mu\text{m}$, when a range set of values of L and Δd are implemented. Best-optimized BB design parameters for the different W_1 widths are provided in the top right of each graph.

A.2.3 BB 1×2 MMI – geometry C

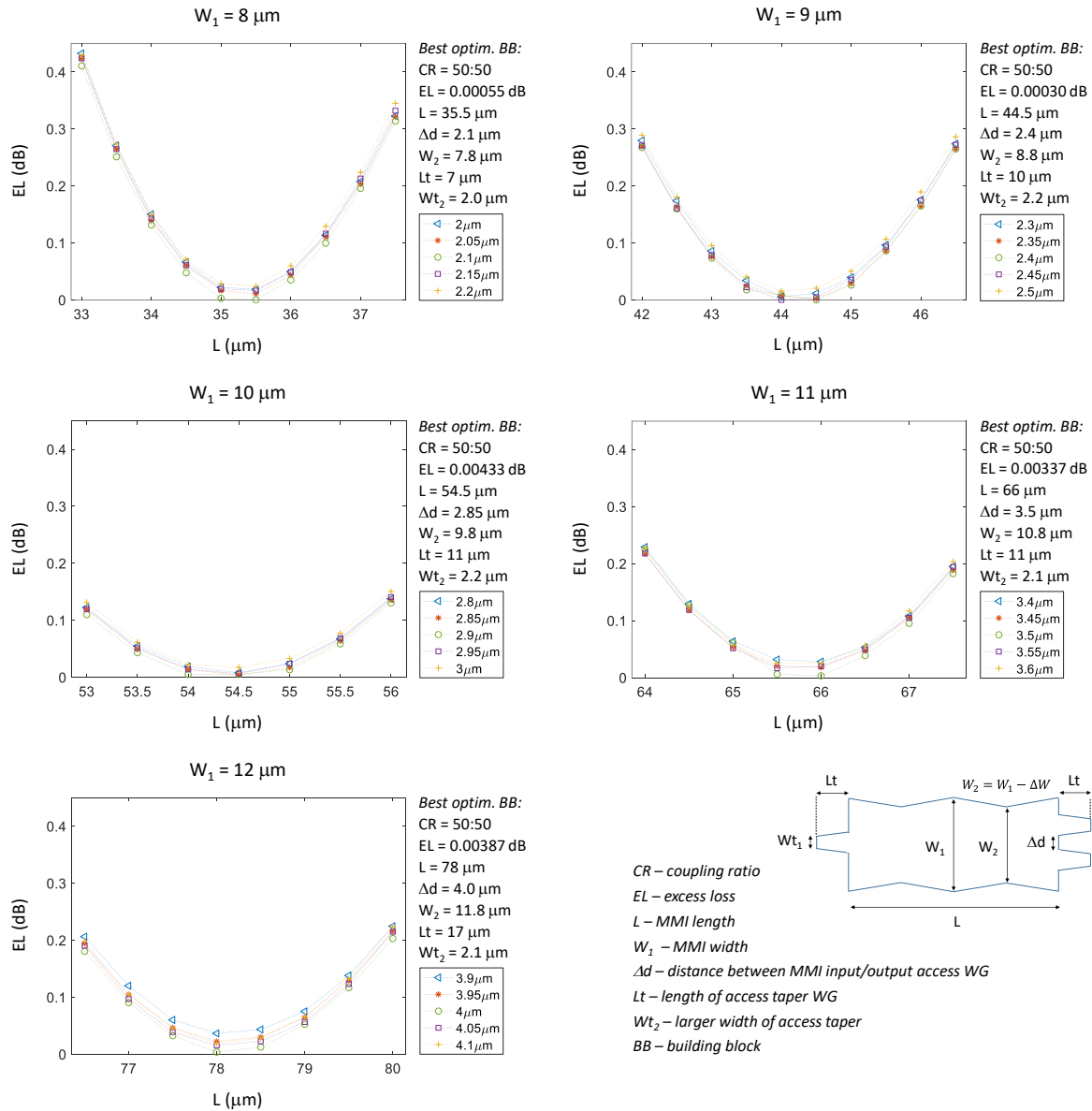


Figure A-9. EL metrics of the BB 1×2 MMI geometric shape C for MMI width $W_1 = 8, 9, 10, 11$ and $12 \mu\text{m}$, when a range set of values of L and Δd are implemented. Best-optimized BB design parameters for the different W_1 widths are provided in the top right of each graph.